AN INVESTIGATION OF SELECTED PROPERTIES OF AS-CAST, V-Ti-Fe ALLOYS

John LeRoy Johnsen
B.S., United States Military Academy, 1956
M.E., Stevens Institute of Technology, 1971

A dissertation submitted to the faculty
of the Oregon Graduate Center
in partial fulfillment of the
requirements for the degree
Doctor of Philosophy
in
Materials Science and Engineering

August, 1985

The dissertation ''An Investigation of Selected Properties of As-Cast, V-Ti-Fe Alloys'' by John LeRoy Johnsen has been examined and approved by the following Examination Committee:

William E. Wood, Thesis Advisor
Professor

John S. Blakemore
Professor

Jack H. Devletian
Associate Professor

Robert M. Drosd
Adjunct Professor

DEDICATION

I dedicate this work to my son,
John William Johnsen, Lance Corporal,
United States Marine Corps, who
lost his life in a motor vehicle
accident on 13 January 1984.

ACKNOWLEDGEMENTS

The Materials Science and Engineering Department of the Oregon Graduate Center has a long-standing tradition of internal cooperation, especially among the students and the technical staff. It is virtually inconceivable that a major research project could be carried out in the department, without some involvement, at one time or another, of most of the people in the department. Accordingly, I would like to thank all of the faculty and technical staff and all of my fellow students for their contributions, however small, to this investigation.

Additionally, I would like to express my special thanks to all those who made exceptional contributions to this work. Specifically, I would like to express my special thanks to the Huck Manufacturing Company, for its early funding of the investigation; to Professor William E. Wood, my thesis advisor, for his guidance throughout the investigation; to Doctor Jack H. Devletian, for his advice on phase diagrams and solidification processes; to Mrs. Janelle M. Cedergreen of Racquet Sports Associates, Inc., for her typing of the manuscript; to Mr. Daniel Danks, for his assistance with the setup photography; to Mr. David K. Johnsen, for his editing of the manuscript and mounting of the figures; to Mrs. Mary P. Johnsen of Racquet Sports Associates, Inc., for her making available her administrative assistant and word processing equipment; to Mr. Robert McCune of the U. S. Bureau of Mines, for his help with the x-ray diffractometry; to Mrs. Barbara P. Ryall, for her accomplishment of all the technical

drawing; to Mr. Milton R. Scholl, for his advice on alloy fabrication; to Mr. Ward C. Stevens, for his consultation on all technical matters; and to Mrs. Donna M. Walker, for her invaluable assistance in the x-ray diffractometry analysis.

Finally, I would like to thank the members of my thesis committee, Professor William E. Wood, Professor John S. Blakemore, Doctor Jack H. Devletian, and Doctor Robert M. Drosd for taking the time from their demanding schedules to review this dissertation and to attend its formal presentation.

TABLE OF CONTENTS

Page

Page

LIST OF TABLES

LIST OF FIGURES

Page

Page

Page

Page

Page

Page

Page

Page

Page

Page

Page

ABSTRACT

An Investigation of Selected Properties
of As-Cast, V-Ti-Fe Alloys

John L. Johnsen, Ph.D.
Oregon Graduate Center, 1985

Supervising Professor: William E. Wood

It is not currently possible to weld titanium alloys to iron alloys by any conventional fusion welding process. When titanium and iron are fused or melted together, they normally form the intermetallic phases TiFe and $TiFe_2$. These phases are inherently brittle and tend to embrittle the materials in which they occur, even when they are present in only small amounts.

One possible method of overcoming the formation of these brittle intermetallic phases involves the addition of a third element to the weld fusion zone. The function of the third element is to destabilize the undesirable intermetallic phases, without forming other undesirable phases in the process.

A review of the alloying characteristics of several candidate elements indicated that vanadium offers the best potential for being able to destabilize the TiFe and $TiFe_2$ intermetallic phases, without forming other undesirable phases. While vanadium does form the equilibrium FeV intermetallic or σ phase, it does so sluggishly and rarely under non-equilibrium conditions.

The objective of this thesis, then, was to investigate selected properties of as-cast V-Ti-Fe alloys, with a view toward determining

their suitability for use in the fusion zone of a conventional capacitor discharge weld. To achieve this objective, an approach consisting of both a theoretical and an experimental effort was employed.

The theoretical effort consisted of a consideration of the elements vanadium, titanium, and iron, the Ti-Fe binary system, the Ti-V binary system, the Fe-V binary system, the V-Ti-Fe ternary system, and fusion weld interfacial phenomena. The experimental effort consisted of the fabrication, testing, and analysis of twenty-six representative V-Ti-Fe alloys. The testing and analysis included chemical analysis, hardness testing, x-ray energy dispersion analysis, microstructure analysis, x-ray diffractometry analysis, bend testing, and fracture analysis.

The results of this investigation indicated that the strengths and ductilities of as-cast V-Ti-Fe alloys vary greatly with interstitial impurity content, but that it is possible to obtain such alloys that possess useful levels of both strength and ductility. In addition, the results indicated that the predominant solidification structure is the columnar dendritic structure, with a simple columnar structure occurring only in the nominally pure vanadium and an equiaxed structure occurring in alloys near the V-Fe equiatomic composition. Finally, the results indicated that the predominant phase that occurs is the retained β(Ti) phase, although the VTiFe ternary intermetallic or γ phase and the TiC phase do occur in small amounts in some compositions.

1. INTRODUCTION

1.1. Background.

In the summer of 1981, the Oregon Graduate Center undertook a research project whose overall objective was to develop a method for the joining of titanium to dissimilar metals. The sponsor of the project was the Huck Manufacturing Company of Carson, California, a manufacturer of sophisticated fasteners for use on commercial aircraft.

The specific objective of the project was to develop a method for the end-to-end joining of titanium alloy round stock to iron alloy round stock, in which the capacitor discharge welding process is employed and by which consistently high tensile strengths are obtained. This objective reflected a requirement that had materialized during the company's application of titanium alloy fasteners to commercial aircraft.1

At that time, it was possible to obtain useful welds of titanium alloys to iron alloys by the use of non-fusion welding processes such as friction welding, pressure welding, and explosive bonding. It was not possible, however, to obtain such welds by the use of any conventional fusion welding process. In any conventional fusion welding process, titanium alloys and iron alloys were and remain metallurgically incompatible.2

Where titanium alloys and iron alloys are fused or melted together, they normally form the intermetallic compounds TiFe and/or $TiFe_2$. These intermetallic compounds are themselves extremely

brittle and tend to embrittle the materials in which they occur, even when they are present in only small amounts. Conventional fusion welds of titanium alloys to iron alloys typically possess no useful engineering strength.3

The new project focused initially on development of the capacitor discharge welding process, and by the end of 1982 it had become possible to produce full-strength capacitor discharge welds of titanium alloy rod to other titanium alloy rod and to a dissimilar but compatible vanadium rod. Unfortunately, during this same period, the associated metallurgical work had been neglected, and it was still not possible to weld titanium alloys to iron alloys.4,4a

Accordingly, in early 1983, the original project was subdivided into two separate but coordinated projects. These were a process development project and an alloy development project. The goal of the latter was to develop an alloy that could be produced in the fusion zone of a capacitor discharge weld and that would be compatible with both the titanium and the iron alloys involved. This dissertation is essentially an outgrowth of that alloy development project.5

1.2 Objective.

The metallurgical solution to the aforementioned problem was not straightforward. It was easy to find an elemental alloy addition, X, that would destabilize the unwanted intermetallic compounds of the Ti-Fe binary system. It was not easy, however, to find one that would destabilize the Ti-Fe system intermetallics, without forming new

intermetallic compounds in the resulting Ti-X, Fe-X, or Ti-Fe-X systems.

After a review of the applicable literature and an assessment of the alloying characteristics of a large number of elements, vanadium was selected as the single most promising candidate elemental alloy addition of the many considered and the first, therefore, to be investigated. After all, vanadium was fully compatible with titanium and produced only one, slow to form intermetallic compound, FeV, with iron.[6,7]

This selection led to the initial objective of the new alloy development project and, concurrently, to the objective of this dissertation. That objective was to investigate selected properties of as-cast, V-Ti-Fe alloys, with a view toward determining their suitability for employment in the fusion zone of a titanium to iron fusion weld. The selected properties were strength, ductility, structure, and composition.

1.3. Approach.

To accomplish this objective, a reasonably conventional approach was adopted. It consisted essentially of two major steps: a theoretical step and an experimental one. As a small departure from the strictly conventional approach, however, these steps were not carried out in sequence. Rather, they were carried out concurrently, and the emerging results of one were allowed to influence the course of the other.

The theoretical step involved a consideration of the elements vanadium, titanium, and iron; the binary systems Ti-Fe, Ti-V, and Fe-V; the ternary system V-Ti-Fe; and fusion weld interfacial phenomena. While the theoretical step was mainly predictive in nature, it was also partly informative. However, it was entirely relevant to the objective of the work and fully supportive of the experimental step.

The experimental step involved the fabrication of representative V-Ti-Fe ternary alloys from constituent materials and the testing and analysis of the resulting specimens. The testing and analysis consisted of chemical analysis, hardness testing, x-ray energy dispersion analysis, microstructure analysis, microhardness testing, x-ray diffractometry analysis, bend testing, and fracture analysis.

In the following sections of this dissertation, the theoretical and experimental steps will be described thoroughly and their results presented in detail. Then, the results of both steps will be discussed in terms of the properties of interest: namely, strength, ductility, structure, and composition. Finally, appropriate conclusions will be drawn and recommendations made.

2. THEORY

2.1. The Elements Vanadium, Titanium, and Iron.

2.1.1. General.

It is not intended that this section constitute a comprehensive assessment of all the properties of elemental vanadium, titanium, and iron. Rather, it is intended that it consist of a brief review of those properties of pure vanadium, titanium, and iron that are relevant either to this investigation or to the capacitor discharge welding process.

Accordingly, the properties that are considered here are atomic weight, density, crystal structure, melting point, specific heat, heat of fusion, thermal conductivity, thermal expansion coefficient, electrical resistivity, tensile strength, yield strength, and elongation. Each of these properties is discussed briefly under the appropriate one of Sections 2.1.2 through 2.1.5.

In the development of this review, every effort was made to obtain data that are comparable among all three of the elements involved. To that end and wherever possible, any given data were taken from the single source judged by the author to contain the most accurate, most up-to-date information on the subject. Where that was not possible, as in the case of mechanical properties, the data provided are annotated accordingly.

The data provided in Sections 2.1.2 through 2.1.5 are summarized in Table 1 which follows Section 2.1.5. This summary is designed to provide to the reader a convenient reference to the

aforementioned properties of vanadium, titanium, and iron. The sources of the data included in Table 1 are specified in the corresponding portions of the text. The arrangement of Table 1 parallels that of the text, wherein the properties are grouped according to whether they are physical, thermal, electrical, or mechanical.

2.1.2. Physical Properties.

All the references consulted were in general agreement as to the atomic weights of the elements vanadium, titanium, and iron. Only variations in the level of precision were found. The atomic weight of vanadium is 50.94, that of titanium is 47.90, and that of iron is 55.85.8 These were the values used in all the conversions from atomic percent to weight percent made in the course of this investigation.

The densities of vanadium, titanium, and iron at 20°C are 6.1 g/cm3, 4.51 g/cm3, and 7.87 g/cm3 respectively.9 Here again, all the references consulted were in agreement as to the densities of the three elements. Significant here, of course, are the densities of vanadium and titanium, especially titanium, in contrast to that of iron.

The crystal structure of pure vanadium is body-centered cubic (BCC) at all temperatures below its melting point.10 Titanium and iron, on the other hand, undergo allotropic transformations and have solid-state structures that are dependent on temperature. The crystal structure of titanium is hexagonal close-packed (HCP) at temperatures below 882°C and body-centered cubic (BCC) at

temperatures above 882°C.11 The structure of iron is body-centered cubic (BCC) at temperatures below 912°C and above 1,394°C and is face-centered cubic (FCC) at temperatures between 912°C and 1,394°C.12

2.1.3. Thermal Properties.

The melting points of pure vanadium, titanium, and iron are approximately 1,914°C, 1,670°C, and 1,538°C respectively.13,14,15 While there seems to be general agreement among the references consulted as to the melting point of iron, there does not appear to be such agreement as to the melting points of vanadium and titanium. This lack of agreement is believed to reflect the relative difficulty involved in controlling contamination in vanadium and titanium. The melting points reported above are all from sources that are themselves critical evaluations of other sources of experimental melting point data.

The specific heats at constant pressure and a temperature of 25°C for vanadium, titanium, and iron are 0.116 cal/g°C, 0.125 cal/g°C, and 0.108 cal/g°C respectively.16 However, the specific heats of these elements all vary significantly with temperature. For titanium and iron, constants are available for use in the Debye-Sommerfeld equation for predicting specific heats at elevated temperatures.17 For vanadium, no such constants or other elevated temperature data were found.

The latent heat of fusion of the elements vanadium, titanium, and iron are 70 cal/g, 104.4 cal/g, and 63.7 cal/g

respectively.18 According to the source from which these values were obtained, the values for vanadium and titanium are of uncertain reliability. The value given for iron is presumed, therefore, to be quite reliable. Noteworthy, is the comparatively high value of the latent heat of fusion of titanium.

The thermal conductivity at 25°C of vanadium is 0.307 W/cm°C, that of titanium is 0.219 W/cm°C, and that of iron is 0.804 W/cm°C.19 As with most thermal properties, the thermal conductivity varies significantly with temperature. Graphs and tables, from which values of thermal conductivity at higher temperatures may be obtained, are available for titanium and iron.20,21 None was found for vanadium. Noteworthy, in this instance, are the low values of thermal conductivity for both vanadium and titanium.

The coefficients of linear expansion for vanadium, titanium, and iron are well established and are 8X10-6/°C, 8.5X10-6/°C, and 12X10-6/°C respectively.22 For temperatures above 25°C, both a graph and a table of expansion coefficients are available for iron, and a limited table of expansion coefficients is available for titanium.23,24 No graph, table, or relationship describing the temperature dependence of the coefficient of linear expansion was found for vanadium.

2.1.4. Electrical Properties.

The electrical resistivity at 20°C of vanadium, titanium, and iron are 24.8 to 26.0 μohm-cm, 42.0 μohm-cm, and

9.71 μohm-cm respectively.25 Values of the electrical resistivity for temperatures above 20°C may be extracted from experimental curves for titanium and iron.26 A similar curve was not found for vanadium. The high electrical resistivities of vanadium and titanium, in contrast to that of iron, is certainly worthy of note.

2.1.5. Mechanical Properties.

The mechanical properties of nominally pure vanadium, titanium, and iron are all influenced greatly by interstitial impurities. However, they are not all influenced in the same way or to the same extent by a particular interstitial element. In general, the mechanical properties of vanadium and titanium are most strongly influenced by the presence of oxygen and nitrogen, while those of iron are most strongly influenced by the presence of carbon and nitrogen.27,28

In view of this and other considerations, such as the varied influences of thermal and mechanical processing, it is clearly impossible to obtain a fully comparable set of data on the mechanical properties of these three elements. As an alternative, some exemplary data have been assembled and are presented in the following paragraphs and summarized in Table 1. The data provided are consistent for each of the elements vanadium, titanium, and iron, but are not comparable among them.

For a high-purity (iodide) vanadium, containing 0.012 weight percent oxygen and 0.008 weight percent nitrogen, the tensile strength, 0.2 percent yield strength, and elongation are 31,600

9.71 μohm-cm respectively.25 Values of the electrical resistivity for temperatures above 20°C may be extracted from experimental curves for titanium and iron.26 A similar curve was not found for vanadium. The high electrical resistivities of vanadium and titanium, in contrast to that of iron, is certainly worthy of note.

2.1.5. Mechanical Properties.

The mechanical properties of nominally pure vanadium, titanium, and iron are all influenced greatly by interstitial impurities. However, they are not all influenced in the same way or to the same extent by a particular interstitial element. In general, the mechanical properties of vanadium and titanium are most strongly influenced by the presence of oxygen and nitrogen, while those of iron are most strongly influenced by the presence of carbon and nitrogen.27,28

In view of this and other considerations, such as the varied influences of thermal and mechanical processing, it is clearly impossible to obtain a fully comparable set of data on the mechanical properties of these three elements. As an alternative, some exemplary data have been assembled and are presented in the following paragraphs and summarized in Table 1. The data provided are consistent for each of the elements vanadium, titanium, and iron, but are not comparable among them.

For a high-purity (iodide) vanadium, containing 0.012 weight percent oxygen and 0.008 weight percent nitrogen, the tensile strength, 0.2 percent yield strength, and elongation are 31,600

lb/in2, 15,300 lb/in2, and 17 percent respectively.29 Initially, all these values would increase substantially with increasing oxygen and nitrogen contents. However, nominally pure vanadium, containing a combination of oxygen and nitrogen in excess of 0.2 weight percent, is extremely brittle and has tensile and yield strengths that are indeterminate and an elongation of 0.0 percent.30

For nominally pure titanium, a typical tensile strength, 0.2 percent yield strength, and elongation are 34,000 lb/in2, 20,000 lb/in2, and 54 percent.31 While the interstitial content of this titanium was not specified in the source, the tensile properties given appear to correspond to those of ASTM Grade 1, unalloyed titanium, whose oxygen and nitrogen levels are 0.018 weight percent (maximum) and 0.03 weight percent (maximum) respectively.32 Pure titanium is also susceptible to embrittlement by interstitial oxygen and nitrogen, although much less susceptible than vanadium.

For relatively pure iron that has been hot rolled, a typical tensile strength, 0.2 percent yield strength, and elongation are 42,000 to 48,000 lb/in2, 26,000 to 32,000 lb/in2, and 22 to 28 percent respectively.33 Here again, the interstitial content of the metal was not specified in the source. However, the properties given are believed to correspond to nominally pure iron having an interstitial carbon content of .005 to .012 weight percent. Pure iron is not generally susceptible to oxygen embrittlement, as are vanadium and titanium.

The mechanical properties of nominally pure vanadium, titanium, and iron are dependent on many factors, including interstitial content, thermal treatment, and mechanical processing. The effects of interstitial content alone are varied, extensive (in most cases), and complex. An in-depth assessment of these properties and all the factors that influence them is certainly beyond the scope of this investigation. Nevertheless, the foregoing presentation of typical or exemplary tensile properties is believed to be worthwhile, at least to the extent that it provides the reader with a feel for what tensile strengths, yield strengths, and elongations might be expected in the three nominally pure metals.

2.2. The Titanium-Iron Binary System.

2.2.1. General.

A consideration of the Ti-Fe binary system is important for several reasons. First, it permits a full appreciation of the implications of the formation of the brittle intermetallic compounds TiFe and $TiFe_2$. Second, it contributes to the fundamental basis for the development of any ternary or higher-order system of which the Ti-Fe system is a part. Third, it provides a reference in terms of which any experimental behavior of the Ti-Fe system can be interpreted.

The Ti-Fe binary system is a fairly complex system. However, there has been a considerable amount of work done on the

Table 1.

SELECTED PROPERTIES OF THE ELEMENTS VANADIUM, TITANIUM, AND IRON

	Vanadium	Titanium	Iron
Physical Properties:			
Atomic Weight	50.94	47.90	55.85
Density at 20°C (g/cm^3)	6.19	4.51	7.87
Crystal Structure	BCC	HCP below 882°C BCC above 882°C	BCC below 912°C and above 1,394°C FCC between 912°C and 1,394°C
Thermal Properties:			
Melting Point (°C)	1,914	1,670	1,538
Specific Heat at 25°C (cal/g°C)	0.116	0.125	0.108
Latent Heat of Fusion (cal/g)	70	104.4*	63.7*
Thermal Conductivity at 25°C (W/cm°C)	0.307	0.219	0.804
Linear Thermal Expansion Coefficient at 25°C (/°C)	$8X10^{-6}$	$8.5X10^{-6}$	$12X10^{-6}$

Table 1. (Cont.)

Electrical Properties:			
Electrical Resistivity at 20°C (μohm-cm)	24.9-26.0	42.0	9.71
Mechanical Properties**:			
Ultimate Tensile Strength (lb/in^2)	31,600	34,000	42,000 to 48,000
0.2% Yield Strength (lb/in^2)	16,700	20,000	26,000 to 32,000
Elongation (%)	17	54	22-28

*Values given are of uncertain reliability.

**Values given are exemplary only. They are consistent for each element. They are not comparable among the elements.

system, and there appears to be general agreement as to its principal features. Accordingly, except where indicated otherwise, the information provided in Sections 2.2.2 through 2.2.4 is from a single, comprehensive source. That source is a recent evaluation of the Ti-Fe binary system by J. L. Murray[34], the ASM/NBS Data Program's Category Editor for binary titanium alloys. Other sources of information included are referred to in the usual manner.

2.2.2. Equilibrium Phases.

As shown in Figure 1, the Ti-Fe binary system contains six distinct equilibrium phases. These are the liquid phase, the α(Ti) phase, the β(Ti) phase, the TiFe intermetallic or δ phase, the $TiFe_2$ intermetallic or C14 phase, and the γ(Fe) phase. The α(Fe) phase shown in the Ti-Fe equilibrium phase diagram has the same crystal structure as the β(Ti) phase and is not, therefore, considered a separate or distinct phase in the system.

The α(Ti) phase is the terminal solid solution phase of iron in titanium at temperatures below 882°C. It has an hexagonal close-packed (HCP) crystal structure and exists as a single phase over a very limited range of compositions below 882°C. The maximum solid solubility of iron in α-titanium is less than .06 weight percent at 590°C.

The β(Ti) phase is the terminal solid solution phase of iron in titanium at temperatures above 882°C. The β(Ti) phase has a body-centered cubic (BCC) crystal structure and exists as a single phase over a considerable range of compositions and

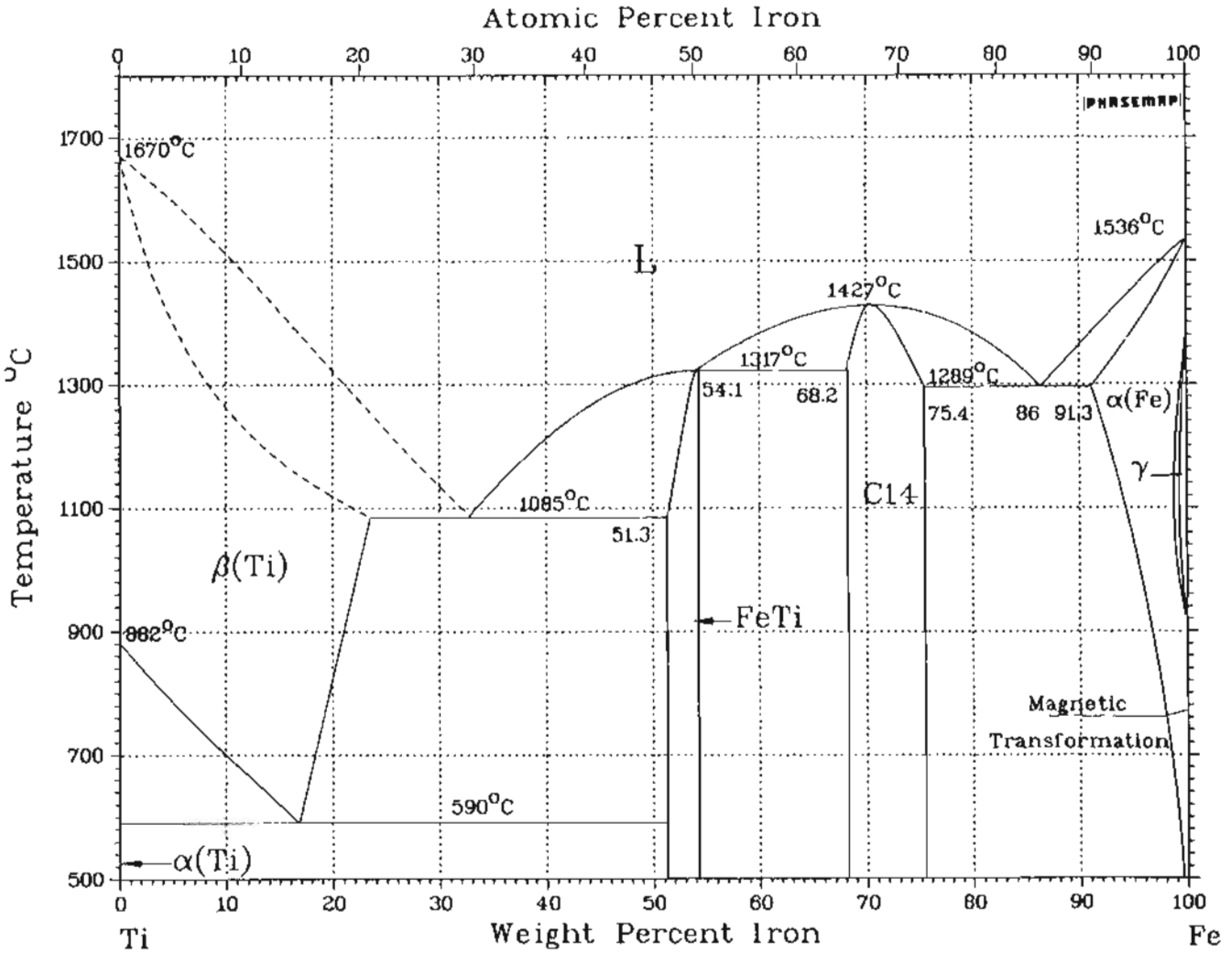

Figure 1. EQUILIBRIUM PHASE DIAGRAM FOR Ti-Fe BINARY SYSTEM.

temperatures. The maximum solid solubility of iron in β-titanium is about 24 weight percent at 1,085°C.

The β(Ti) phase is also the terminal solid solution phase of titanium in iron at temperatures below 911°C and above 1,392°C. Near the iron end of the Ti-Fe equilibrium phase diagram, β(Ti) or α(Fe) exists as a single phase over a considerable range of compositions and temperatures. The maximum solid solubility of titanium in α-iron is about 9 weight percent at 1,298°C.

The TiFe intermetallic or δ phase is an ordered phase whose crystal structure has the caesium chloride structure (CsCl) as its stereotype. As a single phase, it exists from about 51.4 to 54.4 weight percent iron and up to a temperature of 1,317°C. It is noteworthy that as a two-phase component at room temperature it occurs over a range of compositions that extends from nearly pure titanium to approximately 68 weight percent iron.

The $TiFe_2$ intermetallic or C14 phase is also an ordered phase, but one whose crystal structure has the hexagonal magnesium zinc ($MgZn_2$) structure as its stereotype. As a single phase, the C14 phase extends from about 69.2 to 75.5 weight percent iron and up to a temperature of 1,427°C. It is noteworthy here also that, as a two-phase component at room temperature the C14 phase occurs over the entire range of compositions from 54.4 to 99.5 weight percent iron.

The γ(Fe) phase is the terminal solid solution phase of titanium in iron between the temperatures of 911°C and 1,392°C.

It has a face-centered cubic (FCC) crystal structure and exists as a single phase over a limited range of compositions at the iron end of the equilibrium phase diagram. The maximum solid solubility of titanium in γ-iron is 0.7 weight percent at 1,150°C.

With regard to the intermetallic compounds TiFe and $TiFe_2$, it is especially significant that one or both of these phases occurs over nearly the entire range of compositions from pure titanium to pure iron. This, when considered in conjunction with the knowledge that these ordered phases can cause embrittlement even when present in small amounts, shows clearly the extent of the metallurgical incompatibility of titanium and iron.

2.2.3. Equilibrium Reactions.

The Ti-Fe system contains five invariant equilibrium reactions. These are an eutectoid reaction, two eutectic reactions, a peritectic reaction, and a congruent melting reaction. The allotropic transformations that occur in pure titanium and pure iron were described in Section 2.1 and will not, therefore, be considered in this section.

The eutectoid reaction occurs at a composition of 17 weight percent iron and a temperature of 590°C and consists of the transformation of β-titanium to a mixture of α-titanium and the intermetallic compound TiFe.

One of the eutectic reactions occurs at a composition of 33 weight percent iron and a temperature of 1,085°C and consists of the transformation of liquid to a mixture of β-titanium and the

intermetallic compound TiFe.

The other eutectic reaction occurs at a composition of 86 weight percent iron and a temperature of 1,289°C and consists of the transformation of liquid to a mixture of α-iron and the intermetallic compound $TiFe_2$.

The peritectic reaction occurs at a composition of 54 weight percent iron and a temperature of 1,317°C and consists of the transformation of a mixture of liquid and the intermetallic compound $TiFe_2$ to the intermetallic compound TiFe.

Finally, the congruent melting reaction takes place at a composition of about 71 weight percent iron and a temperature of 1,427°C and consists of the congruent melting of the intermetallic compound $TiFe_2$.

2.2.4. Metastable Phases.

Three distinct metastable phases have been observed in the Ti-Fe system. These occur only in the titanium-rich portion of the system and are the hexagonal close-packed (HCP) α' phase, the hexagonal ω phase, and the retained body-centered cubic (BCC) β phase. The orthorhombic α'' phase which occurs in some titanium-base systems has not been observed in the Ti-Fe system.

The hexagonal close-packed (HCP) α' phase forms martensitically during quenching from the equilibrium β(Ti) phase. This transformation takes place, however, only where the concentration of iron is less than 2.9 to 3.5 weight percent.

The hexagonal ω phase is considered to be a transition

phase between the equilibrium β(Ti) and α(Ti) phases. It forms from the metastable β phase either during quenching or during aging between 300°C and 500°C. It occurs only where the iron concentration is between 3.5 and 9.2 weight percent.

The retained β phase forms during quenching from the equilibrium β(Ti) phase. The β(Ti) phase is partially retained where the iron concentration is greater than 3.5 weight percent. It is completely retained where the iron concentration is greater than 9.2 weight percent.

It is significant here that only in the titanium-rich and iron-rich portions of the Ti-Fe system is β(Ti) or α(Fe) the first phase to solidify and, hence, capable of retention. In all other parts of the system, either Ti-Fe or $Ti-Fe_2$ is the first to solidify.

2.3. The Titanium-Vanadium System.

2.3.1. General.

A consideration of the Ti-V binary system is also important for several reasons. First, it demonstrates clearly the inherent metallurgical compatibility of titanium and vanadium. Second, it contributes to the fundamental basis for the development of any ternary or higher order system of which the Ti-V binary system is a part. Third, it provides a reference in terms of which any experimental behavior of the Ti-V system can be interpreted.

In contrast to the Ti-Fe binary system, the Ti-V binary system is a fairly simple system. However, as in the case of the Ti-Fe system, there has been a considerable amount of work done on the Ti-V binary system and, with some notable exceptions, there appears to be general agreement as to its main features. Accordingly, except were indicated otherwise, the information provided in Sections 2.3.2 through 2.3.4 is from a single, comprehensive source. That source is a recent evaluation of the Ti-V binary system conducted by J. L. Murray.35 Other sources are identified in the usual manner.

2.3.2. Equilibrium Phases.

As shown in Figure 2, the Ti-V binary system contains three distinct equilibrium phases. These are the liquid phase, the α(Ti) phase, and the β(Ti) phase. The β_1 and β_2 phases that are mentioned in the next section have the same crystal structure as the β(Ti) phase and are not, therefore, considered to be separate or distinct phases in the Ti-V binary system.

The α(Ti) phase is the terminal solid solution phase of vanadium in titanium at temperatures below 882°C. It has an hexagonal close-packed (HCP) crystal structure and exists as a single phase over a very limited range of compositions below 882°C. The maximum solid solubility of vanadium is α-titanium is about 3.9 weight percent at 500-600°C.

The β(Ti) phase is the terminal solid solution phase of vanadium in titanium at temperatures above 882°C. It is also the terminal solid solution phase of titanium in vanadium at all

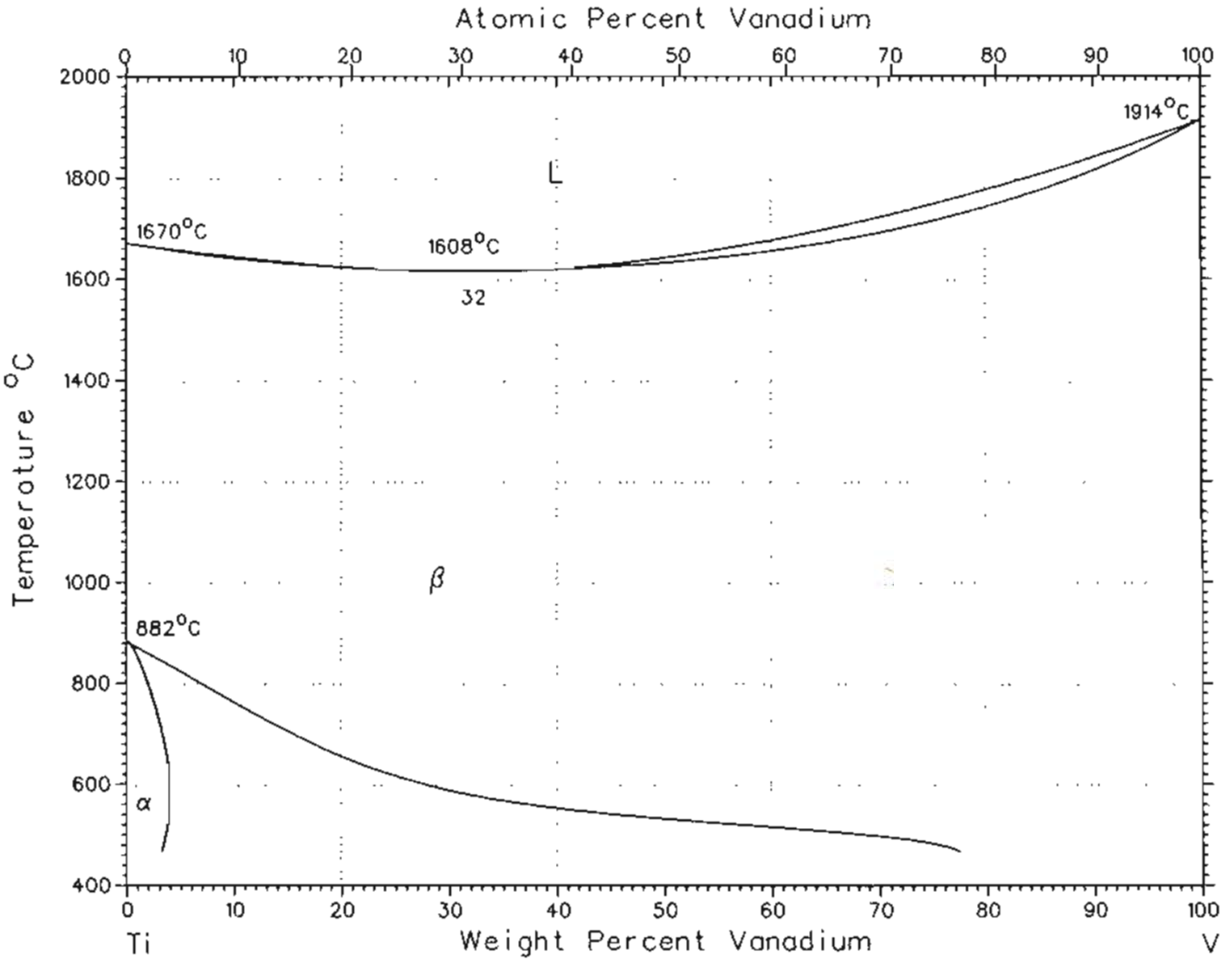

Figure 2. EQUILIBRIUM PHASE DIAGRAM FOR Ti-V BINARY SYSTEM.

temperatures. The β(Ti) phase has a body-centered cubic (BCC) crystal structure and exists as a single phase over a wide range of compositions and temperatures. Above 882°C, it forms a continuous series of solid solutions from pure titanium to pure vanadium.

2.3.3. Equilibrium Reactions.

According to J. L. Murray and as indicated in Figure 2, the Ti-V binary system contains only one invariant equilibrium reaction. This reaction is a minimum melting reaction that occurs at a composition of 32 weight percent vanadium and a temperature of 1,608°C and that involves the transformation of liquid directly to β-titanium.

However, according to O. Nakano, et al.[36] and as indicated in Figure 3, the Ti-V binary system contains also a miscibility gap and an associated monotectoid reaction. This reaction takes place at a composition of about 18 weight percent vanadium and a temperature of 675°C and involves the transformation of β-titanium to a mixture of α-titanium and β-titanium.

With regard to the possible existence of a miscibility gap in the Ti-V binary system, Murray suggests that such indications reflect the existence of a metastable, non-equilibrium miscibility gap and that an equilibrium miscibility gap does not actually exist. However, Nakano's work is too recent to have been included in Murray's evaluation of the Ti-V system, and the question remains unresolved.

2.3.4. Metastable Phases.

Four distinct metastable phases have been observed in

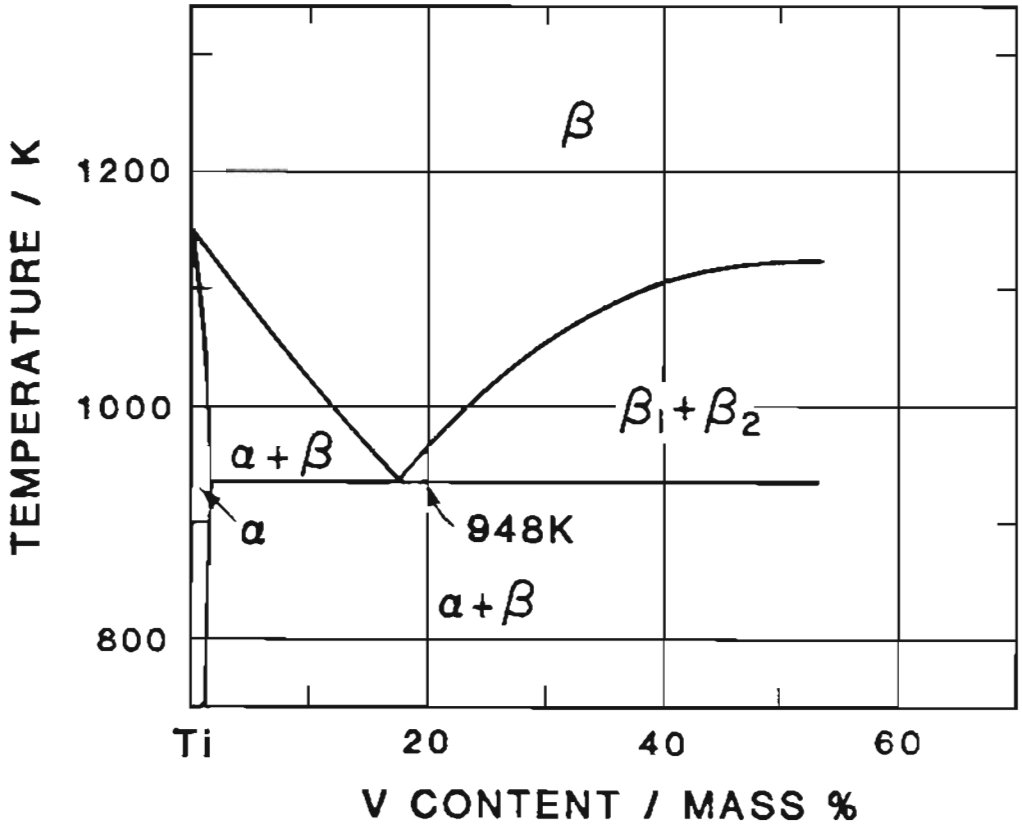

Figure 3. PARTIAL EQUILIBRIUM PHASE DIAGRAM FOR Ti-V SYSTEM.

the Ti-V binary system. These are the hexagonal close-packed (HCP) α' phase, the orthorhombic (distorted hexagonal) α'' phase, the hexagonal ω phase, and the retained body-centered cubic (BCC) β phase.

The hexagonal close-packed (HCP) α' phase forms martensitically during quenching from the equilibrium β(Ti) phase. This transformation takes place, however, only where the concentration of vanadium is less than about 5.3 weight percent.

The orthorhombic (distorted hexagonal) α'' also forms martensitically during quenching from the equilibrium β(Ti) phase. This transformation takes place only where the concentration of vanadium is between about 5.3 and 10.6 weight percent.

The hexagonal ω phase is considered to be a transition phase between the equilibrium β(Ti) and α(Ti) phases. It forms from the metastable β phase either during quenching or during aging between approximately 200°C and 500°C. It normally occurs, however, only where the vanadium concentration is between 12 and 26 weight percent.

The retained β phase forms during quenching from the equilibrium β(Ti) phase. The β(Ti) phase is partially retained where the vanadium concentration is greater than about 10.6 weight percent. It is completely retained where the vanadium concentration is greater than about 15.8 weight percent.

2.4. The Iron-Vanadium Binary System.

2.4.1. General.

A consideration of the Fe-V binary system is important for essentially the same reasons as given previously for a consideration for the Ti-V binary system, and it would serve no useful purpose to repeat them here. There is, however, another matter that must be addressed at this point. That has to do with the fact that β-titanium, α-vanadium, and α-iron all have the same crystal structure and are all, therefore, equivalent phases.

In this section, the body-centered cubic phases of iron and vanadium are referred to as the α-iron phase and the α-vanadium phase respectively. However, in Section 2.5, wherein the V-Ti-Fe ternary system is considered, this obvious conflict with the titanium-oriented nomenclature used earlier had to be resolved. Therefore, in Section 2.5 and in all the sections that follow Section 2.5, α-iron, α-vanadium, and β-titanium are all referred to as β, β(Ti), or β-titanium.

The Fe-V binary system is a relatively simple system. Although, it is somewhat more complex than the Ti-V system just considered. As one might expect, there has been a great deal of work done on the Fe-V system, especially on the iron-rich part of the system, and once again there appears to be general agreement concerning its main characteristics. In view of this, most of the information included in Sections 2.4.2 through 2.4.4 is from still another single, comprehensive source. In this case, the source is a recent

evaluation of the Fe-V binary system by J. F. Smith37, the ASM/NBS Data Program's Category Editor for binary vanadium alloys.

2.4.2. Equilibrium Phases.

As shown in Figure 4, the Fe-V binary system contains four distinct equilibrium phases. These are the liquid phase, the α(Fe) or α(V) phase, the γ(Fe) phase, and the FeV intermetallic of σ phase. Ordinarily, the existence of an ordered σ phase would be a matter of considerable concern. However, in this instance, it is one of less concern, since the Fe-V system σ phase is slow to form and does not usually occur under other than equilibrium conditions.

The α(Fe) or α(V) phase is the terminal solid solution phase of vanadium in iron at temperatures below 911°C and above 1,392°C. It is also the terminal solid solution phase of iron in vanadium at all temperatures. The α(Fe) or α(V) phase has a body-centered cubic (BCC) crystal structure and exists as a single phase over the entire range of compositions from pure iron to pure vanadium, except where it is interrupted by the σ and $\sigma + \alpha$ phase fields.

The γ(Fe) phase is the terminal solid solution phase of vanadium in iron between the temperatures of 911°C and 1,392°C. The γ(Fe) phase has a face-centered cubic crystal structure and exists as a single phase over a limited range of compositions between 911°C and 1,392°C. The maximum solid solubility of vanadium in γ-iron is about 1.3 weight percent at 1,150°C.

The FeV intermetallic or σ phase is an ordered phase

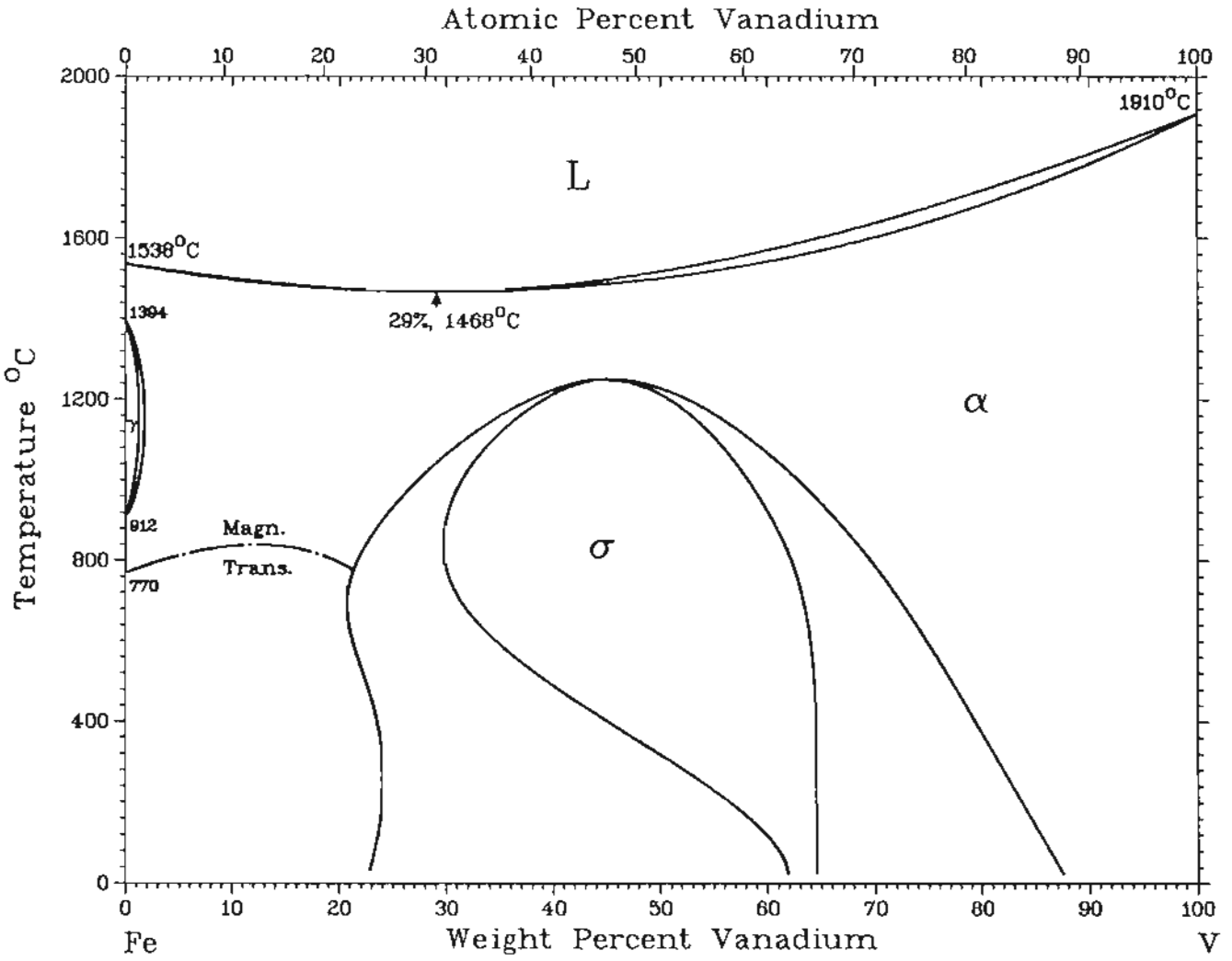

Figure 4. EQUILIBRIUM PHASE DIAGRAM FOR Fe-V BINARY SYSTEM.

whose crystal structure has the iron chromium (FeCr) structure (a cubic superlattice) as its stereotype. As a single phase at room temperature, the σ phase exists over a limited range of compositions from about 62 to 65 weight percent vanadium. At higher temperatures, however, it exists over a much greater range of compositions. At 800°C, for example, it exists from approximately 30 to 70 weight percent vanadium. As a two-phase component at room temperature, it exists over the entire range of compositions from about 23 to 88 weight percent vanadium, except where it is briefly interrupted by the single phase σ field.

2.4.3. Equilibrium Reactions.

The Fe-V binary system contains only two invariant equilibrium reactions. These are a minimum melting reaction and a congruent solid transformation reaction.

The minimum melting reaction takes place at a composition of 29 weight percent vanadium and a temperature of 1,468°C. The reaction involves the transformation of liquid to α-iron (or α-vanadium).

The congruent solid transformation reaction takes place at a composition of about 45 weight percent vanadium and a temperature of approximately 1,250°C and involves the transformation of α-iron (α-vanadium) to the FeV intermetallic or σ phase. However, there is considerable variation in the reaction temperatures reported, and Smith suggests that this is contributed to by metal impurity and by the reaction kinetics. Apparently, the α to σ reaction proceeds

very sluggishly.

2.4.4. Metastable Phases.

Two metastable phases have been observed in the Fe-V binary system. These are the α′ phase, whose crystal structure has the caesium chloride (CsCl) structure as its stereotype, and the retained body-centered cubic (BCC) β phase. The metastable α′ phase of the Fe-V system should not be confused with the α′ phase of the Ti-Fe and Ti-V systems. It is not the same phase.

The α′ phase forms from the retained α phase at temperatures below 700°C and with aging at temperatures of 600°C to 625°C. While the α′ phase is inherently less stable than the competing σ phase, transformation kinetics favor its formation at temperatures below 700°C. Above 700°C, they favor the σ phase formation. In either case, both the α′ phase and the σ phase form reluctantly.

The retained α phase forms during quenching from the equilibrium α(Fe) phase. The α(Fe) phase is completely retained over the entire range of compositions at which α(Fe) normally exists, including those compositions where the equilibrium σ and σ + α phase fields might be expected to interfere. This reflects the sluggish transformation behavior of the metastable α′ and equilibrium σ phases.

2.5. The Vanadium-Titanium-Iron Ternary System.

2.5.1. General.

A characterization of the V-Ti-Fe ternary system at equilibrium is an essential aspect of this investigation. It is essential, in that it provides insights as to the probable effectiveness of vanadium as an elemental alloy addition to the Ti-Fe binary system and also in that it provides a reference against which the experimental behavior of V-Ti-Fe ternary system alloys can be judged.

As it turns out, there is very little information available on the V-Ti-Fe ternary system. Furthermore, the information that is available is somewhat out of date and generally limited to the titanium-rich portion of the system. Inquiries were made of all the usual sources, and the only references identified had to do with some work done on the system by Bi, Pi, and Kornilov in the early 1960's.

To confirm this apparent lack of information on the V-Ti-Fe system, letters of inquiry were written to A. Prince, the ASM/NBS Data Program's Category Editor for all ternary systems, and to V. Ragharan, the ASM/NBS Data Program's Category Editor for vanadium-base ternary systems. In both cases, the responses indicated no knowledge of any work done more recently on the V-Ti-Fe system.[38,39]

2.5.2. Equilibrium Phases.

As was mentioned previously, the investigation of Bi, Pi, and Kornilov were concerned mainly with the titanium-rich portion

of the V-Ti-Fe ternary system. The main and perhaps most useful product of their efforts was a number of vertical and partial isothermal sections of the V-Ti-Fe ternary equilibrium phase diagram. These vertical and partial isothermal sections are described in the following several paragraphs.

The vertical section through V and TiFe shown in Figure 5 is from Bi and Kornilov40 has a number of interesting and revealing features. Probably the most significant among them, however, is the apparent existence of an ordered VTiFe ternary intermetallic compound, referred to in the diagram as the γ phase. This γ(VTiFe) ternary intermetallic phase has an hexagonal crystal structure and must not be confused with the γ(Fe) solid solution phase described earlier.

In a sense, the apparent existence of this γ(VTiFe) intermetallic phase constitutes a realization of the author's worst fears. Namely, that the addition of elemental vanadium to the Ti-Fe binary system might cause the formation of entirely new intermetallic compounds or ordered phases in the resulting V-Ti-Fe system. Neither is it encouraging that the γ phase appears to melt congruently, thus obviating any possibility of avoiding its formation by the retention of some less undesirable phase.

On the other hand, the vertical section shown in Figure 5 indicates also that, for high vanadium concentrations, the first phase to solidify is the β(Ti) or β phase. This is encouraging, since, in substantial portions of the Ti-Fe binary system and

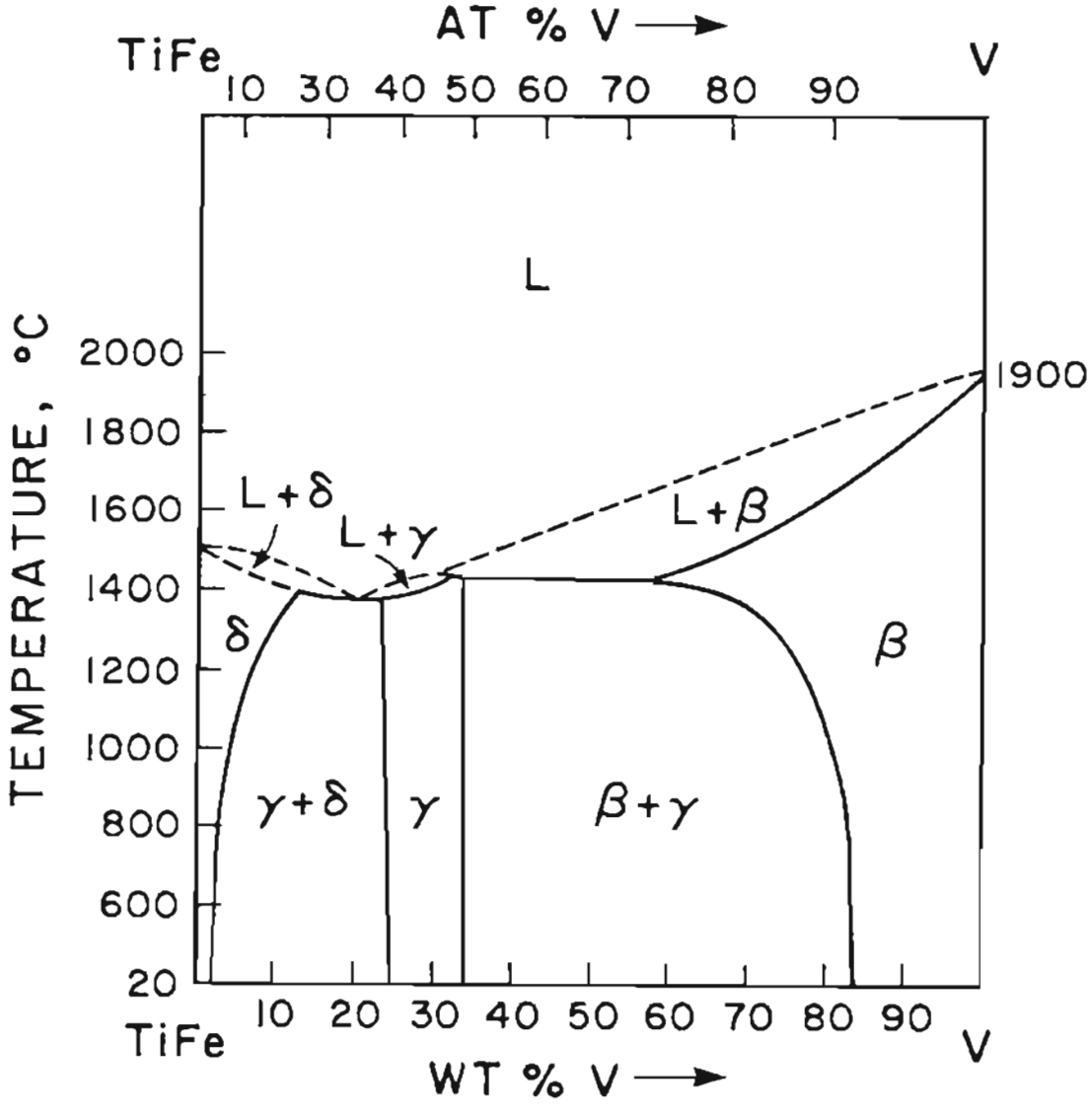

Figure 5. VERTICAL SECTION OF V-Ti-Fe TERNARY EQUILIBRIUM PHASE DIAGRAM THROUGH TiFe AND V.

throughout the Fe-V binary system, the β phase tends to be retained during quenching, in preference to the formation of other, less desirable phases.

The partial vertical section through V and Ti-16Fe shown in Figure 6 is from Pi and Kornilov41 and deals with the limited range of temperatures from 400°C to 700°C. It is instructive, to the extent that it infers the equilibrium phases that exist at room temperature and reveals the incredible complexity that most characterize the V-Ti-Fe ternary system.

The partial room temperature isothermal section of the V-Ti-Fe ternary equilibrium phase diagram shown in Figure 7 is also from Pi and Kornilov42 and makes a substantial contribution to our understanding of at least part of the V-Ti-Fe system. It includes the aforementioned γ(VTiFe) phase and depicts its stability with respect to the equilibrium phases of the Ti-Fe and Ti-V binary systems.

The section appears to err, however, to the extent that it portrays the α+β phase field in the Ti-V binary system as extending only to a composition of about 45 weight percent vanadium. There are indications that, at the time Pi and Kornilov carried out their investigations, that was the generally accepted extent of the α+β phase field. However, it is now believed that the α+β phase field extends nearly to the vanadium end of the phase diagram, as shown earlier in Figure 4.

The isothermal sections of the V-Ti-Fe ternary equilibrium phase diagram provided in Figures 8 and 9 were developed

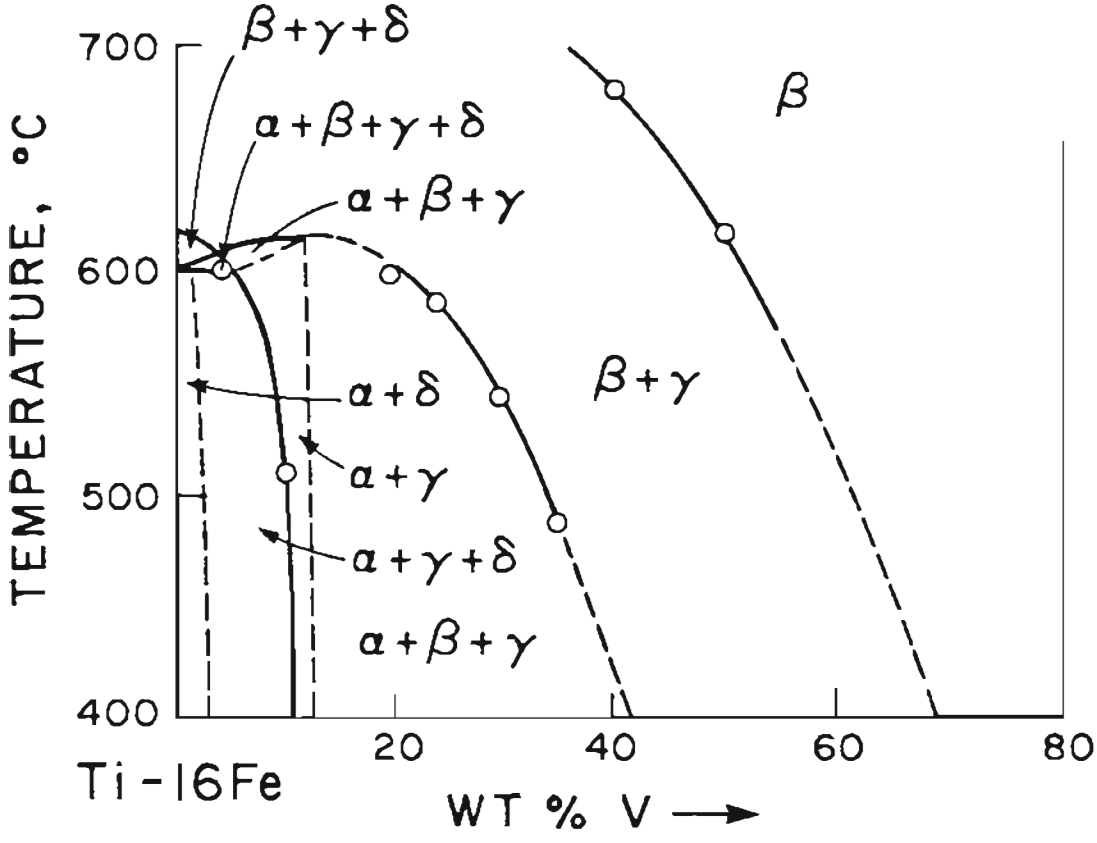

Figure 6. PARTIAL VERTICAL SECTION OF V-Ti-Fe TERNARY EQUILIBRIUM PHASE DIAGRAM THROUGH Ti-16Fe AND V.

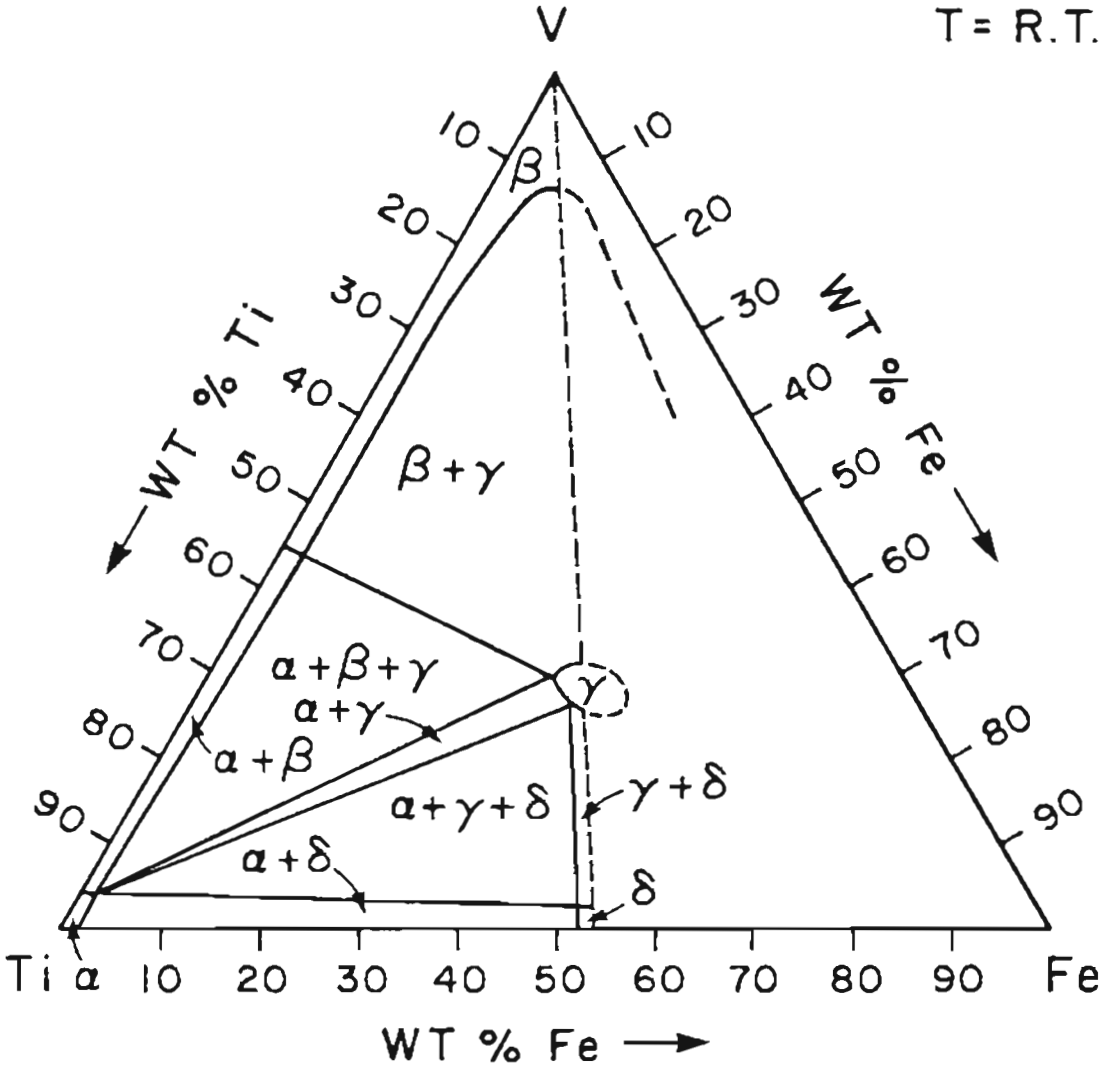

Figure 7. PARTIAL ISOTHERMAL SECTION (T=R.T.) OF V-Ti-Fe TERNARY EQUILIBRIUM PHASE DIAGRAM.

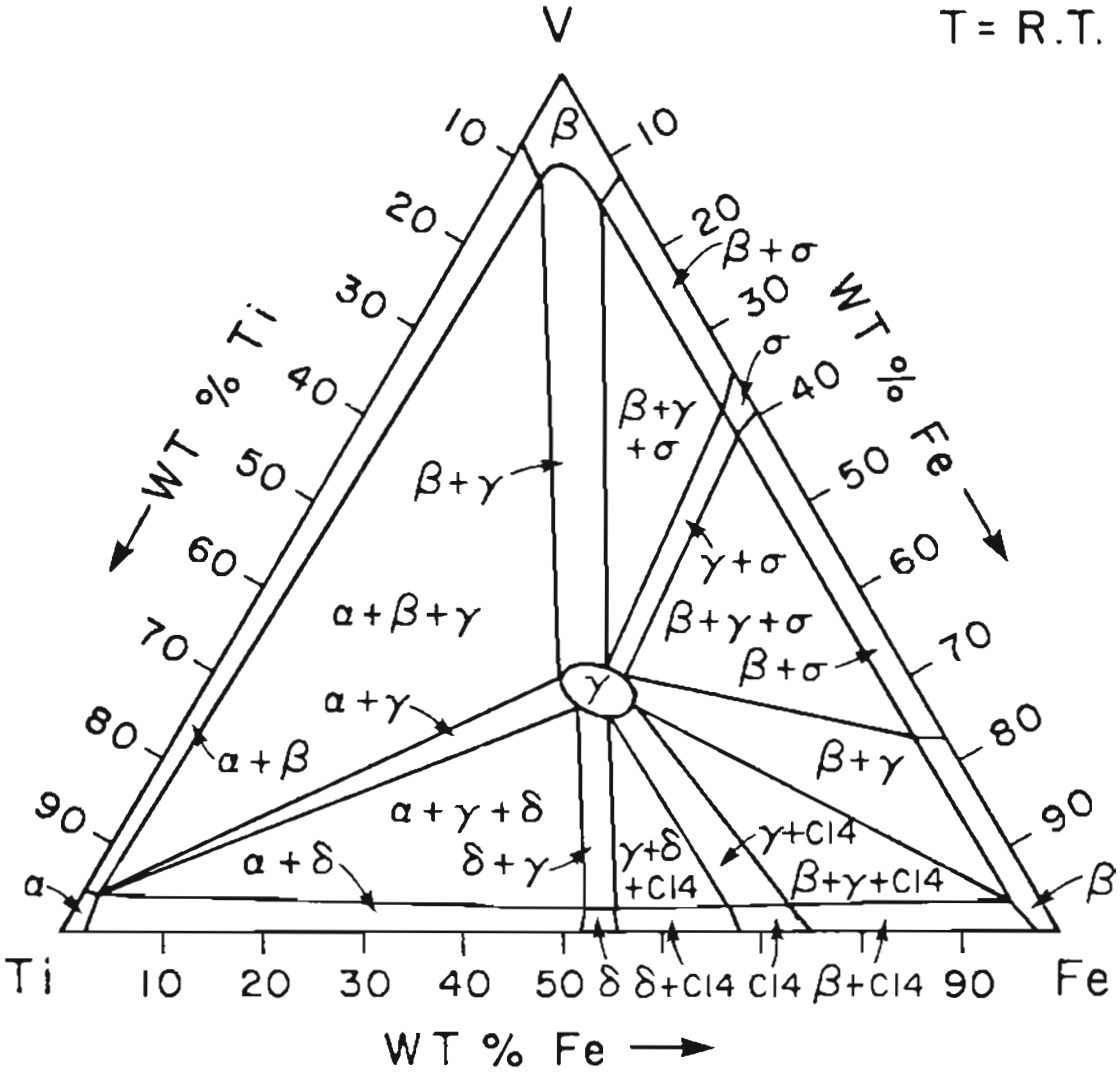

Figure 8. POSSIBLE ISOTHERMAL SECTION (T=R.T.) OF V-Ti-Fe EQUILIBRIUM PHASE DIAGRAM.

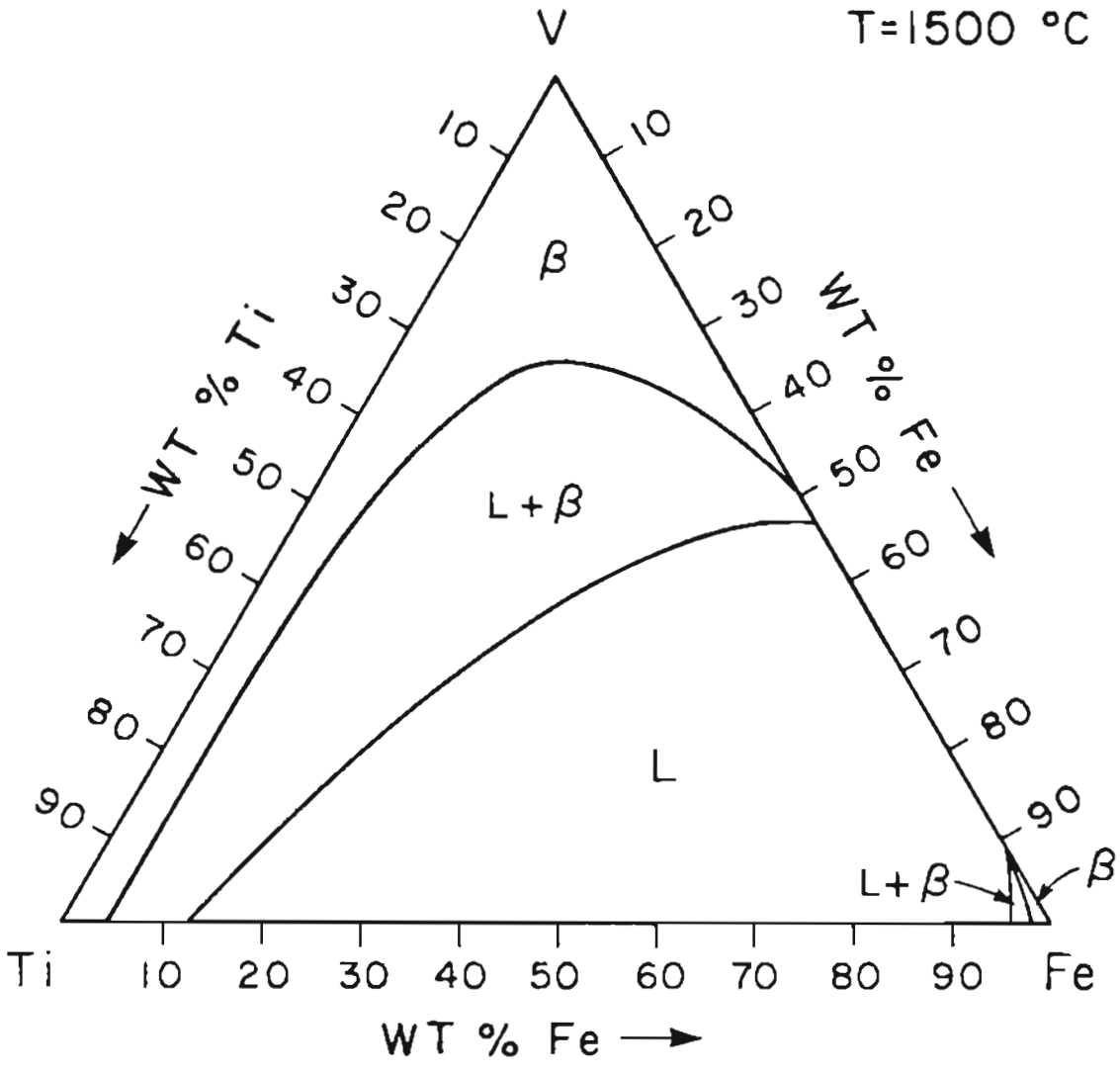

Figure 9. POSSIBLE ISOTHERMAL SECTION (T=1,500°C) OF V-Ti-Fe EQUILIBRIUM PHASE DIAGRAM.

from the Ti-Fe, Ti-V, and Fe-V binary equilibrium phase diagrams described previously, from the V-Ti-Fe ternary system investigations of Bi, Pi, and Kornilov just discussed, and in consideration of the basic rules for the construction of ternary equilibrium phase diagrams.

Furthermore, the isothermal sections provided in Figures 8 and 9 are strictly qualitative in nature and reflect thermodynamic and experimental considerations only to the extent that the diagrams on which they are based incorporate such considerations. Even so, they represent a feasible ternary system and provide not only a basis for the interpretation of the experimental results of this investigation, but also a starting point for further work on the V-Ti-Fe ternary system.

The isothermal sections shown in Figures 8 and 9 contain seven distinct equilibrium phases. These are the liquid phase, the α(Ti) or α phase, the β(Ti) or β phase, the VTiFe intermetallic or γ phase, the TiFe intermetallic or δ phase, the $TiFe_2$ intermetallic or C14 phase, and the FeV intermetallic or σ phase. Inasmuch as all of these phases have been described previously, they will not be discussed further at this point.

2.5.3. Equilibrium Reactions.

All indications are that the V-Ti-Fe ternary system is a very complex system that involves a large number of both variant and invariant equilibrium reactions. Unfortunately, there is little definite information available on these reactions, and their

prediction would, at best, be grossly speculative. In view of this and of the fact that a knowledge of these reactions is not critical to the completion of this investigation, no such prediction will be undertaken.

2.5.4. Metastable Phases.

Of particular significance in the isothermal section shown in Figure 8 is the obviously pervasive nature of the several intermetallic compounds involved. They occur to some extent over nearly the entire range of ternary compositions, and it appears that the likelihood of any V-Ti-Fe system alloy being devoid of intermetallic constituents is extremely remote.

However, the isothermal section shown in Figure 9 is part of an equilibrium phase diagram and, as such, is fully applicable only where equilibrium conditions prevail. The non-equilibrium conditions that are always encountered in fusion welding may result in phase stabilities that vary greatly from those predicted by the equilibrium phase diagram.

For example, it is anticipated that, under non-equilibrium conditions, the σ phase may not form at all and the β phase may be retained to room temperature as a metastable β phase. If that turns out to be the case, then all the equilibrium phase fields involving the σ phase will be altered dramatically and that region of the system may be simplified greatly.

In particular, the formation of metastable phases may have a pronounced effect on the nature and distribution of phases in a

system. While an investigation of the metastable phases that occur in the V-Ti-Fe ternary system has not apparently been conducted, it is certainly likely that they occur. It is especially likely that the metastable β phase occurs.

In fact, one reason for the selection of 1,500°C as the temperature of the isothermal section shown in Figure 9 was this likelihood. This section shows that all the alloys whose properties are investigated in this project solidify initially as β-titanium. This makes possible the retention of the β phase, rather than the formation of the less desirable σ and/or γ phases.

2.6. Fusion Weld Interfacial Phenomena.

2.6.1. General.

Implicit in the objective of this investigation is a need to understand the interfacial phenomena that occur in a capacitor discharge weld of dissimilar metals. Without this understanding, it is not possible to make a valid assessment of the suitability of any particular alloy for employment in the fusion zone of such a weld.

For example, in a fusion weld of titanium to iron, it may be possible to produce in the fusion zone a V-Ti-Fe system alloy that has mechanical properties equivalent to those of the titanium and iron components involved. It may not, however, be possible to produce such an alloy that is also fully compatible with the titanium and iron components involved.

As part of an investigation of hydrogen-induced cold cracking in low-alloy steels, W. F. Savage, et al. looked into the interfacial phenomena that occur in heterogeneous, tungsten-inert-gas (TIG) welds produced in such steels.43 The results of this investigation are quite reasonable and are used in the following sections in the formulation of a model of a capacitor discharge weld of dissimilar metals.

2.6.2. The Traditional Concept.

The traditional concept of the fusion weld, as it might apply to a capacitor discharge weld of similar or dissimilar cylindrical pins, is depicted schematically in Figure 10. According to this concept, the resulting weld consists of a fusion zone, two heat-affected zones, and two regions of unaffected base metal.

The fusion zone consists of material that has been completely melted and thoroughly mixed. The heat-affected zones contain material that has not been melted, but that has undergone some degree of solid-state transformation as a result of the heating to which it was subjected during welding. The base metal is, of course, material that has not been effected in any way by the welding process.

Clearly, this concept of the fusion weld fails to account for at least two transitions that must take place in the fusion weld of dissimilar materials. First, it does not account for the transition that must occur between the composition of the fusion zone and those of the heat-affected zones. Second, it does not account for the transition that must occur between the complete melting of the fusion

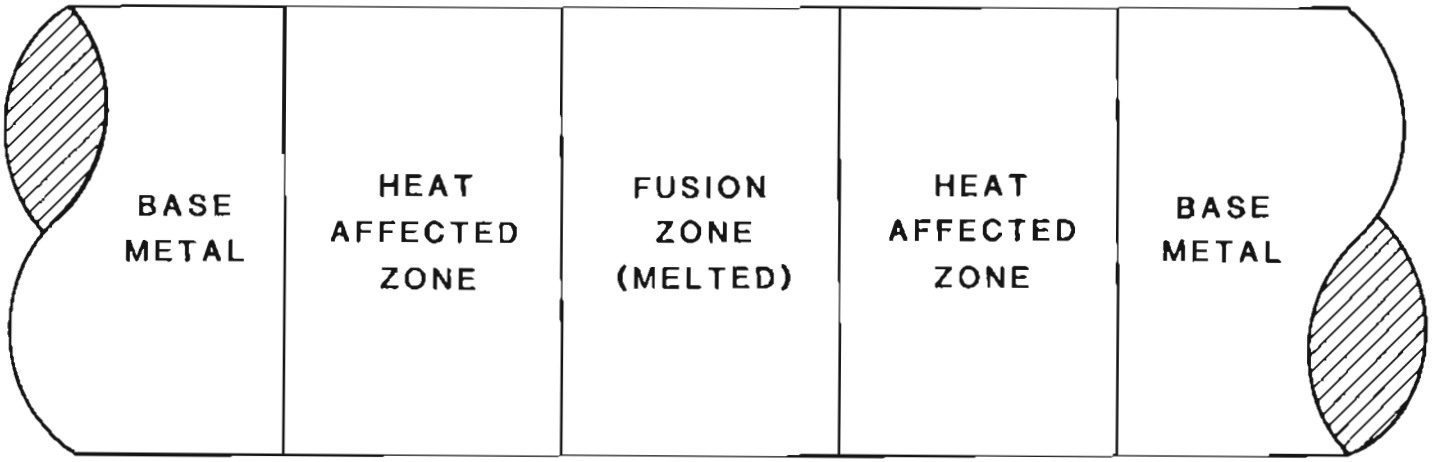

Figure 10. TRADITIONAL CONCEPT OF FUSION WELD.

zone and the total lack of melting of the heat-affected zones.

2.6.3. The Savage Concept.

The Savage concept, on the other hand, does account for these necessary transitions. The concept is shown schematically in Figure 11 and represents the results of both metallographic study and electron beam microprobe analysis. It should be noted that only one side of an hypothetical fusion weld is shown in Figure 11.

According to the Savage concept, a fusion weld of dissimilar metals contains some nine separate regions or zones. These are a composite zone, two unmixed zones, two partially melted zones, two true heat-affected zones, and two regions of uneffected base metal.

The composite zone is a region in which all the material has been completely melted and thoroughly mixed. Its bulk composition reflects the complete intermixing of the melted portions of the dissimilar components and whatever alloy additions may have been made during welding.

The unmixed zones are regions in which the material has been completely melted, but not mixed with the molten material of the composite zone. Their existence is explained in terms of fluid dynamics and the laminar flow that is normally observed near a liquid/solid interface. Their bulk compositions must be the same as the compositions of their corresponding base metals.

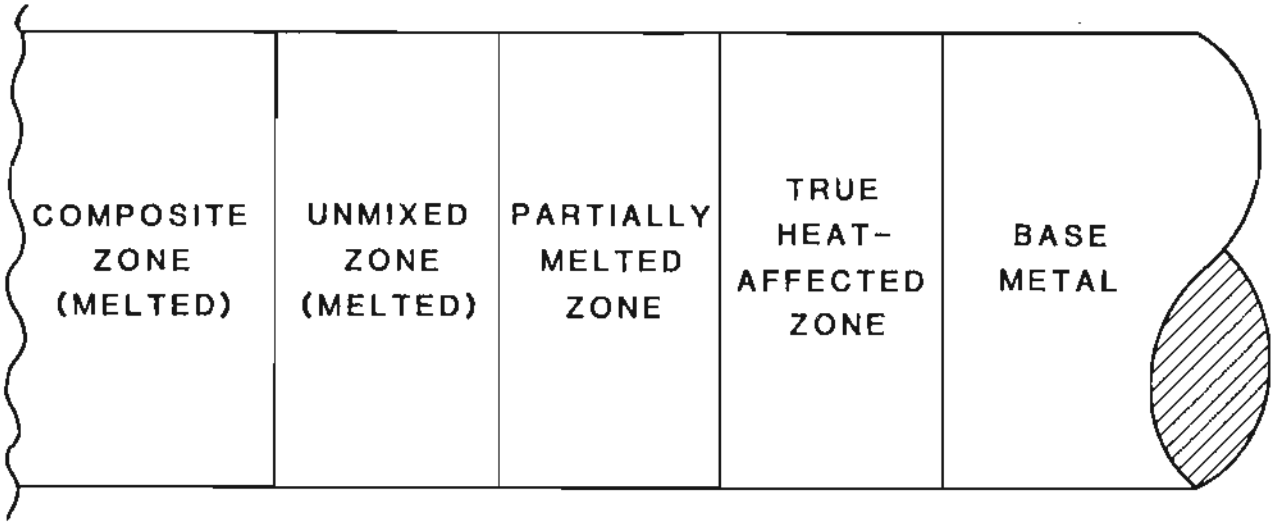

Figure 11. SAVAGE CONCEPT OF FUSION WELD.

The partially melted zones consist of material that, as the name implies, has been only partially melted. The existence of these zones accounts for the temperature gradients that must exist across them and the local variations in melting temperature that must exist within them. The bulk compositions of the partially melted zones are again the same as those of the corresponding base metals.

The true heat-affected zones contain material that has undergone some degree of solid-state transformation, depending on the heat treatment to which it was effectively subjected during welding. They obviously have the same bulk composition as the adjoining base metals and correspond exactly to the heat-affected zone of the traditional concept.

Finally, the base metal regions consist of material that has been completely unaffected by the fusion welding process. The base metal regions of the Savage concept correspond exactly to those of the traditional concept.

2.6.4. The Modified Savage Concept.

Another important region that Savage considered but did not delineate as a separate zone is the region where the composition of the composite zone makes the transition to the base metal composition of the unmixed zone. As pointed out by Savage, its existence is inconsistent with the definition of the composite zone, and it must, therefore, be a part of the unmixed zone.

This transition zone is of special significance in this investigation, inasmuch as it is in this region that the compatibility

or lack thereof of the composite zone with the adjoining unmixed zone of base metal composition is actually manifested. Accordingly, in this work, that region is referred to as the transition zone and leads to the modified Savage concept shown in Figure 12.

2.6.5. The Transition Zone.

With the foregoing discussion in mind, consider an hypothetical capacitor discharge weld of a titanium pin to an iron pin, in which a substantial alloy addition of vanadium has been made. Consider further, that dilution was equal between the titanium and iron components and that the resulting composition of the composite zone is V-10Ti-10Fe in weight percent. This means that, in the transition zone on the titanium side of the weld, the composition must vary from V-10Ti-10Fe to pure titanium and that, in the transition zone on the iron side of the weld, the composition must vary from V-10Ti-10Fe to pure iron.

This situation is described schematically in Figure 13, wherein a plot of elemental concentrations is superimposed on the composite, transition, and unmixed zones on the iron side of the hypothetical weld. As the figure illustrates, there must exist a continuous set of ternary compositions, in the transition from V-10Ti-010Fe to pure iron. This set of compositions has been determined graphically from the assumed concentrations of vanadium, titanium, and iron shown in Figure 13 and is plotted in Figure 14, along with a similar plot of compositions from the titanium side of the weld.

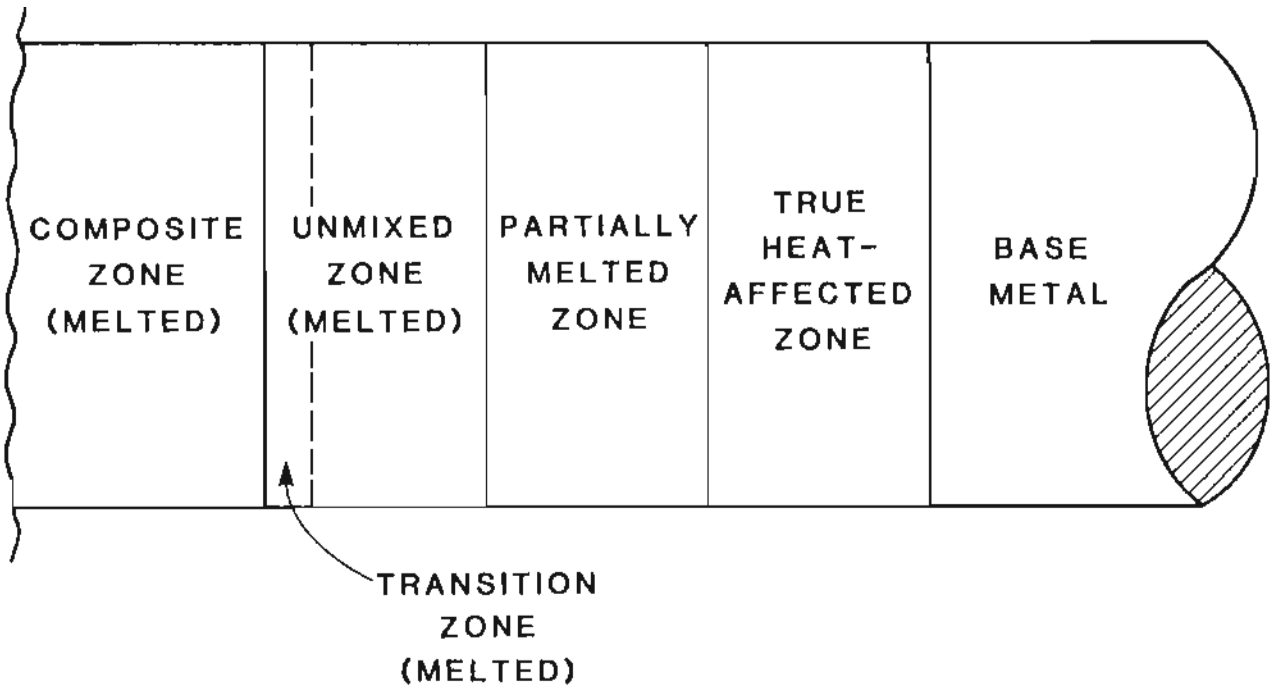

Figure 12. MODIFIED SAVAGE CONCEPT OF FUSION WELD.

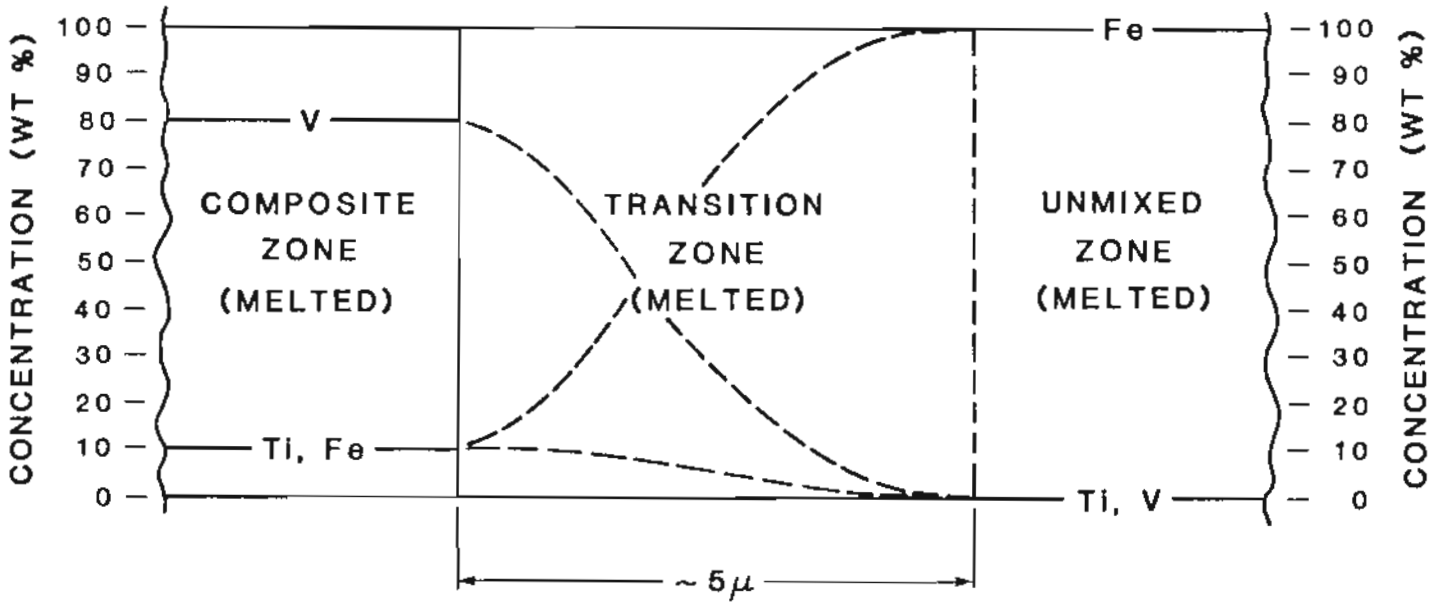

Figure 13. COMPOSITIONS PRESENT IN COMPOSITE AND TRANSITION ZONES OF HYPOTHETICAL TITANIUM TO IRON FUSION WELD.

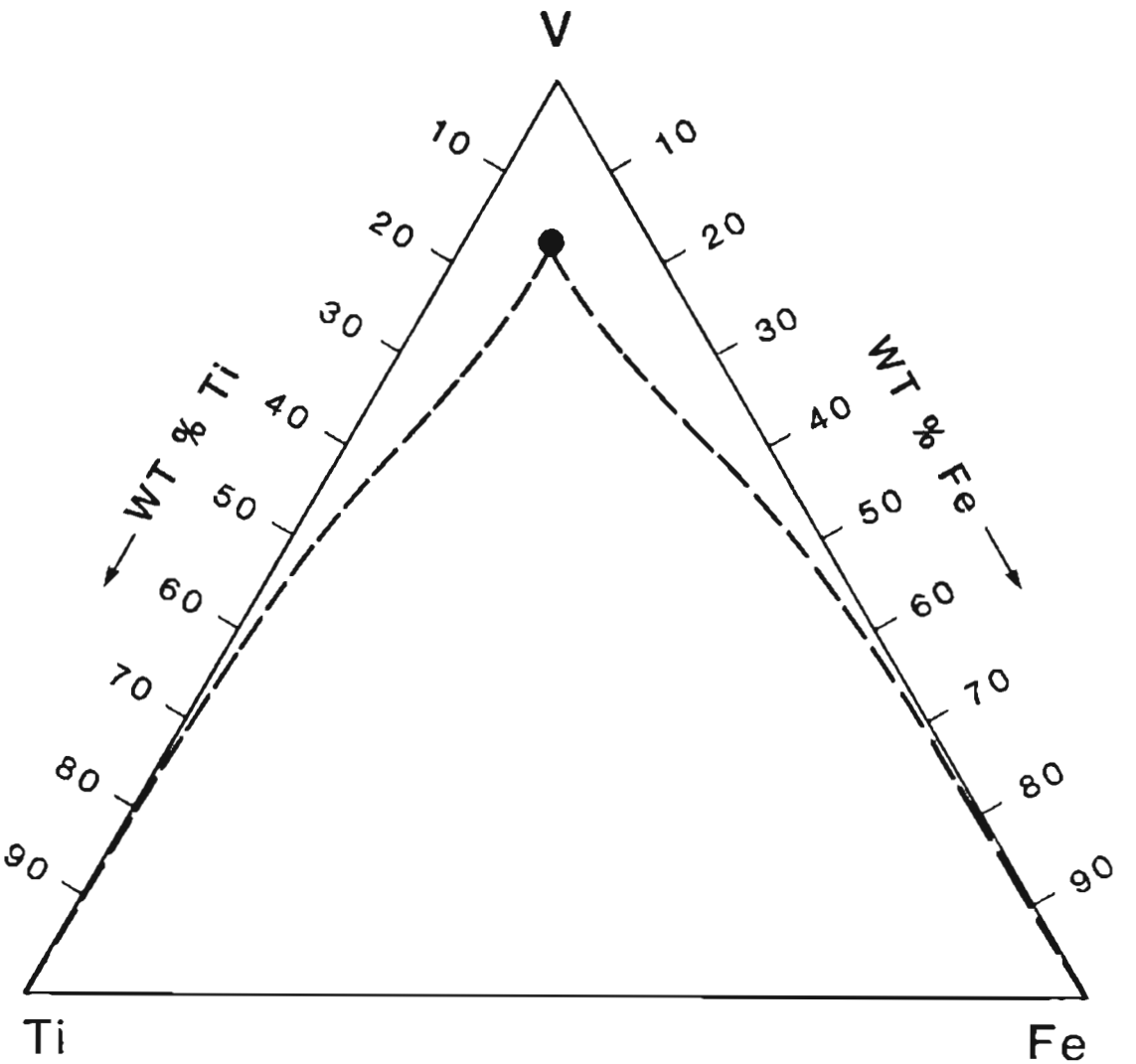

Figure 14. COMPOSITIONS PRESENT IN COMPOSITE AND TRANSITION ZONES OF HYPOTHETICAL TITANIUM TO IRON FUSION WELD.

Theoretically, for a composite zone of composition V-10Ti-10Fe to be fully compatible with both titanium and iron, all the transition zone compositions plotted in Figure 14 must possess mechanical properties that are comparable to those of the titanium and iron components involved. If, on the other hand, the width of the transition zone were sufficiently small, it might be possible to obtain some local constraint from the surrounding material and, as a result, to tolerate lesser mechanical properties.

The width of the transition zone depicted in Figure 13 is estimated to be about 5 microns. This estimate is believed to be reasonable for a typical capacitor discharge weld and is based on the aforementioned tungsten-inert gas work of Savage, et al., and on some capacitor discharge process development work done by W. E. Wood and the author.[44] If this estimate is correct, then it may be reasonable to expect some local constraint from the surrounding material.

In contrast to the tungsten-inert gas welding process employed by Savage, et al., the capacitor discharge process is an extremely rapid process, in which solidification occurs very rapidly and in which high mechanical stresses are involved. As a result, there may be insufficient time or mechanical stability for complete and uniform mixing to take place in the capacitor discharge weld composite zone.

One investigation of the capacitor discharge welding process suggests that mixing in the composite zone is both complete

and uniform.45 Another, however, indicates that it is neither complete nor uniform.46 This disparity of results implies that the extent and nature of melting in the composite zone of the capacitor discharge weld may be a complex function of the process parameters employed and the materials involved.

The applicability of the modified Savage concept of the fusion weld to the capacitor discharge welding process, especially where dissimilar metals are involved, is certainly not clear. However, the concept does provide a reasonable foundation on which to build an understanding of the interfacial phenomena that take place in the capacitor discharge fusion weld.

3. EXPERIMENTATION

3.1. Alloy Fabrication.

3.1.1. General.

One of the major tasks involved in this investigation was the fabrication of representative alloys. Alloys of twenty six different nominal compositions were fabricated and are referred to in this and in subsequent sections as Specimens P-1 through P-26, even though two specimens were actually produced for each alloy composition. The disposition of the resulting specimens for testing and analysis is described in Section 3.2.1.

The nominal compositions of Specimens P-1 through P-26 are tabulated in both atomic and weight percent in Table 2 and are displayed graphically in atomic percent in Figure 15. While the ternary composition diagram of Figure 15 is not ruled in the usual Gibbs fashion, it does employ the usual ternary coordinate system. The lines radiating from the vanadium corner of the diagram are simply lines of constant titanium to iron ratio.

Vanadium and titanium are both highly reactive metals. Furthermore, the mechanical properties of each are strongly influenced by the presence of even small amounts of some interstitial alloying elements, especially oxygen and nitrogen. As a result, special care had to be exercised in all aspects of their handling. For example, powders of these elements had to be protected from extended exposure to the atmosphere, and their elevated temperature processing had to be carried out either in vacuum or inert gas.

Table 2.

NOMINAL COMPOSITIONS OF SPECIMENS P-1 THROUGH P-26

Specimen Designation	Nominal Composition (Atomic Percent)	(Weight Percent)
P-1	V	100.0V
P-2	V-10Ti	90.5V-9.5Ti
P-3	V-7.5Ti-2.5Fe	90.2V-7.1Ti-2.7Fe
P-4	V-5Ti-5Fe	89.8V-4.7Ti-5.5Fe
P-5	V-2.5Ti-7.5Fe	89.5V-2.3Ti-8.2Fe
P-6	V-10Fe	89.1V-10.9Fe
P-7	V-20Ti	81.0V-19.0Ti
P-8	V-15Ti-5Fe	80.3V-14.2Ti-5.5Fe
P-9	V-10Ti-10Fe	79.7V-9.4Ti-10.9Fe
P-10	V-5Ti-15Fe	79.1V-4.6Ti-16.3Fe
P-11	V-20Fe	78.5V-21.5Fe
P-12	V-30Ti	71.3V-28.7Ti
P-13	V-22.5Ti-7.5Fe	70.4V-21.3Ti-8.3Fe
P-14	V-15Ti-15Fe	69.6V-14.0Ti-16.4Fe
P-15	V-7.5Ti-22.5Fe	68.8V-6.9Ti-24.3Fe
P-16	V-30Fe	68.0V-32.0Fe
P-17	V-40Ti	61.5V-38.5Ti
P-18	V-30Ti-10Fe	60.5V-28.4Ti-11.1Fe
P-19	V-20Ti-20Fe	59.5V-18.7Ti-21.8Fe
P-20	V-10Ti-30Fe	58.6V-9.2Ti-32.2Fe
P-21	V-40Fe	57.8V-42.2Fe
P-22	V-50Ti	51.5V-48.5Ti
P-23	V-37.5Ti-12.5Fe	50.5V-35.6Ti-13.9Fe
P-24	V-25Ti-25Fe	49.5V-23.3Ti-27.2Fe
P-25	V-12.5Ti-37.5Fe	48.6V-11.4Ti-40.0Fe
P-26	V-50Fe	47.7V-52.3Fe

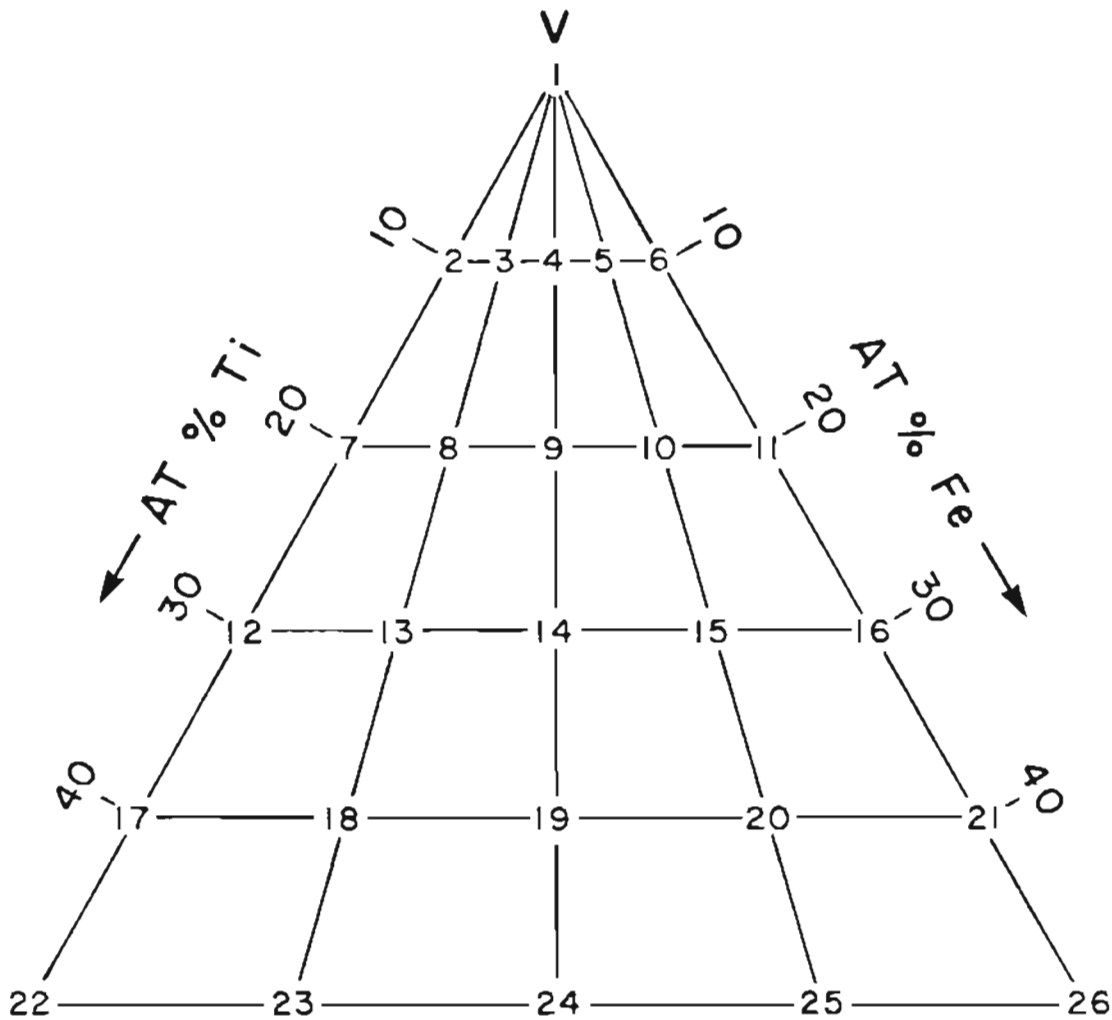

Figure 15. NOMINAL COMPOSITIONS (ATOMIC PERCENT) OF SPECIMENS P-1 THROUGH P-26.

Elemental powders were used as the sources of vanadium, titanium, and iron in the fabrication of Specimens P-1 through P-26. The use of such powders had both advantages and disadvantages. It was advantageous, to the extent that it facilitated the weighing and blending steps of the fabrication process. It was disadvantageous, to the extent that powders are inherently vulnerable to contamination and that powders normally require pressing and sintering before they can be successfully arc melted. The chemistries of the constituent powders used are presented in Section 3.2.2.

The alloy fabrication process employed took into account the need for special handling of the vanadium, titanium, and iron powders and consisted of five separate steps. These steps were weighing, blending, pressing, sintering, and melting and are described in detail in Sections 3.1.2 through 3.1.6. The machining of specimens is described under the test or analysis for which the machining was required.

3.1.2. Weighing.

The weighing of the constituent powders was done using a Mettler Model PN323 precision balance. The powders were weighed to the nearest milligram, then loaded into 100 milliliter capacity, polyethylene, wide-mouth bottles for storage and further processing. The total weight of powder corresponding to each bulk composition was 100 grams. The experimental setup in weighing is shown in Figure 16.

During weighing, every effort was made to minimize the possibility of contamination of either the constituent powders or the

Figure 16. EXPERIMENTAL SETUP USED IN WEIGHING OF CONSTITUENT POWDERS.

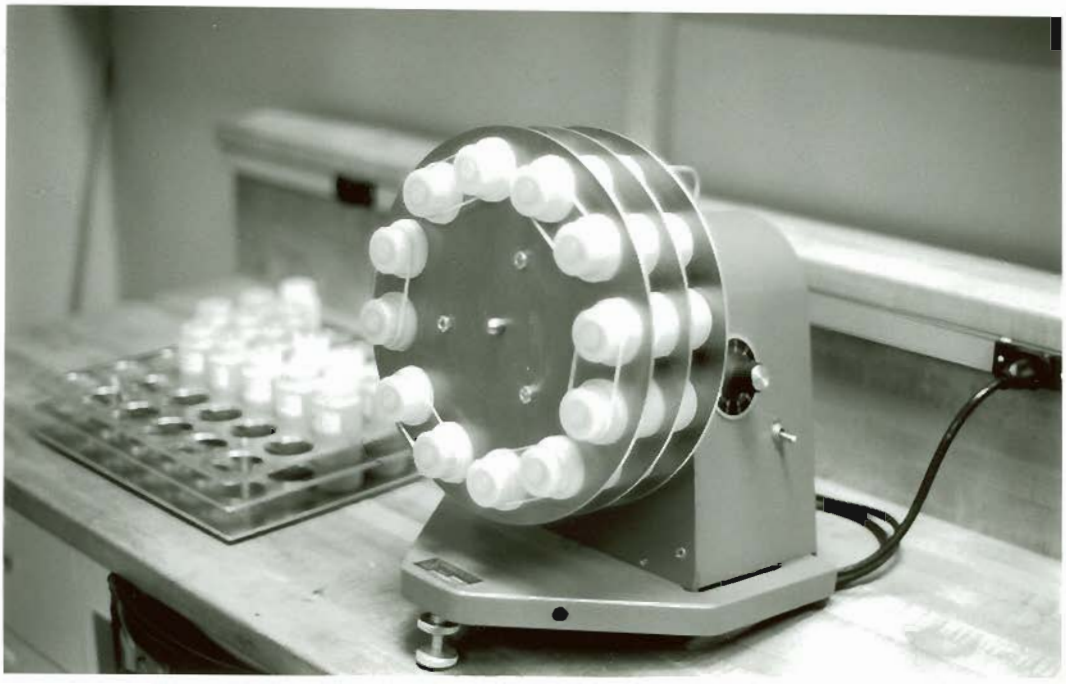

Figure 17. EXPERIMENTAL SETUP USED IN BLENDING OF WEIGHED POWDERS.

resulting powder mixtures. For example, separate plastic weighing dishes were used for each of the three constituent powders, and beakers, spatulas, and scoops were all cleaned thoroughly with acetone after each use.

In addition, exposure of the constituent powders to the atmosphere was minimized by keeping their containers closed, except when the powders were actually being removed. Finally, small amounts of left-over powder were discarded, rather than being returned to their original containers and possibly contaminating the remaining contents.

Noteworthy, in the weighing process, was the use of a locally fabricated aluminum rack to hold the 100 milliliter bottles into which the weighed powders were loaded. The rack turned out to be indispensable in handling the small, unstable bottles and in keeping them in order during weighing and subsequent processing.

3.1.3. Blending.

Blending of the constituent powders was accomplished using a conventional New Brunswick Scientific Company Model TC-6 test tube rotation device that had been fitted with a locally fabricated rack designed to accommodate the 100 milliliter, polyethylene bottles mentioned earlier. Up to twelve such bottles could be held in the rack and rotated at any given time. The experimental setup for blending is shown in Figure 17.

To achieve the maximum blending effect, the polyethylene bottles were secured with rubber bands to prevent their independent

rotation, the axis of rotation of the rack was placed at about 5 to 6 degrees above the horizontal, and the speed of rotation of the rack was set at about 28 revolutions per minute. These conditions appeared to yield the best stirring and, hence, the best blending action.

However, some preliminary runs with pure vanadium powder containing conglomerates did not lead to the breaking up of the conglomerates. The problem was solved, however, by the introduction of a three-fourths inch diameter stainless steel ball into each of the polyethylene bottles. No conglomerates were observed in any of the mixtures that had been blended with the steel ball.

The blending procedure was carried out for a period of two hours, for each group of powder mixtures. At the end of each blending period, a visual inspection of the mixtures indicated that complete blending had taken place. The titanium powder was readily distinguishable from the others and appeared to be uniformly distributed throughout each mixture.

After blending, the stainless steel ball was removed from each of the polyethylene bottles with forceps that were cleaned with acetone after each use. The bottles, with their now thoroughly blended vanadium, titanium, and iron powders, were set aside to await further processing.

3.1.4. Pressing.

As a prerequisite to sintering, the blended powders were pressed into small cylindrical shapes, using the Mohr Machinery Company Model MM-25/3, 20-ton capacity industrial press shown in

Figure 18. For this operation, the press was equipped with a 0.910 inch diameter die and was set to apply a maximum load of 12 tons for a period or dwell time of about 3 seconds. The powders were loaded into the die manually. Otherwise, the press was operated semi-automatically.

To minimize the trauma to which the fragile pressed cylinders might be subjected on ejection, the press was operated in the ''slow'' mode for all functions. The integrity of the pressed cylinders varied greatly with composition. Those having a high titanium content held together best. Those having a high vanadium content were the most fragile. However, all were manageable, provided they were handled carefully.

The thickness of the pressed cylinders also varied with composition. Most of them, however, were about one-half inch thick. From four to six such cylinders were obtained from each batch of 100 grams of powder. Immediately after pressing, the cylinders were prepared for sintering as described in the next section, loaded into the sintering furnace, and placed under vacuum.

To avoid contamination of the powders during pressing, the punch, die, and immediate surroundings were cleaned thoroughly with compressed air and with acetone, after each powder mixture of a given bulk composition had been pressed. To avoid contamination of the operator, a respirator was worn during pressing. It has been observed early that the vanadium-rich powders tended to squirt out between the punch and die during pressing.

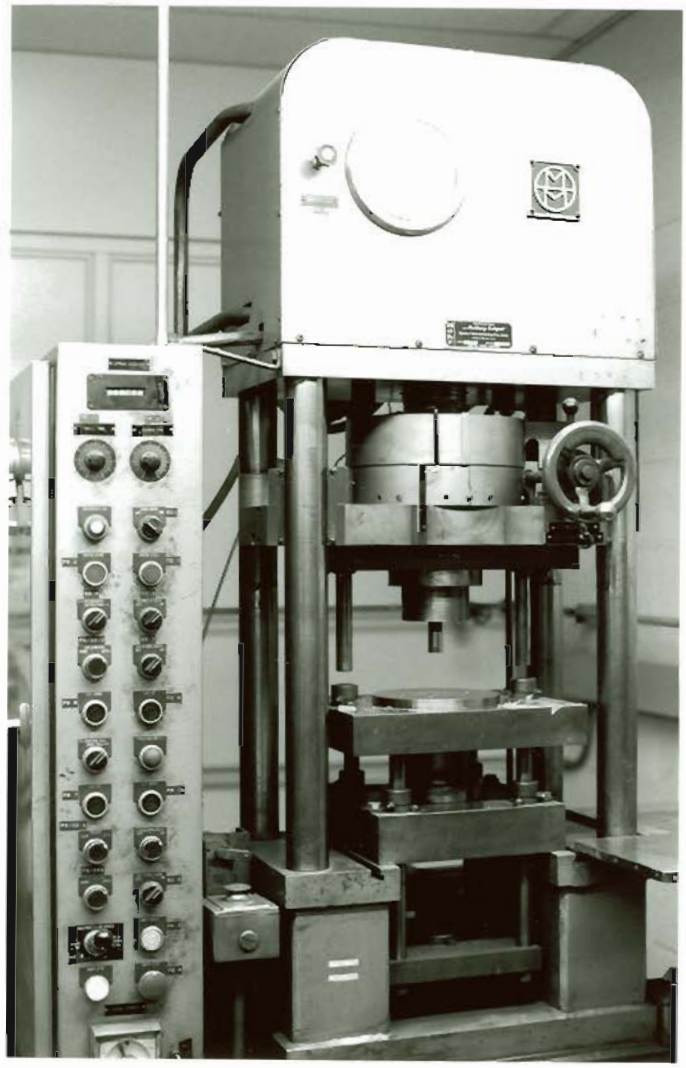

Figure 18. 20-TON CAPACITY, INDUSTRIAL PRESS USED IN PRESSING OF BLENDED POWDERS.

3.1.5. Sintering.

Sintering of the pressed powder cylinders was carried out in a Richard D. Brew and Company Model 580C, high-temperature, controlled-atmosphere furnace. The furnace was equipped with a graphite heating element that made it possible to obtain operating temperatures up to 3,000°C. In addition, the furnace incorporated a high-vacuum system that was capable of producing and maintaining a vacuum of about 7 to 8 microns of mercury, and a gas distribution system that allowed the introduction of a variety of gases at any time during thermal processing. The furnace is shown in Figure 19, with the controller on the left, the tank in the center, and the high-vacuum and gas distribution systems on the right. The power supply is in the rear.

In preparation for sintering, the pressed cylinders were arranged uniformly on six-inch diameter graphite furnace plates. The cylinders were separated from the plates by 0.016 inch thick pieces of pure molybdenum sheet. This was done to preclude any possible reaction between the cylinders and the carbon of the graphic plates. Four to six cylinders were arranged on each plate, depending on how many cylinders of a given bulk composition emerged from the pressing operation. Five such plates were stacked approximately one-half inch apart inside a graphite canister, along with a sixth plate containing zirconium buttons that were intended to act as ''getters.'' The canister was then closed with a graphite lid and loaded into the furnace.

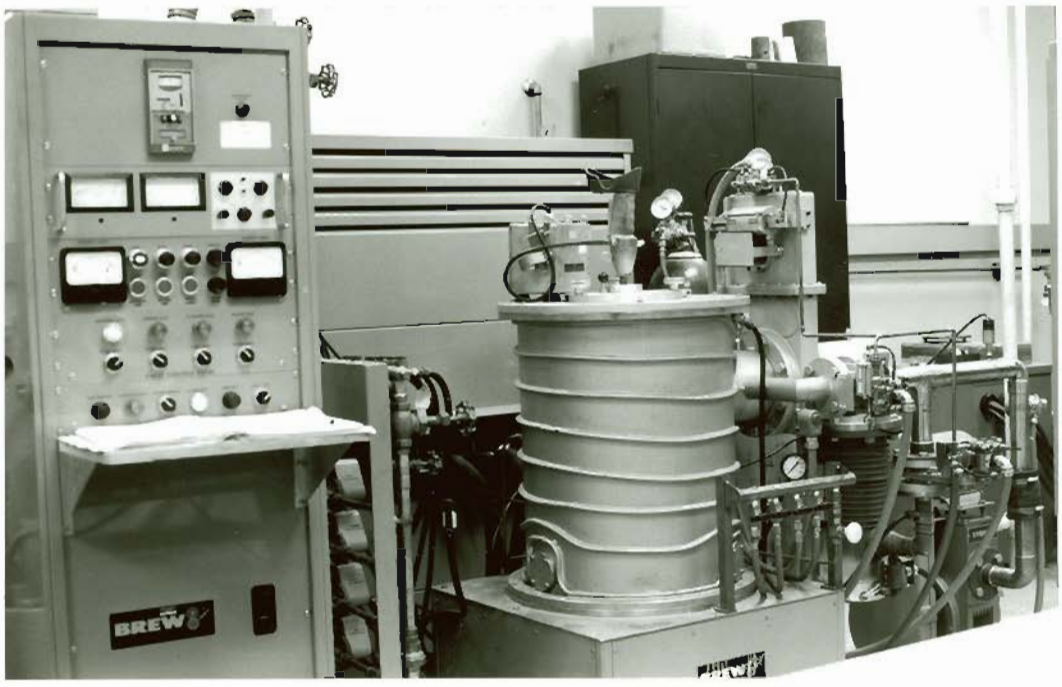

Figure 19. HIGH-TEMPERATURE, CONTROLLED-ATMOSPHERE FURNACE USED IN SINTERING OF PRESSED POWDERS.

At the start of each sintering run, the furnace was pumped down to 10–15 microns of mercury and held there for about 5 minutes. It was then back-filled with dry nitrogen to a partial vacuum of 10 inches of mercury and held there for about 2 minutes. Next, the furnace was again pumped down to 10–15 microns of mercury and held there for about 5 minutes. This time, however, the furnace was back-filled with helium to about 10 inches of mercury and held there for about 2 minutes. Finally, the furnace was once again pumped down to 10–15 microns of mercury and held there for 5 minutes, before the application of power to the furnace heating elements.

Based on the results of several preliminary runs, the target temperature and time were selected to be 900°C and 30 minutes respectively. These were the minimum temperatures and time required for the adequate bonding of the pressed powders. Furthermore, 900°C was the minimum temperature attainable in the furnace, due to controller characteristics, and was the minimum readily measurable with the optical pyrometer. An initial power setting of ''80'' was employed in all the runs. Then, as the measured temperature approached 900°C, the power setting was reduced to ''30,'' where it was left for the remainder of the run. The rising temperature typically overshot the 900°C mark by about 25°C. Toward the end of each run, the temperature tended to drop below 900°C by a similar amount. A vacuum of 10–15 microns of mercury was maintained through the duration of each run.

Following each sintering run, the furnace was allowed to cool, under vacuum, for at least one hour. Then, it was back-filled with helium and allowed to cool for several additional hours, usually overnight. After the furnace had cooled to near room temperature, the sintered cylinders were removed from the furnace and returned to their original polyethylene bottles to await melting, the final step in the alloy fabrication process.

3.1.6. Melting.

The melting of the sintered cylinders was accomplished in a Vacuum Industries vacuum arc melting furnace. The furnace was powered by four constant current, D-C power supplies that were capable of delivering up to 1,300 amperes of operating current. The furnace incorporated also a high-vacuum system capable of producing and maintaining a vacuum of less than 10 microns of mercury. In addition, the furnace included a system for the controlled introduction of several gases, including argon, helium, and nitrogen. The furnace also had a high-frequency start capability. An overall view of the furnace is provided in Figure 20. The furnace tank is on the left, the high-vacuum and gas distribution systems are in the center, and the power supplies are on the right.

The actual melting of the cylinders was done in a locally designed and fabricated, water-cooled copper block that contained five separate molds. Each of the molds was about one-half inch deep, one and one-fourth inches in diameter, and tapered to facilitate removal of the solidified specimens. The copper block, with its five

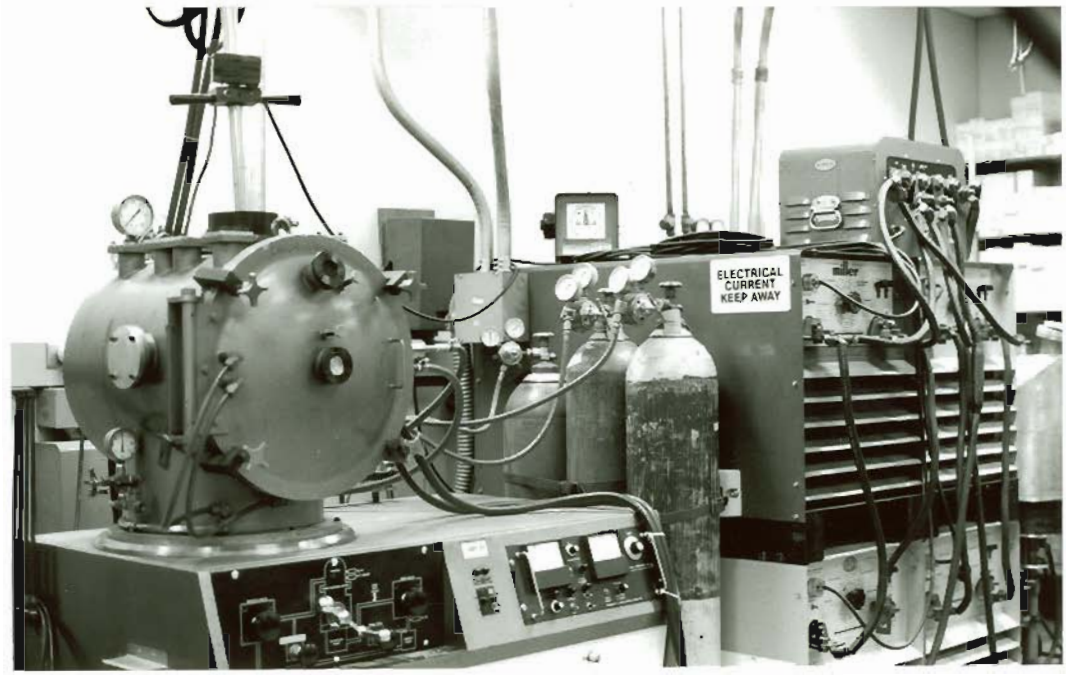

Figure 20. VACUUM ARC MELTING FURNACE USED IN SINTERING OF PRESSED POWDERS.

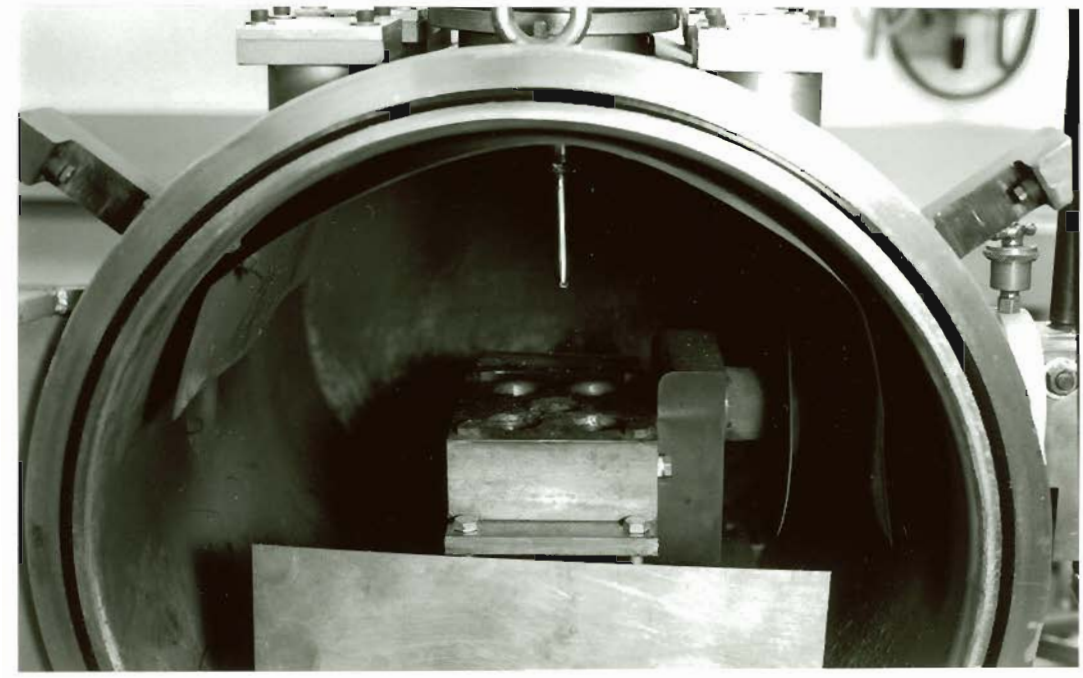

Figure 21. WATER-COOLED, COPPER MOLDS USED IN MELTING OF SINTERED POWDERS.

molds, can be seen in Figure 21, in its normal position inside the furnace. Due to the comparative ease with which the electrode could be manipulated in their vicinity, only the front two molds were used for melting specimens. The center mold was used for melting a pure vanadium ''getter'' at the beginning of each run.

During each run, two sintered cylinders were melted in each of the two front molds, with all four cylinders melted being of the same nominal bulk composition. To facilitate their complete melting, the cylinders were placed in the molds on edge and side by side. In preliminary runs, where the cylinders had been stacked on top of each other, heat flow across the interface between them tended to be poor, and the bottom cylinder tended to melt incompletely. To reduce the possibility of carry-over contamination from the sintering process, each of the sintered cylinders was brushed free of loose particles prior to being placed into the furnace.

At the start of the melting procedure, the furnace was evacuated to less than 10 microns of mercury, where it was held for about 5 minutes. It was then back-filled with dry nitrogen to 10 inches of mercury and held there for another 5 minutes. Next, the same pump-down and back-fill procedure was repeated with helium. Finally, the furnace was once again pumped down to less than 10 microns of mercury, held there for 5 minutes, and then back-filled to 10 inches of mercury with a 50-50 volume percent mixture of argon and helium. This was the atmosphere in which all of the melting took place.

The pure vanadium ''getter'' was melted first, then each of the two pairs of sintered cylinders. Stirring of the molten pools was accomplished by manipulation of the electrode and was continued for about 30 seconds for each specimen. It was found that a working distance of about three-fourths inch provided the best combination of arc stability and stirring action. Greater working distances led to arc instability and wander, and smaller working distances caused the molten material to spatter. A taper at least one inch long and a fairly sharp tip on the tungsten electrode were essential to good arc stability and control. All specimens were melted using a 50 percent power setting, which yielded a constant operating current of about 640 amperes.

On the completion of each melting cycle, the furnace was once again pumped down to less than 10 microns of mercury, where it was held for at least 5 minutes. Then, the furnace was back-filled with helium to about 5 inches of mercury and allowed to stand for an additional 10 minutes. At the conclusion of this 10 minute period, the furnace was opened and the specimens were either turned, in preparation for a second melting, or were removed from the furnace and put into their associated polyethylene bottle for storage. Approximately three hours were required to carry out the dual melting of a given set of sintered cylinders.

Between melts of specimens of differing compositions, the furnace was thoroughly cleaned. This included the wire brushing, acetone cleaning, and vacuum cleaning of the copper molds, the

cleaning and regreasing of the furnace door o-ring, the vacuum cleaning of the entire interior of the furnace tank, and the acetone cleaning of the tungsten electrode. The electrode was also removed from the furnace and reground, whenever necessary, to maintain good arc stability and control.

The arc melting of Specimens P-1 through P-26 was accomplished without significant difficulty, with the exception that some of the more brittle specimens fractured violently at the start of the second melting. While no complete solution to this problem was identified, slow initial heating did seem to reduce the probability of the phenomenon occurring.

3.2. Testing and Analysis.

3.2.1. General.

The methods of testing and analysis employed in this investigation were selected on the basis of three main considerations. These considerations were the needs of the investigation, the availability of facilities, and the cost of pure vanadium powder. The needs of the investigation were to obtain valid experimental data on the strengths, ductilities, structures, and compositions of the alloys being evaluated. The availability of facilities, as it turned out, was more than adequate to support the needs of the investigation. Only the high cost of pure vanadium powder detracted somewhat from the ideality of the testing and analysis program.

Specifically, the high cost of pure vanadium powder led to the selection of non-standard bend testing as a means to obtain information on the strengths and ductilities of the alloys being evaluated. The principal disadvantage of this method of testing is that the values of tensile strength, yield strength, and elongation may not be measured directly, but must be calculated using models whose applicability to real materials is questionable. The standard tensile test, on the other hand, permits the direct measurement of these quantities. In spite of this disadvantage, the non-standard bend testing contributed valuable information to this investigation and led to substantial savings in powder acquisition and specimen fabrication and machining costs.

At the time this investigation was just getting underway, the cost of pure vanadium powder varied from $150 per pound to $600 per pound, depending on the supplier and, presumably, on the purity. However, none of the suppliers consulted was equipped to provide specifications of the interstitial contents of their powders. In at least one case, the supplier could not even provide a statement of the overall purity of his powder. The pure vanadium powder actually used in this investigation was purchased from the Shieldalloy Corporation at a cost of $150 per pound and was described simply as 99.7 percent pure vanadium powder. The implications of this selection were formidable and are addressed, as applicable, in the following sections.

Based on the several considerations mentioned earlier, the following methods of testing and analysis were selected for employment in this investigation: chemical analysis, hardness testing, x-ray energy dispersion analysis, microstructure analysis, x-ray diffratometry analysis, bend testing, and fracture analysis. The employment of each of these methods of testing and analysis is described in detail in the following sections. As a minimum, the purpose, procedure, and results of each method are presented.

The disposition of specimens for testing and analysis is shown in Figure 22. As was mentioned previously, two specimens were actually produced for each alloy composition or specimen designation P-1 through P-26. As shown in Figure 22, one of the specimens (a) was set aside for x-ray energy dispersion analysis, while the other (b) was used for all the remaining testing and analysis. As shown also in Figure 22, the portion of specimen (b) used for x-ray diffractometry analysis and hardness testing was subsequently machined to the proper dimensions and used for bend testing and fracture analysis.

3.2.2. Chemical Analysis.

One of the first analyses conducted in this investigation was a chemical analysis of the constituent vanadium, titanium, and iron powders and of sintered and arc-melted constituent vanadium. The purpose of the analysis was to ascertain the levels of the interstitial impurities oxygen, nitrogen, hydrogen, and carbon in the constituent powders and to determine the changes in these levels that were likely to occur in vanadium as a result of sintering and

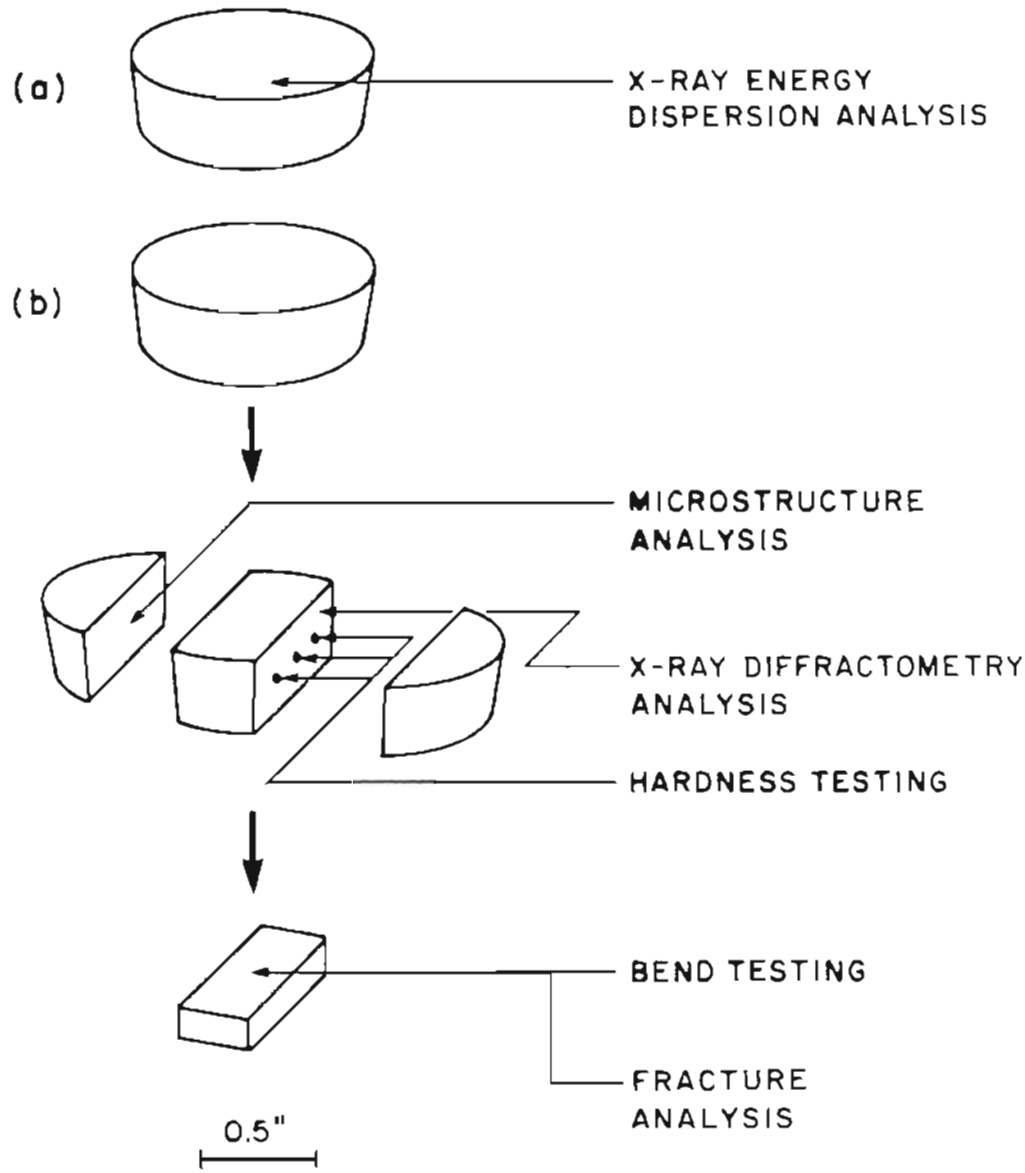

Figure 22. DISPOSITION OF SPECIMENS P-1 THROUGH P-26 FOR TESTING AND ANALYSIS.

arc-melting. The chemical analysis was done by the United States Bureau of Mines in Albany, Oregon.

The results of the chemical analysis are provided in Table 3. In general, they indicate an intolerably high interstitial content in the pure vanadium powder, a tolerably high interstitial content in the pure titanium powder, and a remarkably low interstitial content in the pure iron powder. In addition, they indicate that the levels of oxygen, nitrogen, and carbon in the pure vanadium powder increase substantially with sintering. The modest additional changes that are shown to occur as a result of arc-melting are not considered to be reliable, inasmuch as different samples were used for each of the analyses.

Obviously, the single most significant result of this analysis has to do with the high interstitial content of the constituent vanadium powder. The oxygen content alone exceeds considerably the combined amount of oxygen and nitrogen tolerable in ductile vanadium. This means that the constituent vanadium powder was inherently brittle as received and probably even more brittle after alloy fabrication processing. Furthermore, this surely has undesirable implications with regard to the mechanical properties of all the Specimens P-1 through P-26.

3.2.3. Hardness Testing.

Hardness testing was done to obtain some indication of the probable strengths of the Specimens P-1 through P-26. The testing was accomplished using a Wilson Instrument Company Model 3JR hardness

Table 3.

INTERSTITIAL CONCENTRATION DATA FOR CONSTITUENT VANADIUM, TITANIUM, AND IRON POWDERS AND FOR SINTERED AND ARC-MELTED CONSTITUENT VANADIUM

Specimen Designation	Interstitial Concentration (PPM)*			
	Oxygen	Nitrogen	Hydrogen	Carbon
Vanadium Powder, Shieldalloy Lot Number RM9036	4,280	895	48	360
Titanium Powder, OGC Designation Number Ti-13	3,085	450	427	115
Iron Powder, OGC Designation Number Fe-11	370	24	8	10
Vanadium, Sintered, Shieldalloy Lot Number RM9036	5,880	975	15	450
Vanadium, Arc-Melted, Shieldalloy Lot Number RM9036	5,045	1,065	4	510

* Data are based on chemical analyses performed by United States Bureau of Mines, Albany, Oregon.

tester. A Brale sphero-conical diamond penetrator and a 150 kilogram test load were employed to obtain Rockwell C hardness numbers.

Three widely separated indentations were made in each of Specimens P-2 through P-26, as shown in Figure 22. Only one successful indentation was made in Specimen P-1 (100.0V), inasmuch as all other attempts to obtain an indentation in Specimen P-1 resulted in fracture of the specimen.

The results of the hardness testing are tabulated in Table 4 and displayed graphically in Figures 23 through 28. The Rockwell hardness (HRC) values for individual indentations are remarkable for their consistency for each specimen. This suggests that, on a rather gross scale, the as-cast specimens were reasonably homogeneous and isotropic.

Figure 23 shows the average hardness values located in conjunction with the compositions (in atomic percent) of the specimens from which they were obtained. This permits an overall assessment of the hardness trends, as they relate to specimen composition. However, Figures 24 through 28 probably provide an even more useful means of assessing these trends.

In Figures 24 through 28, the average Rockwell C hardness values are plotted against various ratios of titanium to iron (in weight percent). In each figure, the ratio of titanium to iron is constant. Furthermore, each of the Figures 24 through 28 (in weight percent) is identical to the corresponding portion of Figure 23 (in atomic percent).

Table 4.

ROCKWELL HARDNESS DATA FOR SPECIMENS P-1 THROUGH P-26

Specimen Designation	Hardness (HRC) Indent #1	Indent #2	Indent #3	Average
P-1	*	37.8	*	38
P-2	29.0	30.0	30.0	30
P-3	27.5	27.4	29.0	28
P-4	28.0	29.0	27.9	28
P-5	39.4	39.0	39.2	39
P-6	50.2	50.4	50.0	50
P-7	36.6	36.2	36.6	36
P-8	33.4	33.6	34.0	34
P-9	34.6	35.4	36.0	35
P-10	41.8	39.2	40.8	41
P-11	52.5	52.8	52.8	53
P-12	40.2	40.6	40.4	40
P-13	40.0	39.6	39.1	40
P-14	40.2	39.2	40.8	40
P-15	43.8	43.6	43.1	44
P-16	47.2	47.1	46.4	47
P-17	43.0	42.8	43.0	43
P-18	43.2	43.0	43.5	43
P-19	46.2	46.0	46.0	46
P-20	46.8	47.2	47.2	47
P-21	42.0	42.1	42.2	42
P-22	45.5	45.2	44.8	45
P-23	49.2	50.2	49.4	50
P-24	55.4	55.6	55.0	55
P-25	51.0	51.2	51.1	51
P-26	41.3	41.9	41.6	42

* Specimen fractured on application of test load.

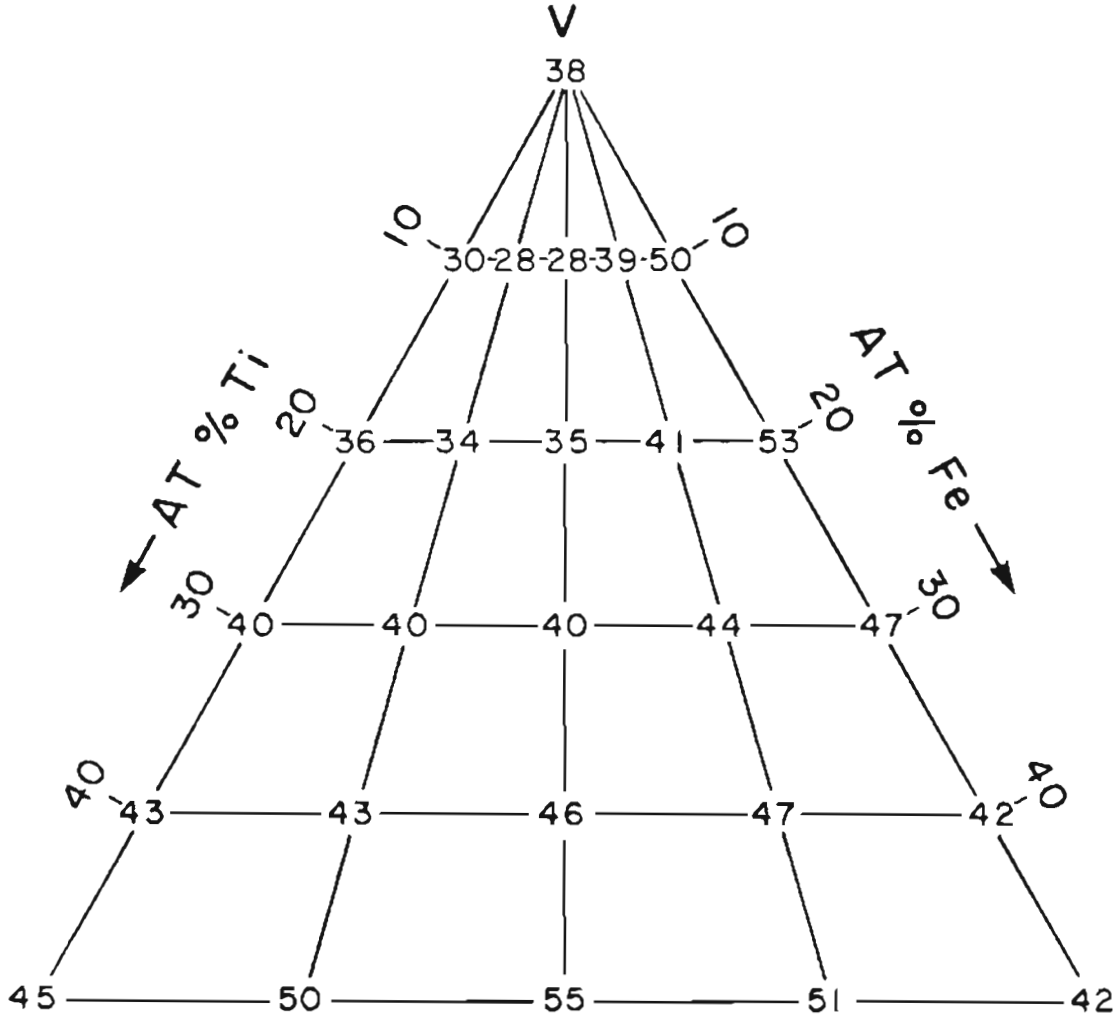

Figure 23. AVERAGE ROCKWELL HARDNESS VALUES (HRC) FOR SPECIMENS P-1 THROUGH P-26.

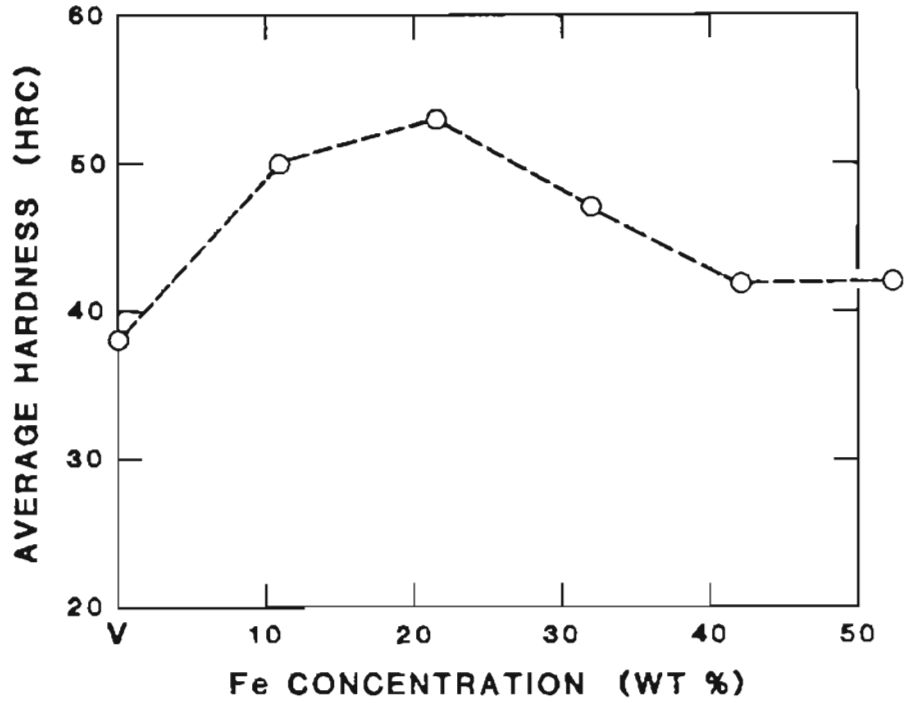

Figure 24. AVERAGE ROCKWELL HARDNESS (HRC) VERSUS Fe CONCENTRATION (WEIGHT PERCENT).

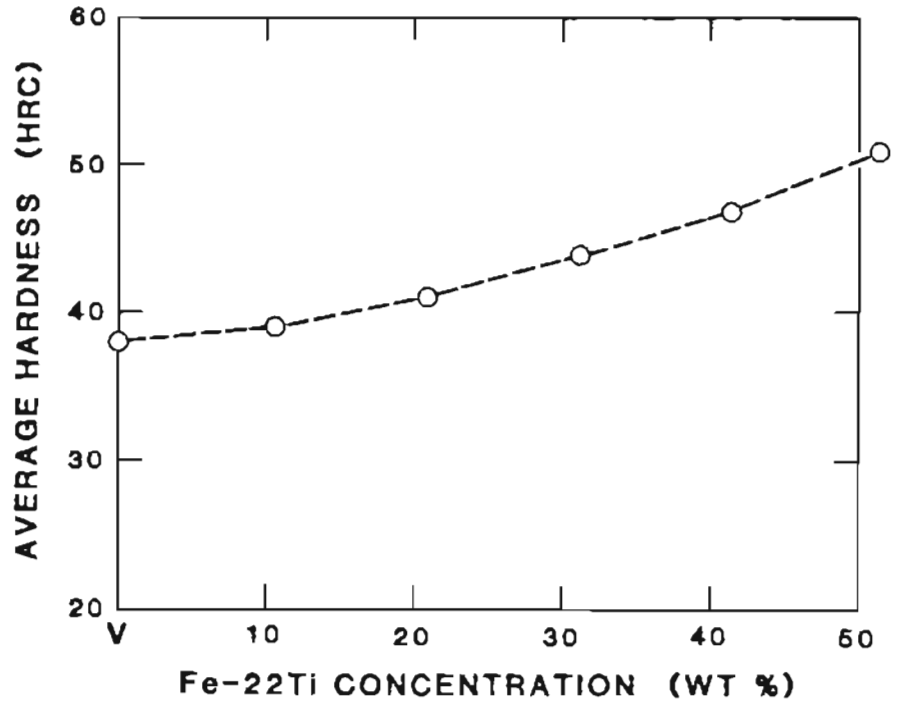

Figure 25. AVERAGE ROCKWELL HARDNESS (HRC) VERSUS Fe-22Ti CONCENTRATION (WEIGHT PERCENT).

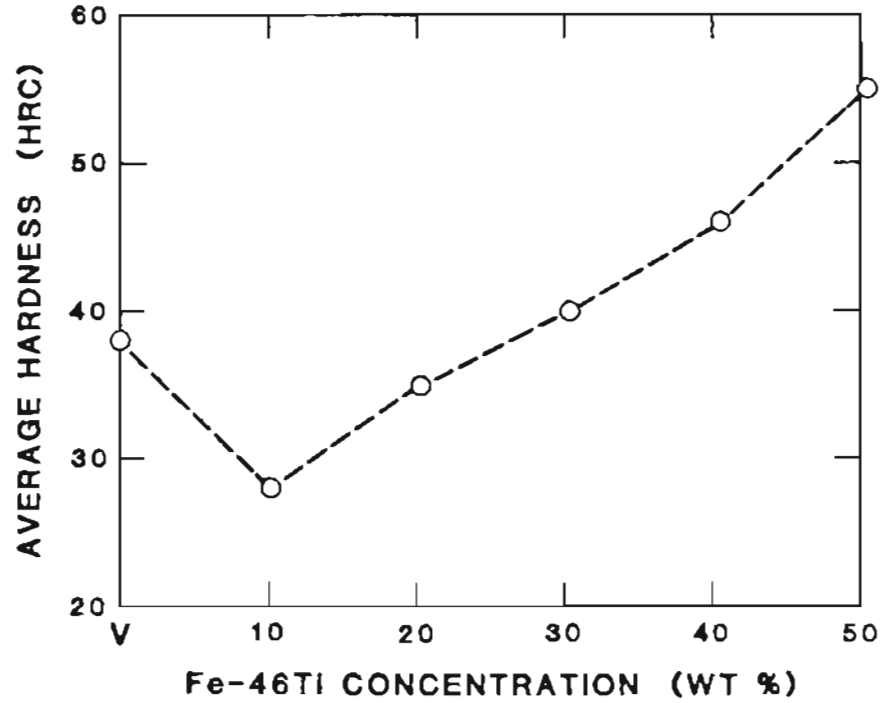

Figure 26. AVERAGE ROCKWELL HARDNESS (HRC) VERSUS Fe-46Ti CONCENTRATION (WEIGHT PERCENT).

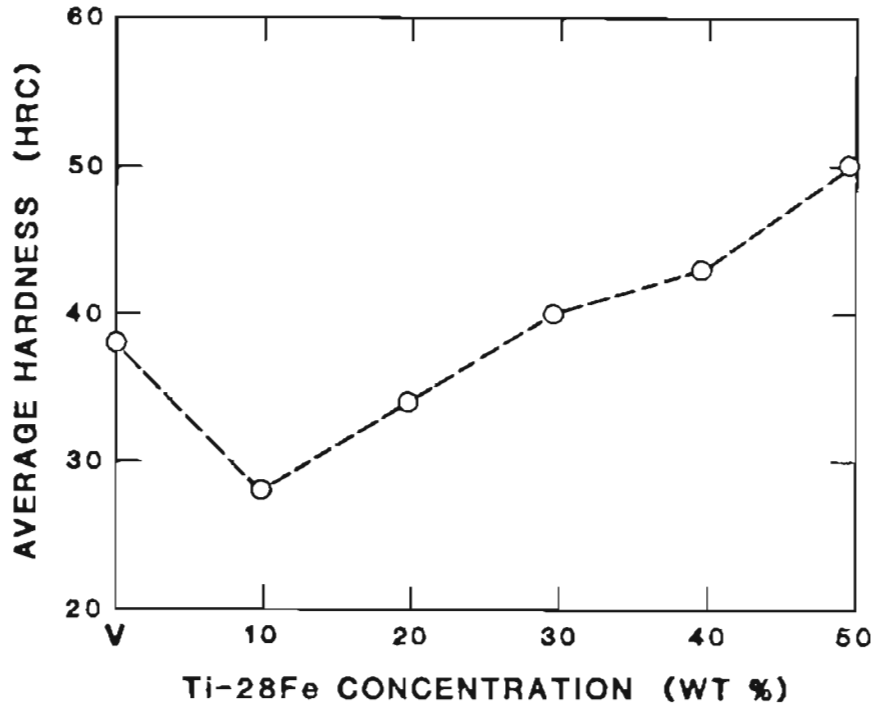

Figure 27. AVERAGE ROCKWELL HARDNESS (HRC) VERSUS Ti-28Fe CONCENTRATION (WEIGHT PERCENT).

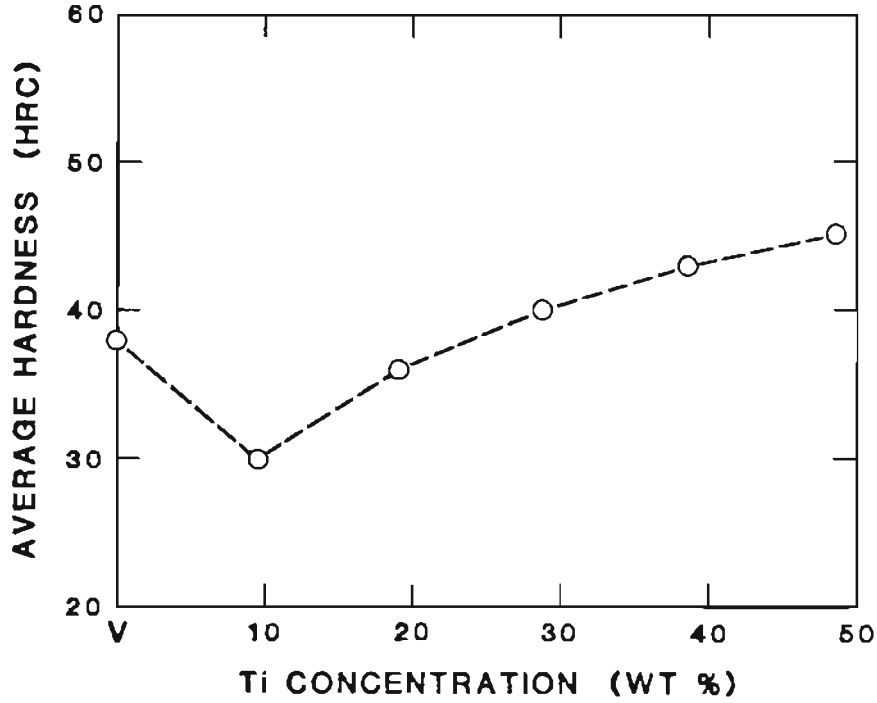

Figure 28. AVERAGE ROCKWELL HARDNESS (HRC) VERSUS Ti CONCENTRATION (WEIGHT PERCENT).

The trends in all instances appear to reflect the influences of two separate but competing mechanisms. The first is some mechanism by which increases in titanium concentration produce decreases in hardness. The second is the normal solid solution hardening mechanism, by which increases in titanium (or iron) concentration produce increases in hardness.

In the case shown in Figure 24, there is no involvement of titanium and, therefore, no initial decrease in hardness. Only the usual solid solution hardening mechanism is operating here. By this mechanism, increases in hardness are obtained as a result of the increases in lattice strain associated with the coexistence of the dissimilar iron and vanadium atoms.

However, in the cases shown in Figures 25, 26, 27, and 28, there is an involvement of titanium and, hence, there are initial decreases in hardness. In the case shown in Figure 25, wherein the involvement of titanium is limited, the decrease is relative and appears only as an initial suppression of the solid solution hardening effect. In the cases shown in Figures 26, 27, and 28, wherein the involvement of titanium is extensive, the initial decreases are absolute and considerable.

A very similar phenomenon was observed by W. Rostoker in his study of the hardness and tensile properties of V-Ti alloys and may be observed in the top graph of Figure 29.47 His explanation of the phenomenon is essentially that whatever oxygen atoms are present associate themselves preferentially with the titanium atoms, which are

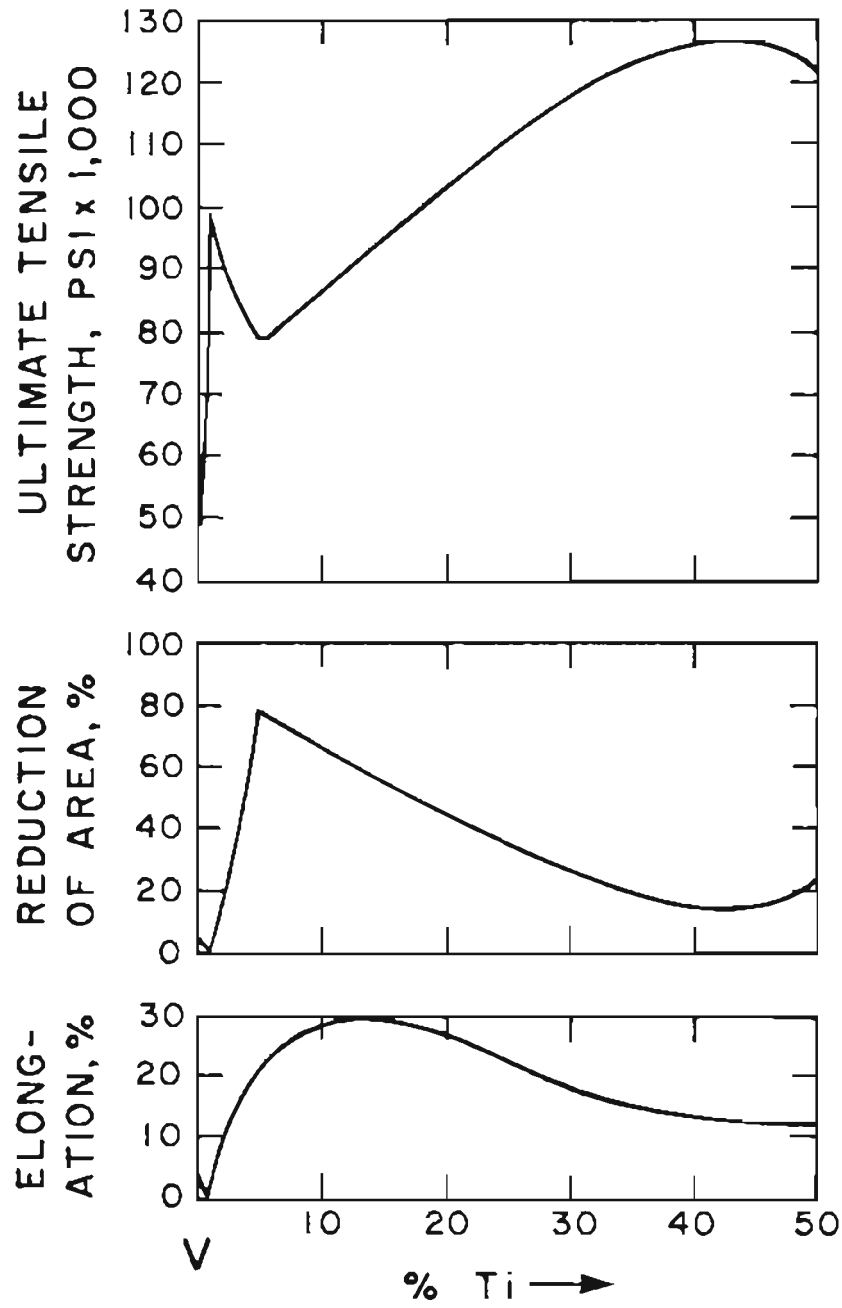

Figure 29. TENSILE PROPERTIES OF V-Ti ALLOYS.

much better suited to accommodate them than are the vanadium atoms. This leads to a reduction in lattice strain and, hence, to a reduction in hardness.

Still another unusual phenomenon may be observed in the top graph of Figure 29. This phenomenon involves the rapid increase in the ultimate tensile strength of V-Ti alloys that accompanies small additions (i.e., less than one weight percent) of titanium. Here, Rostoker's explanation is essentially that the small amounts of titanium form oxides and nitrides that emerge as fine precipitates. These precipitates cause lattice distortions and, thereby, increases in hardness. This phenomenon could not have been observed in this investigation, since such small additions of titanium were not employed.

The probable strengths of Specimens P-1 through P-26, as inferred by the hardness testing results provided above, are considered in Section 4.

3.2.4. X-Ray Energy Dispersion Analysis.

Quantitative x-ray energy dispersion analysis was carried out on a small number of specimens to insure that no substantial changes had occurred in their nominal compositions, as a result of thermal or other processing. The analysis was carried out by the United States Bureau of Mines in Albany, Oregon, using a Philips Model PV-9500/70 fully quantitative, x-ray energy dispersion analysis system. According to Bureau of Mines personnel, the system had an accuracy of $\pm$ 1 to 3 percent in the measurement of the alloy compositions.

Three specimens of representative nominal composition were subjected to this analysis. These were Specimens P-4 (89.8V-4.7Ti-5.5Fe), P-18 (60.5V-28.4Ti-11.1Fe), and P-20 (58.6V-9.2Ti-32.2Fe). According to the analysis, the compositions of Specimens P-4, P-18, and P-20 were (89.3V-4.8Ti-5.9Fe), (59.5V-28.8Ti-11.7Fe), and (57.4V-9.1Ti-33.5Fe) respectively. Clearly, the nominal compositions of the three specimens lie well within the range of accuracy of the measured compositions. Hence, no substantial changes in composition appear to have taken place as a result of thermal or other processing.

3.2.5. Microstructure Analysis.

The main purpose of the microstructure analysis was to ascertain the principal characteristics of the solidification structures of the as-cast Specimens P-1 through P-26. The analysis was done using both the light and scanning electron microscopes. No attempt was made in the analysis to determine cooling rates on the basis of dendrite arm spacing, since, in the arc melting process employed, the cooling rate is primarily a function of the manner in which the electrode is manipulated by the operator. All other factors being equal, cooling rates can vary greatly from one arc melt to the next.

In preparation for microscopic examination, the specimens were first ground on silicon carbide paper to 600 grit, then polished with diamond paste and lapping oil to .05 micron diamond. Following this initial polishing, the specimens were once again ground

on the 600 grit silicon carbide paper, then polished a second time to .05 micron diamond. In accordance with Rostoker's recommendations,[48] special care was exercised in the grinding of the vanadium-rich specimens, to avoid unnecessary work hardening of the specimen surfaces. This included the use of light grinding pressures and the frequent changing of grinding papers.

No single etchant or etching process was identified that would reveal the solidification structures of all twenty-six of the specimens examined. For example, an oxalic acid electrolytic etch was extremely effective at bringing out the structures of those specimens having vanadium contents of about 80 percent or more. However, this etch was completely ineffective at revealing the structures of specimens having vanadium contents of 60 percent or less. Another etch, a hydrofluoric acid-nitric acid-glycerine swab etch, had just the reverse effectiveness, with respect to these specimens.

After numerous trials with several different etches, including a sulfuric acid swab etch, the two etches mentioned in the preceding paragraph were selected for use in this analysis and for use, where necessary, as a dual etch. In accordance with this approach, all twenty-six specimens were first subjected to a uniform oxalic acid electrolytic etch. Then, those that had responded inadequately or not at all were subjected to an additional hydrofluoric acid-nitric acid-glycerine swab etch. The time of application of the $HF-HNO_3$-glycerine swab etch was adjusted according to the response of the specimen surface. The particulars of each of these etching

processes are discussed in the following paragraphs.

The oxalic acid etchant consisted simply of a 5 percent solution of oxalic acid. The oxalic acid electrolytic etching procedure was accomplished using a locally designed and fabricated fixture that permitted the convenient electrolytic etching of specimens that had been previously mounted in either conductive or non-conductive cylindrical mounts. Initial attempts to establish electrical contact with the specimen by way of a conductive mount were not generally successful. The conductive mounting material seemed to be inconsistent in its electrical resistivity, in that a given applied voltage could not be counted on to produce consistently the same current. In view of this, electrical contact for all electrolytic etching was made directly to the specimen surface.

Immediately prior to electrolytic etching, each specimen was thoroughly cleaned with acetone. It was then secured in the aforementioned fixture, where it was located about two inches from and facing a 1.25 inch diameter stainless steel cathode. Once the specimen had been secured in the fixture, the fixture was immersed in the oxalic acid solution, and a potential of 5 volts d-c was applied to the system. This potential resulted in a current of about 1 ampere and was maintained for approximately 15 seconds in each case. The oxalic acid solution was stirred vigorously throughout this period. At the end of the 15 second period, the potential was removed from the system, the fixture was removed from the oxalic acid solution, and the

specimen was removed from the fixture and again thoroughly cleaned.

The hydrofluoric acid-nitric acid-glycerine swab etch involved a considerably simpler process, although greater care had to be exercised in the handling of the hydrofluoric and nitric acids than had to be exercised in the handling of the oxalic acid. The nominal composition of the etchant was 10 parts HF, 10 parts HNO_3, and 30 parts glycerine by volume. The etchant was simply swabbed onto the specimen surface, with swabbing continued until the desired surface response was obtained. This was normally one to one and one-half minutes, depending on the composition of the specimen. Only the specimens that had not responded well to the oxalic acid electrolytic etch were subjected to this procedure (i.e., specimens whose vanadium contents were 60 percent or less). As before, the specimens were thoroughly cleaned after etching.

The solidification structures observed in Specimens P-1 through P-26 fell into three general categories. These were columnar, columnar dendritic, and equiaxed. However, the columnar dendritic structure was by far the most prevalent structure. Both light and SEM micrographs of these structures are provided in Appendix C. In each case, at least two light micrographs are provided, one with a magnification of 104X and another with a magnification of 256X. The first is intended to provide an overall view of the structure, while the second is intended to provide some detail of the structure. In the case of Specimen P-1, two SEM micrographs are also included, to provide additional detail of features of particular interest in that

structure.

As mentioned above, the columnar dendritic solidification structure was by far the most prevalent structure observed in Specimens P-1 through P-26. In fact, this structure may be seen in most of the micrographs provided in Appendix C. The only exceptions to this structure were those of Specimen P-1, P-20, P-21, P-25, and P-26. Specimen P-1 has a columnar solidification structure, and Specimens P-20, P-21, P-25, and P-26 all had what appeared to be equiaxed solidification structures. Specimens P-20, P-21, P-25, and P-26 are all, of course, compositionally contiguous, as shown in Figure 15.

As shown in Figures C-1 and C-2 in Appendix C, the solidification structure of Specimen P-1 (100.0V) is clearly columnar, which is in accordance with the essential lack of alloy content in that specimen. In addition to the well-defined grain and sub-grain boundaries shown in Figures C-3 and C-4, the structure contains a relatively uniform distribution of what appear to be etch pits. These pits were observed also before etching and appeared at that time to be associated with grinding marks. Furthermore, they appear to be idiomorphic and are very similar in appearance to the dislocation-related etch pits that comprise the sub-grain boundary shown in Figure C-4. Finally, there is no evidence to suggest that they are the former dwelling places of hard particles that have been removed during grinding or polishing. In view of all this, it is tentatively concluded that these are dislocation-related etch pits that were revealed by

the action of the water used in grinding.

The apparently equiaxed solidification structures of Specimens P-20, P-21, P-25, and P-26 may be seen in Figures C-41 through C-44 and C-51 through C-54 in Appendix C. Unlike the columnar and columnar dendritic structures of all the other specimens, there are no elongated grains to be found anywhere in the structures of these specimens. It appears that, in these specimens, the kinetics of nucleation and growth may have been such as to dominate the solidification process and, thereby, overtake the usual columnar growth of dendritic structures. This may have been contributed to also by the close proximity of the V-Fe minimum melting point and associated small liquidus-solidus spread. However, there is also the likelihood that these equiaxed grains formed during some, thus far unidentified solid-state transformation.

The columnar dendritic structures of the remaining specimens may, of course, be observed in the micrographs associated with each of the specimens and provided in Appendix C. Most of the grains visible in these micrographs have been transversely sectioned to one extent or another and appear, therefore, more equilateral than elongated. Furthermore, in many instances, adjoining grains differ greatly in appearance, giving the impression of a two-phase structure Specimen P-4, whose structure is shown in Figures C-9 and C-10, is a good example of this. In such instances, the x-ray energy dispersion analysis system associated with the SEM was used to compare the compositions of the adjoining grains, and no substantial differences

were found. In fact, no microscopic evidence of the existence of more than a single phase was found in any of the twenty-six specimens examined. This includes Specimen P-21, whose intragranular cross hatching shown in Figure C-44, is devoid of material, appears to coincide with orthogonal crystallographic directions, and is believed, therefore, to be an artifact associated with over-etching.

3.2.6. X-Ray Diffractometry Analysis.

X-ray diffractometry analysis was performed on a representative number of Specimens P-1 through P-26 to identify the phases present in the as-cast V-Ti-Fe alloys. Of particular interest, of course, were the possible formation of the FeV binary and VTiFe ternary intermetallic phases described earlier in Sections 2.4 and 2.5. The presence of either of these phases, especially in large amounts, could detract materially from the usefulness of the as-cast alloys.

Specifically, the analysis was performed on sixteen of the Specimens P-1 through P-26. These were the nominally pure vanadium specimen (P-1), the five specimens in the V-Fe binary system (P-6, P-11, P-16, P-21, and P-26), the five specimens in the V-Ti-Fe ternary system having a titanium to iron ratio of unity (P-4, P-9, P-14, P-19, and P-24), and the five specimens in the V-Ti binary system (P-2, P-7, P-12, P-17, and P-22).

The diffractometry was accomplished using a Philips Model APD 3600 computer-controlled diffractometer located at the U. S. Bureau of Mines in Albany, Oregon. Each specimen was exposed to

nickel-filtered CuKα radiation over a 13 millimeter square area of its surface for 60 minutes. During this period, the specimen was also rotated through angles of twice the Bragg angle (2θ) of 0 degrees to 90 degrees. The resulting diffracted beam intensities and corresponding angles were recorded concurrently.

After all sixteen specimens had been run, the results were obtained in both graphical and tabular form. The graphical form consisted of a plot or trace of diffracted beam intensity versus twice the Bragg angle (2θ), along with one or more reference traces from the Powder Data File. Two of these traces were acquired for each specimen and are provided, as received, in Appendix D. In each case, the two traces are the same, with the exception that the vertical scale of the second trace has been changed to permit better resolution of the lesser peaks.

Of the many traces obtained, five turned out to be of particular significance. These five traces have been fully indexed and are provided in Figures 30 through 34. The parenthetical numbers or Miller indices associated with each peak specify the family of planes from which that particular reflection was obtained. The set of the locations and intensities of all the peaks in a given trace is generally unique, according to the composition and crystal structure (or structures) of the material from which the trace was obtained.

The trace provided in Figure 30 was obtained from Specimen P-1 (100.0V) and corresponds well to the accompanying reference trace for pure vanadium. The differences between the relative

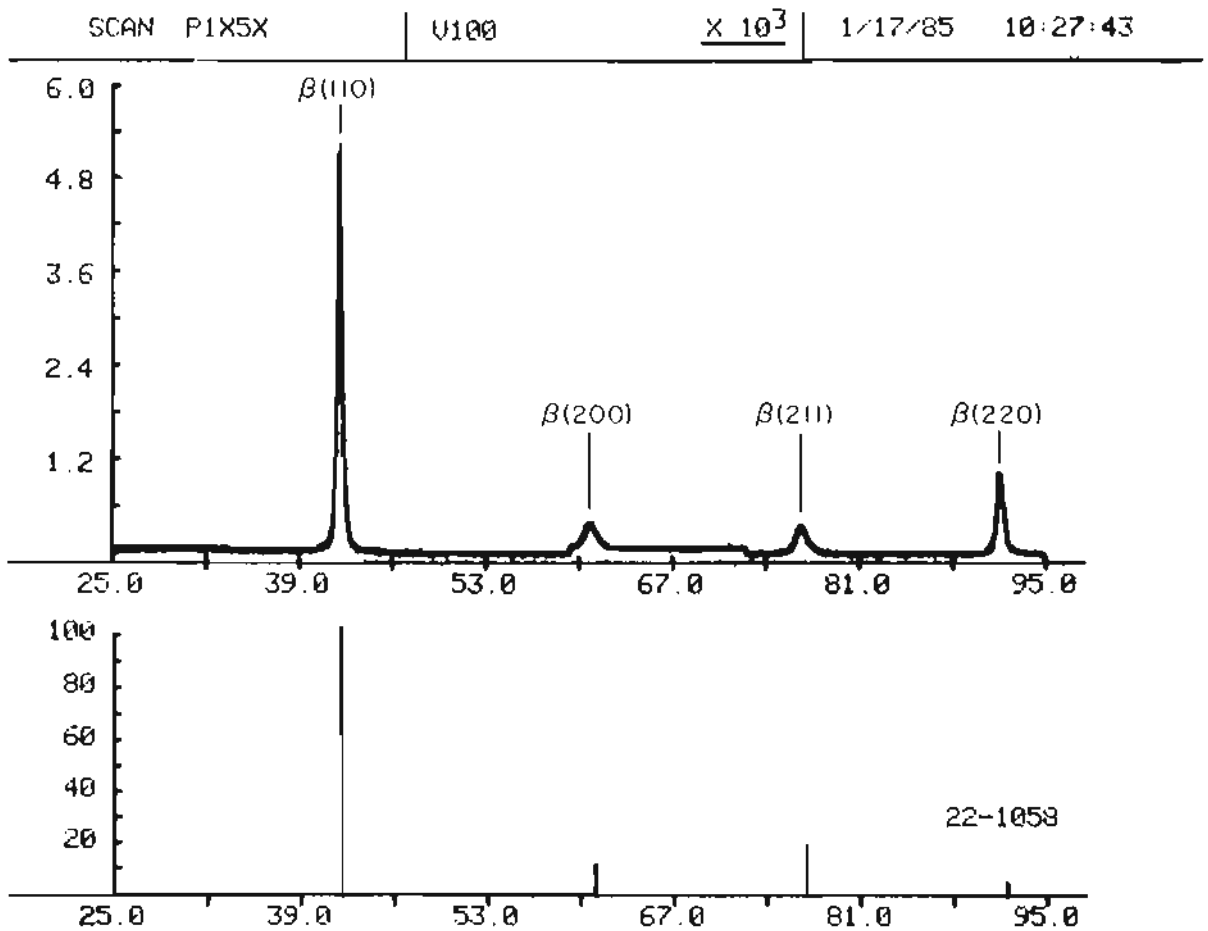

Figure 30. X-RAY DIFFRACTOMETRY TRACE FOR SPECIMEN P-1 (100.0V).

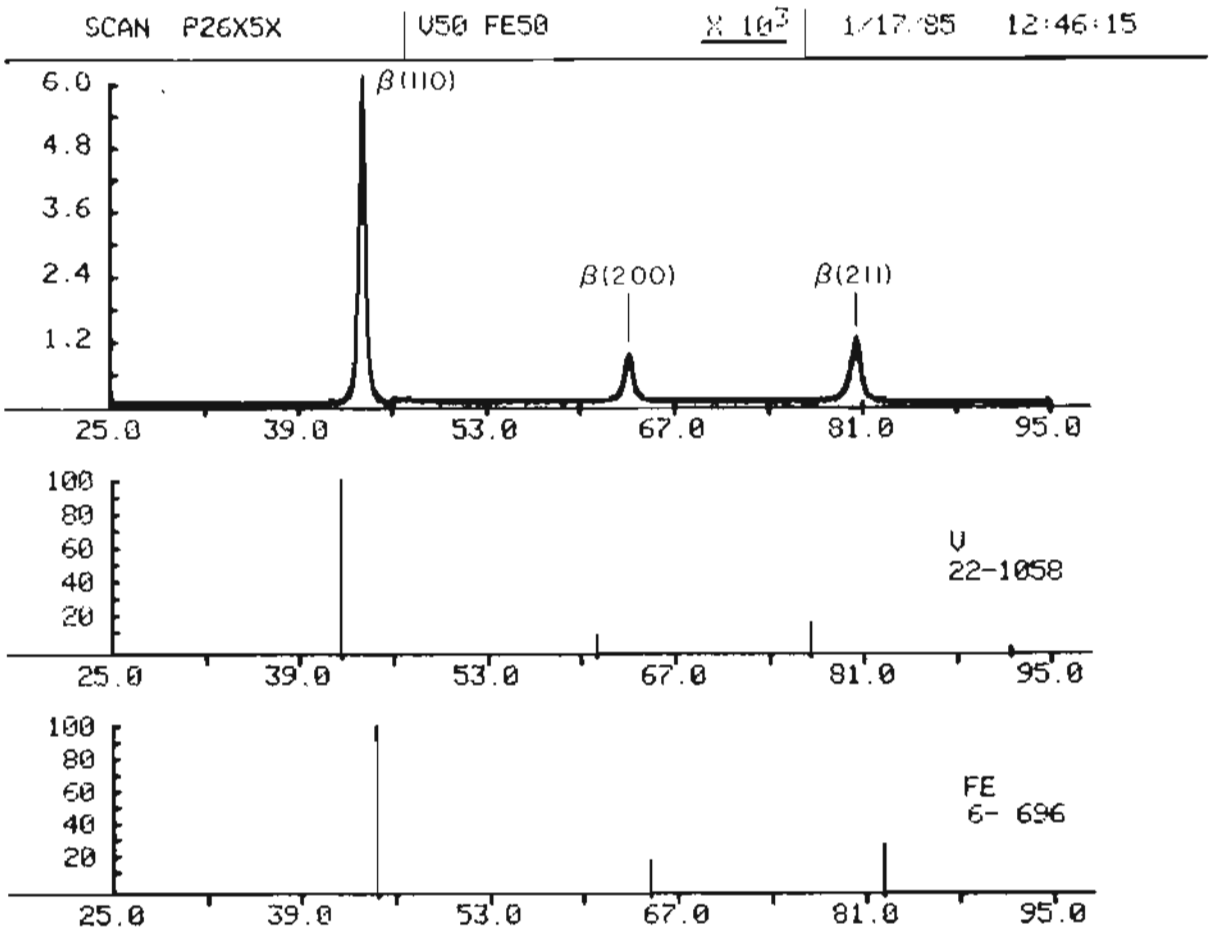

Figure 31. X-RAY DIFFRACTOMETRY TRACE FOR SPECIMEN P-26 (47.7V-52.3Fe).

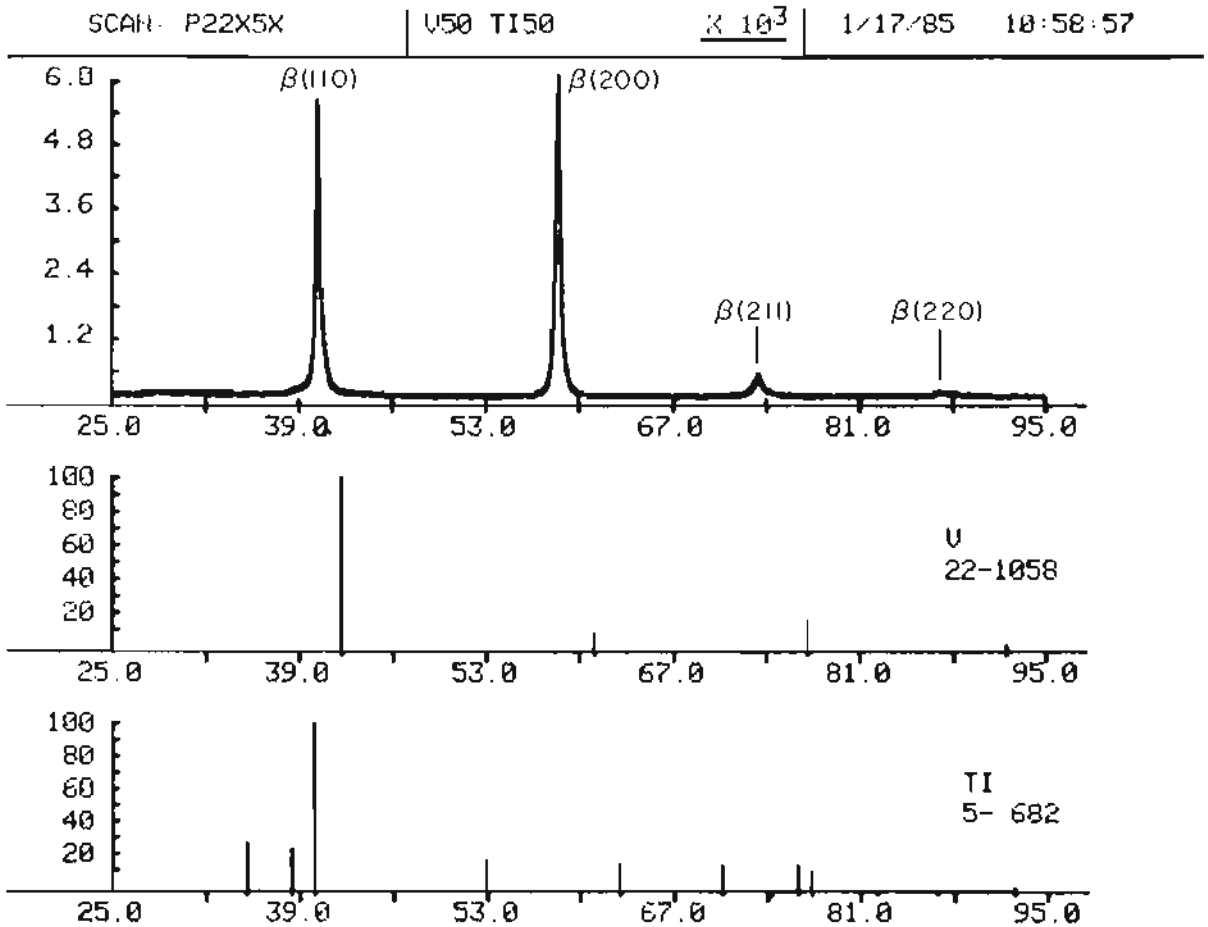

Figure 32. X-RAY DIFFRACTOMETRY TRACE FOR SPECIMEN P-22 (51.5V-48.5Ti).

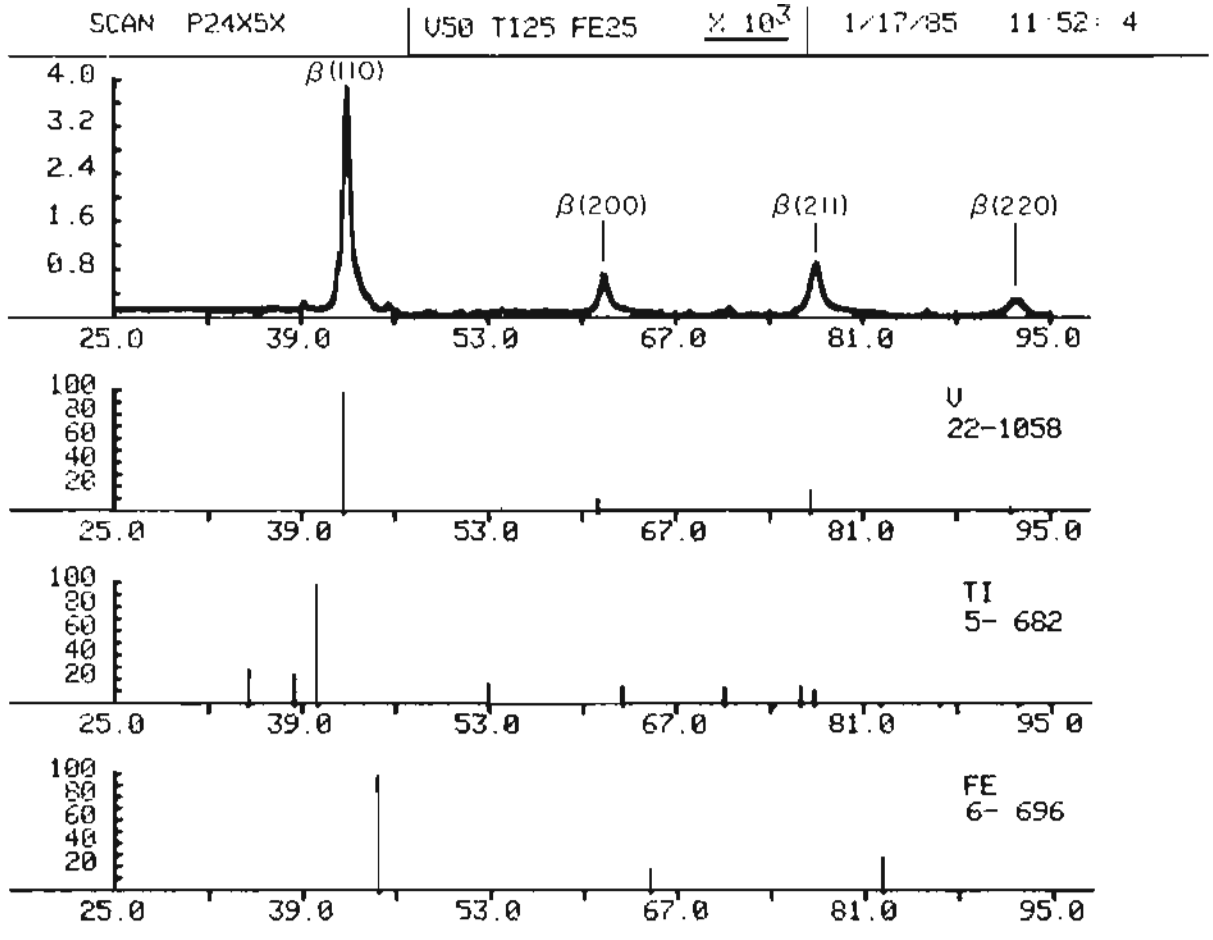

Figure 33. X-RAY DIFFRACTOMETRY TRACE FOR SPECIMEN P-24 (49.5V-23.3Ti-27.2Fe).

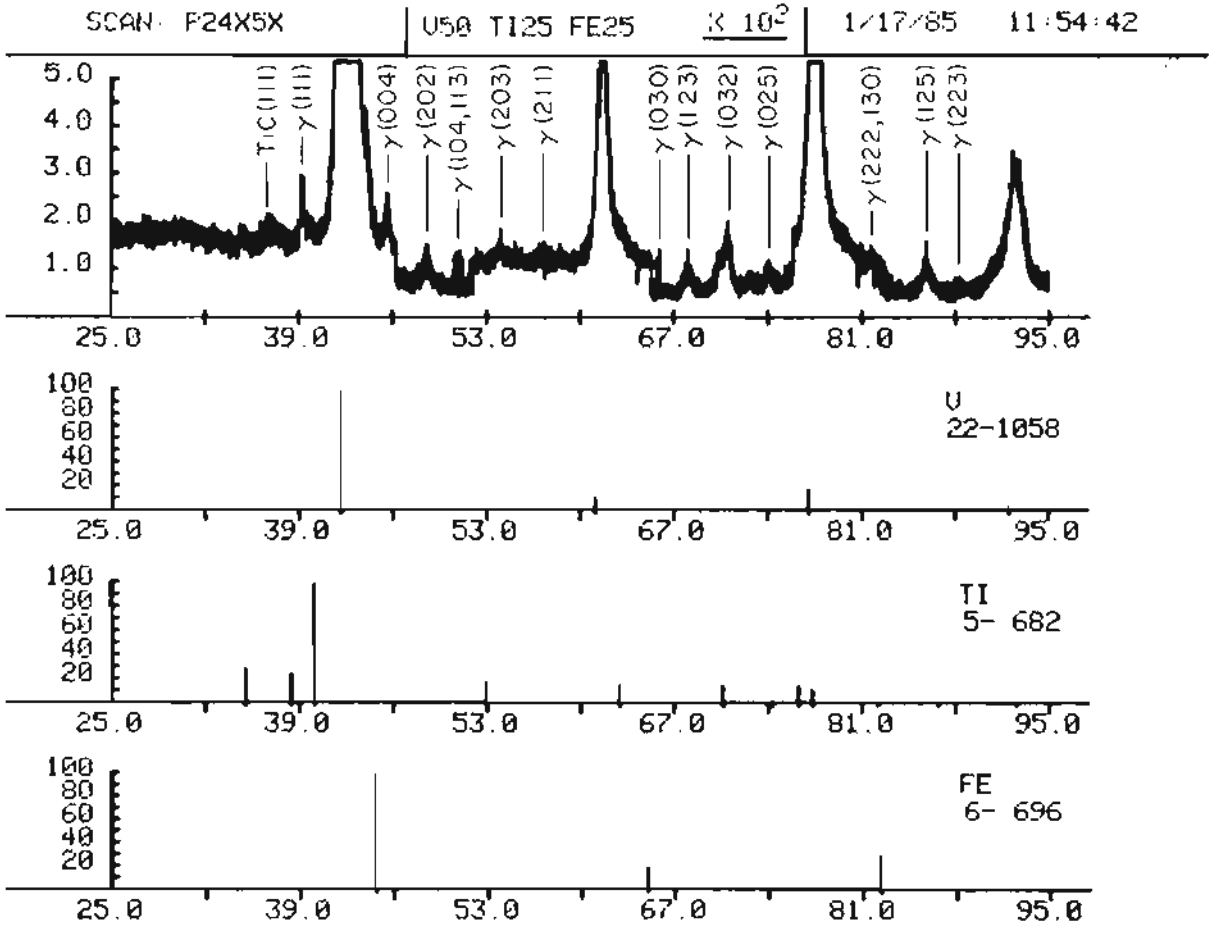

Figure 34. X-RAY DIFFRACTOMETRY TRACE FOR SPECIMEN P-24 (49.5V-23.3Ti-27.2Fe).

intensities of the peaks in the experimental trace and those in the reference trace is attributed to some preferential orientation of the crystals in the as-cast specimen. There is no evidence in this trace of any phases other than the body-centered cubic phase of pure vanadium, although other phases that might be present in small amounts (e.g., less than one percent) would probably not be discernible from the trace.

The trace provided in Figure 31 was obtained from Specimen P-26 (47.7V-52.3Fe) and corresponds well to the high-temperature, body-centered cubic α(V) or β(Ti) phase of an alloy of that composition. In addition there is no evidence in the trace of the occurrence of the brittle FeV intermetallic or σ phase. The σ phase, with its numerous superlattice reflections, would be easily distinguishable, if present in any substantial amounts. This all indicates rather conclusively that α(V) or β(Ti) has been retained completely in the as-cast specimen.

The trace shown in Figure 32 was obtained from Specimen P-22 (51.5V-48.5Ti) and, as in the previous case, corresponds to the high-temperature, body-centered cubic α(V) or β(Ti) phase. There is no evidence of the presence of any of the hexagonal close-packed α(Ti) phase. Such a presence would be indicated by the appearance of lines corresponding to those in the α(Ti) reference trace at the bottom of Figure 32. This all indicates, once again, that the α(V) or β(Ti) phase has been retained completely.

The traces provided in Figures 33 and 34 are the same, with the exception that the vertical scale of the trace in Figure 34 was altered to permit a better resolution of the lesser peaks. The traces were obtained from Specimen P-24 (49.5V-23.3Ti-27.2Fe). The major peaks correspond to the body-centered cubic α(V) or β(Ti). However, in this case there is strong evidence of the existence of one or more additional phases. The presumption, obviously, is that numerous lesser peaks correspond to the hexagonal VTiFe intermetallic or γ phase.

To determine the validity of this, the lattice parameters found by Bi and Kornilov in their x-ray analysis of the γ phase[49] were used to calculate the d-spacings and Bragg angles for the various allowed reflecting of the hexagonal structure of space group P63/MMC. These lines were then compared with the lesser peaks in Figure 34 and were found to match with considerable precision. This means that not only did the lesser peaks correspond to the VTiFe γ phase, but that it was the same phase that Bi and Kornilov had observed. However, as suggested in Figure 33, the amount of the γ phase present is fairly small, perhaps only a few weight percent.

There is one lesser peak in the trace in Figure 34 that does not correspond to the ternary γ phase and that occurs in some of the other titanium-bearing alloys as well. It does not appear in any of the V-Fe binary alloys. This lesser peak is believed to correspond to the cubic TiC phase. A second small peak associated with this phase, the (200) peak, can just barely be seen on the left

shoulder of the β(Ti) (110) peak.

In addition to obtaining the traces for each of the sixteen specimens, their lattice parameters were also calculated. The results are provided in Table 5 and are plotted versus Fe, Fe-46Ti, and Ti concentration in Figures 35, 36, and 37 respectively. The plot in Figure 35 suggests that usual change in lattice parameter that is normally associated with the change in solute content in a single phase solid solution. The same conditions appear to prevail as well in the plot in Figure 37. There is no indication in either of these plots of the emergence of one or more additional phases.

The plot shown in Figure 36, however, is another story. As the Fe-46Ti concentration reaches about 30 weight percent, the lattice parameter ceases to change. While it is entirely possible that this simply represents a balance between the contrasting effects on the lattice parameter of the iron and titanium atoms, it is perhaps more likely that it indicates the emergence of a second phase. It is recognized that, in a ternary system, a constant lattice parameter is not a necessary condition for the existence of a two-phase region. On the other hand, a constant lattice parameter is not inconsistent with it.

3.2.7. Bend Testing.

The purpose of the bend testing conducted in this investigation was to obtain information on the strengths and ductilities of Specimens P-1 through P-26. The bend testing was accomplished using an Instron Dynamic Test System equipped with a locally fabricated three-point bend testing fixture. The overall setup employed in the

Table 5.

LATTICE PARAMETERS FOR BODY-CENTERED CUBIC PHASE
IN X-RAY DIFFRACTOMETRY SPECIMENS

Specimen Designation	Lattice Parameter (Angstrom Units)
P-1	3.0376
P-2	3.0462
P-4	3.0098
P-6	3.0106
P-7	3.0671
P-9	3.0152
P-11	2.9732
P-12	3.0991
P-14	3.0078
P-16	2.9480
P-17	3.1337
P-19	3.0054
P-21	2.9300
P-22	3.1559
P-24	3.0096
P-26	2.9157

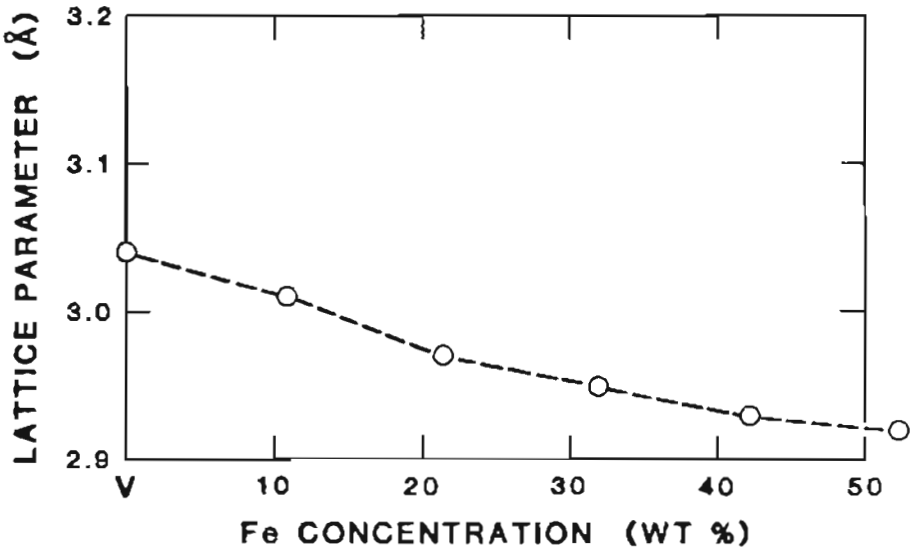

Figure 35. LATTICE PARAMETER (ANGSTROM UNITS) VERSUS Fe CONCENTRATION (WEIGHT PERCENT).

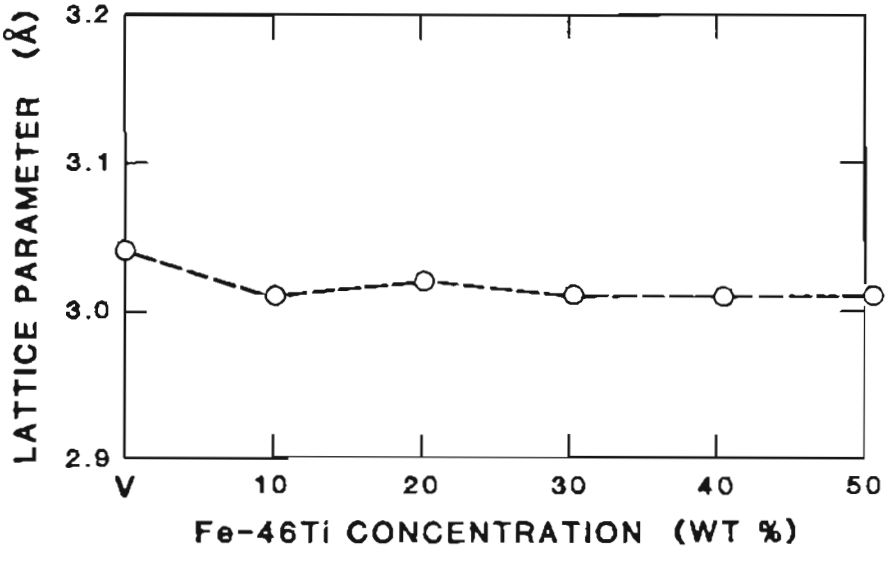

Figure 36. LATTICE PARAMETER (ANGSTROM UNITS) VERSUS Fe-46Ti CONCENTRATION (WEIGHT PERCENT).

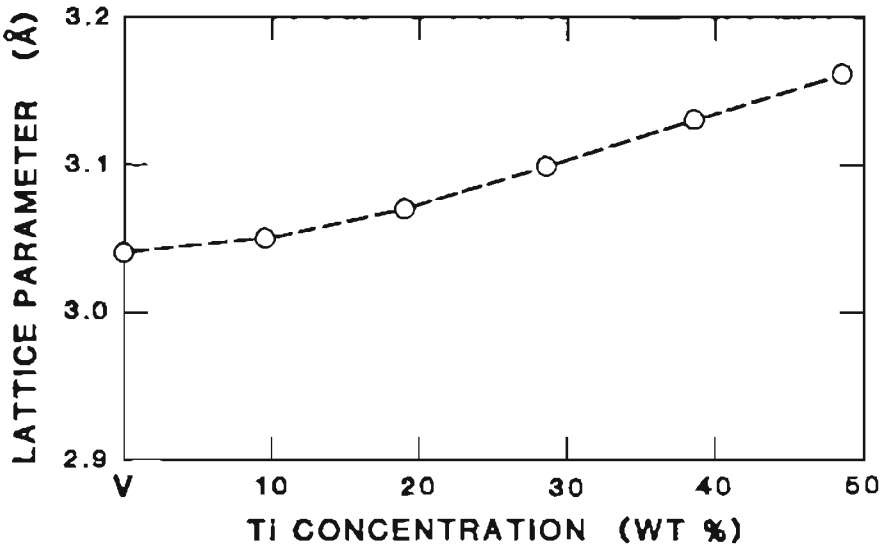

Figure 37. LATTICE PARAMETER (ANGSTROM UNITS) VERSUS Ti CONCENTRATION (WEIGHT PERCENT).

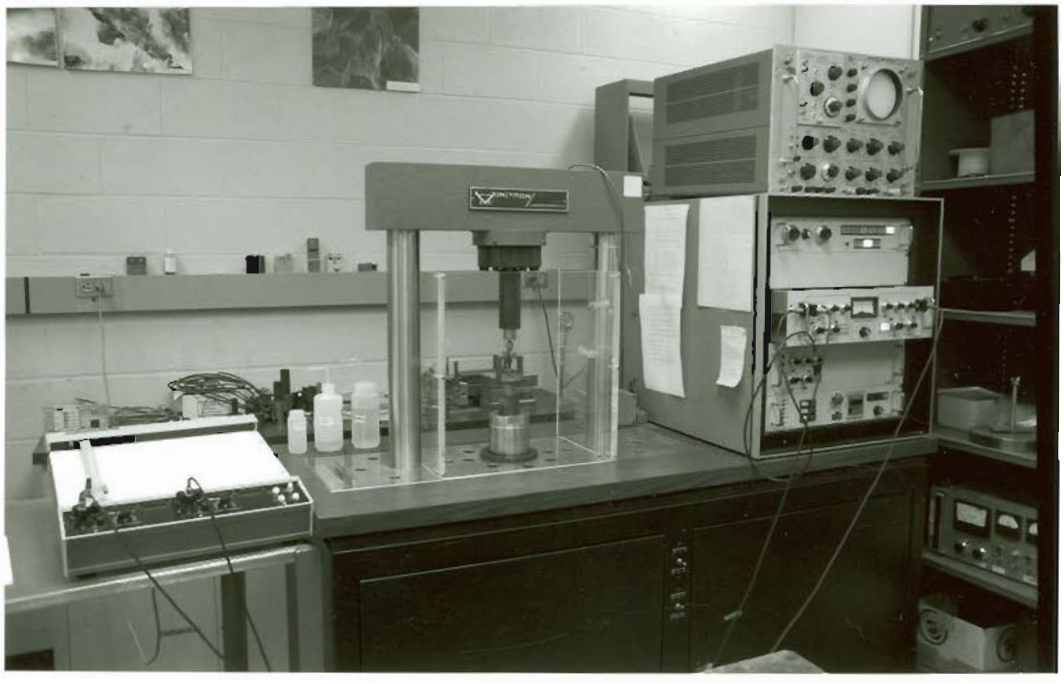

Figure 38. OVERALL EXPERIMENTAL SETUP USED IN BEND TESTING

bend testing is shown in Figure 38, with the x-y recorder on the left, the cross-head and bend testing fixture in the center, and system controller on the right. The three-point bend testing fixture is shown separately in Figure 39. The critical dimensions of the fixture and bend testing experimental configuration are shown schematically in Figure 40.

As mentioned earlier, the specimens for bend testing were obtained from the specimens that had previously been used for hardness testing and x-ray diffractometry analysis. Preparation of the specimens consisted essentially of the grinding of the specimens to the proper dimensions for bend testing. This was accomplished using a Thompson/Matrix Model B5 industrial surface grinder. The composition of the grinding wheel was aluminum oxide, the speed was 1,800 revolutions per minute, the feed rate was 6-8 inches per second, and the depth of each cut was 1.25 mils. Lower feed rates and/or greater depths of cut were found to cause local overheating and associated discoloration of the specimen surface.

The machinability of the bend testing specimens varied considerably with composition. Some of the specimens emerged from the grinding with smooth, clean edges. Others emerged with edges that were chipped to varying degrees. Still others (Specimens P-1, P-6, and P-25) were, for all practical purposes, demolished as a result of grinding. The responses of these specimens to grinding is believed to correspond closely to their inherent ductility or lack thereof. Accordingly, the responses have been categorized according to severity (apparent brittleness) and are depicted graphically in Figure 41. The

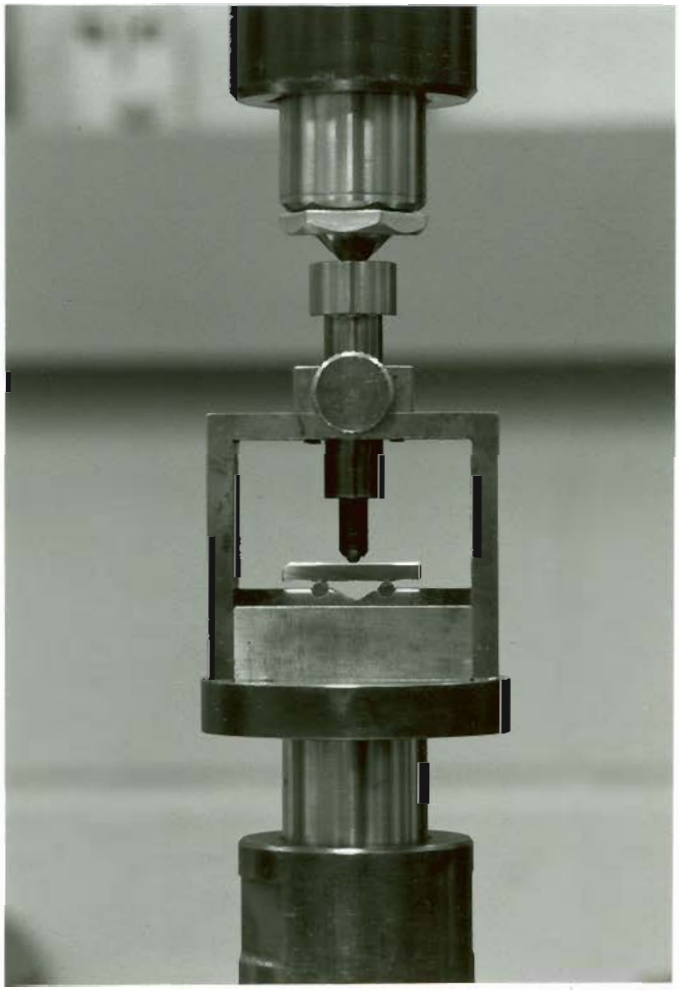

Figure 39. THREE-POINT BENDING FIXTURE USED IN BEND TESTING

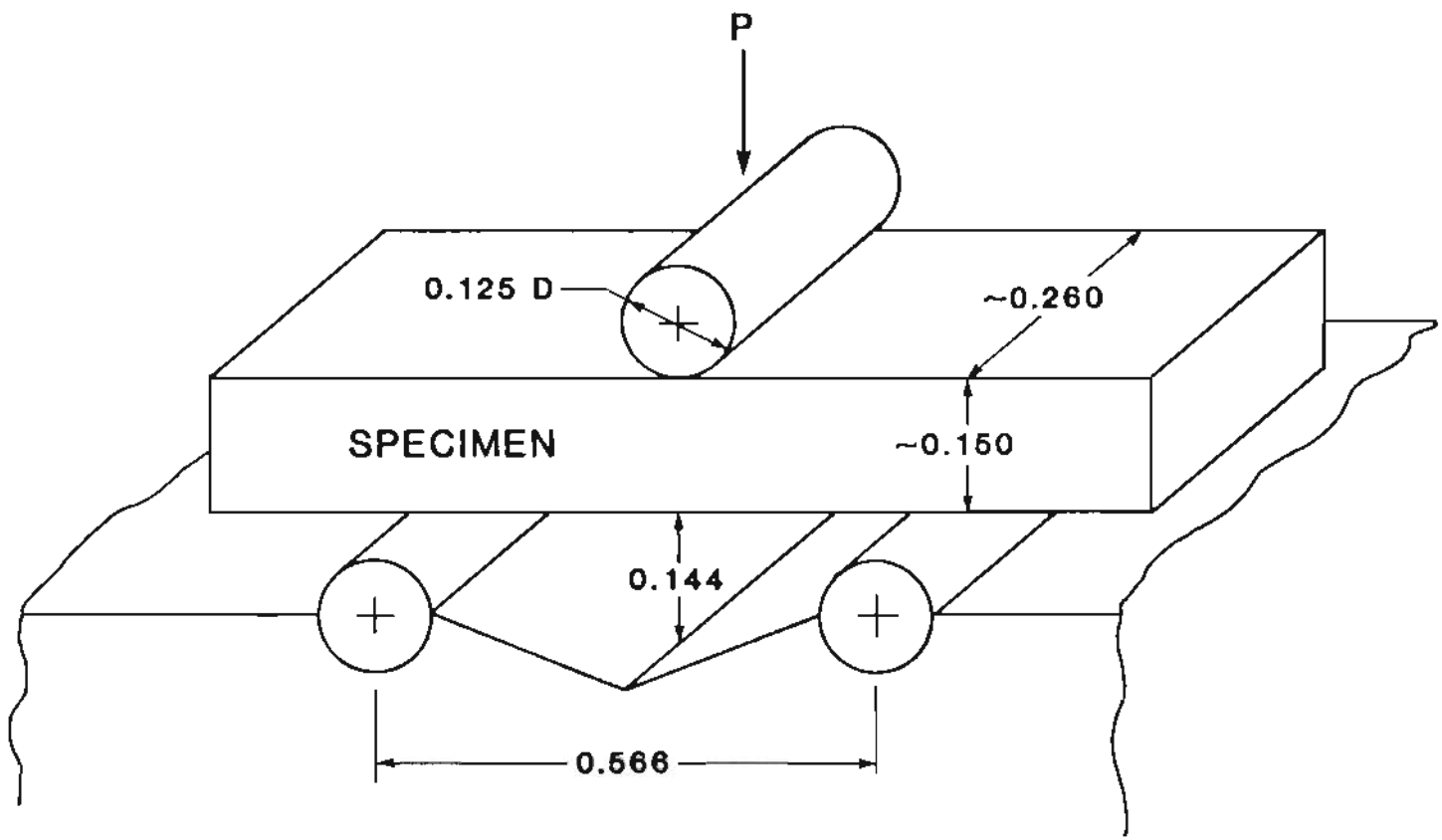

Figure 40. EXPERIMENTAL CONFIGURATION FOR BEND TESTING.

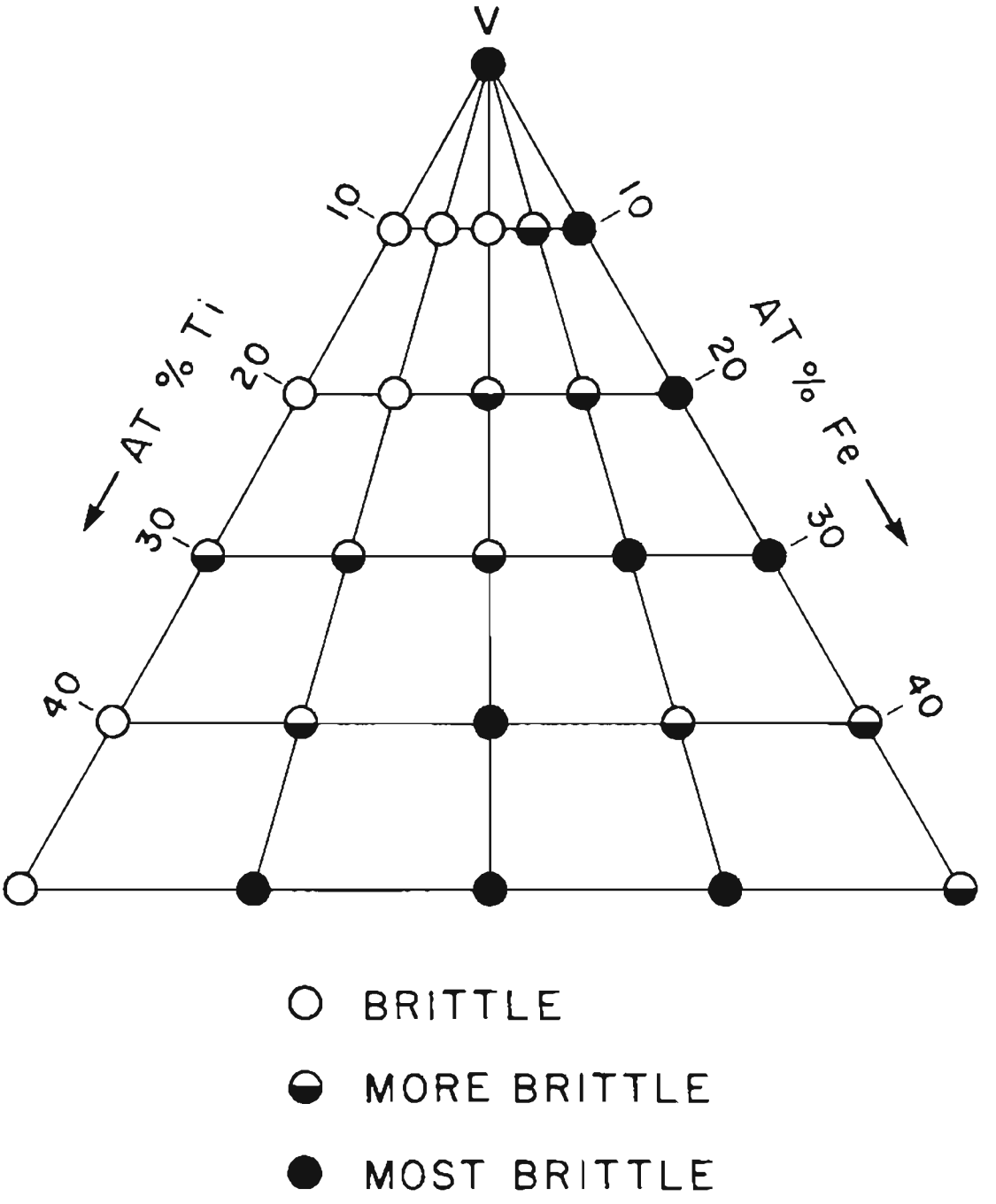

Figure 41. BRITTLENESS OF SPECIMENS P-1 THROUGH P-26, AS IMPLIED BY SPECIMEN RESPONSE TO MACHINING.

responses indicated, although generalized and subjective, are nevertheless informative, in that they are roughly consistent with results obtained by other methods of testing and analysis.

As shown in Figure 40, the experimental configuration for bend testing provided for three-point bending, with 0.566 inches between supports and a centrally applied load. The load was applied through 0.125 inch diameter hardened steel pins. For the actual testing, the dynamic test system was operated in the stroke mode of control, with the stroke or deflection changed at the rate of about 0.1 inches per minute. The applied displacement and corresponding load were recorded simultaneously on a Hewlett-Packard x-y recorder. The resulting load-displacement curves are provided in Figures E-1 through E-23 in Appendix E, along with the applicable load and displacement conversion factors in Tables E-1 and E-2. It is important to note that the 20 percent load range and 10 percent stroke range were used for all testing.

Since none of the load-displacement curves obtained showed any evidence of specimen yielding, only the maximum breaking load could be extracted from each of the curves. This was done graphically, and the results are tabulated in the second column of Table 7. Now, according to simple beam theory, the maximum outer fiber stress in a beam of uniform rectangular cross section is given by the relationship

$$\sigma_{MAX} = \frac{6M}{bh^2},$$

Table 6.

ACTUAL DIMENSIONS OF BEND TESTING SPECIMENS P-1 THROUGH P-26

Specimen Designation	Actual Height (In)	Actual Width (In)
P-1	*	*
P-2	.152	.250
P-3	.152	.263
P-4	.152	.260
P-5	.146	.262
P-6	*	*
P-7	.151	.258
P-8	.147	.259
P-9	.151	.258
P-10	.151	.266
P-11	.150	.263
P-12	.154	.250
P-13	.152	.261
P-14	.150	.253
P-15	.150	.259
P-16	.150	.258
P-17	.153	.261
P-18	.152	.264
P-19	.154	.258
P-20	.151	.262
P-21	.151	.261
P-22	.151	.258
P-23	.153	.268
P-24	.155	.263
P-25	*	*
P-26	.153	.264

* Specimen could not be machined, due to extreme brittleness.

Table 7.

MAXIMUM LOAD/STRESS DATA FOR BEND TESTING SPECIMENS P-1 THROUGH P-26

Specimen Designation	Maximum Load (Lb)	Maximum Outer Fiber Stress (Lb/Sq In)	Adjusted Maximum Outer Fiber Stress (Lb/Sq In)
P-1	*	*	*
P-2	553	81,300	48,800
P-3	528	73,800	44,300
P-4	337	47,600	28,600
P-5	246	37,400	22,400
P-6	*	*	*
P-7	1,450	209,300	125,600
P-8	468	71,000	42,600
P-9	412	59,500	35,700
P-10	282	39,500	23,700
P-11	161	23,100	13,900
P-12	859	123,000	73,800
P-13	443	62,400	37,400
P-14	302	45,000	27,000
P-15	216	31,500	18,900
P-16	282	41,200	24,700
P-17	829	115,200	69,100
P-18	302	42,000	25,200
P-19	267	37,000	22,200
P-20	367	52,200	31,300
P-21	533	76,000	45,600
P-22	1,034	149,200	89,500
P-23	161	21,800	13,100
P-24	226	30,400	18,200
P-25	*	*	*
P-26	743	102,100	61,200

* Specimen could not be machined, due to extreme brittleness.

where M is the maximum bending moment applied to the beam, b is the width of the beam, and h is the height or, in this case, thickness of the beam. Using this relationship, the maximum outer fiber stress corresponding to each specimen breaking load was calculated and is listed in the third column of Table 7.

The foregoing relationship for the maximum outer fiber stress is a theoretical relationship whose validity depends on the validity of a fairly considerable number of assumptions. Included are the assumptions that the beam is homogeneous and isotropic, that the beam has a uniform cross section, that the beam is initially straight, that the beam undergoes only limited deflection, that the vertical planes of the beam remain vertical, that the longitudinal fibers of the beam operate independently, and that the compressive and tensile modulii of the beam are equal. Obviously, several of these assumptions are not properly applicable to real specimens.

To ascertain the validity of the results obtained by using the foregoing relationship, several mild steel reference specimens were subjected to the same bend testing as the regular specimens. The reference specimens were of known composition, hardness, and tensile properties. After the reference specimens has been tested, the foregoing relationship was used to calculate for each the maximum outer fiber stress at yield. The values obtained were nearly twice the normal tensile yield strengths for these materials and cast serious doubt on the correctness of the stresses that had been calculated for the regular specimens.

This discrepancy has been observed and analyzed by several investigators, although most recently by A. R. Rosenfield, who suggests that the discrepancy results from the invalidity of the assumption that for any given material the compressive and tensile modulii are equal.50 This is not a precisely valid assumption for ductile materials. It is certainly not a valid assumption for brittle materials. For example, concrete has a very high compressive modulus and, at the same time, an extremely low tensile modulus. The practical effect of unequal compressive and tensile modulii is a shift in the position of the neutral axis away from the centerline of the beam. This, in turn, has a formidable effect on the results obtained from the simple beam theory relationship for maximum outer fiber stress.

According to Rosenfield, the true tensile yield stress of a material is given by the relationship

$$\sigma_{YIELD} = 0.6\,\sigma_{MAX}$$

where σ_{MAX} is the maximum outer fiber stress at yield obtained from the earlier relationship. The application of this adjustment to the yield stresses calculated previously for the several steel reference specimens, yielded values for the yield stress that were fully consistent with the values of yield stress expected for these materials. Based on this close agreement, it was decided to apply the same adjustment to the values of maximum outer fiber stress that had been calculated previously for the regular specimens. The results are

provided in column four of Table 7 and are believed to represent good approximations of the true breaking stresses of the regular specimens.

The values of adjusted maximum outer fiber stress provided in Table 7 are, with some exceptions, comparatively low and are believed to reflect the relative brittleness of all the regular specimens tested. The exceptions are found in the V-Ti binary alloys (that is, Specimens P-2, P-7, P-12, P-17, and P-22), where the higher concentrations of titanium appear to have ameliorated to some extent the embrittling effects of the inherently brittle vanadium constituent. In any consideration of these results, however, it must be kept in mind that the fracture of brittle materials has a statistical nature and that the fracture of such materials usually takes place over a fairly wide range of breaking stresses. Hence, inasmuch as only one specimen was tested for each alloy composition, the reliability of the values presented in Table 7 is certainly questionable.

In addition to being tabulated in Table 7, the values of adjusted maximum outer fiber stress are also plotted against various ratios of titanium to iron in Figures 42, 43, 44, 45, and 46. In each figure, the specified ratio of titanium to iron is constant. The resulting curves are not in themselves especially remarkable. However, when they are compared with the corresponding sections of Figure 41, they become somewhat revealing, in that they appear to correspond closely to the changes in relative brittleness indicated in the figure. That is, wherever the relative brittleness increases, the

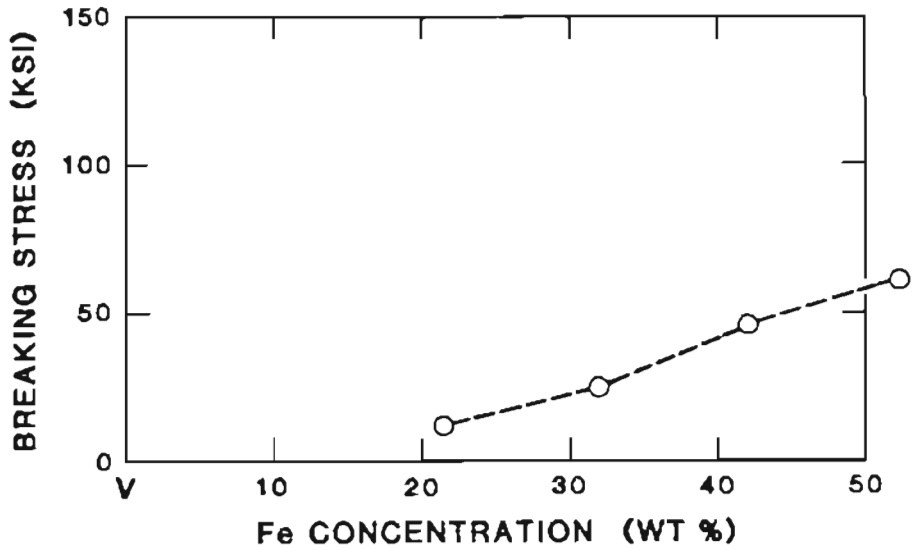

Figure 42. BREAKING STRESS (KSI) VERSUS Fe CONCENTRATION (WEIGHT PERCENT).

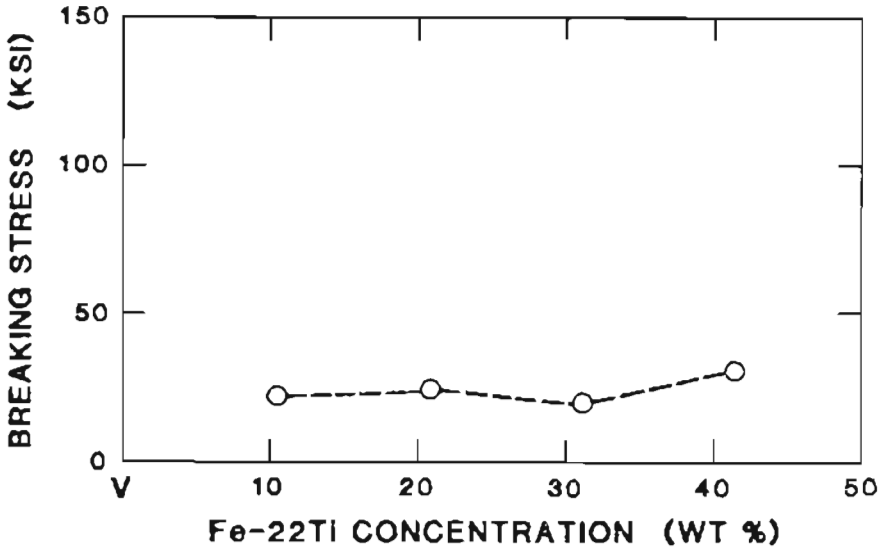

Figure 43. BREAKING STRESS (KSI) VERSUS Fe-22Ti CONCENTRATION (WEIGHT PERCENT).

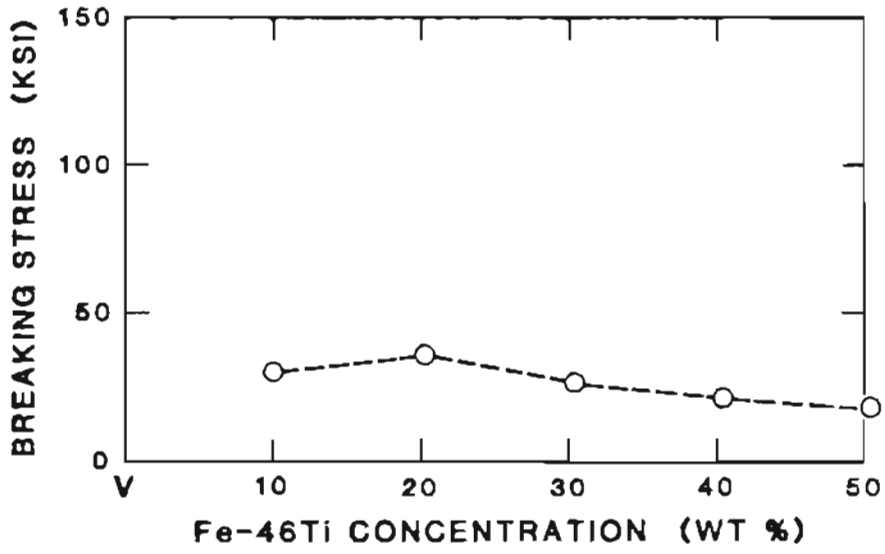

Figure 44. BREAKING STRESS (KSI) VERSUS Fe-46Ti CONCENTRATION (WEIGHT PERCENT).

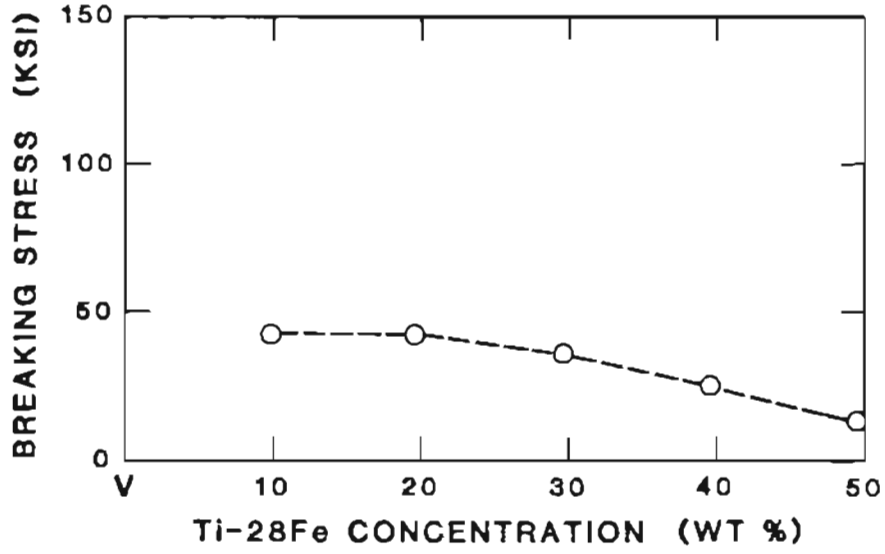

Figure 45. BREAKING STRESS (KSI) VERSUS Ti-28Fe CONCENTRATION (WEIGHT PERCENT).

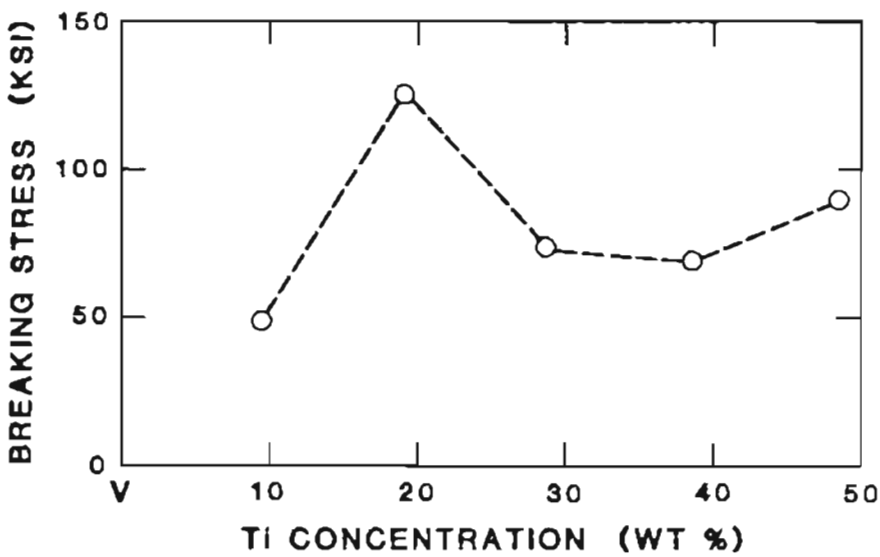

Figure 46. BREAKING STRESS (KSI) VERSUS Ti CONCENTRATION (WEIGHT PERCENT).

adjusted maximum outer fiber stress decreases, and wherever the relative brittleness decreases, the adjusted stress increases. While this apparent correlation is entirely qualitative, it does support the notion that the primary limitation on the strength of these specimens is their overall lack of ductility.

3.2.8. Fracture Analysis.

The morphology of its fracture surface is frequently indicative of the properties of a material, especially a crystalline material. The purpose of the fracture analysis carried out in this investigation was to obtain a qualitative assessment of the ductility or lack thereof of the bend testing specimens, as indicated by their fracture surface morphologies.

The analysis consisted basically of the microscopic examination of each of the bend testing specimen fracture surfaces, to determine in each case the predominant fracture surface morphology. This was accomplished using a JEOL Company Model JSM-35 scanning electron microscope (SEM). The SEM is well suited to the observation of fracture surfaces, in that it provides a considerable depth of field, even at high magnification.

The results of the microscopic examination of the fracture surfaces are provided graphically in Figures F-1 through F-48 in Appendix F. In each case, at least two fracture surface micrographs are provided. The first provides an overall view (30X) of the fracture surface. The second provides a close-up view (1,000X) of the predominant fracture surface morphology. In the case of Specimen

P-4, two additional micrographs are provided to illustrate another significant feature observed.

By far, the most prevalent fracture surface morphology in the specimens examined was transgranular brittle cleavage. This was the predominant morphology in all the specimens examined, with the exception of those lying in the V-Ti binary system (i.e., Specimens P-7, P-12, P-17, and P-22), in which quasi-brittle fracture appeared to be the most prevalent morphology. No evidence of ductile fracture was found in any of the specimens examined.

In those specimens whose fracture surfaces indicated that brittle cleavage had occurred, the principal feature observed was the familiar river pattern. This pattern can be seen in the 1,000X micrographs provided for these specimens in Appendix F. In addition, fractures along planes orthogonal to the usual fracture surface planes and, at the same time, orthogonal to each other were frequently observed. Such fractures can be seen in Figures F-7 and F-8 and suggest the possibility that they occurred along the mutually orthogonal (100) planes of a cubic crystal structure.

In those specimens whose fracture surfaces indicated quasi-brittle fracture (namely, Specimens P-7, P-12, P-17, and P-22), the principal feature is not so familiar and varies in appearance as the titanium content changes. The nature of the fracture surface of Specimen P-17 (61.5V-38.5Ti) is unique within the quasi-brittle group and may correspond more closely to a hot crack that formed during solidification than to a quasi-brittle fracture that occurred during

bend testing.

Certainly, the single most significant result of this analysis was that none of the specimens examined showed any signs of ductile fracture. Although, the brittleness of the V-Ti binary specimens was definitely less than that of the others.

4. DISCUSSION

4.1. Alloy Strengths.

Of the several methods of testing and analysis employed in this investigation, two were specifically intended to provide information concerning the strengths of the twenty-six, as-cast V-Ti-Fe alloys represented by Specimens P-1 through P-26. These two methods were hardness testing and bend testing. The purposes, procedures, and results of each of these methods are presented in Sections 3.2.3 and 3.2.7.

The method of bend testing was selected as an alternative to the more direct method of tensile testing, for the reasons stated in Section 3.2.7. The main disadvantage of the bend testing method was that the resulting tensile and yield strengths had to be calculated using theoretical models, rather than being measured directly, as in the tensile testing method. However, as it turned out, neither method could have contributed substantially to an assessment of the strengths of the twenty-six, as-cast alloys.

According to the results of the bend testing provided in Section 3.2.7, none of the specimens tested possessed any discernible degree of ductility. As a result, it was only possible to calculate the maximum outer fiber stress associated with the brittle fracture of each of the specimens. These breaking stresses appeared to be solely an inverse function of the relative brittleness of the specimens and in no way related to the probable strengths of either brittle or ductile V-Ti-Fe alloys.

On the other hand, the results of the hardness testing provided in Section 3.2.3 did appear to be directly related to the probable strengths of ductile V-Ti-Fe alloys. This was the case, inasmuch as the trends observed in the hardness values of the brittle V-Ti alloys were essentially identical to those that Rostoker had observed in the hardness values and tensile strengths of ductile V-Ti alloys.51 Furthermore, the trends observed in the hardness values of the brittle V-Fe alloys were the same as one might associate with the solid-solution hardening of ductile V-Fe alloys. Finally, the albeit rough correspondence between indentation hardness and yield strength has been well established.52

The reason for the obvious disparity between the bend testing and hardness testing methods in the extent to which the results of each are related to the strengths of V-Ti-Fe alloys is probably based on the nature of the stresses involved in each. While both of the methods undoubtedly involve tri-axial states of stress, they do not both involve predominantly the same types of stress. The bend testing method involves predominantly tensile stresses that are strictly limited according to specimen brittleness. In contrast, the hardness testing method involves predominantly compressive and associated hydrostatic stresses that operate to obviate the effects of specimen brittleness.53

According to the hardness testing results obtained in this investigation, the Rockwell hardness of a brittle V-10Ti alloy is about 30 HRC. According to Rostoker, the Vickers hardness and ultimate tensile strength of a ductile V-10Ti alloy are 194 HVC (<20

HRC) and 91,570 lb/in2 respectively.54 Now, if the hardness of a brittle V-Ti-Fe alloy is in fact directly related to the hardness and tensile strength of the corresponding ductile alloy, and there are strong indications that it is, then it seems reasonable to predict that those brittle V-Ti-Fe alloys having hardness values in excess of about 30 HRC should, as ductile alloys, have tensile strengths in excess of 91,570 lb/in2.

It is certainly recognized that the relationship suggested in the foregoing discussion between the hardnesses of brittle V-Ti-Fe alloys and the strengths of the corresponding ductile alloys has not been specified and undoubtedly depends on many factors, including the specific mechanical properties of the brittle and ductile alloys involved. Even so, its employment as the basis for the prediction made in the preceding paragraph is believed to be justified, in that the prediction provides some otherwise non-existent idea of the probable strengths of the ductile V-Ti-Fe alloys and, hence, an indication of the advisability of their further investigation.

4.2 Alloy Ductilities.

According to the results of the bend testing provided in Section 3.2.7 and the fracture analysis provided in Section 3.2.8, none of the specimens evaluated in this investigation possessed any discernible degree of ductility. The bend testing load-displacement curves obtained and provided in Appendix E indicated only elastic behavior near the point of fracture, and the resulting fracture surfaces showed only signs of brittle cleavage and quasi-brittle fracture. The general

brittleness of these specimens is clearly a reflection of the high interstitial oxygen and nitrogen contents of the constituent vanadium powder.

However, as pointed out in Section 3.2.7, there were also obvious and substantial differences in the levels of brittleness among the specimens. This was apparent in the responses of the specimens to machining and in the morphologies of the bend testing fracture surfaces. In their responses to machining, the less brittle alloys developed smooth edges, while the more brittle alloys developed chipped edges. Similarly, the fracture surfaces of the less brittle alloys indicated quasi-brittle fracture, while those of the more brittle alloys indicated transgranular brittle cleavage.

As implied previously, this variation in brittleness is believed to reflect the ability of titanium to ameliorate the embrittling effects of the interstitial oxygen and nitrogen impurities, except where the VTiFe intermetallic or γ phase may assert its influence. In any event, the variation is described qualitatively in Figure 41, which indicates that many of the V-Ti-Fe alloys were less brittle than the nominally pure vanadium specimen. On the basis of this, it seems reasonable to suggest that, had ductile vanadium been employed in the fabrication of Specimens P-1 through P-26, many of the resulting specimens would have been even more ductile than the nominally pure vanadium.

4.3. Alloy Structures.

The structures of the twenty-six, as-cast specimens were, of course, solidification structures and were typical of structures nor

mally associated with substantial alloy contents and rapid solidification and cooling rates. Three distinct structures were observed in the as-cast specimens. These were the columnar, columnar dendritic, and equiaxed structures. The columnar structure was observed only in Specimen P-1 (100.0V) and obviously reflected the inherent lack of alloy content in that specimen. The columnar dendritic structure was the predominant structure observed and was characteristic of the structures of all the remaining specimens, with the exception of Specimens P-20, P-21, P-25, and P-26. These four specimens possessed fine, equiaxed structures.

The source of the fine, equiaxed structures observed in Specimens P-20 (58.6V-9.2Ti-32.2Fe), P-21 (57.8V-42.2Fe), P-25 (48.6V-11.4Ti-40.0Fe), and P-26 (47.7V-52.3Fe) is not entirely clear. One explanation for the occurrence of this unusual structure is simply that the solidification conditions were such as to favor nucleation and growth as the dominant solidification process, as in the chill zone of a conventional casting. However, the probable existence of substantial temperature gradients does not support this explanation. A more likely explanation is that of M. C. Flemings, who holds that such fine, equiaxed structures form as a result of the partial remelting of dendrites to form small dendrite particles that, in effect, become nuclei for the formation of fine, equiaxed grains. According to Flemings, the partial remelting of the dendrites is caused by thermal convection in the partially solidified material.55 It appears also that the proximity of Specimens P-20, P-21, P-25, and P-26 to the minimum melting point in the V-Fe binary system may be a

contributing factor.

4.4. Alloy Compositions.

The nominal elemental compositions of the twenty-six, as-cast specimens evaluated in this investigation are specified in Section 3.1.1, and chemical analysis has confirmed their general validity. In addition, the exceptional consistency of the hardness testing results shown in Table 4 for individual specimens implies a high uniformity of properties and, hence, of composition. Accordingly, the following paragraphs deal solely with the phase compositions of the as-cast specimens.

On the basis of the x-ray diffractometry results detailed in Section 3.2.6, three distinct phases were determined to occur in the sixteen specimens analyzed. These were the retained β(Ti) phase, the VTiFe intermetallic or γ phase, and the titanium mono-carbide or TiC phase. The retained β(Ti) phase was the predominant phase present in all the specimens analyzed. The γ phase was present in small amounts, probably only a few weight percent, in Specimens P-19 (59.5V-18.7Ti-21.8Fe) and P-24 (49.5V-23.3Ti-27.2Fe). The TiC phase was present also in small amounts in Specimens P-2, P-7, P-9, P-12, P-14, P-16, P-19, and P-21 (See Table 2 and Figure 15 for nominal compositions).

Neither of the two minority phases was discernible in the typically complex solidification structures of any of the as-cast specimens, either by light or scanning electron microscopy. In those instances where the presence of a second phase was suspected, the

x-ray energy dispersion analysis system associated with the scanning electron microscope was employed to confirm or deny its presence. In all such instances, the apparent second phase was determined to be nothing more than a manifestation of the usual phenomenon of preferential etching according to crystallographic orientation.

Of particular significance here are the considerable extent to which the β(Ti) phase was retained and the limited extent to which the γ phase was formed. The β(Ti) phase is apparently the first phase to solidify in all the alloys evaluated and is typically retained on quenching in both the V-Ti and the V-Fe binary systems. It is not surprising, then, that it was retained also in the V-Ti-Fe ternary system. The small amount of γ phase formed suggests that the kinetics of the non-equilibrium solidification and cooling processes favor the retention of the β(Ti) phase, rather than the formation of large amounts of the γ phase as might be predicted for equilibrium cooling.

The fact that the brittle VFe intermetallic or σ phase did not form is encouraging, but not especially surprising. As was discussed in Sections 2.3.3 and 2.3.4, the σ phase does not ordinarily form under non-equilibrium conditions. The occurrence of the γ phase, on the other hand, is not encouraging, even though it occurred in only very small amounts. It is typical of intermetallic phases to embrittle the materials in which they occur, even when they are present in only small amounts. This may well be reflected in the exceptional brittleness of Specimens P-19 (59.5V-18.7Ti-11.8Fe), P-23 (50.5V-35.6Ti-13.9Fe), P-24 (49.5V-23.3Ti-27.2Fe), and P-25

(48.6V-11.4Ti-40.0Fe), the four specimens whose nominal compositions lie closest to the predicted γ phase field.

5. CONCLUSIONS AND RECOMMENDATIONS

5.1. Primary Conclusions.

Based on the results of this investigation, the following primary conclusions are drawn:

The strengths and ductilities of as-cast, vanadium-rich V-Ti-Fe alloys vary greatly with interstitial impurity content. However, it is possible to obtain such alloys that possess useful levels of both strength and ductility.

The columnar dendritic structure is the predominant solidification structure in as-cast, vanadium-rich V-Ti-Fe alloys. A columnar structure appears only in nominally pure vanadium, and an equiaxed structure appears only in alloys near the V-Fe equiatomic composition.

The retained β(Ti) phase is the predominant phase that occurs in as-cast, vanadium-rich V-Ti-Fe alloys. The VTiFe intermetallic or γ phase and the titanium mono-carbide or TiC phase also occur, but only for limited compositions and in relatively small amounts.

5.2. Secondary Conclusions.

Based on the results of this investigation, the following secondary conclusions are drawn:

Vanadium, titanium, and iron differ greatly in certain of their physical, thermal, electrical, and mechanical properties. They differ especially in their densities, melting points, heats of fusion, thermal conductivities, and electrical resistivities.

The mechanical properties of vanadium, titanium, and iron vary greatly according to interstitial impurity content. The mechanical properties of vanadium are especially sensitive to the interstitial oxygen and nitrogen contents.

In the Ti-Fe, Fe-V, and Ti-V binary systems, where the β(Ti) phase is the first phase to solidify, the β(Ti) phase tends to be retained on quenching.

The V-Ti-Fe ternary system is a complex system that involves many equilibrium and non-equilibrium reactions and on which only a limited amount of work has been done.

A thorough understanding of weld interfacial phenomena, as they apply to the capacitor discharge welding process, is an essential element in any further pursuit of this alloy development effort.

The quality of the constituent vanadium used in the fabrication of V-Ti-Fe alloys is critical to the quality of the resulting specimens. Early chemical analysis is essential to the success of any project that involves the use of that element.

The method of alloy fabrication employed in this investigation was entirely satisfactory, with the exception that the sintering atmosphere should have been improved to reduce the oxygen contamination associated with that step.

The methods of testing and analysis employed in this investigation were entirely adequate. Although, many more specimens should have undergone bend testing and specimens representing all twenty-six compositions should have been subjected to x-ray

diffractometry analysis.

5.3. Recommendations.

Based on the results of this investigation, the following recommendations are made:

That the analysis of the V-Ti-Fe ternary equilibrium system be continued and expanded, to include both thermodynamic predictions and experimental evaluations of phase stabilities.

That a research project be initiated to determine the applicability of the modified Savage concept of weld interfacial phenomena to the capacitor discharge welding process.

That the experimental portion of this investigation be repeated, using low interstitial (iodide) or electrolytic vanadium as the elemental vanadium constituent of the experimental alloys.

APPENDIX A

REFERENCES

1. Huck Titanium-Dissimilar Metal Welding Program - Statement of Objectives and Intent, Huck Manufacturing Company, Carson, CA, 1981, pp. 1-2.

2. W. E. Wood and J. L. Johnsen: The Joining of Titanium to Dissimilar Metals - A Review of the Literature, Oregon Graduate Center, Beaverton, OR, 1981, pp. 1-14.

3. S. M. Gurevich, et al: Auto. Weld., 1962, 15 (8), p. 21.

4. W. E. Wood and J. L. Johnsen: The Joining of Titanium to Dissimilar Metals - Progress Report: 15 May 1982, Oregon Graduate Center, Beaverton, OR, 1982, p. 1.

4a. W. E. Wood and J. L. Johnsen: The Joining of Titanium to Dissimilar Metals - Progress Report: 31 January 1983, Oregon Graduate Center, Beaverton, OR, 1983, p. 3.

5. W. E. Wood and J. L. Johnsen: The Joining of Titanium to Dissimilar Metals - Plan for the Period 1 February 1983 through 31 January, 1984, Oregon Graduate Center, Beaverton, OR, 1983, pp. 6, 10-11.

6. J. L. Murray: Bul. Alloy Phase Diag., 1981, 2 (1), pp. 48-50.

7. V. F. Smith: Bul. Alloy Phase Diag., 1984, 5 (2), pp. 84-86.

8. H. Baker, ed.: Metals Handbook Ninth Edition, Volume 2 Properties and Selection: Nonferrous Alloys and Pure Metals, American Society of Metals, Metals Park, OH, 1979, pp. 822, 814, 742.

9. H. Baker, pp. 822, 815, 743.

10. J. L. Murray: Bul. Alloy Phase Diag., 1981, 2 (1), p. 140.

11. J. L. Murray: Bul. Alloy Phase Diag., 1981, 2 (3), p. 394.

12. V. F. Smith, p. 213.

13. J. L. Murray: Bul. Alloy Phase Diag., 1981, 2 (1), p. 49.

14. J. L. Murray: Bul. Alloy Phase Diag., 1981, 2 (3), p. 321.

15. V. F. Smith, p. 184.

16. R. C. Weast, ed.: Handbook of Chemistry and Physics, CRC Press, Inc., Boca Raton, FL, 1981, p. D-189.

17. R. C. Weast, p. D-185.

18. R. C. Weast, pp. B-231 - B-235.

19. R. C. Weast, pp. E-14 - E-16.

20. H. Baker, pp. 816, 743.

21. C. Smithells: Metals Reference Book, Plenum Press, New York, 1967, pp. 686-743.

22. R. C. Weast, p. D-189.

23. H. Baker, pp. 741, 747.

24. C. Smithells, p. 647.

25. R. C. Weast, pp. F-171 - F-172.

26. H. Baker, pp. 745, 815.

27. W. Rostoker: The Metallurgy of Vanadium, John Wiley and Sons, Inc., New York, 1958, p. 71.

28. E. C. Bain and H. W. Paxton: Alloying Elements in Steel, American Society for Metals, Metals Park, OH, 1966, p.270.

29. W. Rostoker, p. 70.

30. W. Rostoker, p. 71.

31. H. Baker, p. 816.

32. D. Benjamin, ed.: Metals Handbook Ninth Edition, Volume 3 Properties and Selection: Stainless Steels, Tool Materials, and Special Purpose Metals, American Society of Metals, Metals Park, OH, 1980, p. 357.

33. H. E. McGannon: The Making, Shaping, and Treating of Steel, Herbick and Held, Pittsburgh, PA, 1971, p. 1076.

34. J. L. Murray: Bul. Alloy Phase Diag., 1981, 2 (3), pp. 320-334, 394.

35. J. L. Murray: Bul. Alloy Phase Diag., 1981, 2 (1), pp. 48-55, 140.

36. O. Nakano, et al.: J. Jap. Inst. Met., 1981, 45 (7), pp. 653-660.

37. V. F. Smith, pp. 184-194, 213.

38. A. Prince: Personal Communication, November 5, 1984.

39. V. Raghavan: Personal Communication, November 26, 1984.

40. T-K Bi and I. I. Kornilov: Rus. J. Inorg. Chem., 1960, 5 (4), p. 434.

41. C. Pi and I. I. Kornilov: Rus. J. Inorg. Chem., 1961, 6 (6), p. 695.

42. C. Pi and I. I. Kornilov, p. 695.

43. W. F. Savage: Weld. Res. Suppl., 1976, pp. 260-s - 283-s.

44. W. E. Wood and J. L. Johnsen: The Joining of Titanium to Dissimilar Metals - Progress Report: 30 June 1982, Oregon Graduate Center, Beaverton, OR, 1982, pp. 7-8.

45. W. E. Wood and J. L. Johnsen: The Joining of Titanium to Dissimilar Metals - Progress Report: 30 June 1982, Oregon Graduate Center, Beaverton, OR, 1982, pp. 8-9.

46. J. H. Devletian: Rapid Solidification Welding of 304 RSP Stainless Steel by Capacitor Discharge Process, Presented to 66th Annual Convention of AWS, Las Vegas, NV, 1985.

47. W. Rostoker, pp. 83-89.

48. W. Rostoker, pp. 141-142.

49. T-K Bi and I. I. Kornilov, pp. 435-436.

50. A. R. Rosenfield, et al.: J. Mat. Sci., 1985, 20 (3), pp. 935-940.

51. W. Rostoker, pp. 83-89.

52. J. H. Westbrook and H. Conrad, ed.: The Science of Hardness Testing and Its Research Applications, American Society of Metals, Metals Park, OH, 1973, pp. 1-11.

53. J. H. Westbrook and H. Conrad, pp. 51-72.

54. W. Rostoker, p. 86.

55. M. C. Flemings: Solidification Processing, McGraw-Hill, Inc., New York, 1974, pp. 154-157.

APPENDIX B

BIBLIOGRAPHY

Alper, A., ed., Phase Diagrams, Materials Science and Technology, Academic Press, New York, 1970.

Annual Book of ASTM Standards, Section 3, Volume 03.01, Metals-Mechanical Testing: Elevated and Low Temperature Tests, American Society for Testing and Materials, Philadelphia, PA, 1983.

Ansara, I., Comparison of Methods for Thermodynamic Calculation of Phase Diagrams, Int. Met. Rev., 1979, (1): 20-53.

Armitage, C., A Study of the Iron-Nickel-Vanadium System, Ph.D. Thesis, University of Wisconsin, Ann Arbor, MI, 1960.

Bain, E. C. and Paxton, H. W., Alloying Elements in Steel, American Society for Metals, Metals Park, OH, 1966.

Baker, H., ed., Metals Handbook Ninth Edition, Volume 2 Properties and Selection: Nonferrous Alloys and Pure Metals, American Society of Metals, Metals Park, OH, 1979.

Benjamin, D., ed., Metals Handbook Ninth Edition, Volume 3 Properties and Selection: Stainless Steels, Tool Materials, and Special Purpose Metals, American Society of Metals, Metals Park, OH, 1980.

Bi, T-K and Kornilov, I. I., The Phase Diagram of the TiFe-V System, Rus. J. Inorg. Chem., 1960, 5 (4): 434-436.

Blackburn, M., et al., Titanium Alloys, Stress Corrosion Cracking in High Strength Steels and in Titanium and Aluminum Alloys, ed. Brown, B., Naval Research Laboratory, Washington, D.C., 1972, 245-275.

Cahn, J., Obtaining Inferences about Relative Stability and Metastable Phase Sequences from Phase Diagrams, Bul. Alloy Phase Diag., 1980, 1 (2): 27-32.

Chang, Y. and Smith, J., ed., Calculation of Phase Diagrams and Thermochemistry of Alloy Phases, Proceedings of September, 1979 Symposium, The Metallurgical Society of AIME, New York, 1980.

Cros, B., Phase Equilibriums in Vanadium-Metal-Oxygen Systems, V. The Vanadium-Iron-Oxygen System at 1,273 °K, Bul, Soc. Chim. Fr., 1976, (9-10, Pt 1): 1381-1387.

Cullity, B. D., Elements of X-Ray Diffraction, Second Edition, Addison-Wesley Publishing Company, Inc., Reading, MA, 1978.

Devletian, J. H., Rapid Solidification Welding of 304 RSP Stainless Steel by Capacitor Discharge Process, Presented to 66th Annual Convention of AWS, Las Vegas, NV, 1985.

Doane, D. and Kirkaldy, J., ed., Hardenability Concepts with Applications to Steel, The Metallurgical Society of AIME, New York, 1978.

Donachie, M., ed., Titanium and Titanium Alloys Source Book, American Society of Metals, Metals Park, OH, 1982.

Eliseeva, O. I. and Shirokov, V. V., Internal Oxidation of V-Ti System Alloys, Sov. Mat. Sci., 1983, 19 (5): 434-437.

Elliot, R. and Rostoker, W., The Occurrence of Laves-Type Phases Among Transition Elements, Trans. ASM, 1958, 50: 617-633.

Eyring, LeR. and O'Keefe, M., ed., The Chemistry of Extended Defects in Non-Metallic Solids, North-Holland Publishing Company, Amsterdam, 1970.

Fedotov, S. G., et al., The Influence of Aluminum and Oxygen on the Formation of Metastable Phases in Titanium Alloys Containing β-Stabilizing Elements, Rus. Met., 1974, (4): 121-126.

Flemings, M. C., Solidification Processing, McGraw-Hill, Inc., New York, 1974.

Frage, N. R., et al., Solubility of N in the Ti-Fe System, Izvest. VUZ Chern. Met., 1974, (6): 13-15.

Goodman, D., et al., The Centennial of the Gibbs-Konovalov Rule for Congruent Points, Bul. Alloy Phase Diag., 1981, 2 (1): 29-34.

Gurevich, S. M. et al., Properties of Welded Joints in Ti-V, Ti-V-Al, and Ti-Zr-Al Alloys with an Elevated Oxygen Content, Met. Term. Obra. Met., 1973, (10): 832-834.

Gurevich, S. M., et al., Welding Titanium to Steel, Anto. Weld., 1962, 15 (8): 21-26.

Guseva, L. N. and Dolinskaya, L. K., Metastable Phase Equilibria in the Systems Ti-V and Ti-Nb, Dak. Akad. Nauk SSSR, 1982, 266 (3): 334-337.

Hansen, M., Constitution of Binary Alloys, McGraw-Hill Book Company, Inc., New York, 1958.

Hasson, D. and Hamilton, C., ed., Advanced Processing Methods for Titanium, Proceedings of October, 1981 Symposium, The Metallurgical Society of AIME, New York, 1982.

Hausner, H., Handbook of Powder Metallurgy, Chemical Publishing Company, Inc., New York, 1973.

Hillert, M., A Discussion of Methods of Calculating Phase Diagrams, Bul. Alloy Phase Diag., 1981, 2 (3): 265-268.

Hillert, M., Methods of Calculating Phase Diagrams, Calculation of Phase Diagrams and Thermochemistry of Alloy Phases, ed. Y. Chang and J. Smith, The Metallurgical Society of AIME, New York, 1980, 1-13.

Hillert, M., Prediction of Iron-Base Phase Diagrams, Hardenability Concepts with Applications to Steel, ed. D. Doane and J. Kirkaldy, The Metallurgical Society of AIME, New York, 1978, 5-25.

Hillert, M., Predictions of the Slopes of Phase Boundaries, Bul. Alloy Phase Diag., 1982, 3 (1): 4-8.

How to Use Titanium - Properties and Fabrication of Titanium Mill Products, Titanium Metals Corporation of America, West Caldwell, NJ, Descriptive Brochure.

Huck Titanium-Dissimilar Metal Welding Program - Statement of Objectives and Intent, Huck Manufacturing Company, Carson, CA, 1981.

Hull, D. and Bacon, D. J., Introduction to Dislocations, Third Edition, Pergamon Press, Oxford, 1984.

Jaffee, R. and Promisel, N., ed., The Science, Technology and Application of Titanium, Proceedings of May, 1968 International Conference, Pergamon Press, Ltd., Oxford, 1970.

Kaufman, L. and Bernstein, H., Computer Calculation of Phase Diagrams, Academic Press, New York, 1970.

Kaufman, L. and Dew-Hughes, D., Illustration of Ternary Diagram Synthesis - Mn-Ti-Fe and Al-Ti-Fe, Calculation of Phase Diagrams and Thermochemistry of Alloy Phases, ed. Y. Chang and J. Smith, The Metallurgical Society of AIME, New York, 1980, 47-71.

Kaufman, L. and Nesor, H., Computer Analysis of Alloy Systems, Technical Report AFML-TR-73-56, ManLabs, Inc., Cambridge, MA, 1973.

Khaled, T., et al., The Effect of Interstitials on Phase Equilibria in P[Ti, Zr, Hf] - x [β-Stabilizer(s)] Alloy Systems, Met. Trans., 1981, 12A (2): 1293-1298.

Kieffer, R. and Braun, H., Vanadin-Niob-Tantal, Die Metallurgie der reinen Metalle und ihrer Legierungen, Springer-Verlag, Berlin, 1963.

Kimura, H. and Izumi, O., ed., Titanium '80, Science and Technology, Proceedings of the Fourth International Conference on Titanium, Metallurgical Society of AIME, New York, 1980.

Kornilov, I. I., et al., On the Nature of Solid Solutions of Titanium-Vanadium-Oxygen and Titanium-Vanadium-Aluminum-Oxygen, Phys. Met. Met., 1972, 33 (4): 212-215.

Lin, P., et al., Computation of Phase Diagrams of Ternary Additive and Reciprocal Ionic Systems, Calculation of Phase Diagrams and Thermochemistry of Alloy Systems, ed. Y. Chang and J. Smith, The Metallurgical Society of AIME, New York, 1980, 27-45.

Lin, S., Titanium-Vanadium-Oxygen Systems, Part I: Phase Study, Part II: Structure Study, Part III: Vaporization Study, Diss. Abstr. B., 1968, 28 (8): 3242-B.

Lushnikova, T. V., et al., Phase Diagram of the Fe-V-O System in the Region of Mono-Oxide Solid Solutions, Trudy Chelyabinsk. Politekh. Inst., 1975, (163): 9-11.

Lyatsoskaya, V. S., et al., Effect of Heat Treatment on the Structure and Properties of Titanium-Vanadium Alloys, Izv. Vyssh. Uchev. Zaved. Tsvet. Met., 1971, 14 (5): 128-132.

Lysaght, V. E. and DeBellis, A., Hardness Testing Handbook, American Chain and Cable Company, Inc., 1974.

Maksimov, Yu. A., et al., Properties of Ti-V and Ti-V-Al Alloys with Oxygen, Met. Term. Obra. Met., 1970, (11): 922-924.

Masing, G., Ternary Systems, Dover Publications, Inc., New York, 1960.

Massalski, T. and Pops, H., Intermediate Phases in Metallic Phase Diagrams, Phase Diagrams, Materials Science and Technology, ed. A. Alpert, Academic Press, New York, 1970, 221-263.

McGannon, H. E., ed., The Making, Shaping, and Treating of Steel, Herbick and Held, Pittsburgh, PA, 1971.

Menon, E. S. K. and Krishnan, R., Phase Transformations in Ti-V Alloys, Part 1: Martensitic Transformations, J. Mat. Sci., 1983, 18 (2): 365-374.

Menon, E. S. K. and Krishnan, R., Phase Transformations in Ti-V Alloys, Part 2: γ and ω Formation, J. Mat. Sci., 1983, 18 (2): 375-382.

Mikhailov, G. G. and Lushnikova, T. V., Phase Equilibriums in the Low-Oxygen Region of the Iron-Vanadium-Oxygen System, Sb. Nauch. Trudy Chelyabinsk. Politekh. Inst. Trudy, 1974, (147): 10-15.

Molchanova, E. K., Phase Diagrams of Titanium Alloys, Daniel Davey and Company, Inc., New York, 1965.

Morris, A., Problem Manual for Metallurgical Thermodynamics, Arthur E. Morris, Rolla, MO, 1981.

Murray, J. L., The Fe-Ti (Iron-Titanium) System, Bul. Alloy Phase Diag., 1981, 2 (3): 320-334, 393.

Murray, J. L., The Ti-V (Titanium-Vanadium) System, Bul. Alloy Phase Diag., 1981, 2 (1): 48-55, 139.

Nakano, O., et al., Miscibility Gap in the Titanium-Vanadium System, J. Jap. Inst. Met., 1981, 45 (7): 653-660.

Nash, W. A., Theory and Problems of Strength of Materials, McGraw-Hill Book Company, New York, 1957.

Paxton, H. W., Seminar Coordinator, Ductility, Papers Presented at Seminar of ASM on 14-15 October, 1967, ASM, Metals Park, OH, 1968.

Petzow, G., Metallographic Etching, ASM, Metals Park, OH, 1978.

Pi, C. and Kornilov, I., Equilibrium Diagram of the Ti-V-Fe System, Trudy Inst. Met. In Baikova Akad. Nauk., 1961, (8): 54-57.

Pi, C. and Kornilov, I. I., Equilibrium Diagram of the Ti-V-TiFe Ternary System, Rus. J. Inorg. Chem., 1961, 6 (6): 694-696.

Prince, A., Alloy Phase Equilibria, Elsevier Publishing Company, Amsterdam, 1966.

Prince, A., Multicomponent Alloy Constitution Bibliography, 1955-1973, The Metals Society, London, 1978.

Prince, A., Personal Communication, November 5, 1984.

Prince, A., To Speculate or Not to Speculate, Bul. Alloy Phase Diag., 1981, 2 (2): 149-152.

Raghavan, V., Personal Communication, November 26, 1984.

Menon, E. S. K. and Krishnan, R., Phase Transformations in Ti-V Alloys, Part 2: γ and ω Formation, J. Mat. Sci., 1983, 18 (2): 375-382.

Mikhailov, G. G. and Lushnikova, T. V., Phase Equilibriums in the Low-Oxygen Region of the Iron-Vanadium-Oxygen System, Sb. Nauch. Trudy Chelyabinsk. Politekh. Inst. Trudy, 1974, (147): 10-15.

Molchanova, E. K., Phase Diagrams of Titanium Alloys, Daniel Davey and Company, Inc., New York, 1965.

Morris, A., Problem Manual for Metallurgical Thermodynamics, Arthur E. Morris, Rolla, MO, 1981.

Murray, J. L., The Fe-Ti (Iron-Titanium) System, Bul. Alloy Phase Diag., 1981, 2 (3): 320-334, 393.

Murray, J. L., The Ti-V (Titanium-Vanadium) System, Bul. Alloy Phase Diag., 1981, 2 (1): 48-55, 139.

Nakano, O., et al., Miscibility Gap in the Titanium-Vanadium System, J. Jap. Inst. Met., 1981, 45 (7): 653-660.

Nash, W. A., Theory and Problems of Strength of Materials, McGraw-Hill Book Company, New York, 1957.

Paxton, H. W., Seminar Coordinator, Ductility, Papers Presented at Seminar of ASM on 14-15 October, 1967, ASM, Metals Park, OH, 1968.

Petzow, G., Metallographic Etching, ASM, Metals Park, OH, 1978.

Pi, C. and Kornilov, I., Equilibrium Diagram of the Ti-V-Fe System, Trudy Inst. Met. In Baikova Akad. Nauk., 1961, (8): 54-57.

Pi, C. and Kornilov, I. I., Equilibrium Diagram of the Ti-V-TiFe Ternary System, Rus. J. Inorg. Chem., 1961, 6 (6): 694-696.

Prince, A., Alloy Phase Equilibria, Elsevier Publishing Company, Amsterdam, 1966.

Prince, A., Multicomponent Alloy Constitution Bibliography, 1955-1973, The Metals Society, London, 1978.

Prince, A., Personal Communication, November 5, 1984.

Prince, A., To Speculate or Not to Speculate, Bul. Alloy Phase Diag., 1981, 2 (2): 149-152.

Raghavan, V., Personal Communication, November 26, 1984.

Raghavan, V., The Fe-N-V (Iron-Nitrogen-Vanadium) System, Bul. Alloy Phase Diag., 1984, 5 (2): 194-198, 223-224.

Rand, M., Qualitative Predictions from Solid-State Physics - What Do Phase Diagram Calculators Want?, Bul. Alloy Phase Diag., 1982, 3 (2): 134-140.

Rosenfield, A. R., et al., Estimating Damage Laws from Bend-Test Data, J. Mat. Sci., 1985, 20 (3): 935-940.

Rostoker, W., The Metallurgy of Vanadium, John Wiley and Sons, Inc., New York, 1958

Savage, W. F., A Study of Weld Interface Phenomena in a Low Alloy Steel, Weld. Res. Suppl., 1976: 260-s - 283-s.

Schmahl, N. G. and Dillenburg, H., Gleichgewichtsuntersuchungen an Eisenoxidhaltigen Mischphasen innerhalb der Dreistoffsysteme Fe-Al-O, Fe-Cr-O, und Fe-V-O, Zeit. Phys. Chem., 1969, 65 (1-4): 119-138.

Seibold, A., Phasengleichgewichte in den ternaeren Systemen Ti-Fe-O und Ti-Al-Fe, Z. Metallkde, 1981, 72 (10): 712-719.

Shakin, E. L. and Mikhailov, G. G., Phase Equilibria in the Fe-Ti-O System, Trudy Chelyabinsk. Politekh. Inst., 1975, (163): 12-15.

Shikama, T., et al., Interaction of Interstitial Oxygen and Nitrogen with Scavenger Substitutional Atoms in Vanadium, Proc. Sixth Int. Conf. Int. Friction and Ultra. Atten. in Solids, Tokyo, 1977: 459-463.

Smithells, C., Metals Reference Book, Plenum Press, New York, 1967.

Smith, V. F., The Fe-V (Iron-Vanadium) System, Bul. Alloy Phase Diag., 1984, 5 (2): 184-194, 213.

Spencer, P., Calculation of Phase Diagrams for Alloy Systems Showing Sigma-Phase Formation, Calculation of Phase Diagrams and Thermochemistry of Alloy Phases, ed. Y. Chang and J. Smith, The Metallurgical Society of AIME, New York, 1980, 15-25.

Timoshenko, S., Strength of Materials, Robert E. Krieger Publishing Company, Huntington, NY, 1976.

Uhrenius, B., A Compendium of Ternary Iron-Base Phase Diagrams, Hardenability Concepts with Applications to Steel, ed. D. Doane and J. Kirkaldy, The Metallurgical Society of AIME, New York, 1978, 28-81.

Verbetskii, V. N., et al., Interaction of Hydrogen with Alloys of the Fe-Ti-V System, which Crystallize with the β-Titanium Structure, Russ. J. Inorg. Chem., 1983, 28 (2): 262-265.

Vladimirov, L. P., et al., Physiochemical Properties of Iron-Oxygen-Titanium Melts, Russ. J. Phys. Chem., 1974, 48 (1): 87-88.

Westbrook, J. H. and Conrad, H., ed., The Science of Hardness Testing and Its Research Applications, ASM, Metals Park, OH, 1973.

Weast, R. C., ed., Handbook of Chemistry and Physics, CRC Press, Inc., Boca Raton, FL, 1981.

Wood, W. E. and Johnsen, J. L., The Joining of Titanium to Dissimilar Metals - A Review of the Literature, Oregon Graduate Center, Beaverton, OR, 1981.

Wood, W. E. and Johnsen, J. L., The Joining of Titanium to Dissimilar Metals - Plan for the Period 1 February 1983 through 31 January 1984, Oregon Graduate Center, Beaverton, OR, 1983.

Wood, W. E. and Johnsen, J. L., The Joining of Titanium to Dissimilar Metals - Progress Report: 15 May 1982, Oregon Graduate Center, Beaverton, OR, 1982.

Wood, W. E. and Johnsen, J. L., The Joining of Titanium to Dissimilar Metals - Progress Report: 30 June 1982, Oregon Graduate Center, Beaverton, OR, 1982.

Wood, W. E. and Johnsen, J. L., The Joining of Titanium to Dissimilar Metals - Progress Report: 31 January 1983, Oregon Graduate Center, Beaverton, OR, 1983.

Zenek, O., et al., Untersuchungen im Dreistoffsystem Ti-Fe-O, Monat. Chem., 1969, 100 (6): 2075-2083.

APPENDIX C

SOLIDIFICATION STRUCTURE MICROGRAPHS

Figure C-1. LIGHT MICROGRAPH OF SOLIDIFICATION STRUCTURE OF SPECIMEN P-1 (100.0V), 104X.

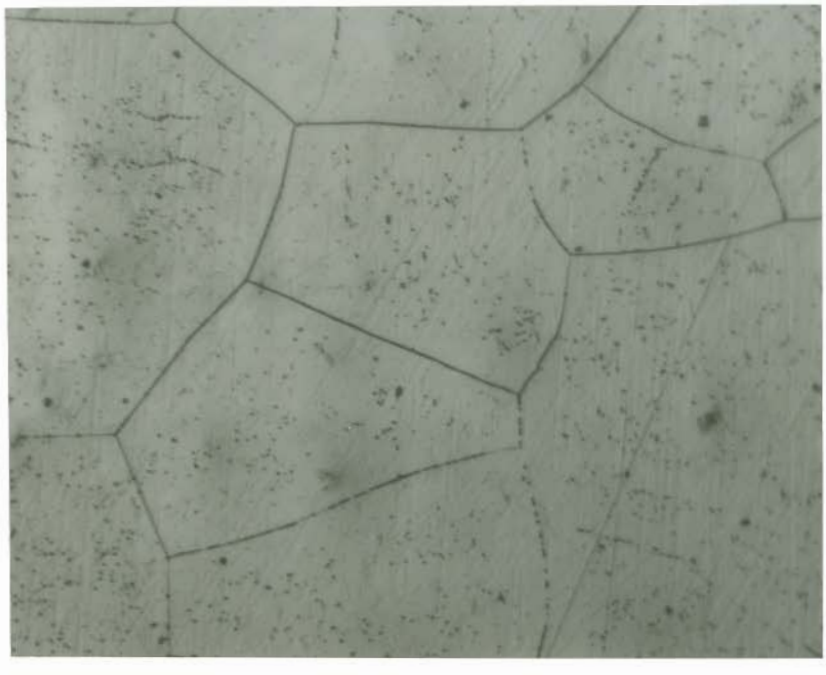

Figure C-2. LIGHT MICROGRAPH OF SOLIDIFICATION STRUCTURE OF SPECIMEN P-1 (100.0V), 256X.

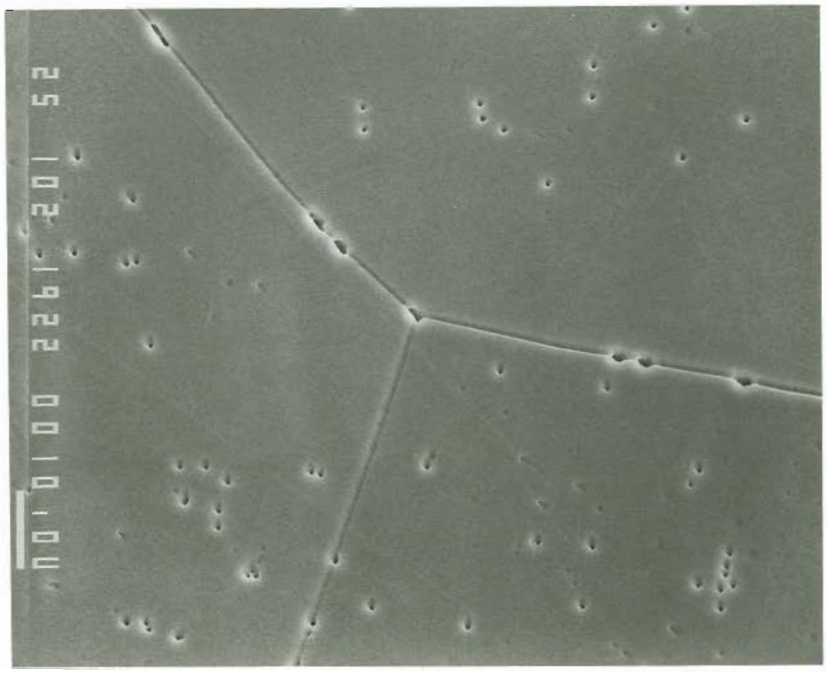

Figure C-3. SEM MICROGRAPH OF SOLIDIFICATION STRUCTURE OF SPECIMEN P-1 (100.0V), 1,000X.

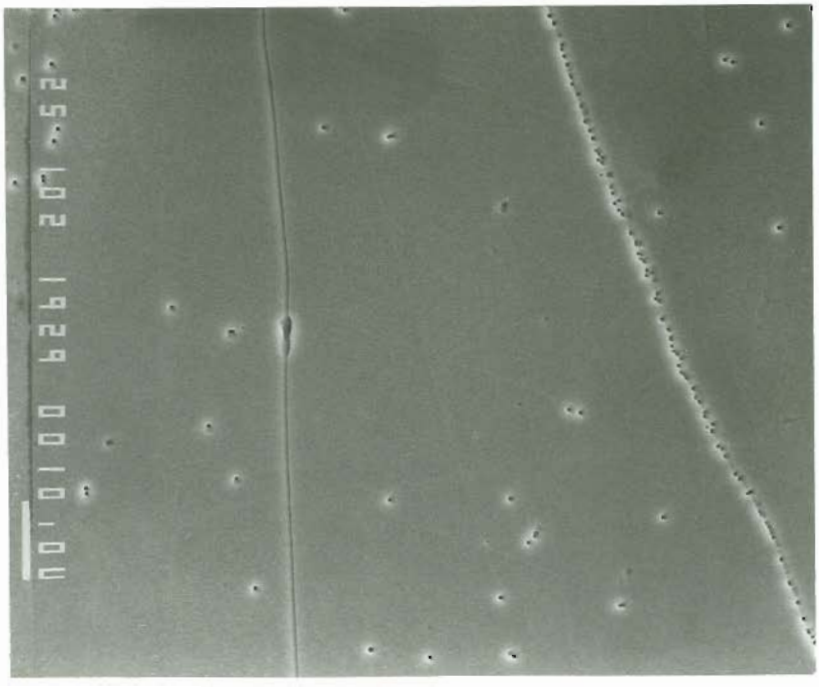

Figure C-4. SEM MICROGRAPH OF SOLIDIFICATION STRUCTURE OF SPECIMEN P-1 (100.0V), 1,000X.

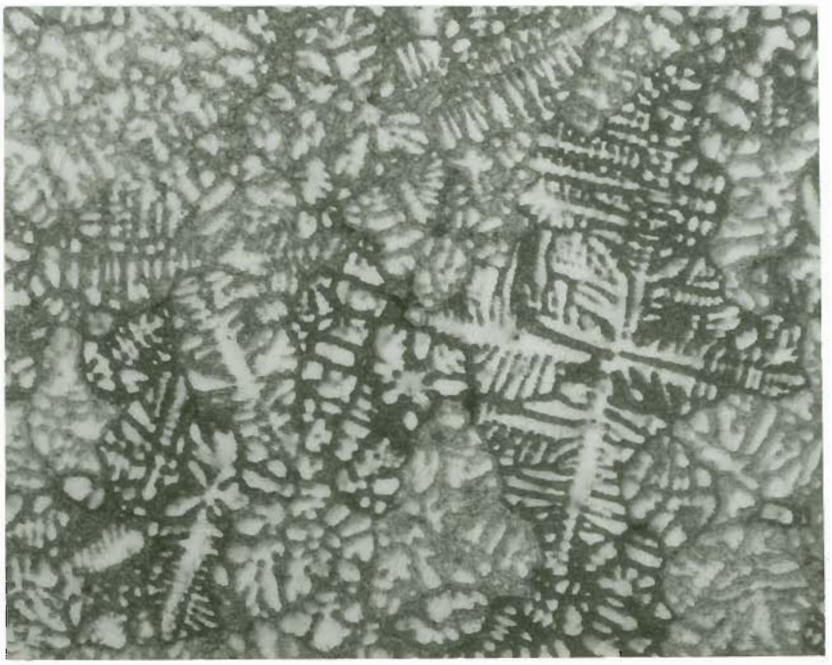

Figure C-5. LIGHT MICROGRAPH OF SOLIDIFICATION STRUCTURE OF SPECIMEN P-2 (90.5V-9.5Ti), 104X.

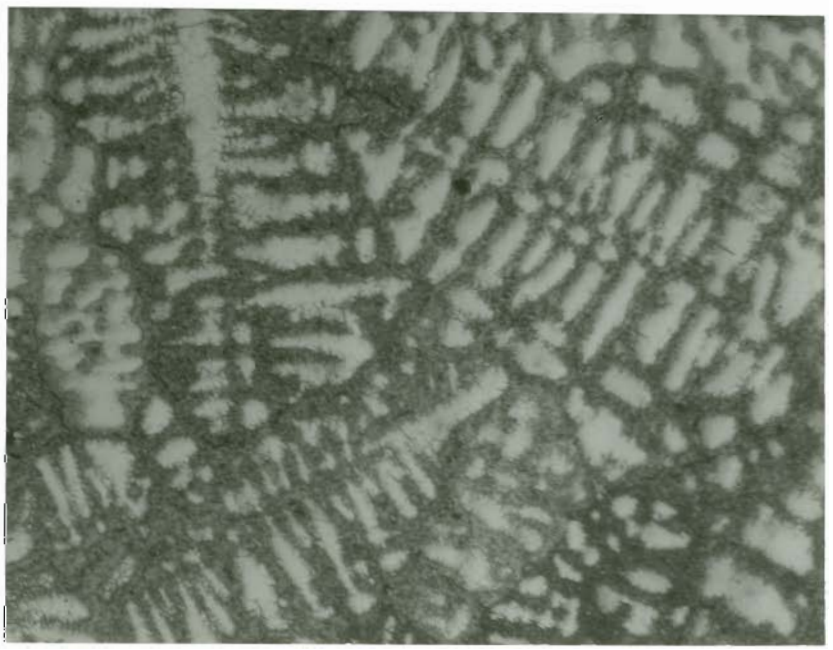

Figure C-6. LIGHT MICROGRAPH OF SOLIDIFICATION STRUCTURE OF SPECIMEN P-2 (90.5V-9.5Ti), 256X.

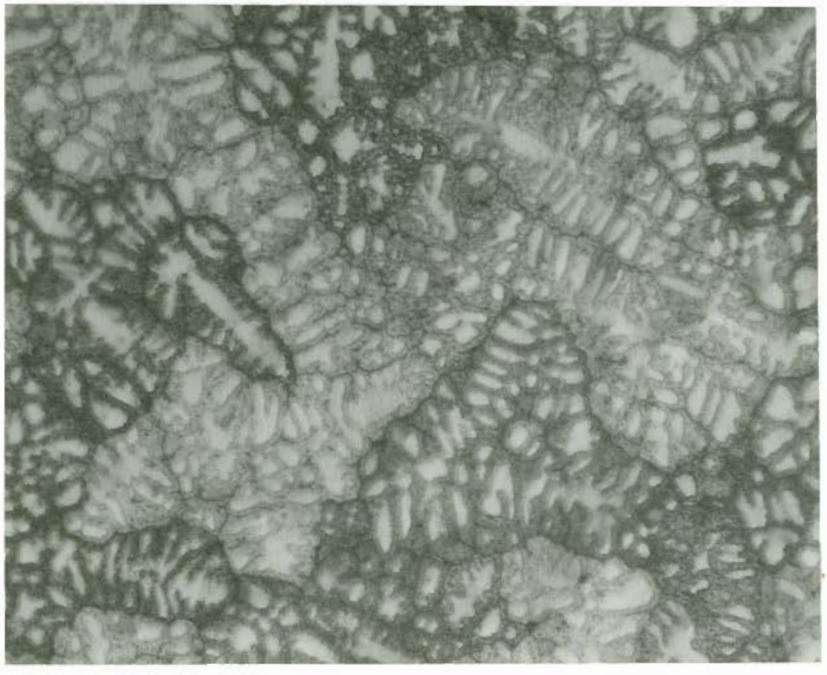

Figure C-7. LIGHT MICROGRAPH OF SOLIDIFICATION STRUCTURE OF SPECIMEN P-3 (90.2V-7.1Ti-2.7Fe), 104X.

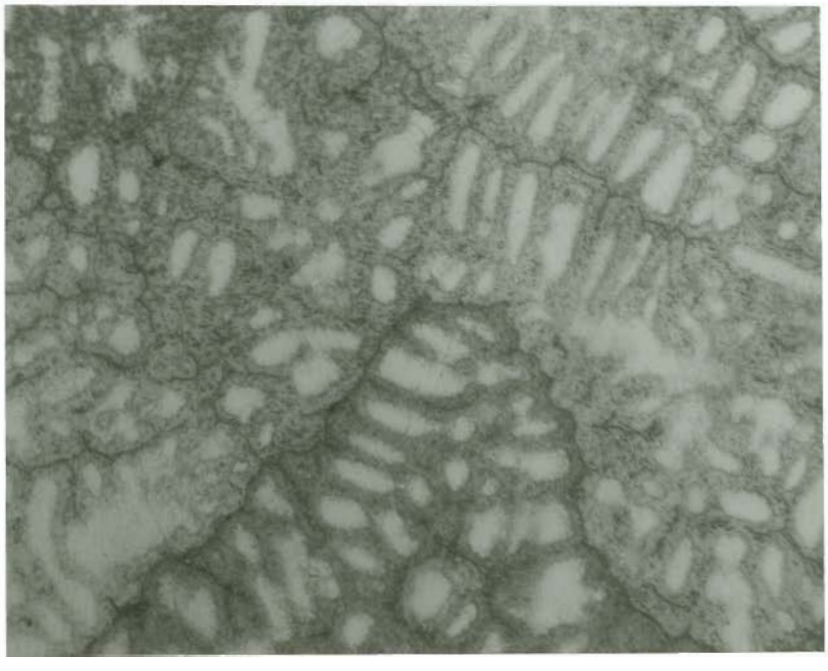

Figure C-8. LIGHT MICROGRAPH OF SOLIDIFICATION STRUCTURE OF SPECIMEN P-3 (90.2V-7.1Ti-2.7Fe), 256X.

Figure C-9. LIGHT MICROGRAPH OF SOLIDIFICATION STRUCTURE OF SPECIMEN P-4 (89.8V-4.7Ti-5.5Fe), 104X.

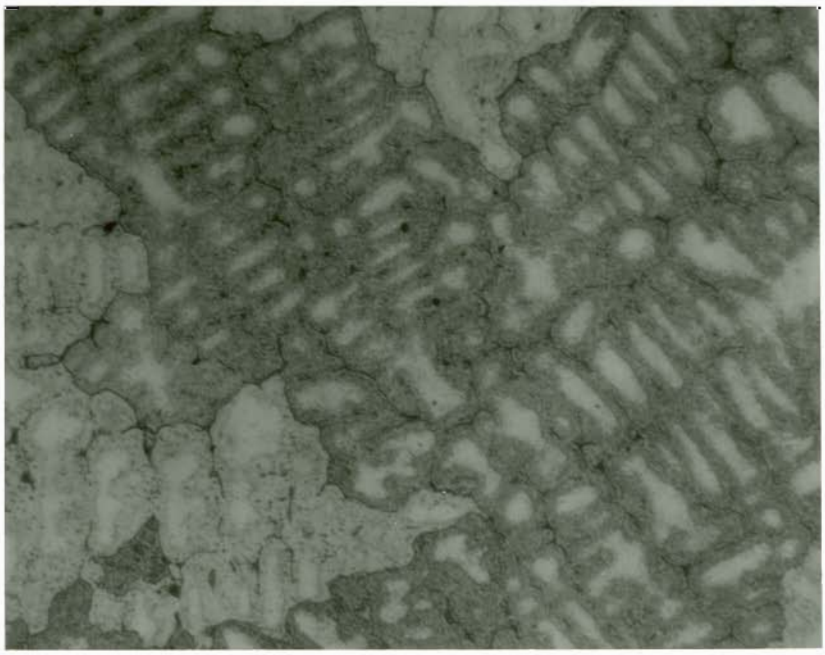

Figure C-10. LIGHT MICROGRAPH OF SOLIDIFICATION STRUCTURE OF SPECIMEN P-4 (89.8V-4.7Ti-5.5Fe), 256X.

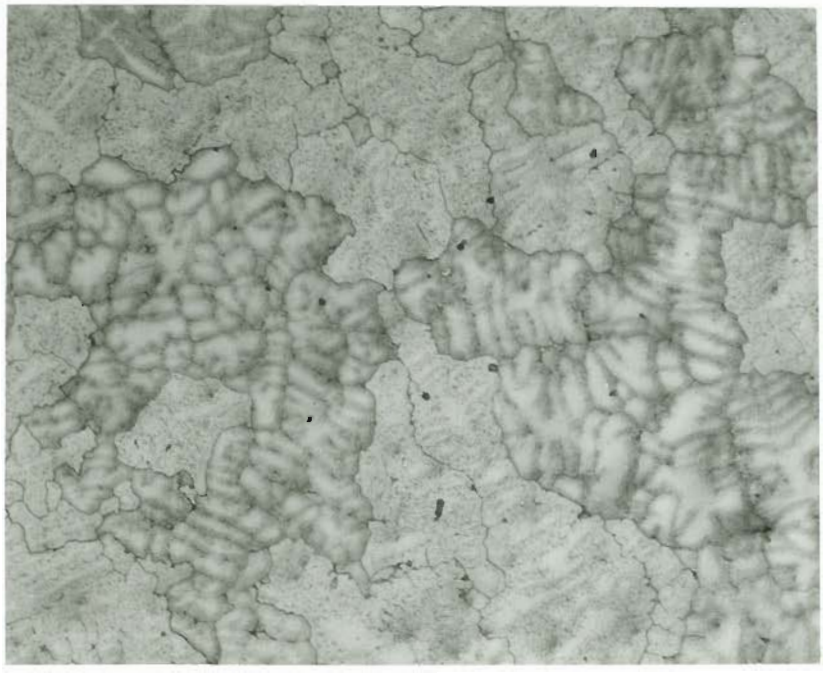

Figure C-11. LIGHT MICROGRAPH OF SOLIDIFICATION STRUCTURE OF SPECIMEN P-5 (89.5V-2.3Ti-8.2Fe), 104X.

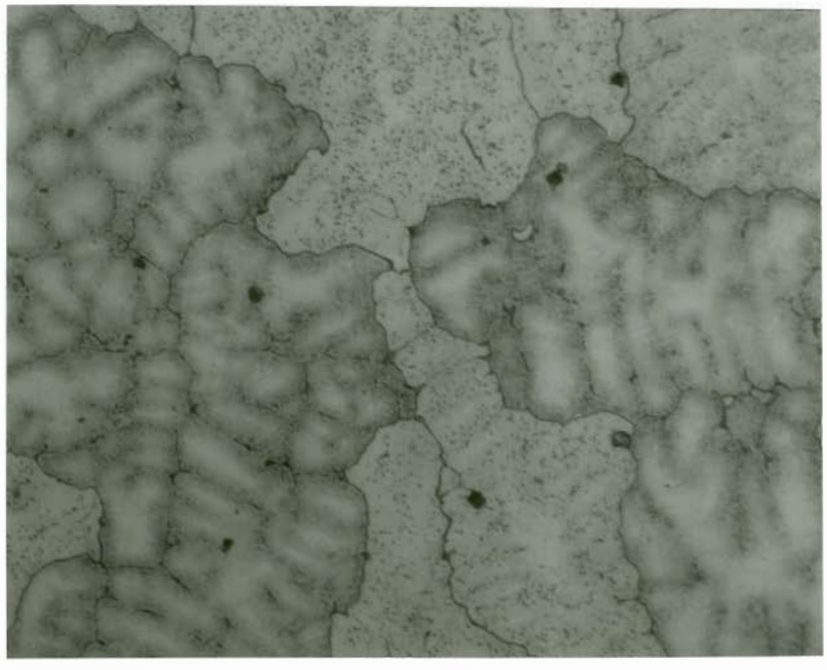

Figure C-12. LIGHT MICROGRAPH OF SOLIDIFICATION STRUCTURE OF SPECIMEN P-5 (89.5V-2.3Ti-8.2Fe), 256X.

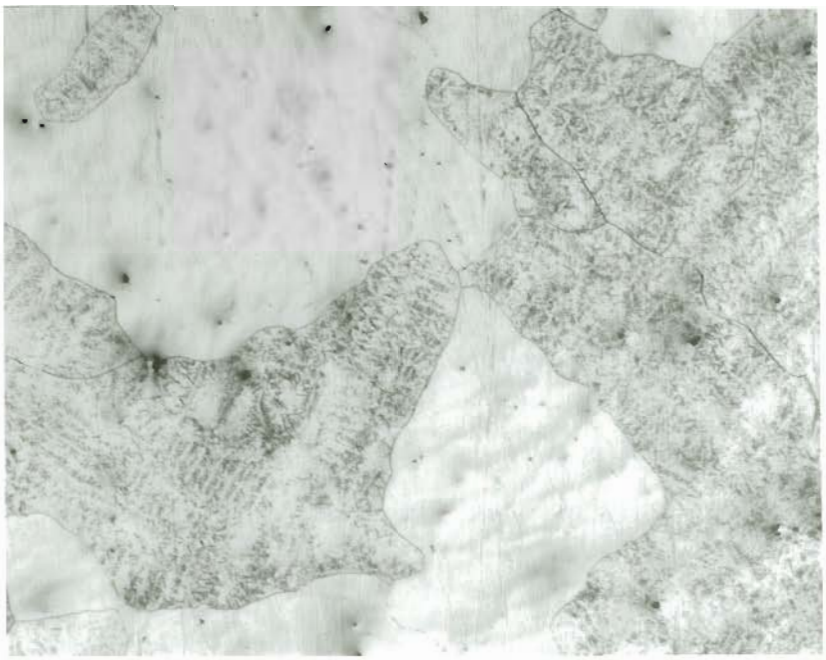

Figure C-13. LIGHT MICROGRAPH OF SOLIDIFICATION STRUCTURE OF SPECIMEN P-6 (89.1V-10.9Fe), 104X.

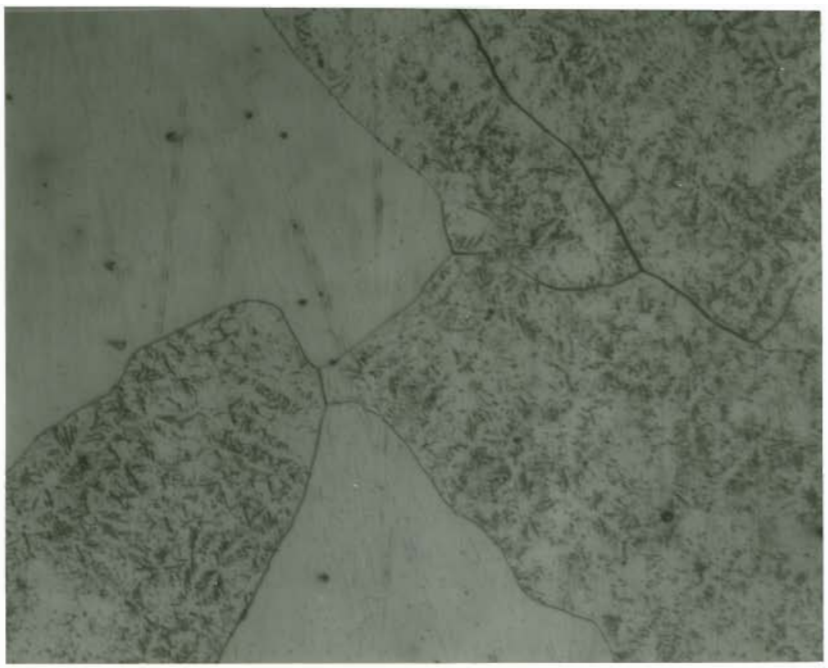

Figure C-14. LIGHT MICROGRAPH OF SOLIDIFICATION STRUCTURE OF SPECIMEN P-6 (89.1V-10.9Fe), 256X.

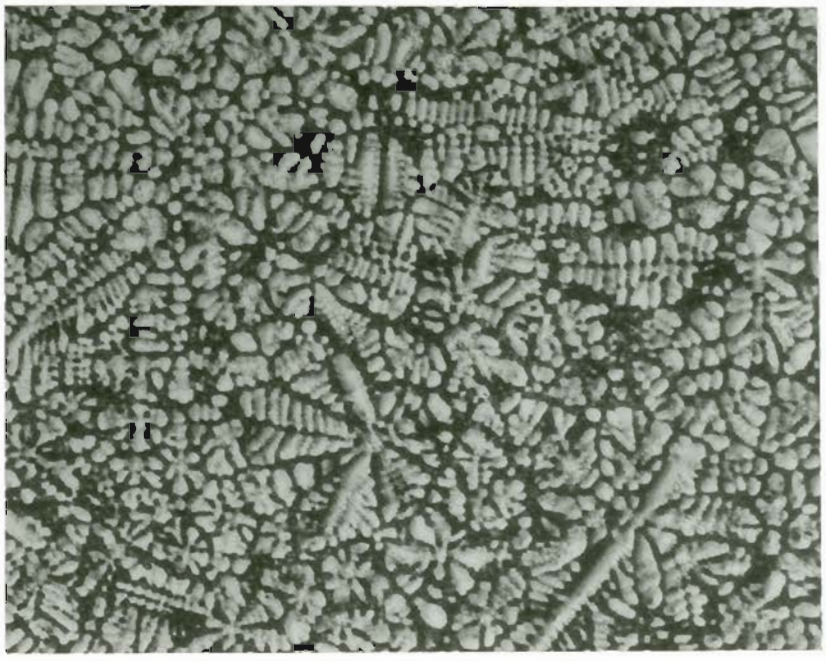

Figure C-15. LIGHT MICROGRAPH OF SOLIDIFICATION STRUCTURE OF SPECIMEN P-7 (81.0V-19.0Ti), 104X.

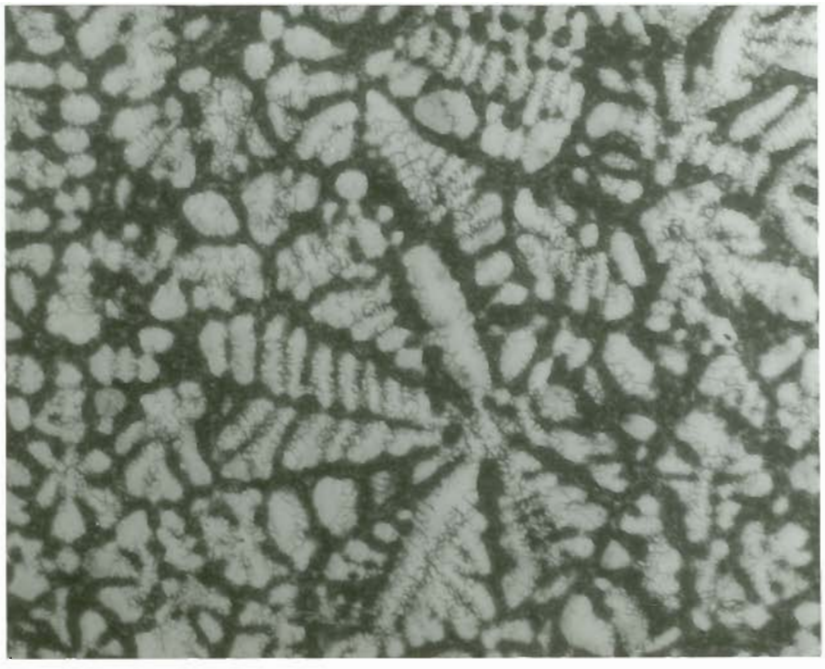

Figure C-16. LIGHT MICROGRAPH OF SOLIDIFICATION STRUCTURE OF SPECIMEN P-7 (81.0v-19.0Ti), 256X.

Figure C-17. LIGHT MICROGRAPH OF SOLIDIFICATION STRUCTURE OF SPECIMEN P-8 (80.3V-14.2Ti-5.5Fe), 104X.

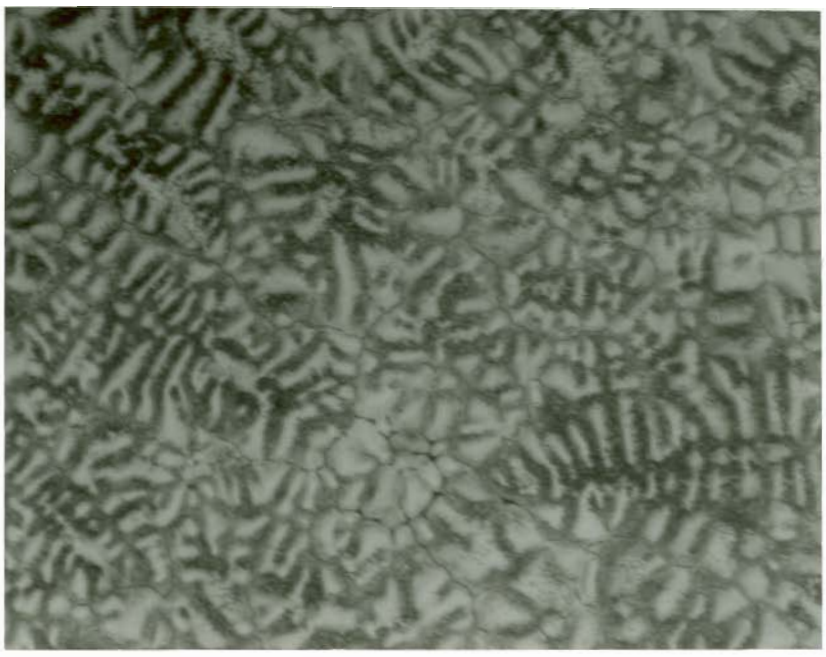

Figure C-18. LIGHT MICROGRAPH OF SOLIDIFICATION STRUCTURE OF SPECIMEN P-8 (80.3V-14.2Ti-5.5Fe), 256X.

Figure C-19. LIGHT MICROGRAPH OF SOLIDIFICATION STRUCTURE OF SPECIMEN P-9 (79.7V-9.4Ti-10.9Fe), 104X.

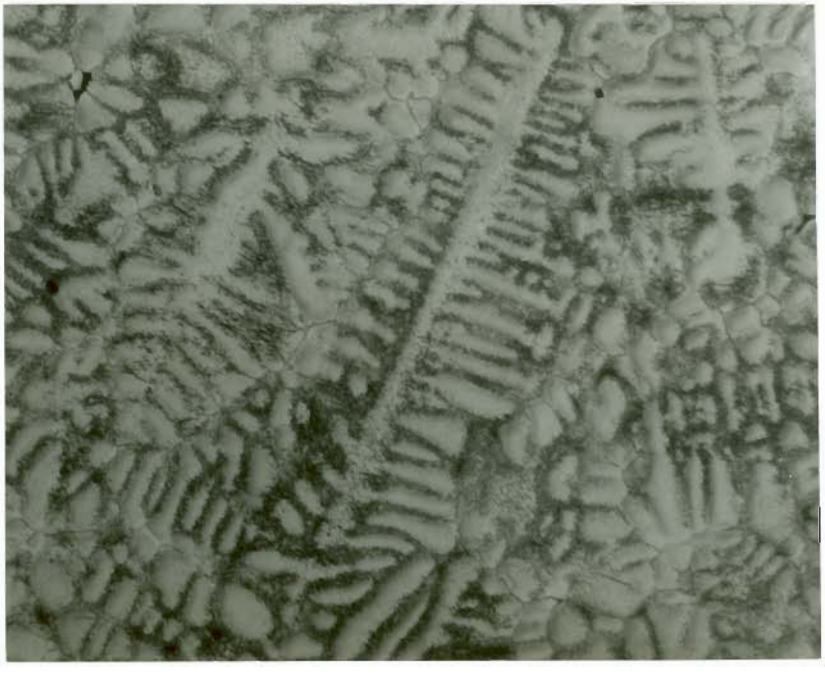

Figure C-20. LIGHT MICROGRAPH OF SOLIDIFICATION STRUCTURE OF SPECIMEN P-9 (79.7V-9.4Ti-10.9Fe), 256X.

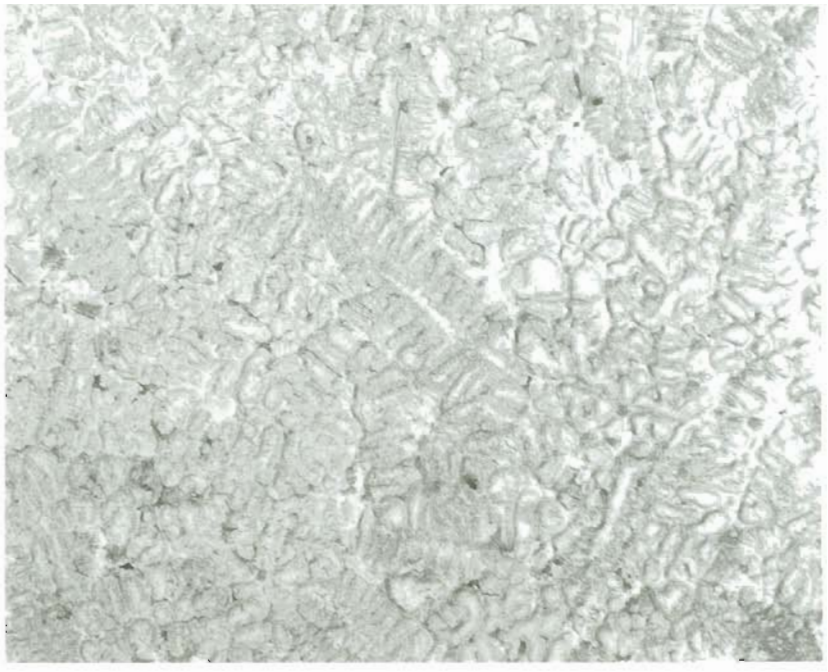

Figure C-21. LIGHT MICROGRAPH OF SOLIDIFICATION STRUCTURE OF SPECIMEN P-10 (79.1V-4.6Ti-16.3Fe), 104X.

Figure C-22. LIGHT MICROGRAPH OF SOLIDIFICATION STRUCTURE OF SPECIMEN P-10 (79.1V-4.6Ti-16.3Fe), 256X.

Figure C-23. LIGHT MICROGRAPH OF SOLIDIFICATION STRUCTURE OF SPECIMEN P-11 (78.5V-21.5Fe), 104X.

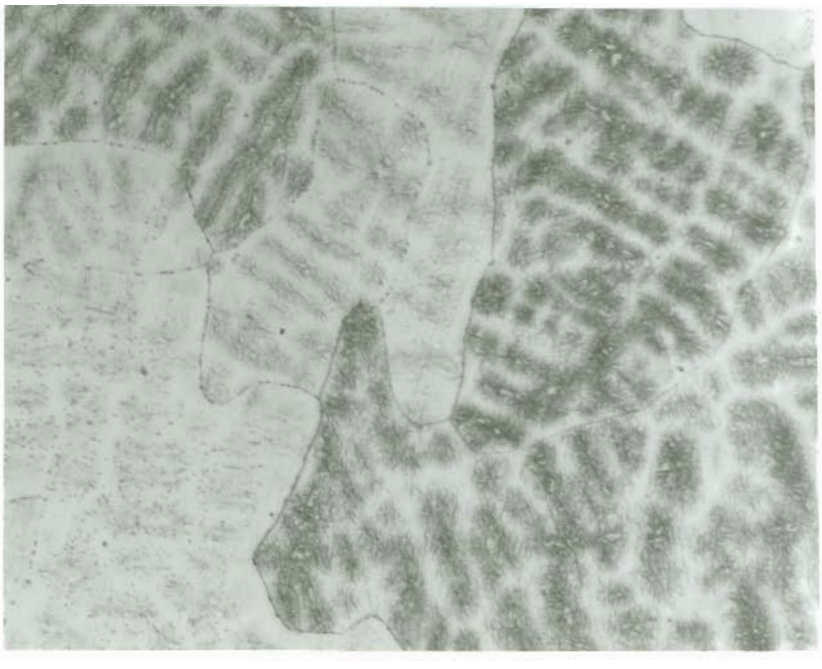

Figure C-24. LIGHT MICROGRAPH OF SOLIDIFICATION STRUCTURE OF SPECIMEN P-11 (78.5V-21.5Fe), 256X.

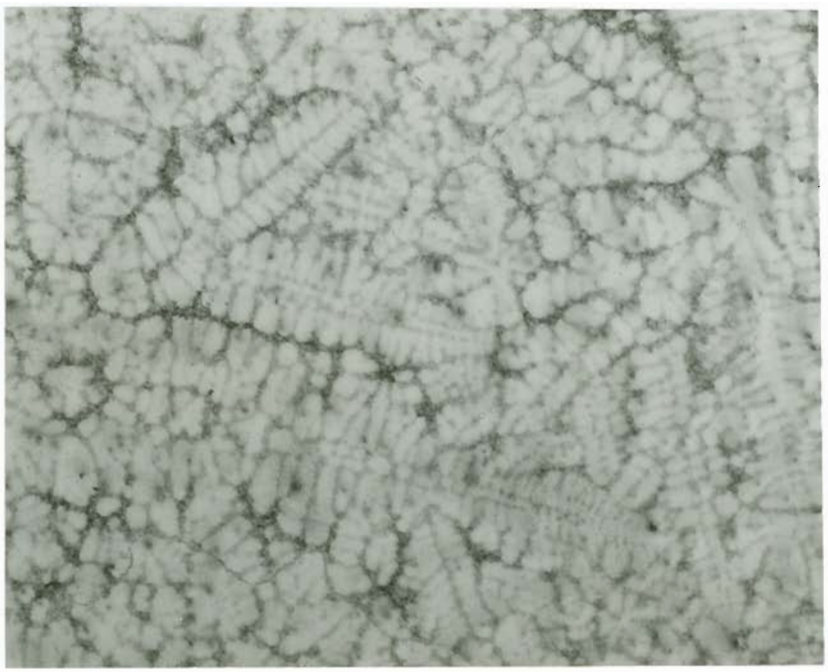

Figure C-25. LIGHT MICROGRAPH OF SOLIDIFICATION STRUCTURE OF SPECIMEN P-12 (71.3V-28.7Ti), 104X.

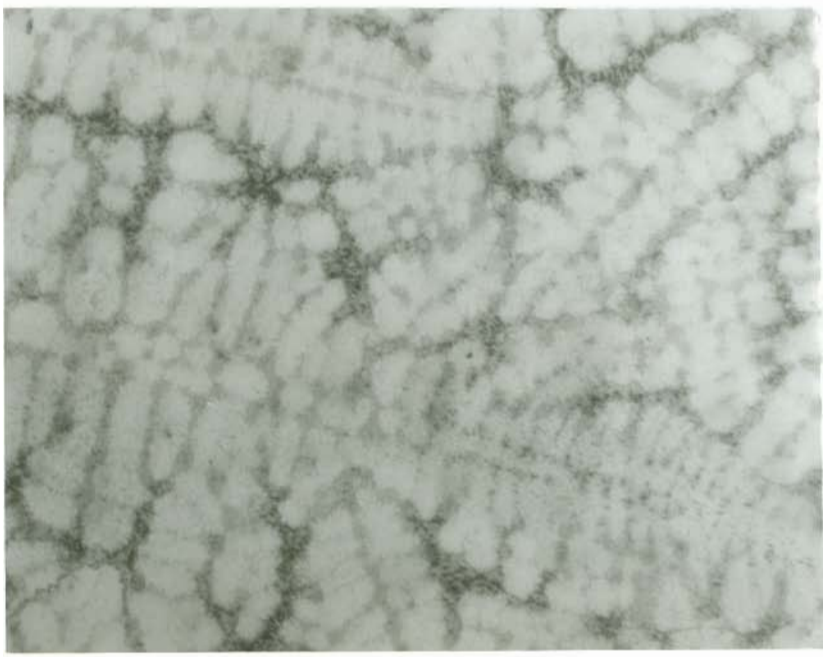

Figure C-26. LIGHT MICROGRAPH OF SOLIDIFICATION STRUCTURE OF SPECIMEN P-12 (71.3V-28.7Ti), 256X.

Figure C-27. LIGHT MICROGRAPH OF SOLIDIFICATION STRUCTURE OF SPECIMEN P-13 (70.4V-21.3Ti-8.3Fe), 104X.

Figure C-28. LIGHT MICROGRAPH OF SOLIDIFICATION STRUCTURE OF SPECIMEN P-13 (70.4V-21.3Ti-8.3Fe), 256X.

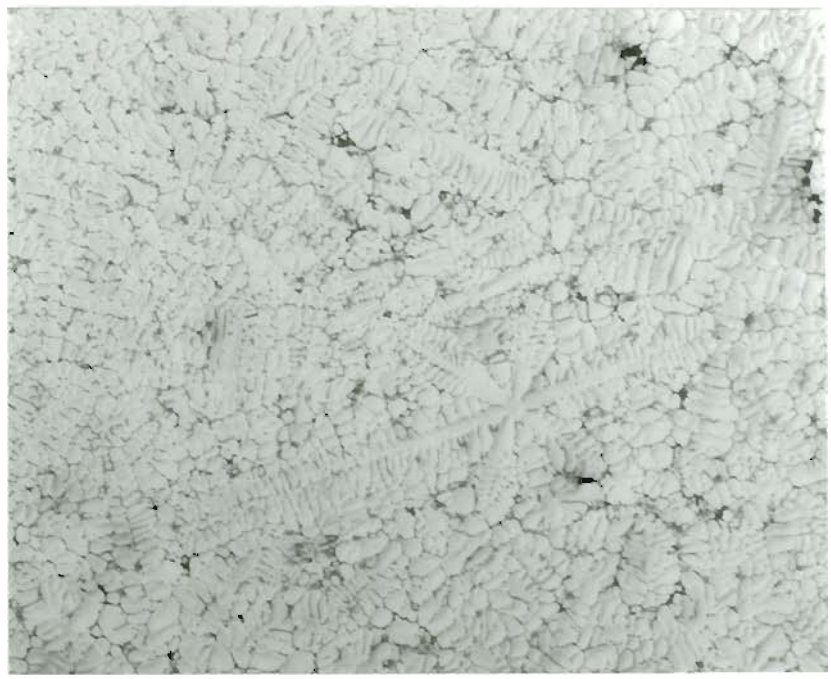

Figure C-29. LIGHT MICROGRAPH OF SOLIDIFICATION STRUCTURE OF SPECIMEN P-14 (69.6V-14.0Ti-16.4Fe), 104X.

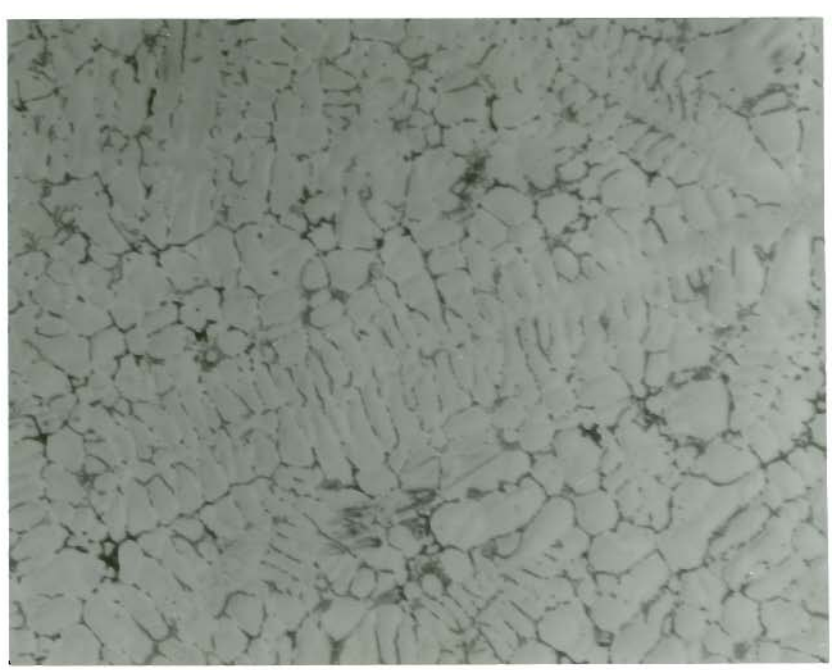

Figure C-30. LIGHT MICROGRAPH OF SOLIDIFICATION STRUCTURE OF SPECIMEN P-14 (69.6V-14.0Ti-16.4Fe), 256X.

Figure C-31. LIGHT MICROGRAPH OF SOLIDIFICATION STRUCTURE OF SPECIMEN P-15 (68.8V-6.9Ti-24.3Fe), 104X.

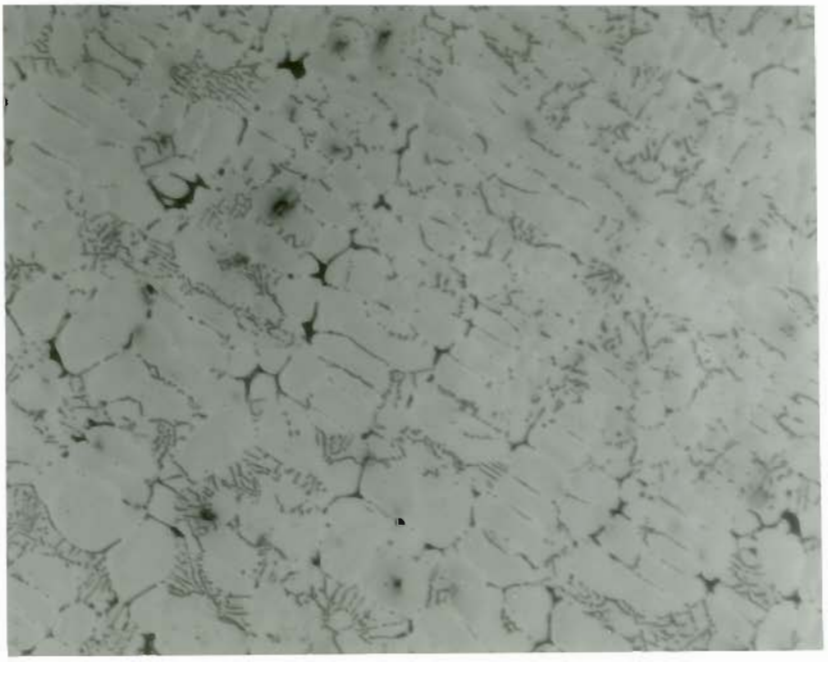

Figure C-32. LIGHT MICROGRAPH OF SOLIDIFICATION STRUCTURE OF SPECIMEN P-15 (68.8V-6.9Ti-24.3Fe), 256X.

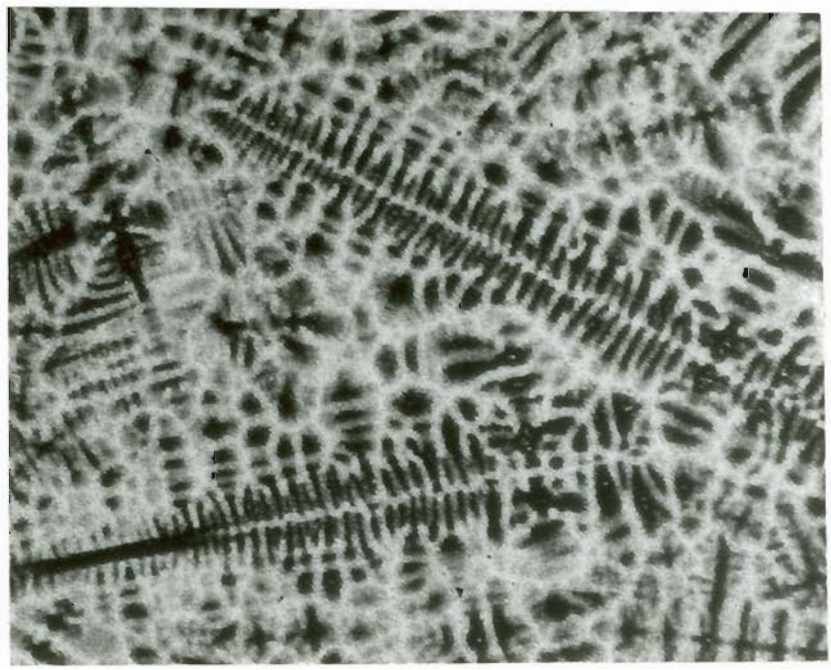

Figure C-33. LIGHT MICROGRAPH OF SOLIDIFICATION STRUCTURE OF SPECIMEN P-16 (68.0V-32.0Fe), 104X.

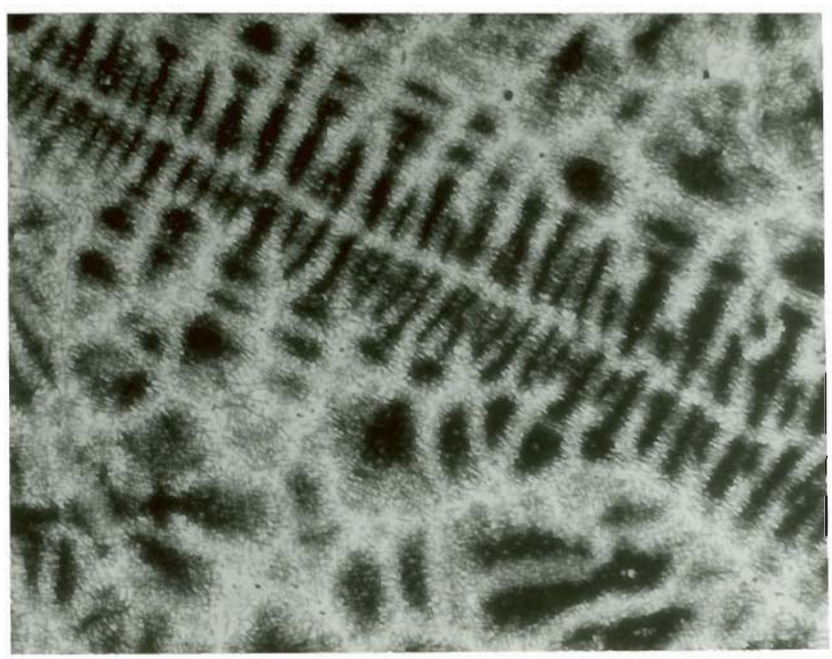

Figure C-34. LIGHT MICROGRAPH OF SOLIDIFICATION STRUCTURE OF SPECIMEN P-16 (68.0V-32.0Fe), 256X.

Figure C-35. LIGHT MICROGRAPH OF SOLIDIFICATION STRUCTURE OF SPECIMEN P-17 (61.5V-38.5Ti), 104X.

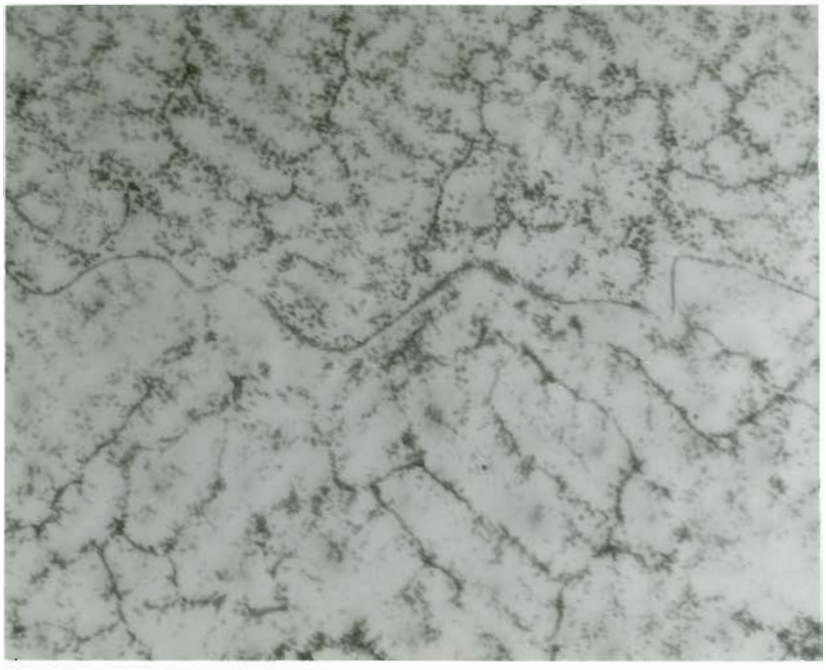

Figure C-36. LIGHT MICROGRAPH OF SOLIDIFICATION STRUCTURE OF SPECIMEN P-17 (61.5V-38.5Ti), 256X.

Figure C-37. LIGHT MICROGRAPH OF SOLIDIFICATION STRUCTURE OF SPECIMEN P-18 (60.5V-28.4Ti-11.1Fe), 104X.

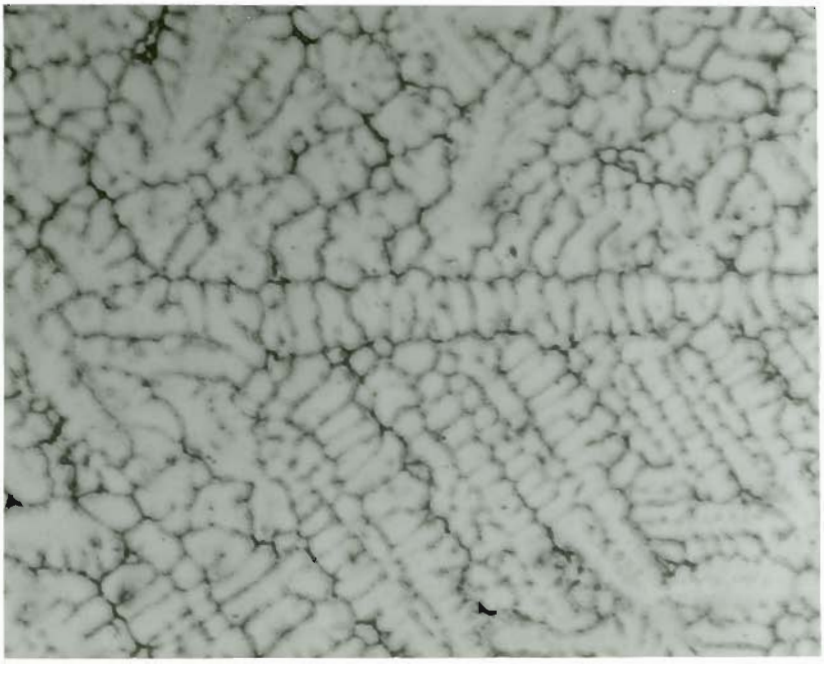

Figure C-38. LIGHT MICROGRAPH OF SOLIDIFICATION STRUCTURE OF SPECIMEN P-18 (60.5V-28.4Ti-11.1Fe), 256X.

Figure C-39. LIGHT MICROGRAPH OF SOLIDIFICATION STRUCTURE OF SPECIMEN P-19 (59.5V-18.7Ti-21.8Fe), 104X.

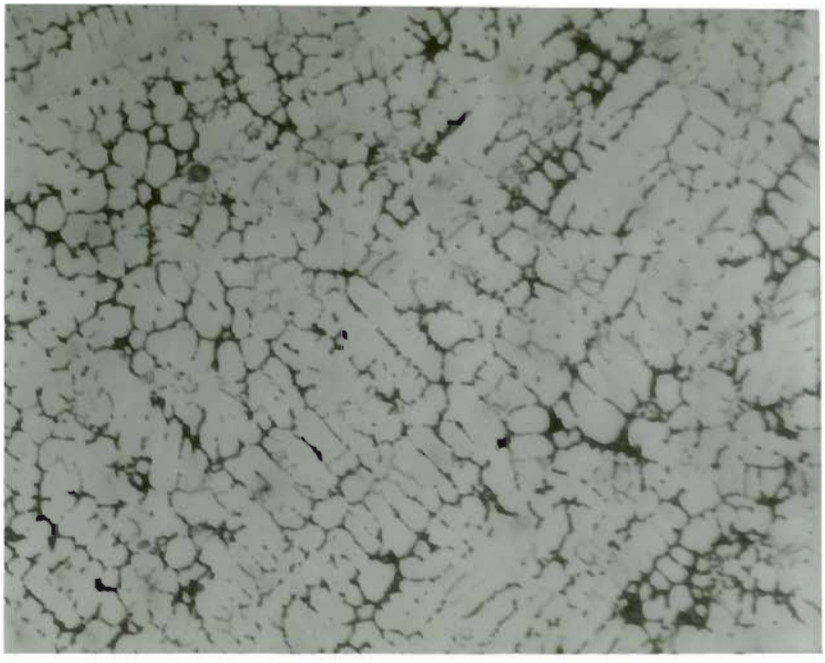

Figure C-40. LIGHT MICROGRAPH OF SOLIDIFICATION STRUCTURE OF SPECIMEN P-19 (59.5V-18.7Ti-21.8Fe), 256X.

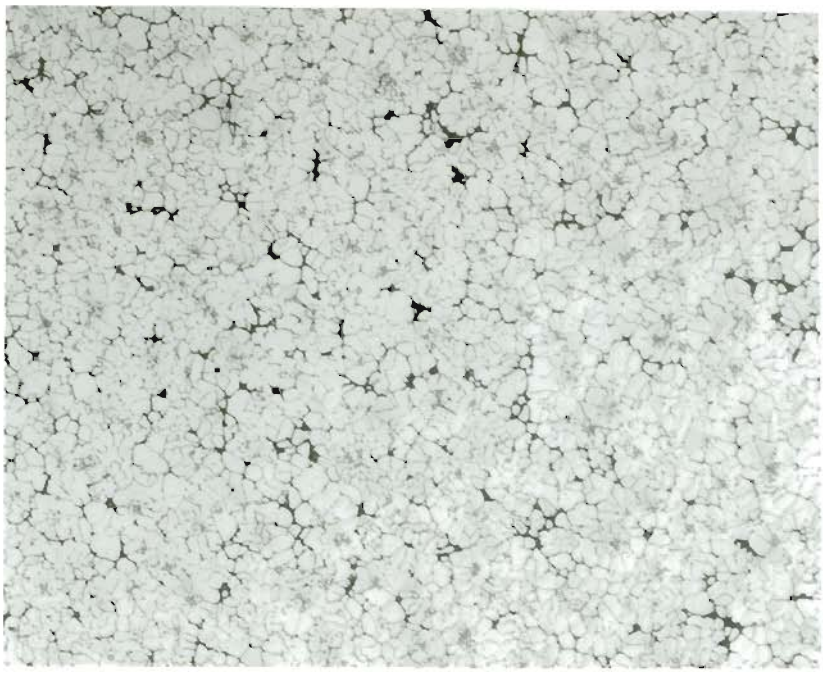

Figure C-41. LIGHT MICROGRAPH OF SOLIDIFICATION STRUCTURE OF SPECIMEN P-20 (58.6V-9.2Ti-32.2Fe), 104X.

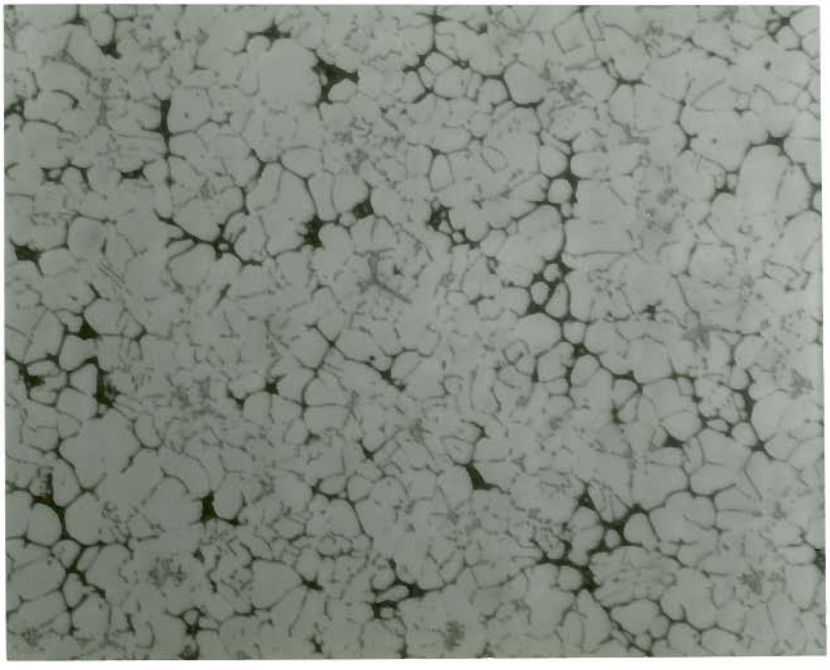

Figure C-42. LIGHT MICROGRAPH OF SOLIDIFICATION STRUCTURE OF SPECIMEN P-20 (58.6V-9.2Ti-32.2Fe), 256X.

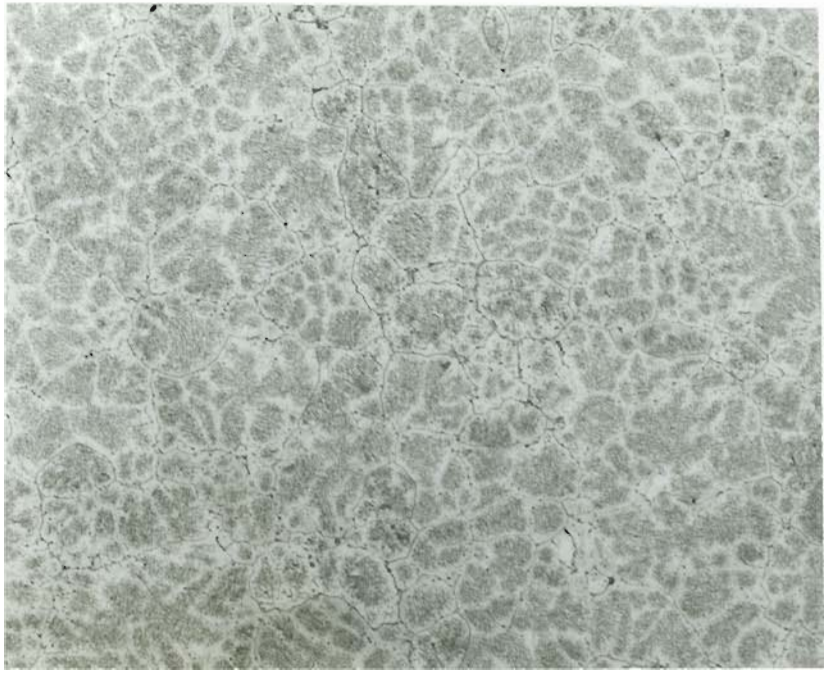

Figure C-43. LIGHT MICROGRAPH OF SOLIDIFICATION STRUCTURE OF SPECIMEN P-21 (57.8V-42.2Fe), 104X.

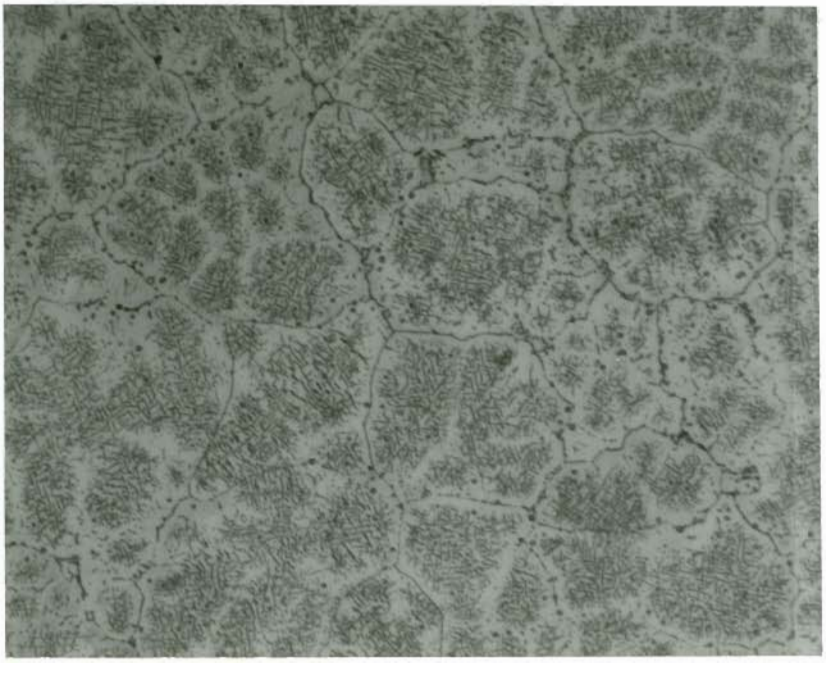

Figure C-44. LIGHT MICROGRAPH OF SOLIDIFICATION STRUCTURE OF SPECIMEN P-21 (57.8V-42.2Fe), 256X.

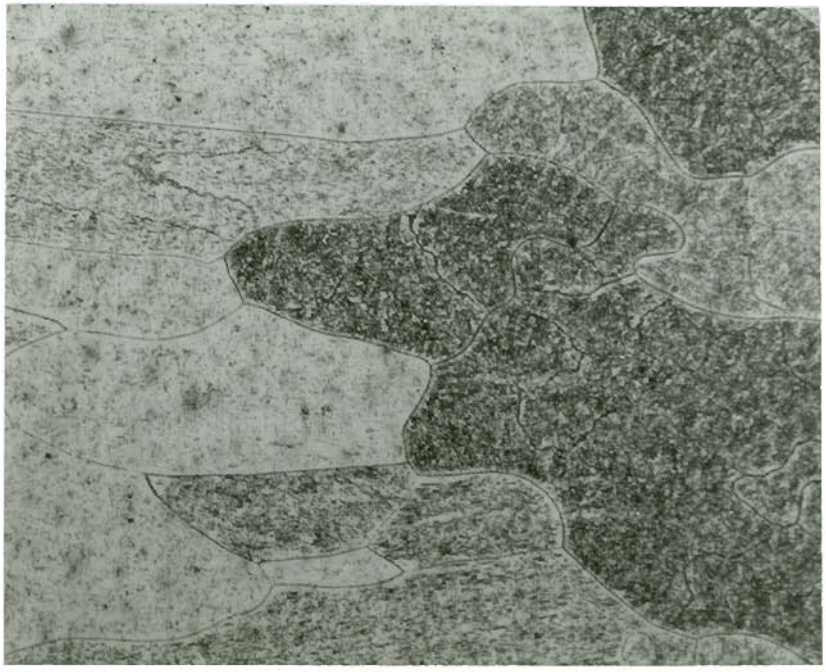

Figure C-45. LIGHT MICROGRAPH OF SOLIDIFICATION STRUCTURE OF SPECIMEN P-22 (51.5V-48.5Ti), 104X.

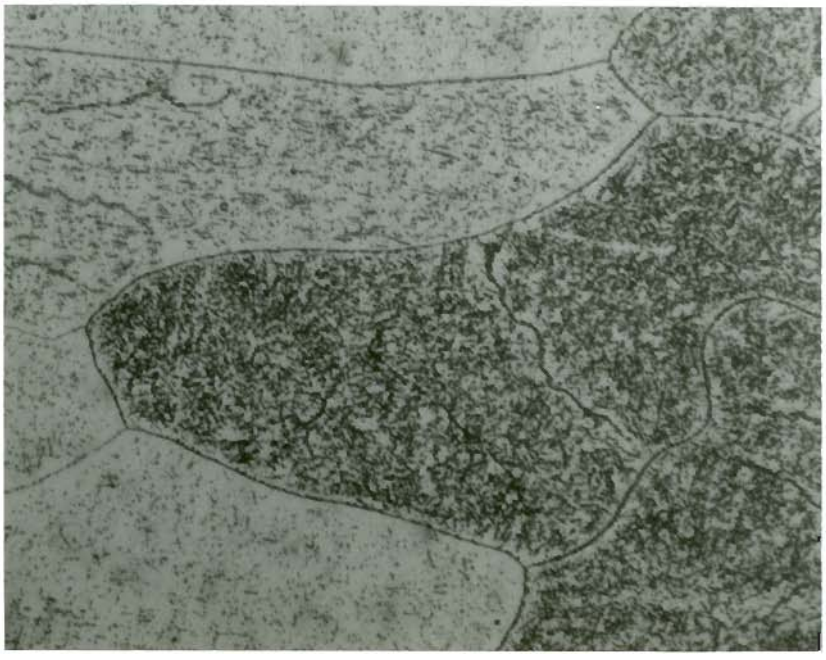

Figure C-46. LIGHT MICROGRAPH OF SOLIDIFICATION STRUCTURE OF SPECIMEN P-22 (51.5V-48.5Ti), 256X.

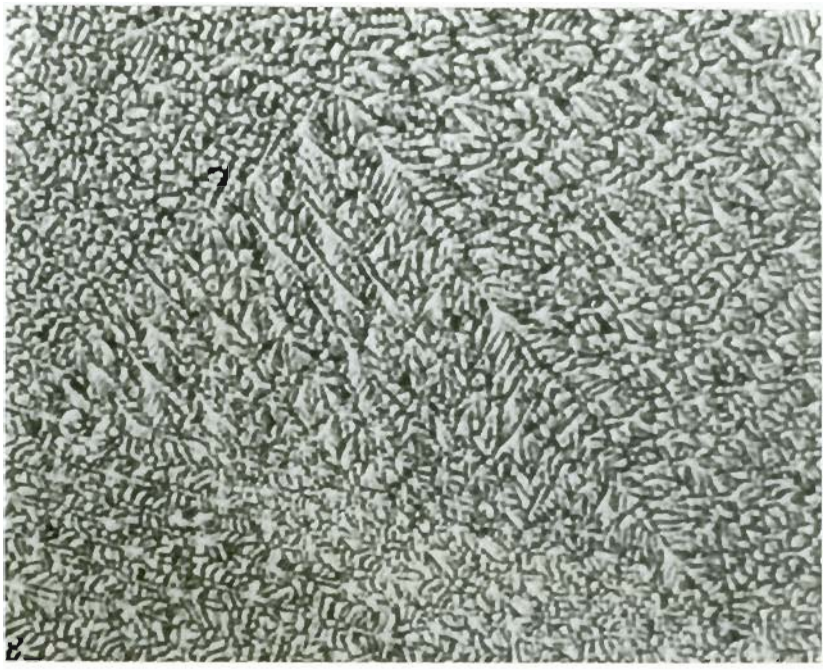

Figure C-47. LIGHT MICROGRAPH OF SOLIDIFICATION STRUCTURE OF SPECIMEN P-23 (50.5V-35.6Ti-13.9Fe), 104X.

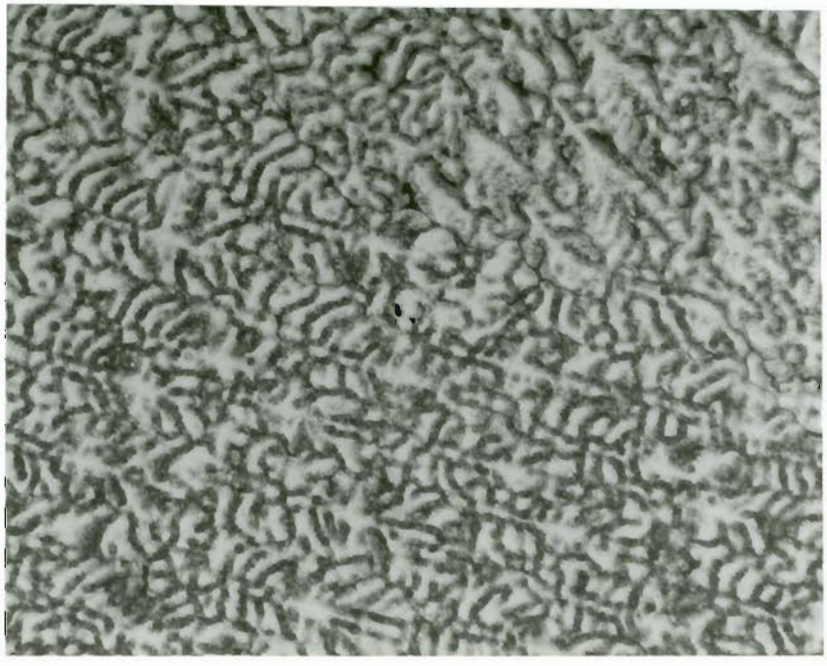

Figure C-48. LIGHT MICROGRAPH OF SOLIDIFICATION STRUCTURE OF SPECIMEN P-23 (50.5V-35.6Ti-13.9Fe), 256X.

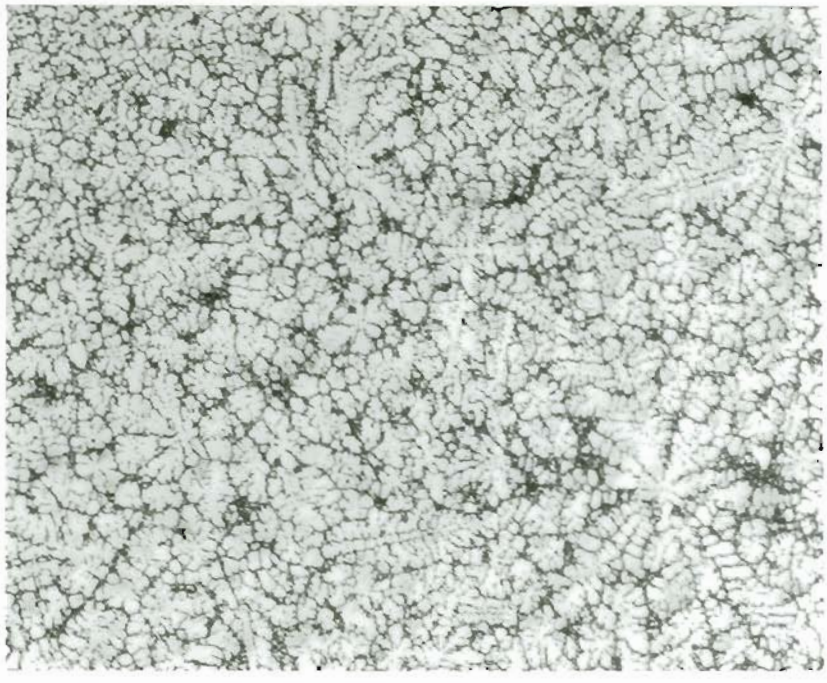

Figure C-49. LIGHT MICROGRAPH OF SOLIDIFICATION STRUCTURE OF SPECIMEN P-24 (49.5V-23.3Ti-27.2Fe), 104X.

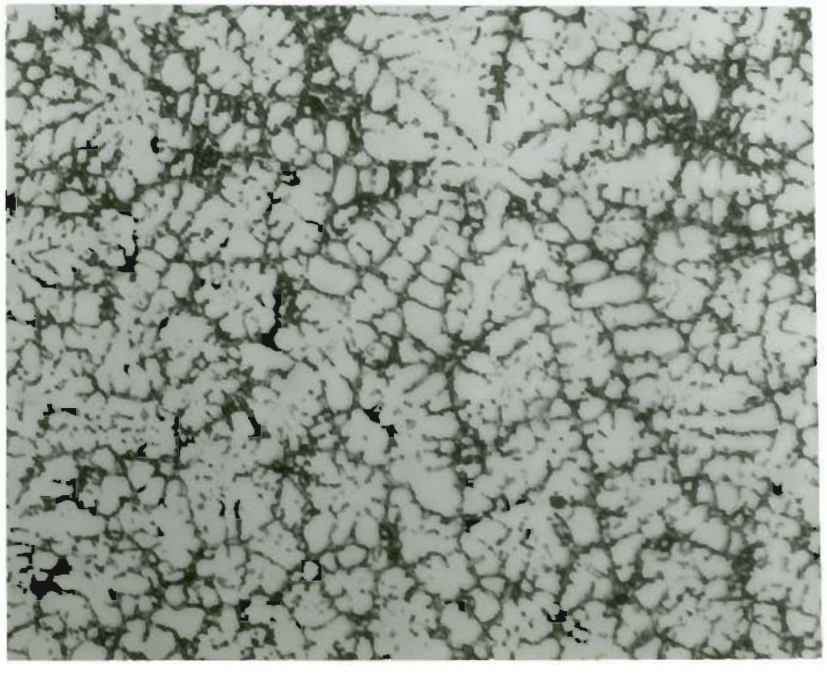

Figure C-50. LIGHT MICROGRAPH OF SOLIDIFICATION STRUCTURE OF SPECIMEN P-24 (49.5V-23.3Ti-27.2Fe), 256X.

Figure C-51. LIGHT MICROGRAPH OF SOLIDIFICATION STRUCTURE OF SPECIMEN P-25 (48.6V-11.4Ti-40.0Fe), 104X.

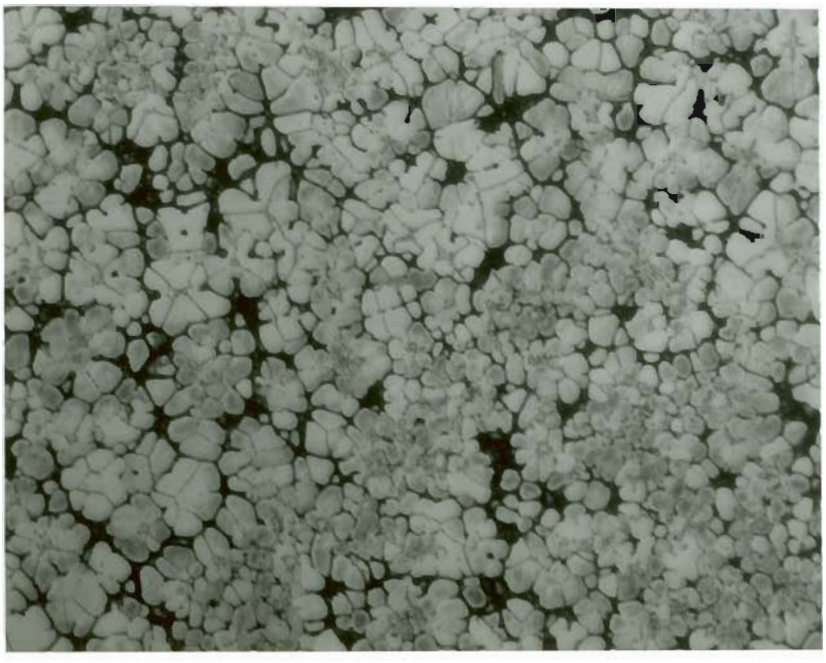

Figure C-52. LIGHT MICROGRAPH OF SOLIDIFICATION STRUCTURE OF SPECIMEN P-25 (48.6V-11.4Ti-40.0Fe), 256X.

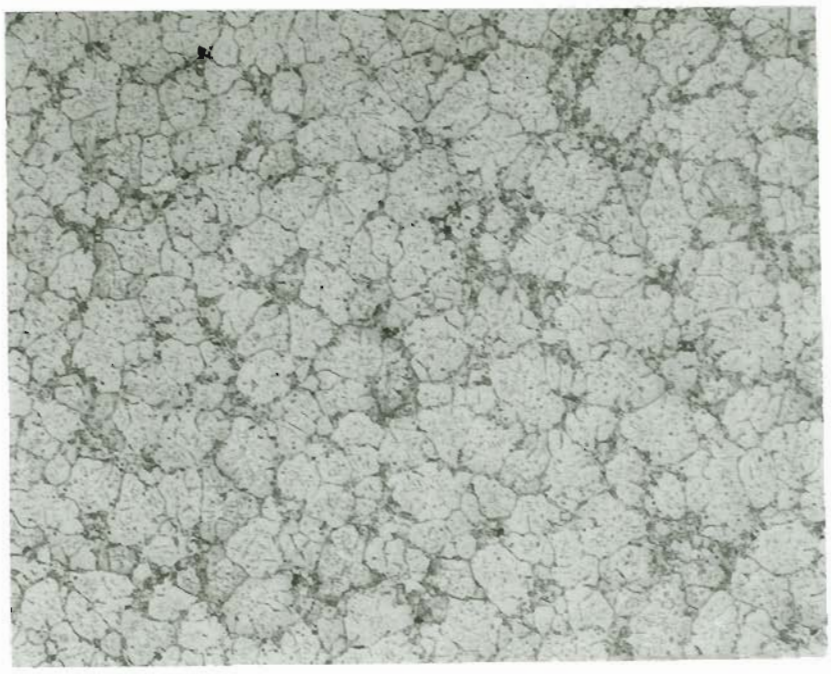

Figure C-53. LIGHT MICROGRAPH OF SOLIDIFICATION STRUCTURE OF SPECIMEN P-26 (47.7V-52.3Fe), 104X.

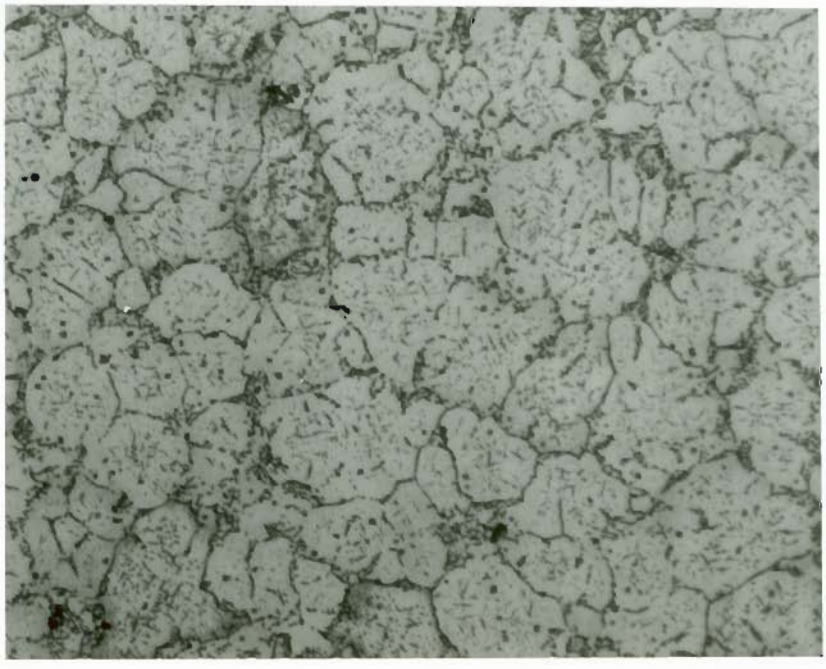

Figure C-54. LIGHT MICROGRAPH OF SOLIDIFICATION STRUCTURE OF SPECIMEN P-26 (47.7V-52.3Fe), 256X.

APPENDIX D

X-RAY DIFFRACTOMETRY TRACES

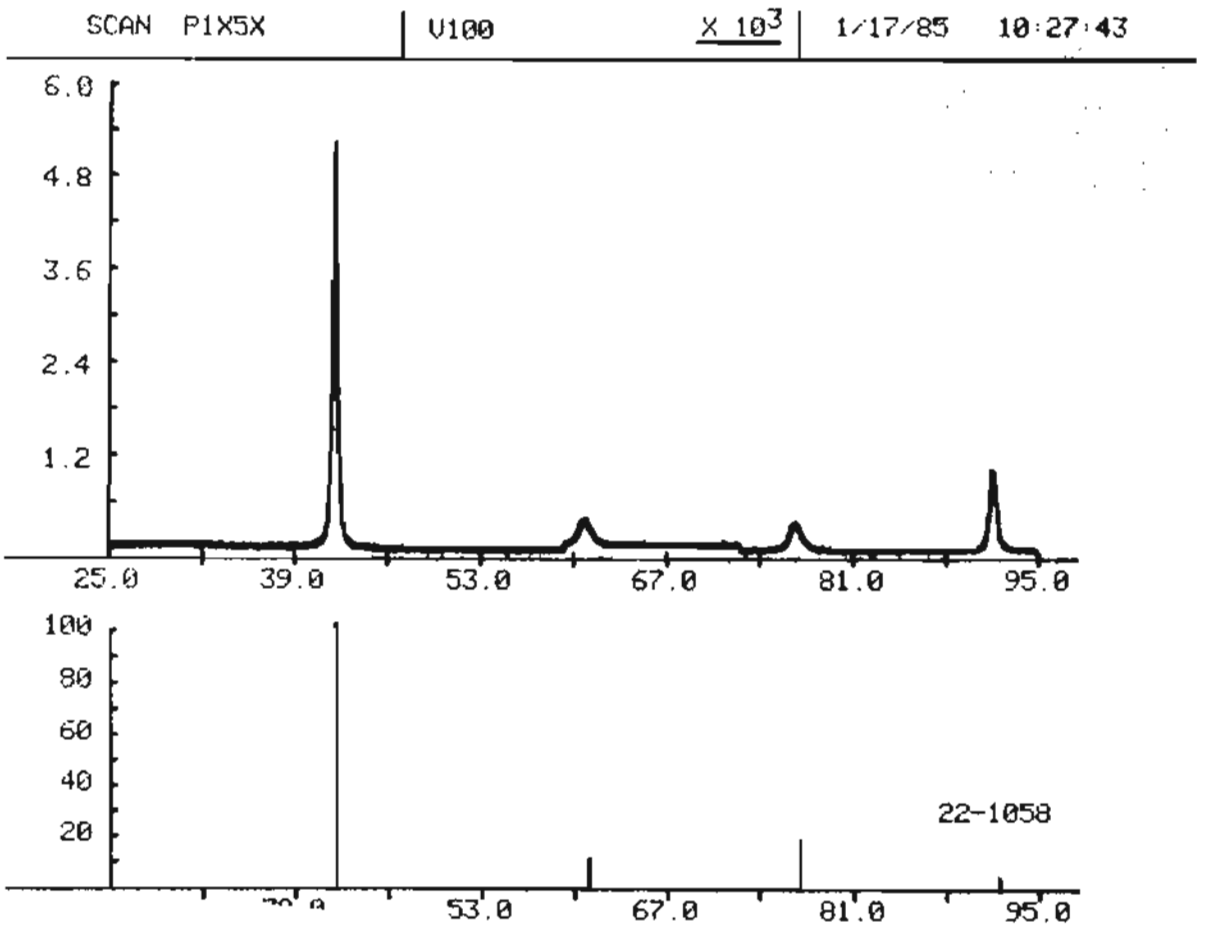

Figure D-1. X-RAY DIFFRACTOMETRY TRACE FOR SPECIMEN P-1 (100.0V).

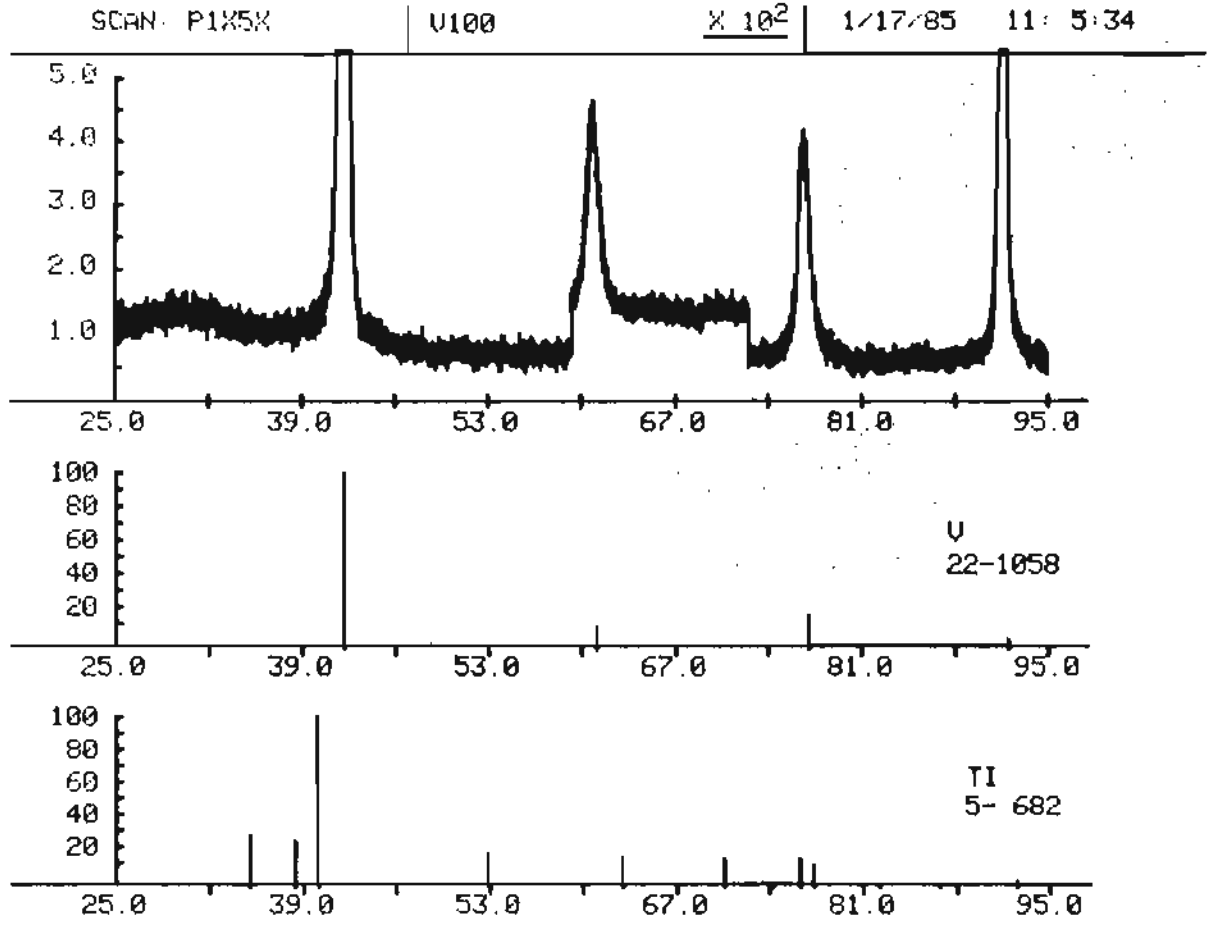

Figure D-2. X-RAY DIFFRACTOMETRY TRACE FOR SPECIMEN P-1 (100.0V).

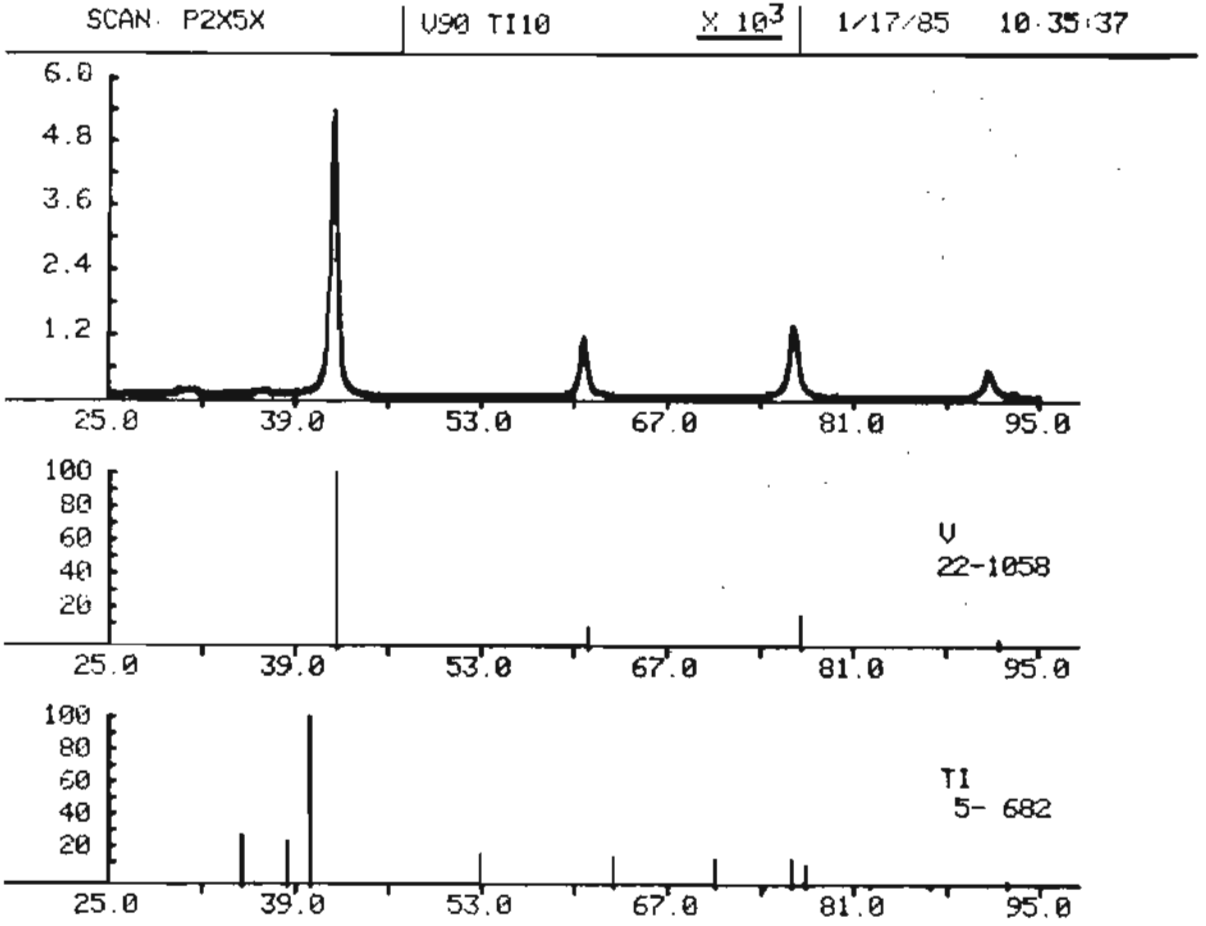

Figure D-3. X-RAY DIFFRACTOMETRY TRACE FOR SPECIMEN P-2 (90.5V-9.5Ti).

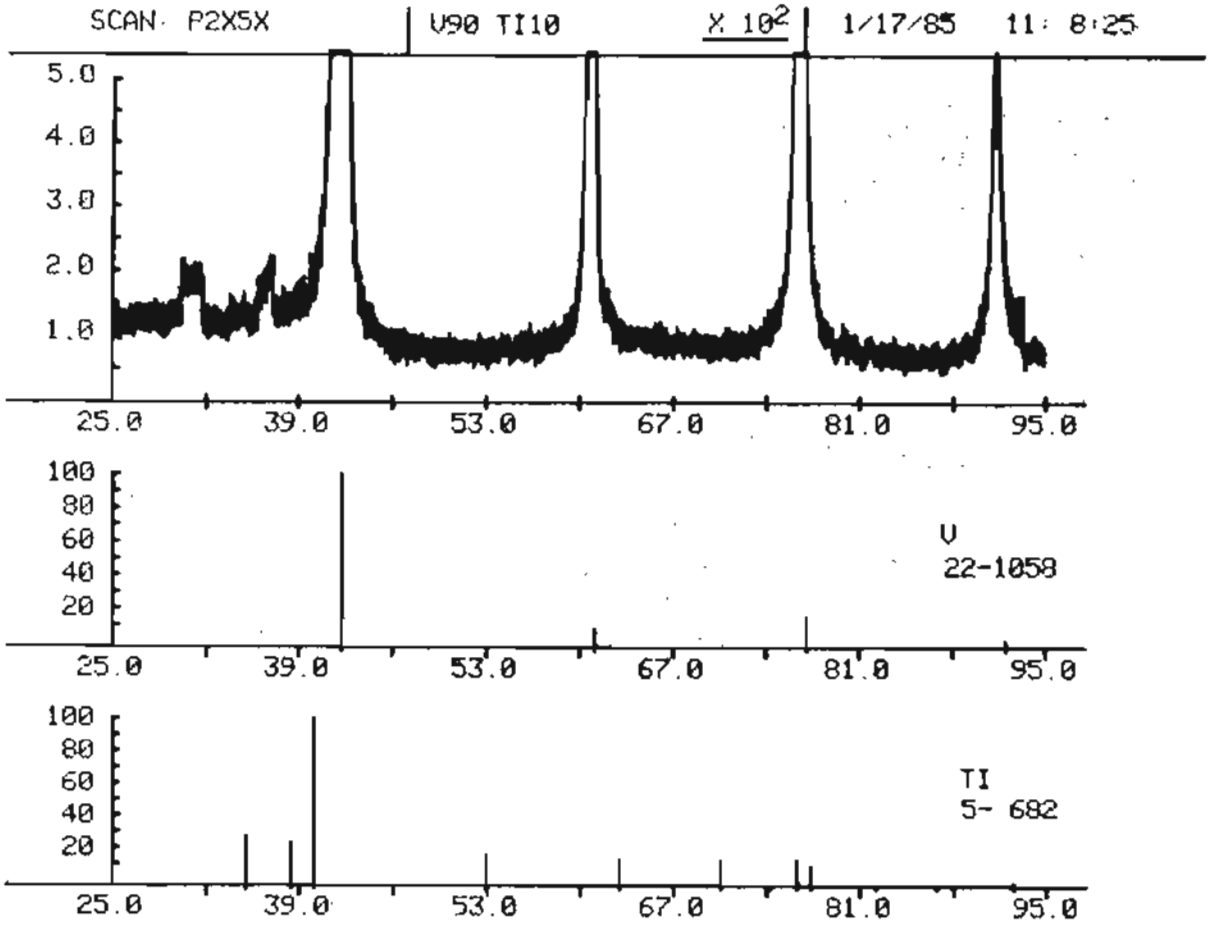

Figure D-4. X-RAY DIFFRACTOMETRY TRACE FOR SPECIMEN P-2 (90.5V-9.5Ti).

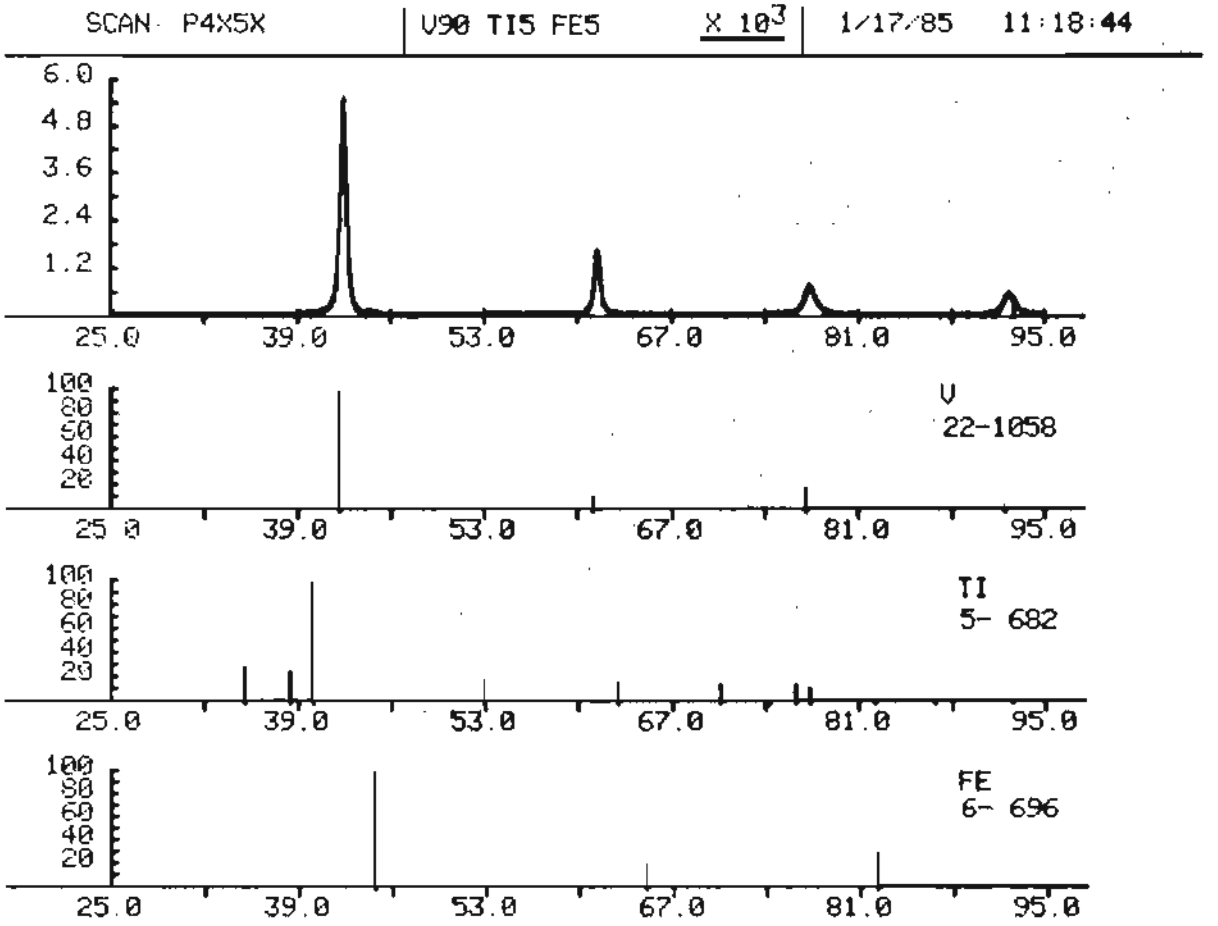

Figure D-5. X-RAY DIFFRACTOMETRY TRACE FOR SPECIMEN P-4 (89.8V-4.7Ti-5.5Fe).

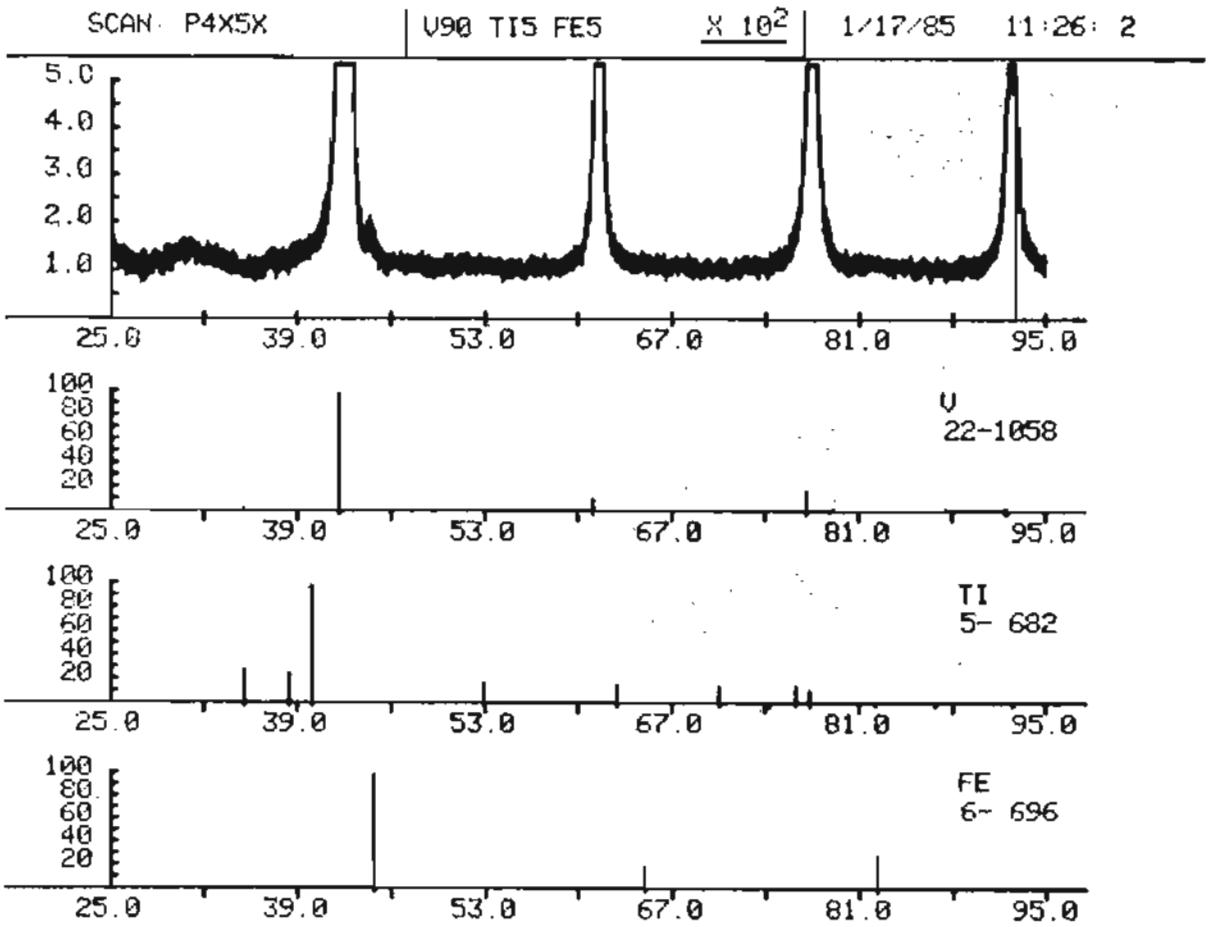

Figure D-6. X-RAY DIFFRACTOMETRY TRACE FOR SPECIMEN P-4 (89.8V-4.7Ti-5.5Fe).

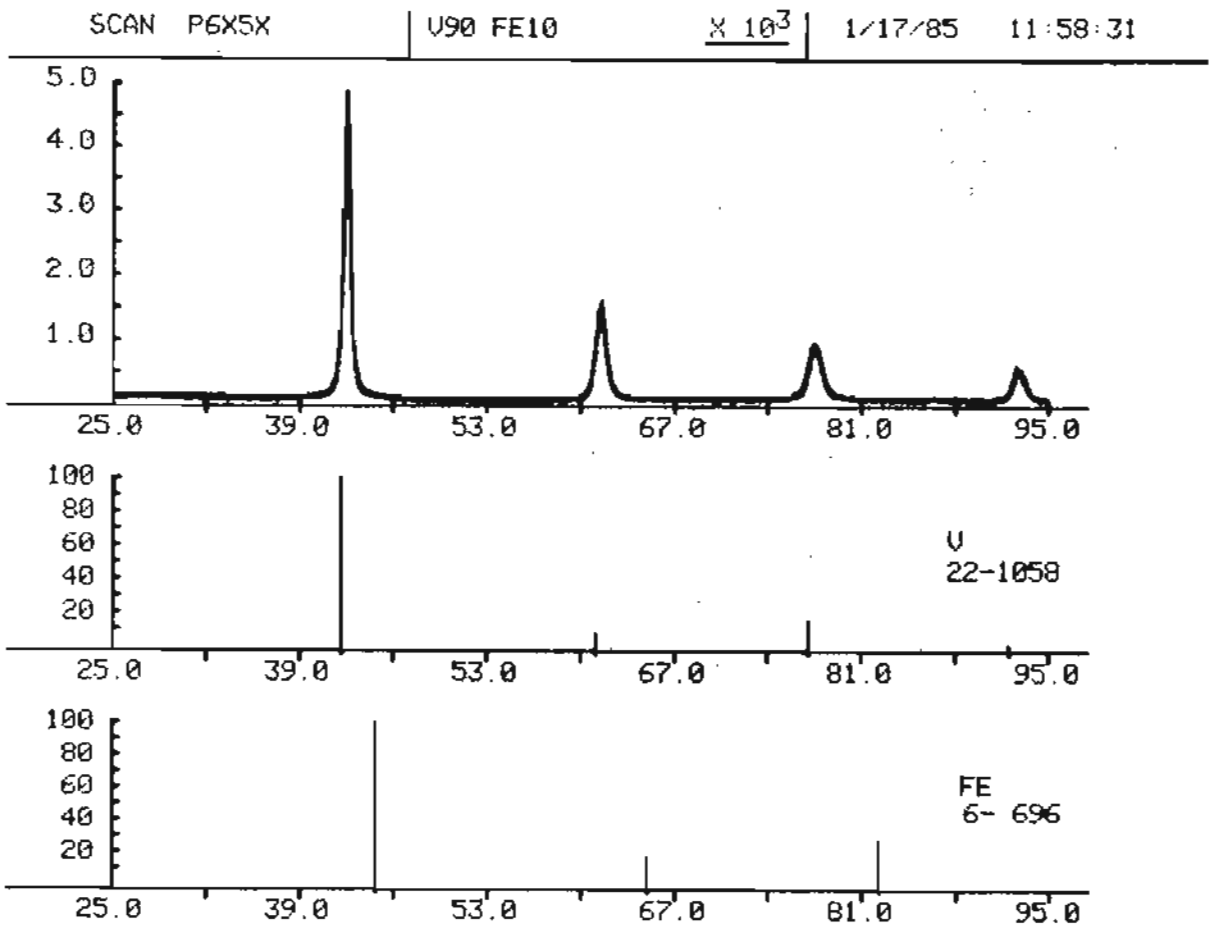

Figure D-7. X-RAY DIFFRACTOMETRY TRACE FOR SPECIMEN P-6 (89.1V-10.9Fe).

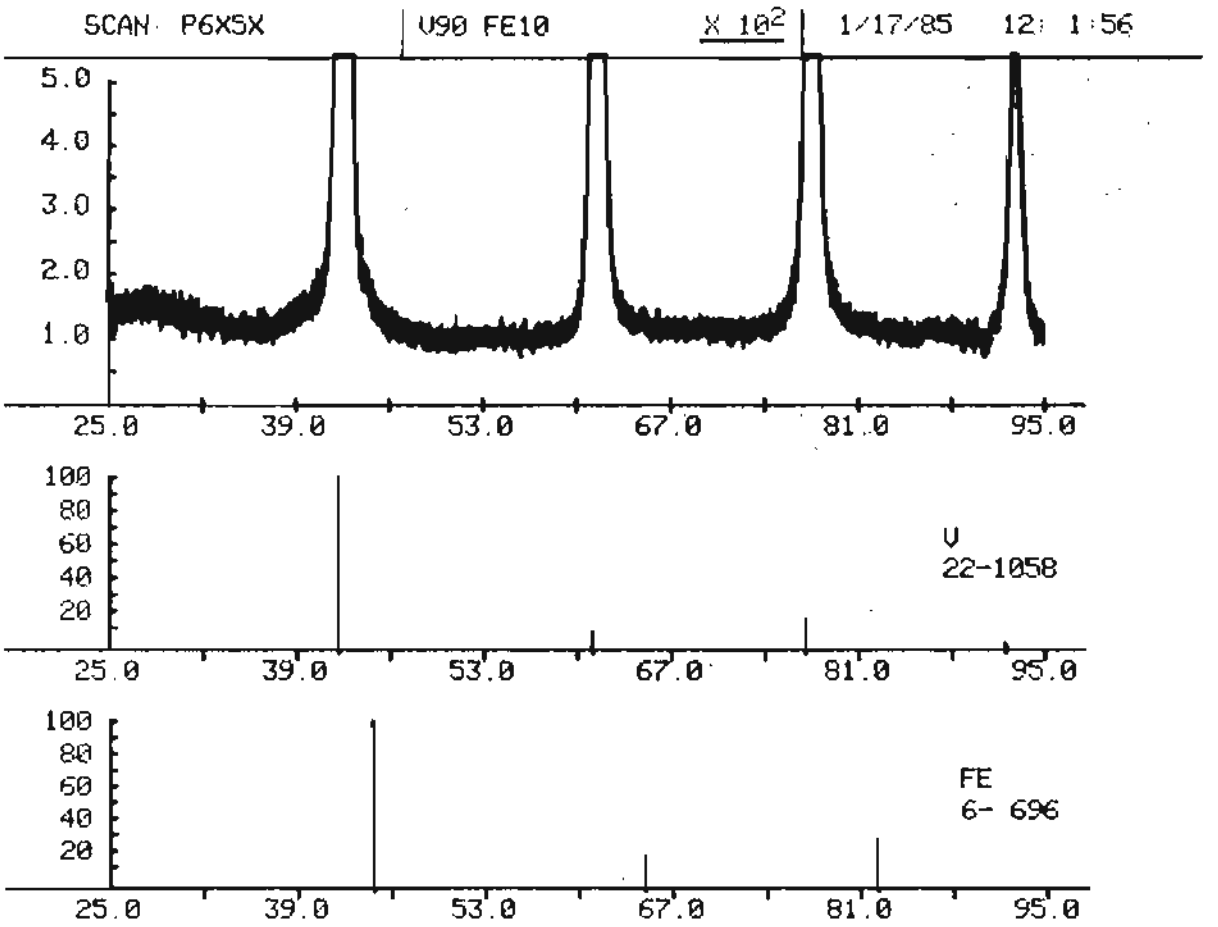

Figure D-8. X-RAY DIFFRACTOMETRY TRACE FOR SPECIMEN P-6 (89.1V-10.9Fe).

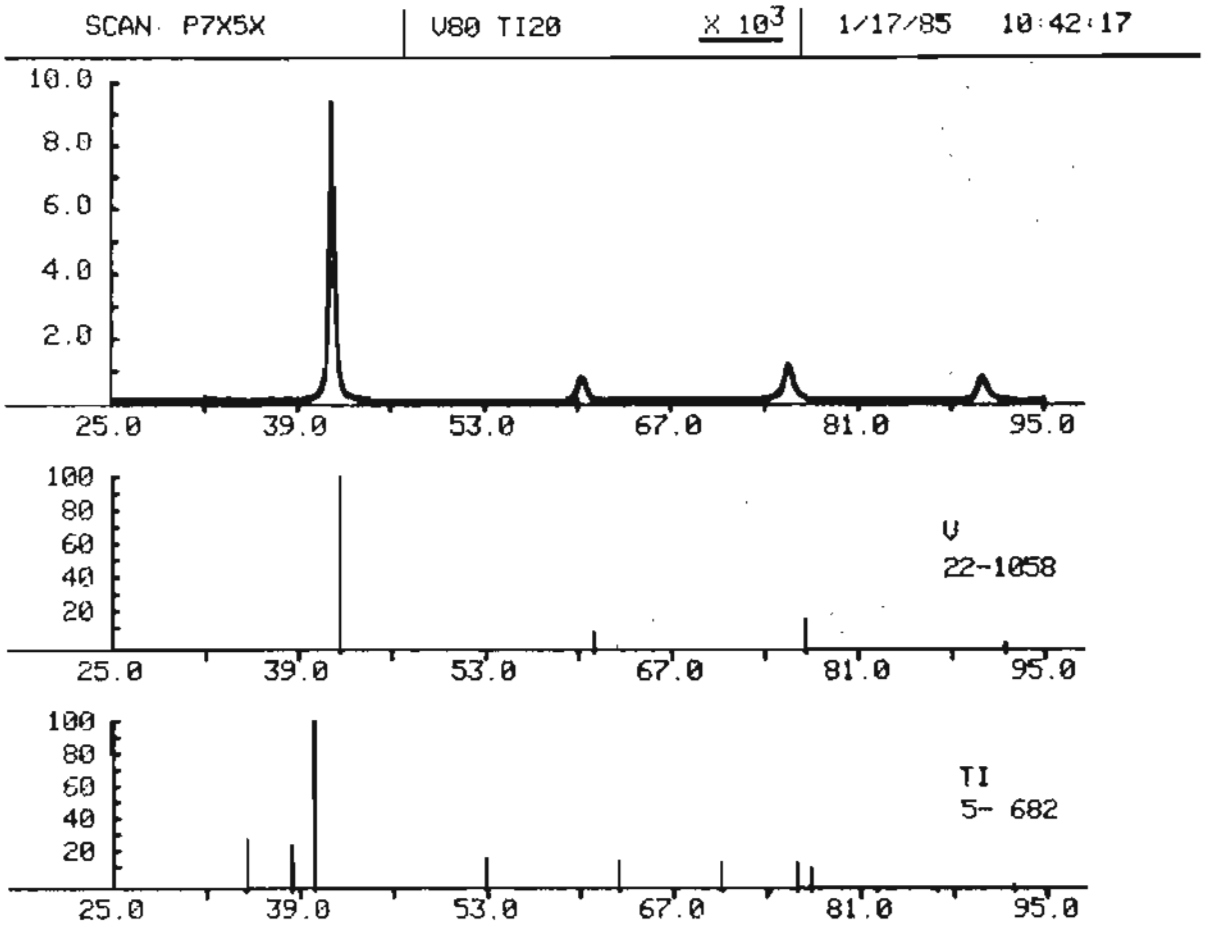

Figure D-9. X-RAY DIFFRACTOMETRY TRACE FOR SPECIMEN P-7 (81.0V-19.0Ti).

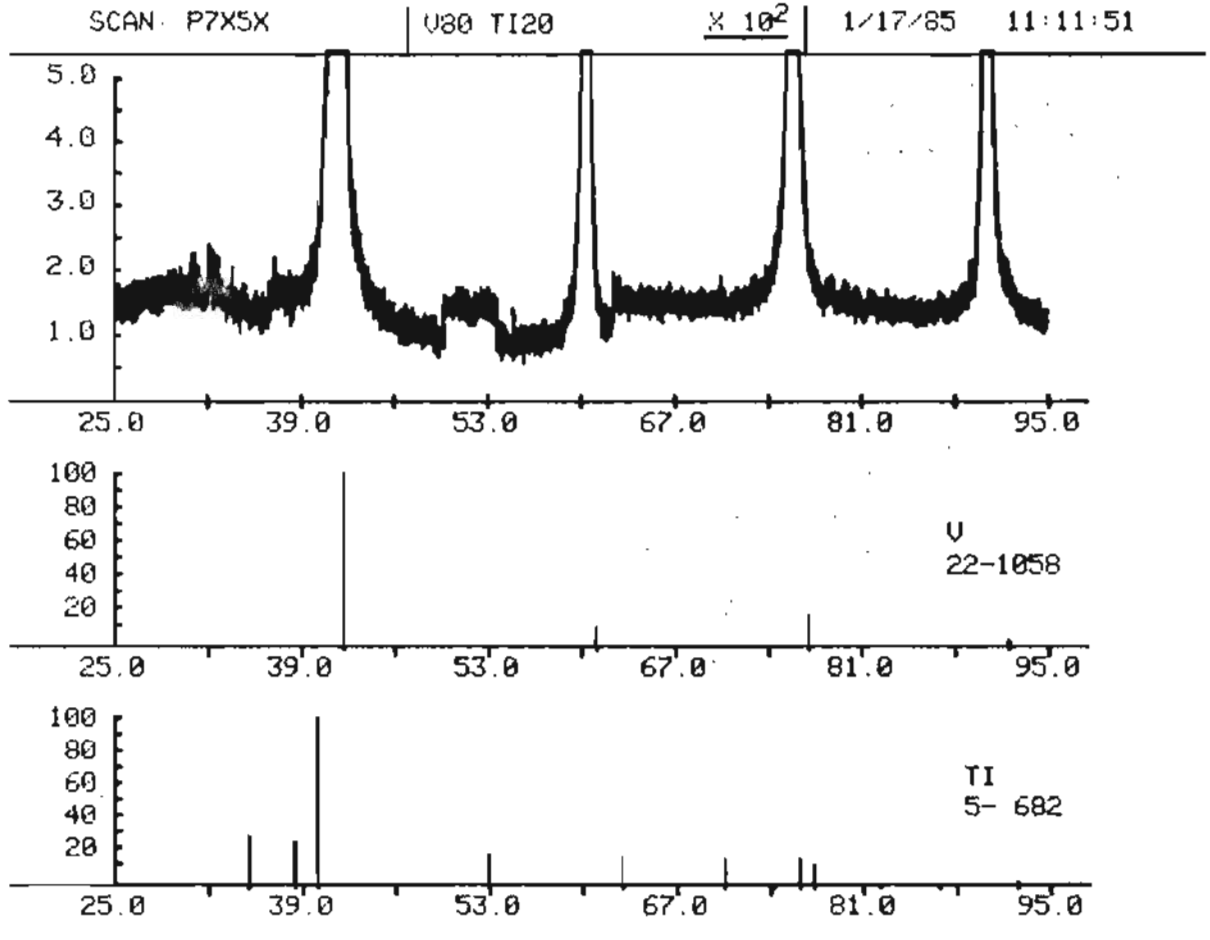

Figure D-10. X-RAY DIFFRACTOMETRY TRACE FOR SPECIMEN P-7 (81.0V-19.0Ti).

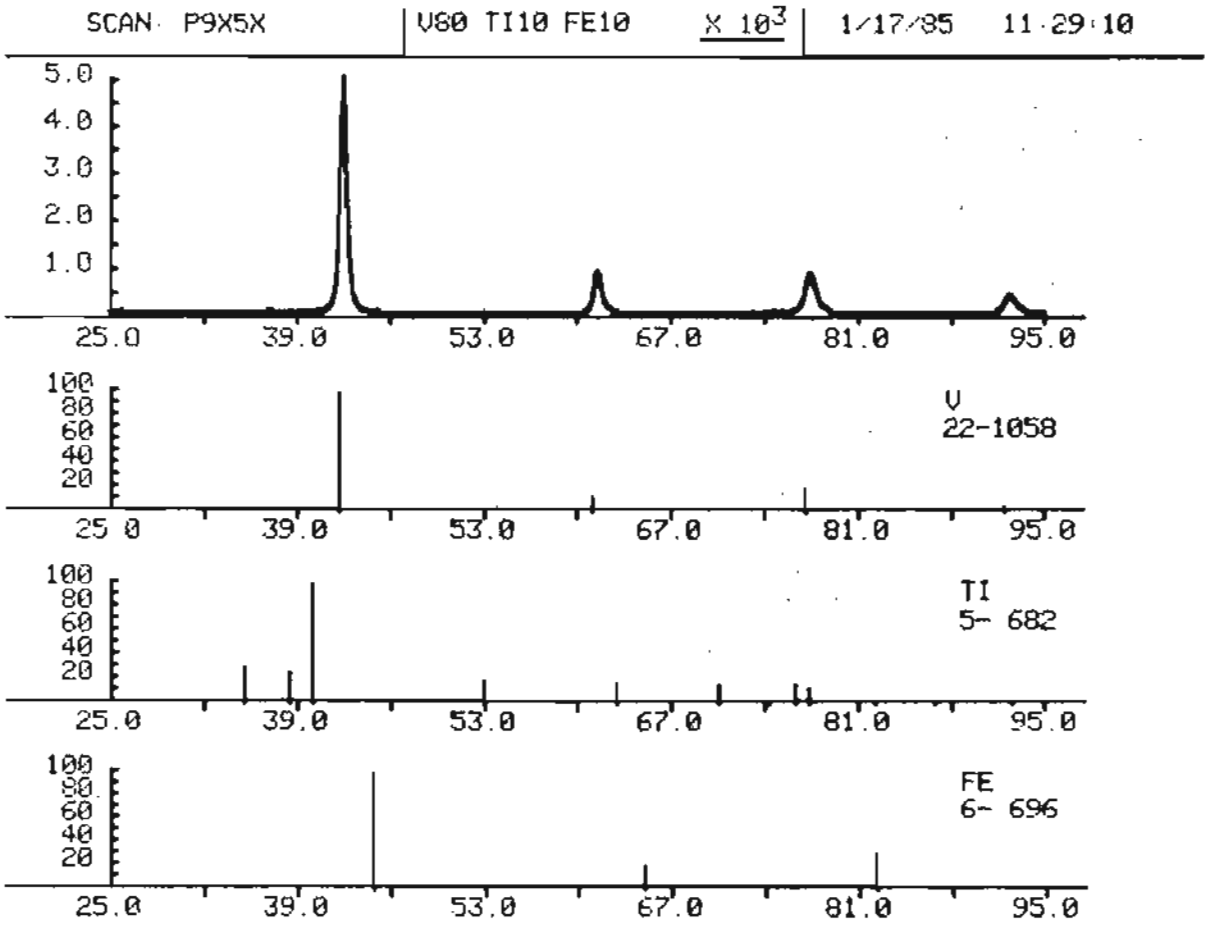

Figure D-11. X-RAY DIFFRACTOMETRY TRACE FOR SPECIMEN P-9 (79.7V-9.4Ti-10.9Fe).

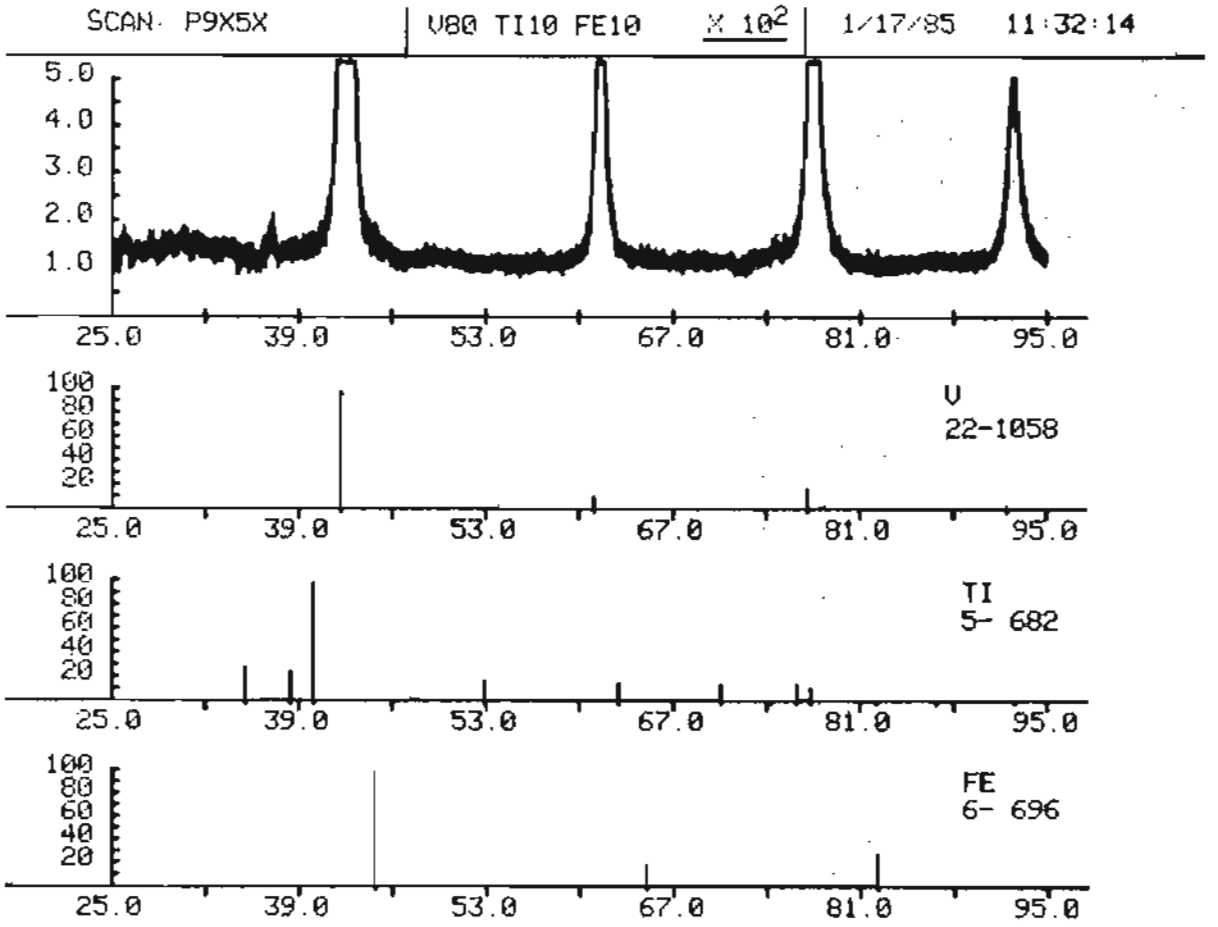

Figure D-12. X-RAY DIFFRACTOMETRY TRACE FOR SPECIMEN P-9 (79.7V-9.4Ti-10.9Fe).

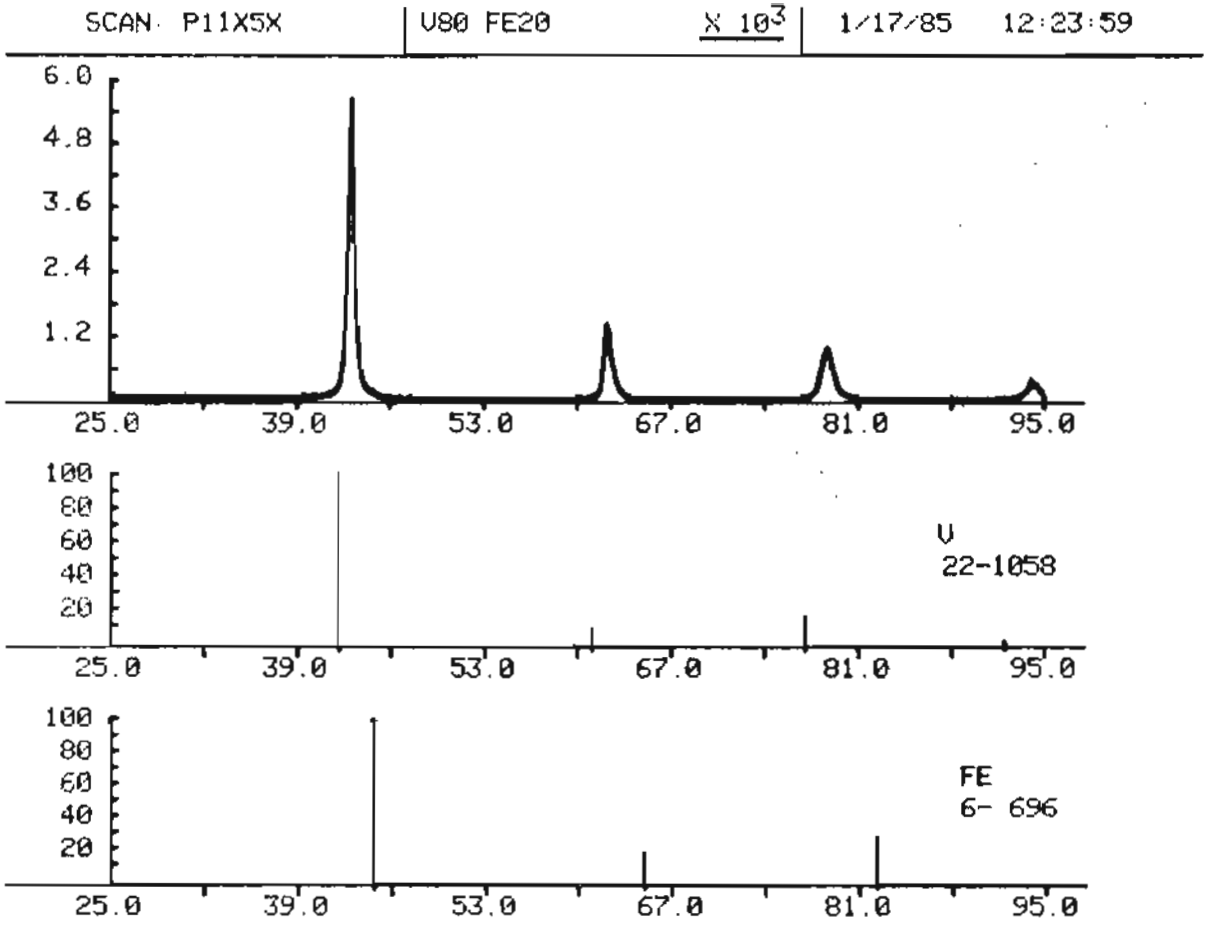

Figure D-13. X-RAY DIFFRACTOMETRY TRACE FOR SPECIMEN P-11 (78.5V-21.5Fe).

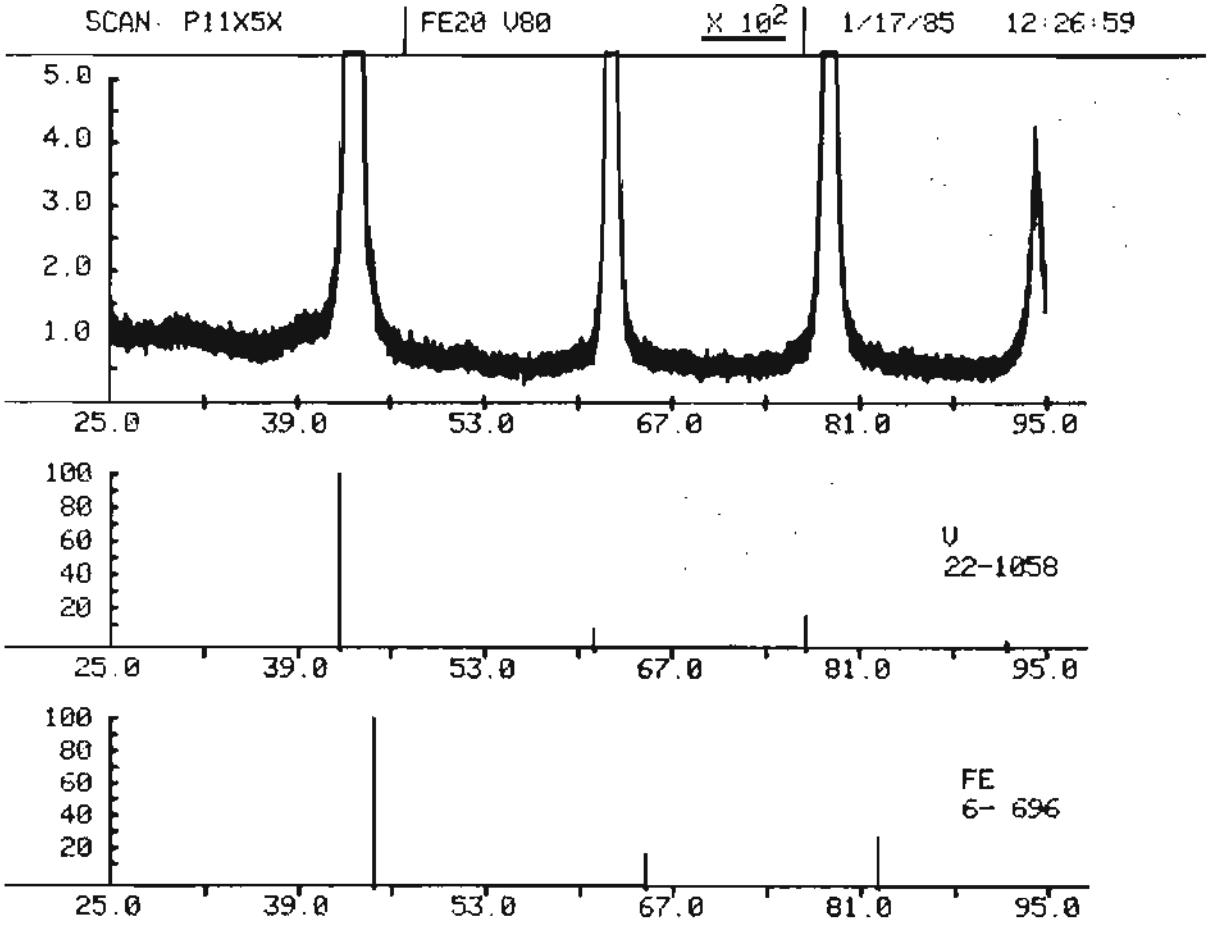

Figure D-14. X-RAY DIFFRACTOMETRY TRACE FOR SPECIMEN P-11 (78.5V-21.5Fe).

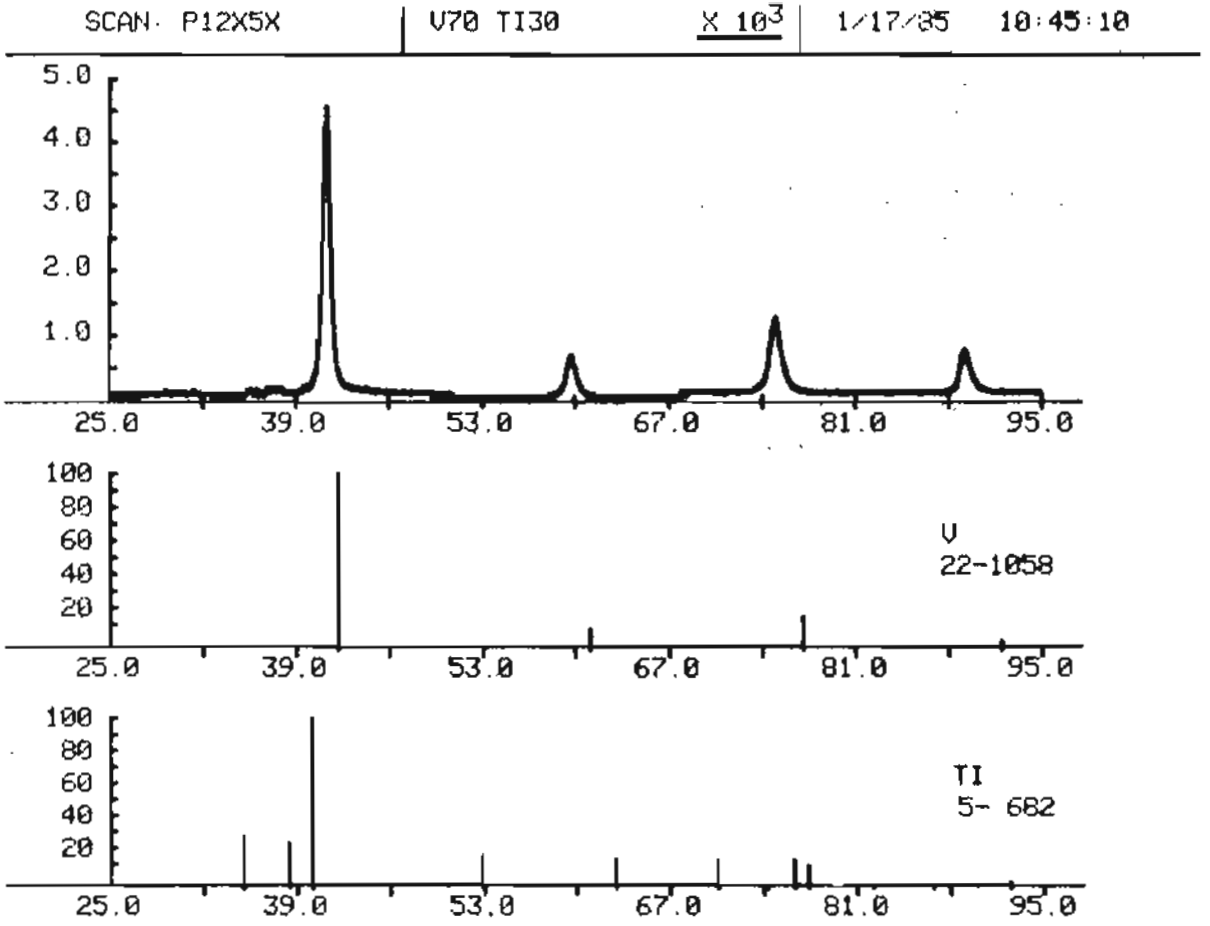

Figure D-15. X-RAY DIFFRACTOMETRY TRACE FOR SPECIMEN P-12 (71.3V-28.7Ti).

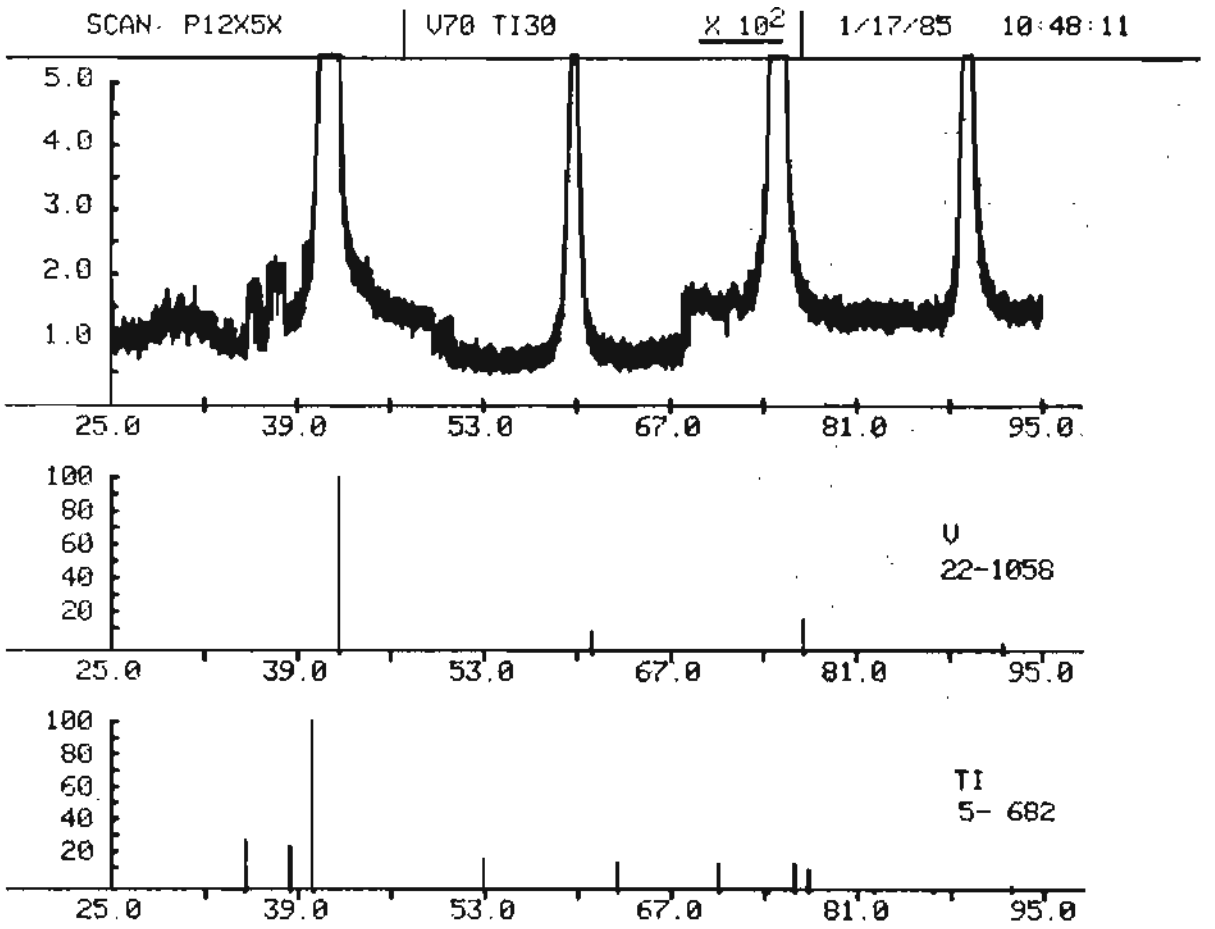

Figure D-16. X-RAY DIFFRACTOMETRY TRACE FOR SPECIMEN P-12 (71.3V-28.7Ti).

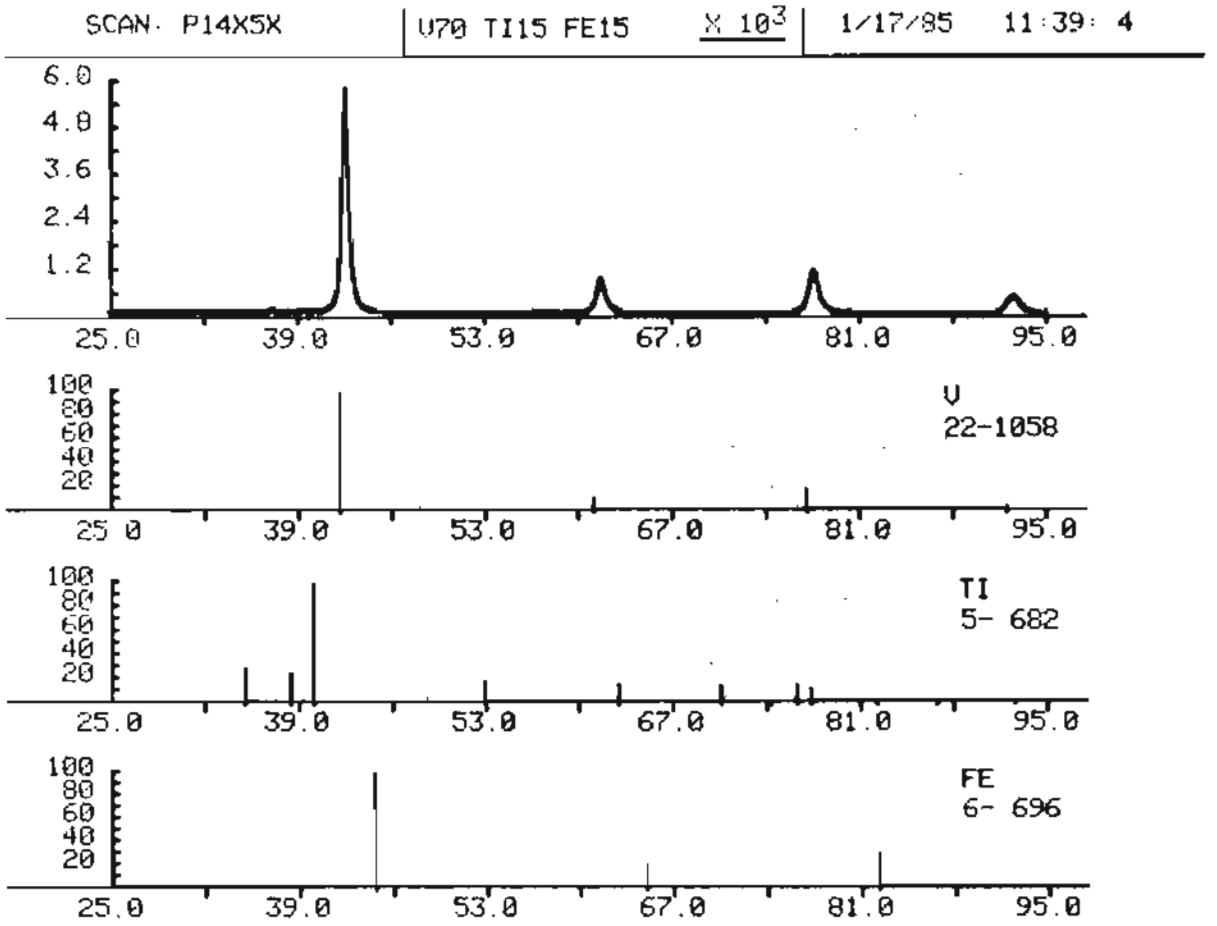

Figure D-17. X-RAY DIFFRACTOMETRY TRACE FOR SPECIMEN P-14 (69.6V-14.0Ti-16.4Fe).

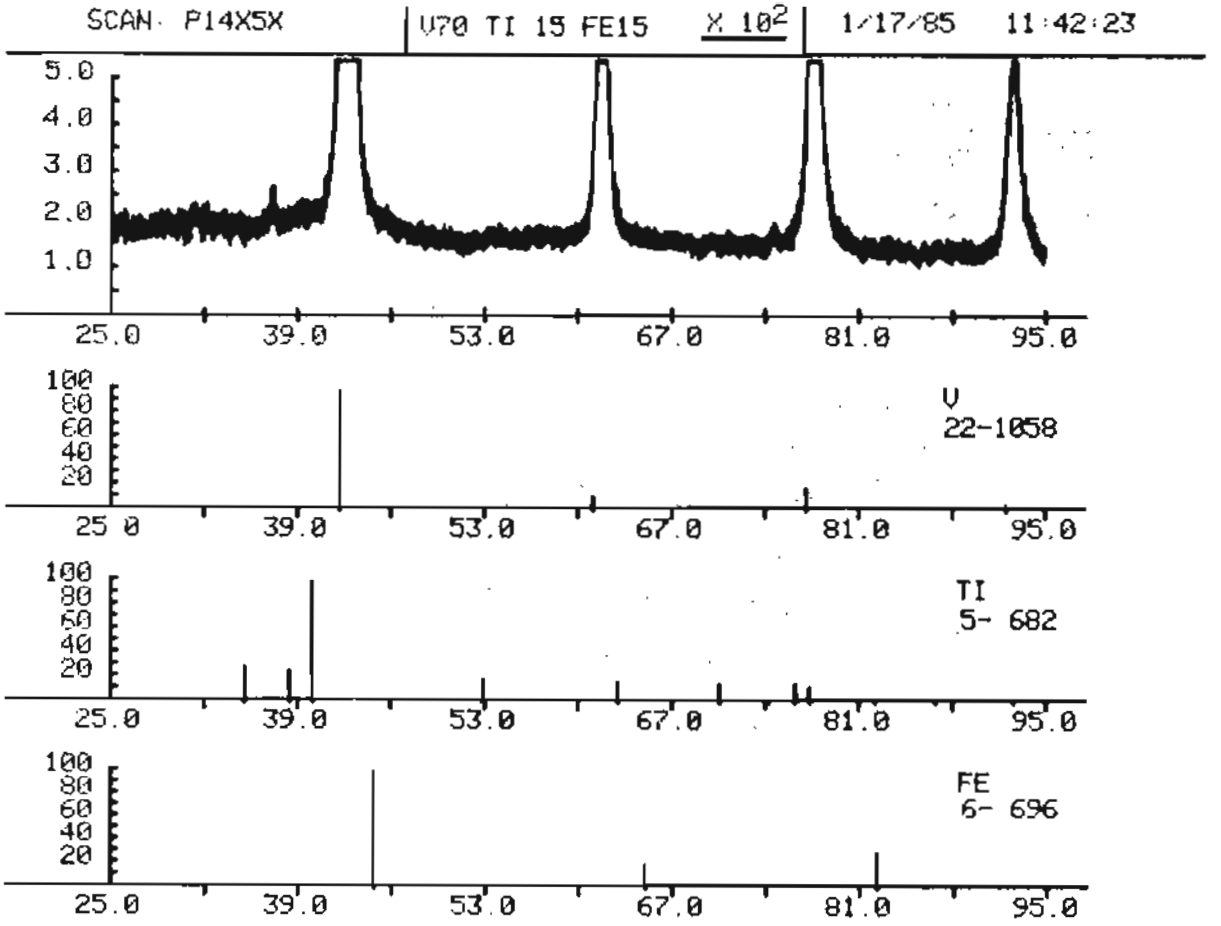

Figure D-18. X-RAY DIFFRACTOMETRY TRACE FOR SPECIMEN P-14 (69.6V-14.0Ti-16.4Fe).

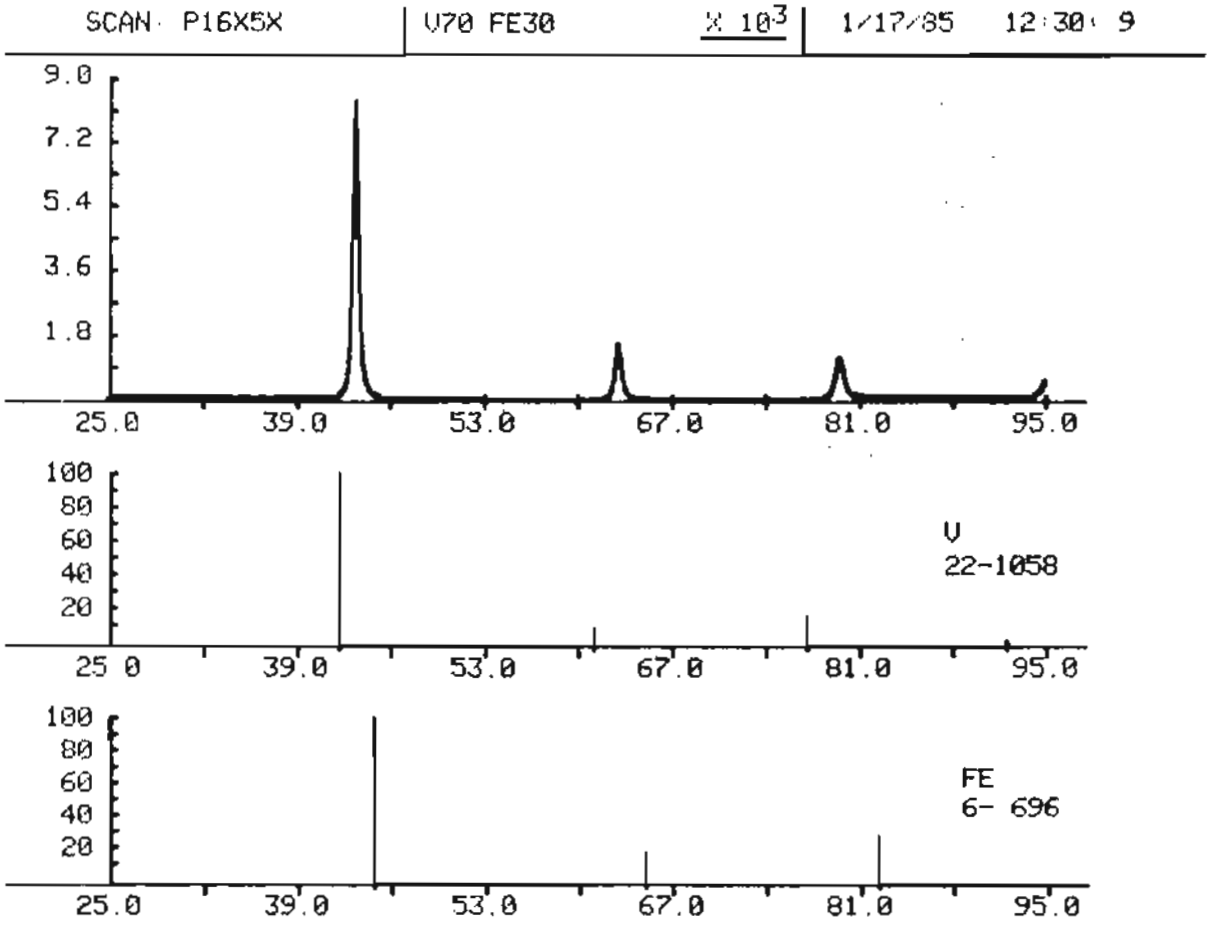

Figure D-19. X-RAY DIFFRACTOMETRY TRACE FOR SPECIMEN P-16 (68.0V-32.0Fe).

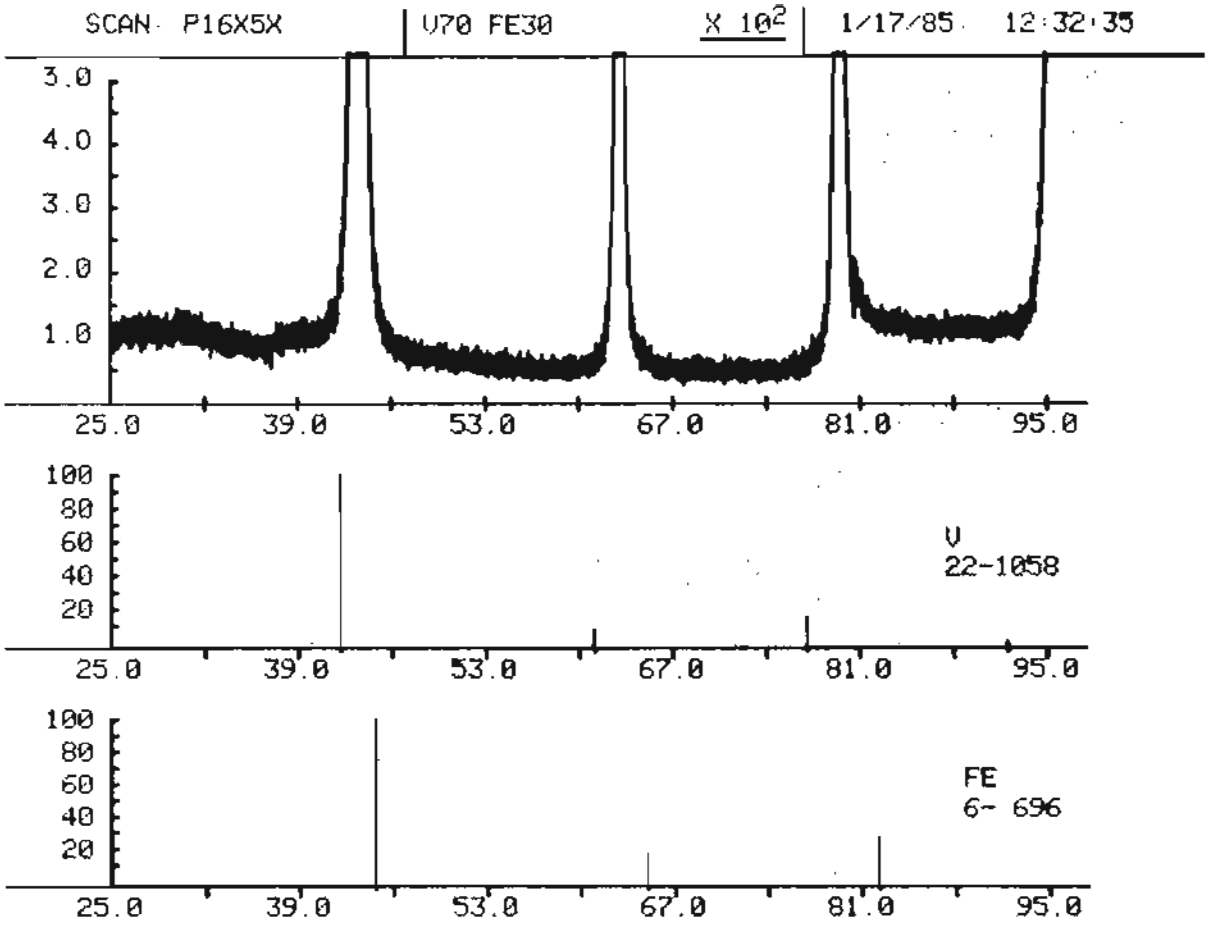

Figure D-20. X-RAY DIFFRACTOMETRY TRACE FOR SPECIMEN P-16 (68.0V-32.0Fe).

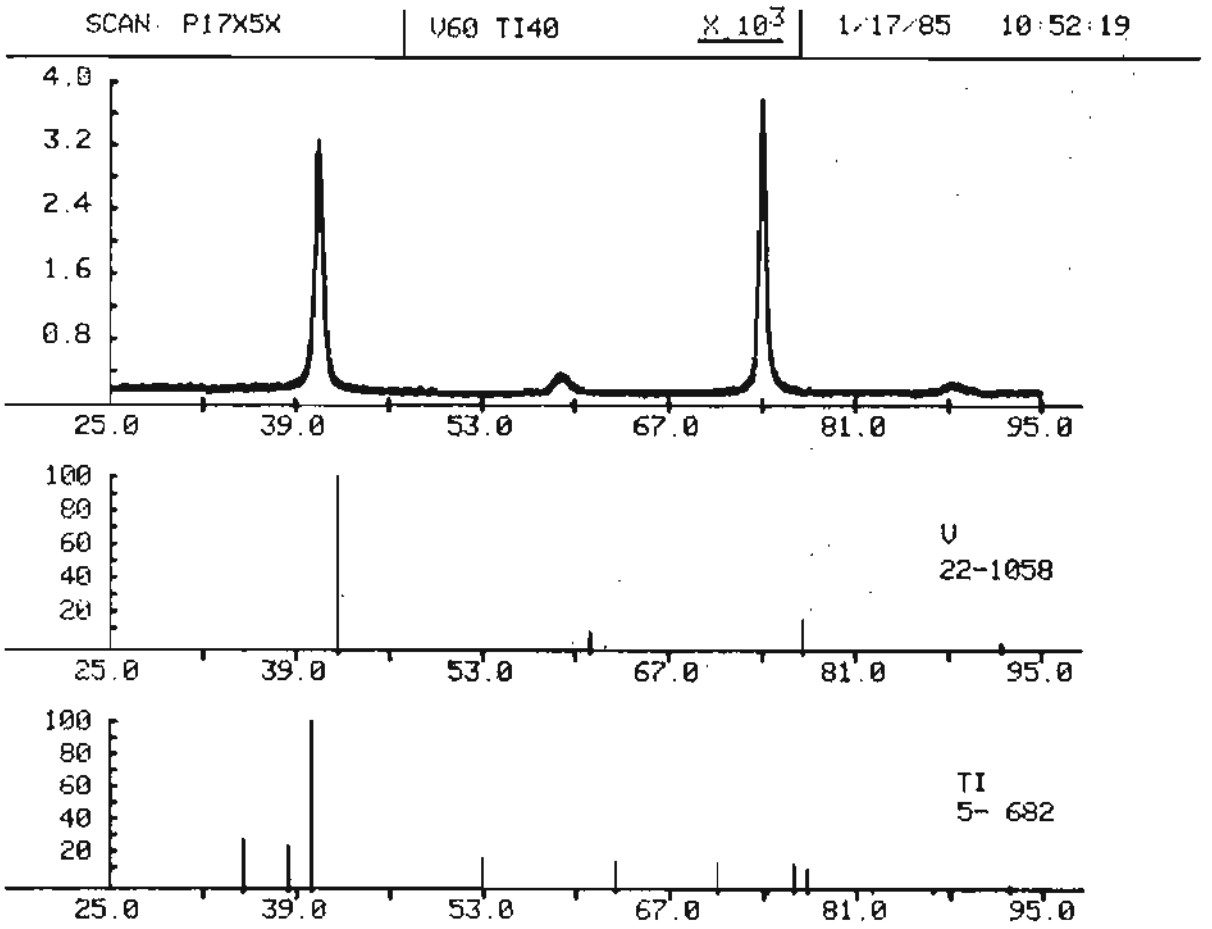

Figure D-21. X-RAY DIFFRACTOMETRY TRACE FOR SPECIMEN P-17 (61.5V-38.5Ti).

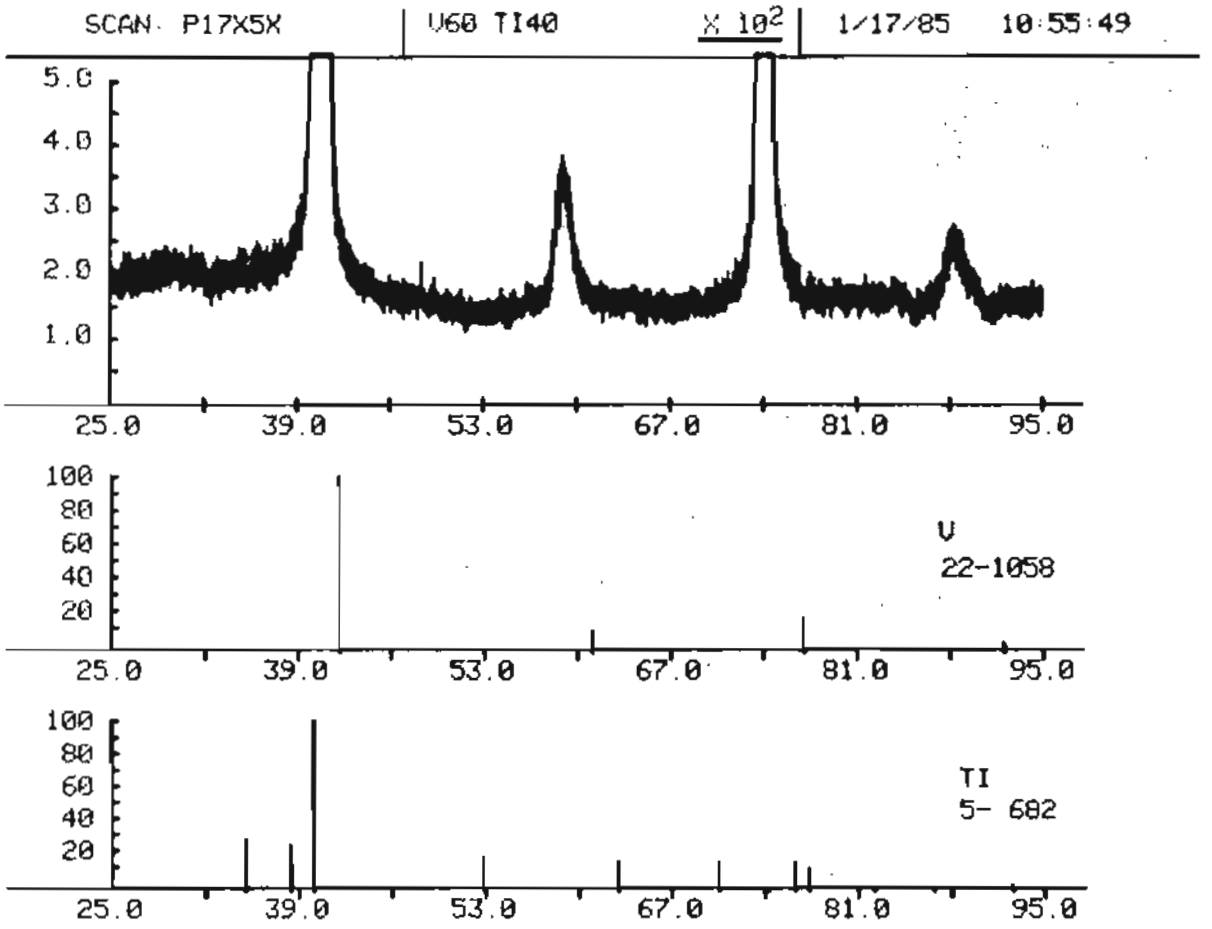

Figure D-22. X-RAY DIFFRACTOMETRY TRACE FOR SPECIMEN P-17 (61.5V-38.5Ti).

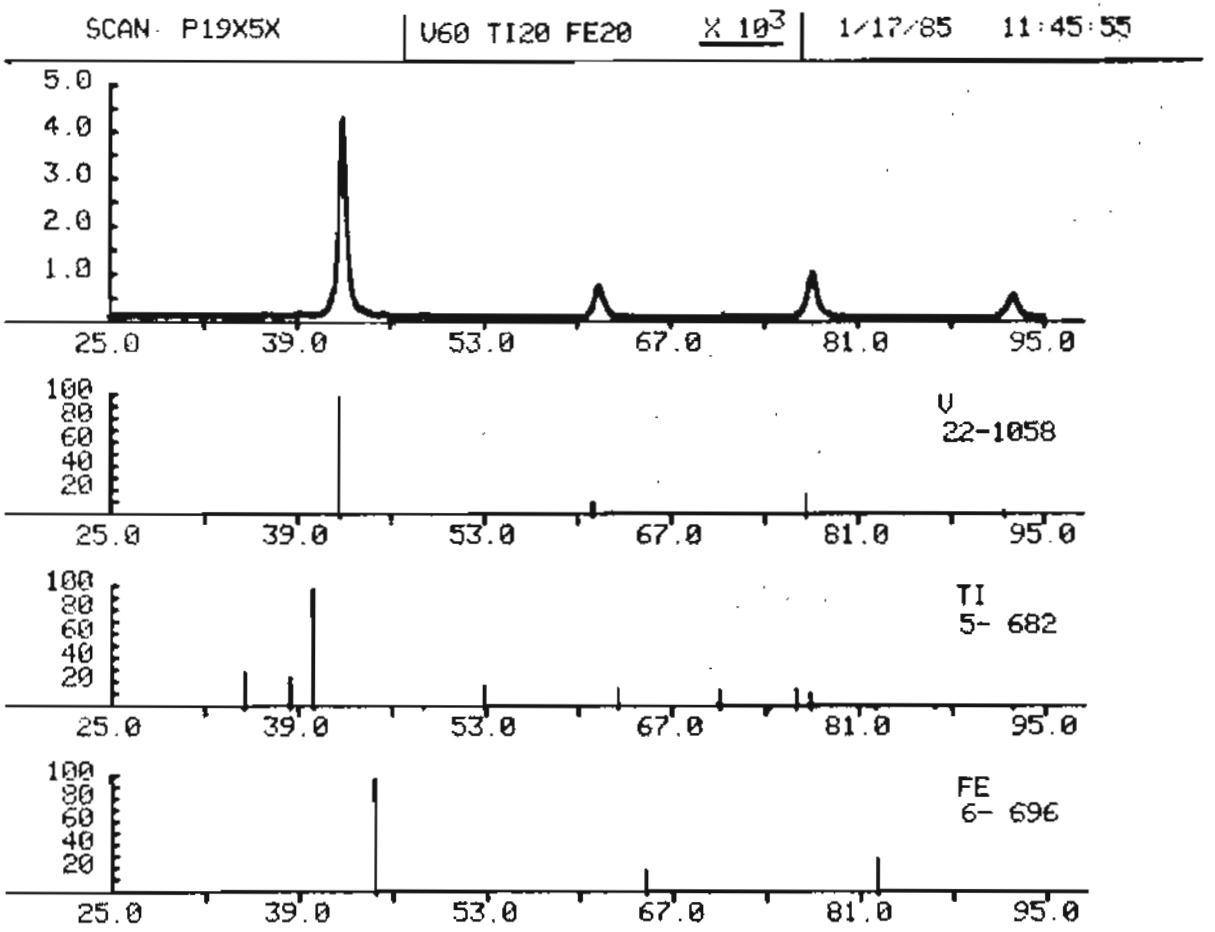

Figure D-23. X-RAY DIFFRACTOMETRY TRACE FOR SPECIMEN P-19 (59.5V-18.7Ti-21.8Fe).

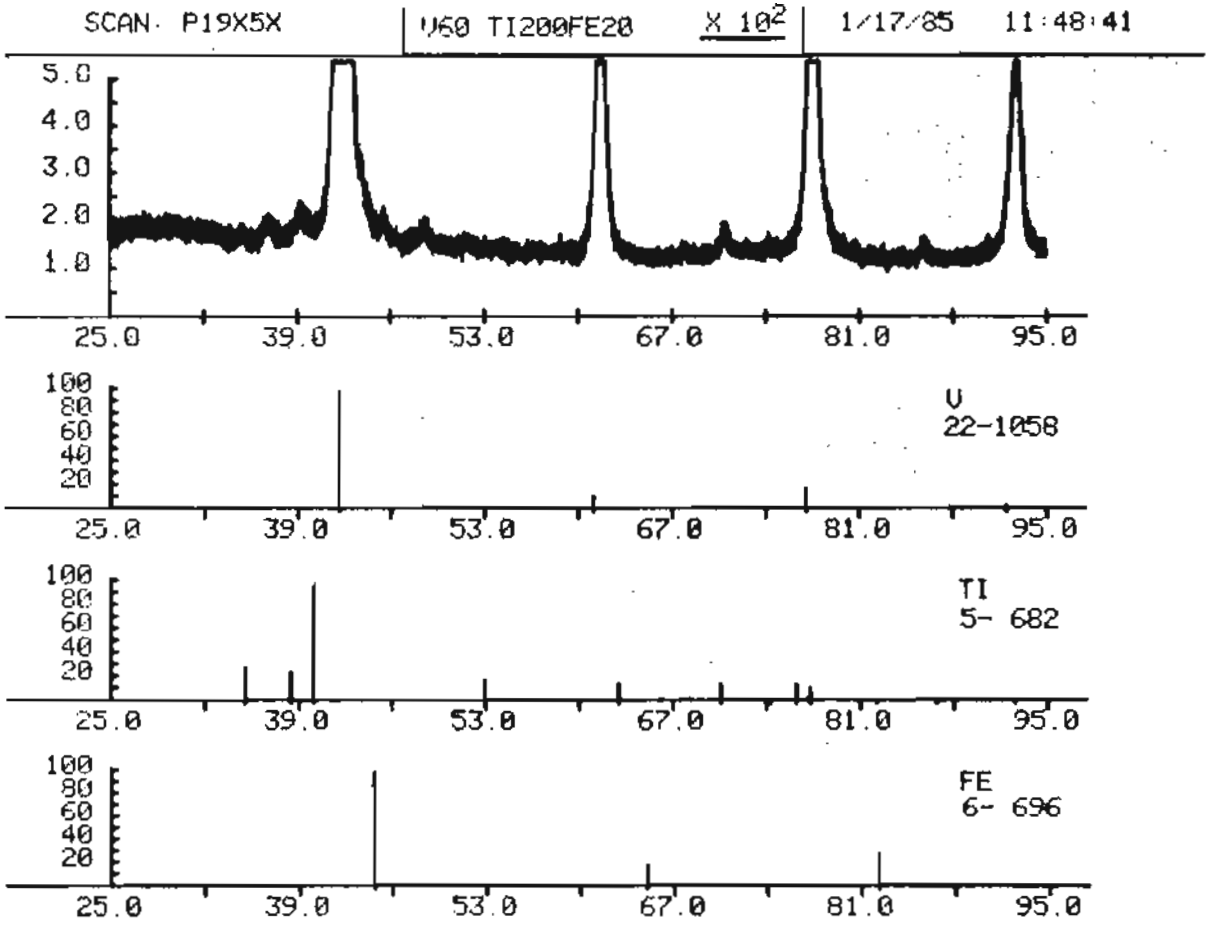

Figure D-24. X-RAY DIFFRACTOMETRY TRACE FOR SPECIMEN P-19 (59.5V-18.7Ti-21.8Fe).

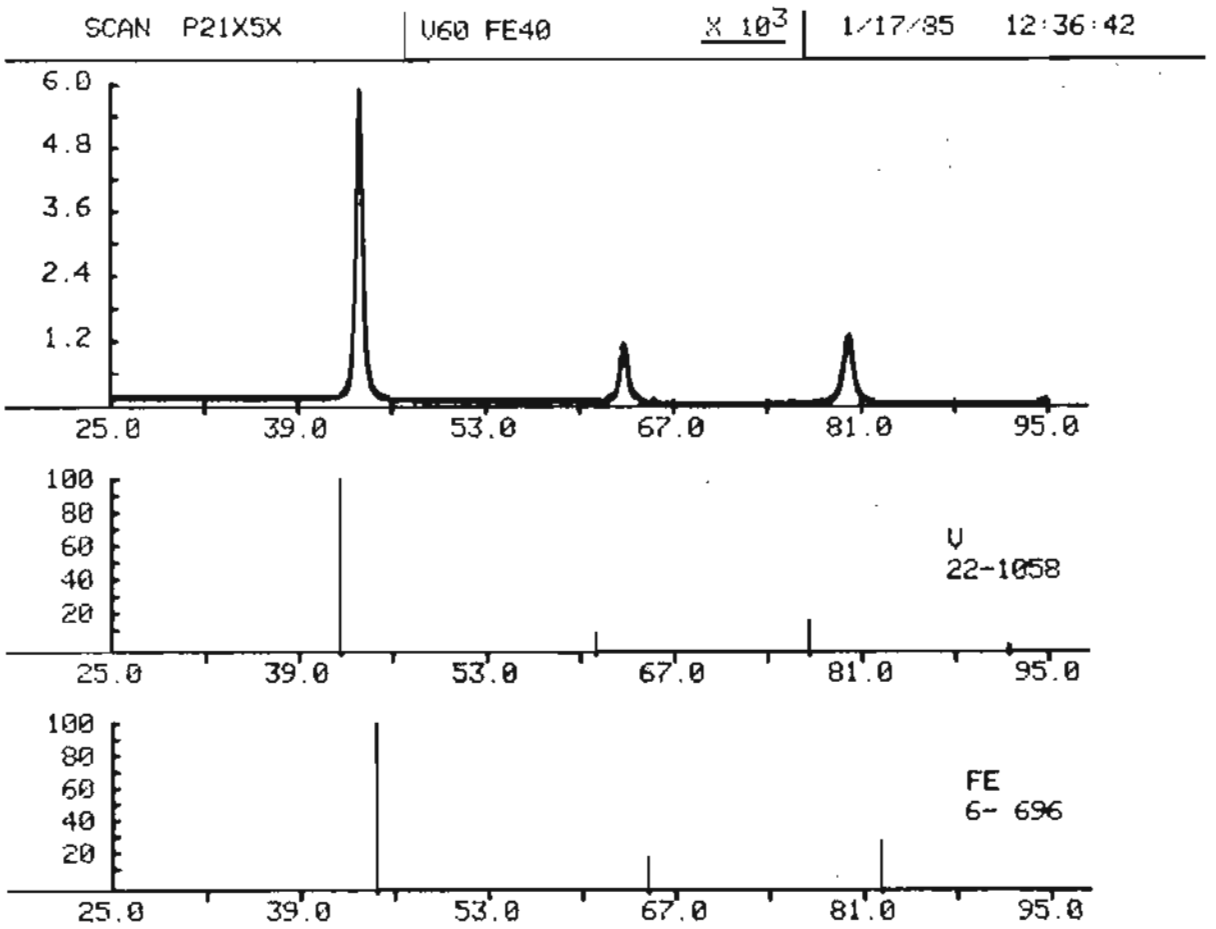

Figure D-25. X-RAY DIFFRACTOMETRY TRACE FOR SPECIMEN P-21 (57.8V-42.2Fe).

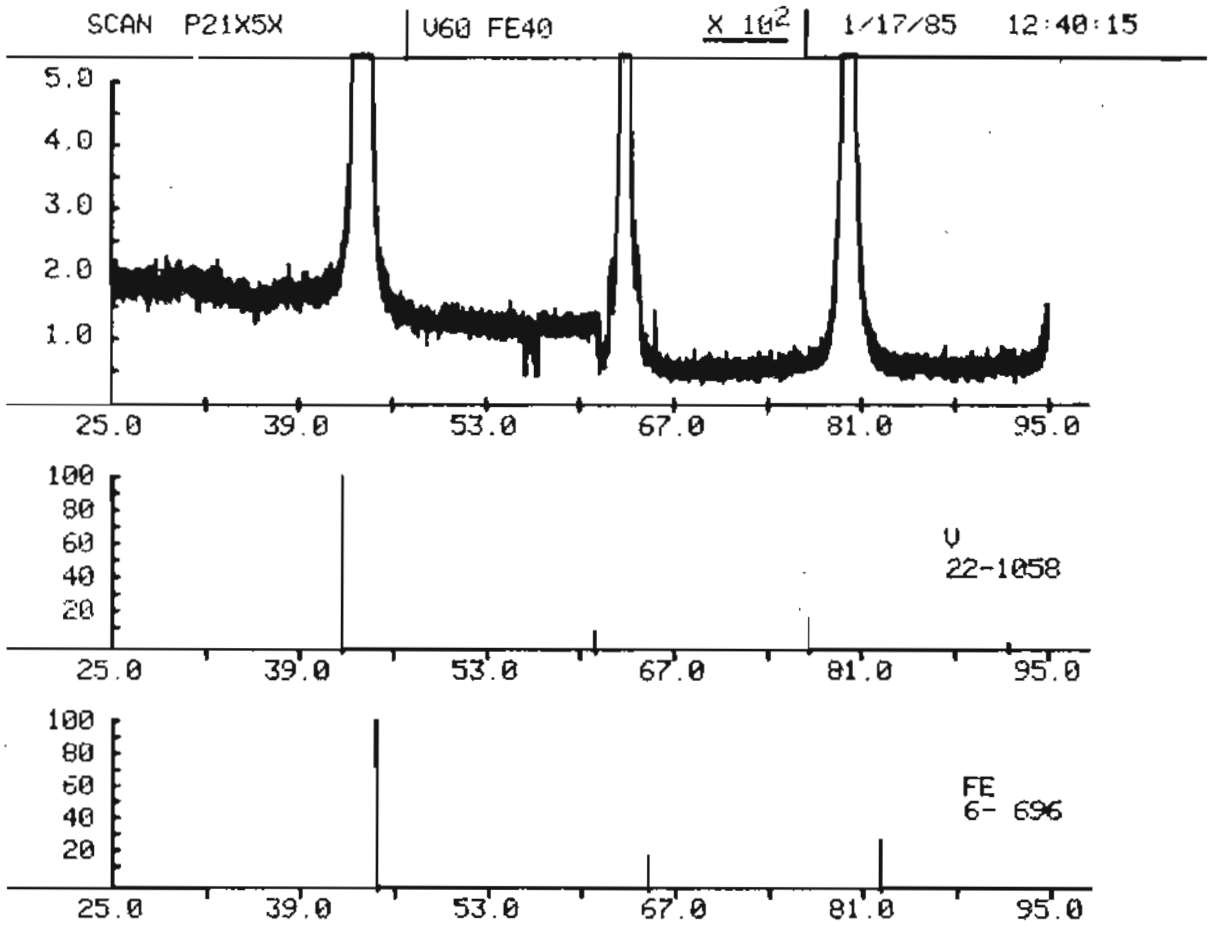

Figure D-26. X-RAY DIFFRACTOMETRY TRACE FOR SPECIMEN P-21 (57.8V-42.2Fe).

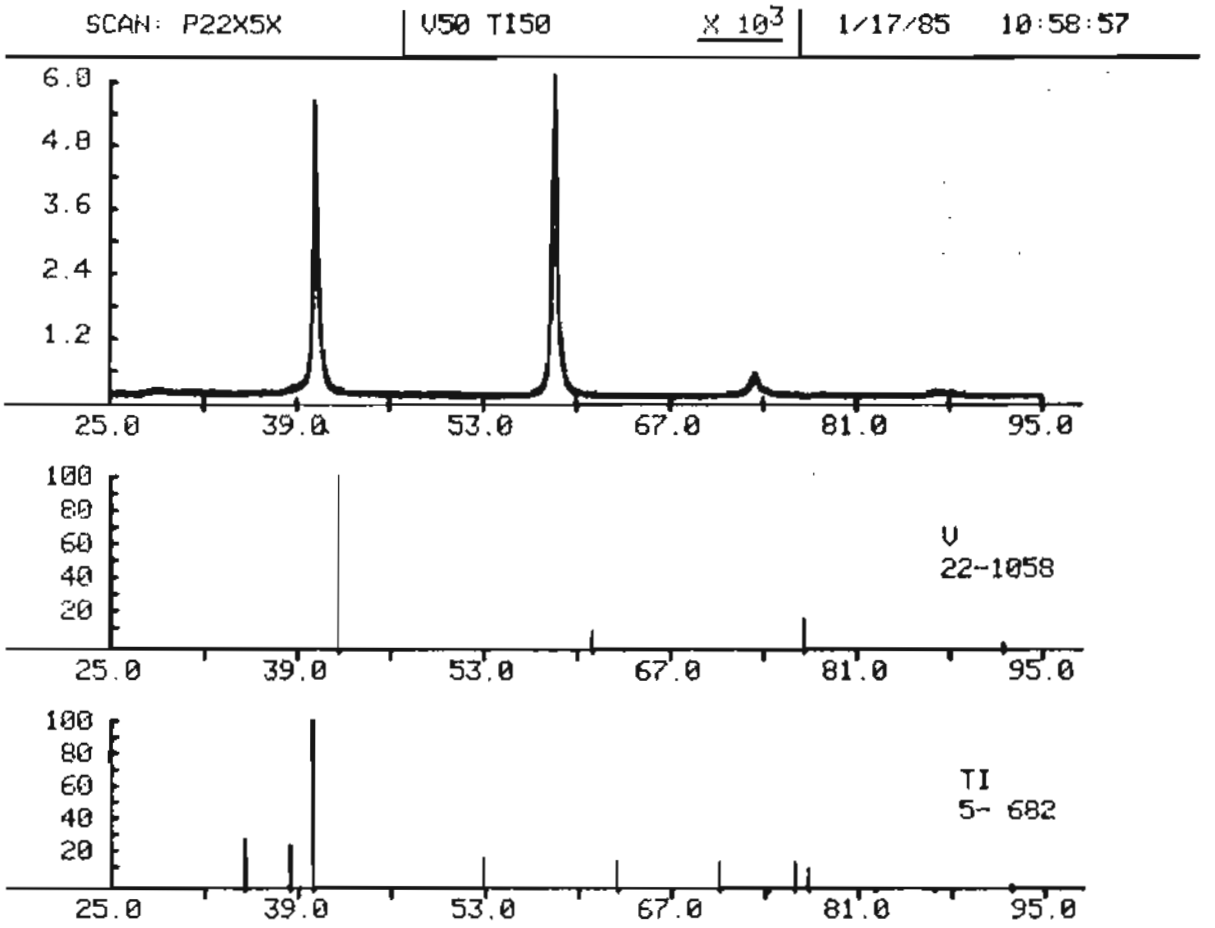

Figure D-27. X-RAY DIFFRACTOMETRY TRACE FOR SPECIMEN P-22 (51.5V-48.5Ti).

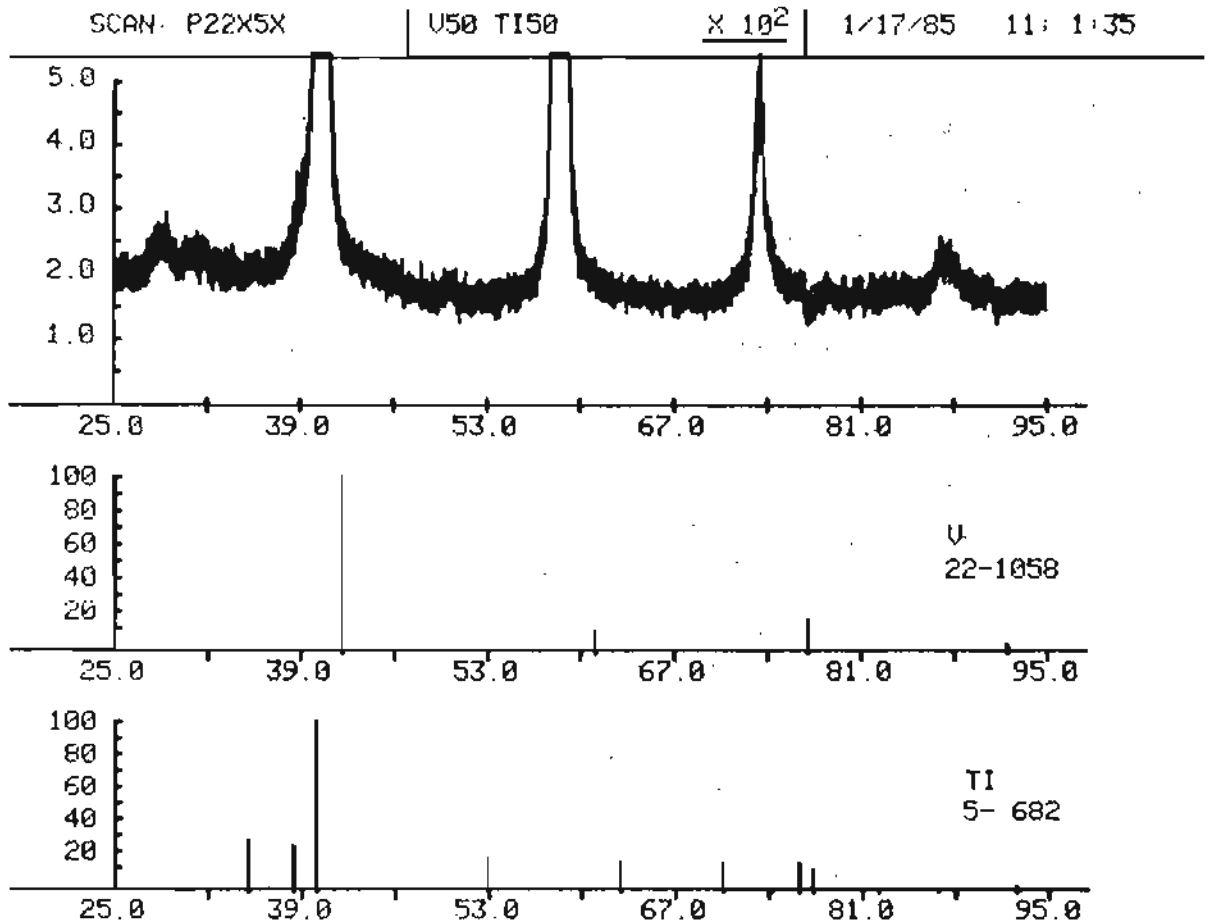

Figure D-28. X-RAY DIFFRACTOMETRY TRACE FOR SPECIMEN P-22 (51.5V-48.5Ti).

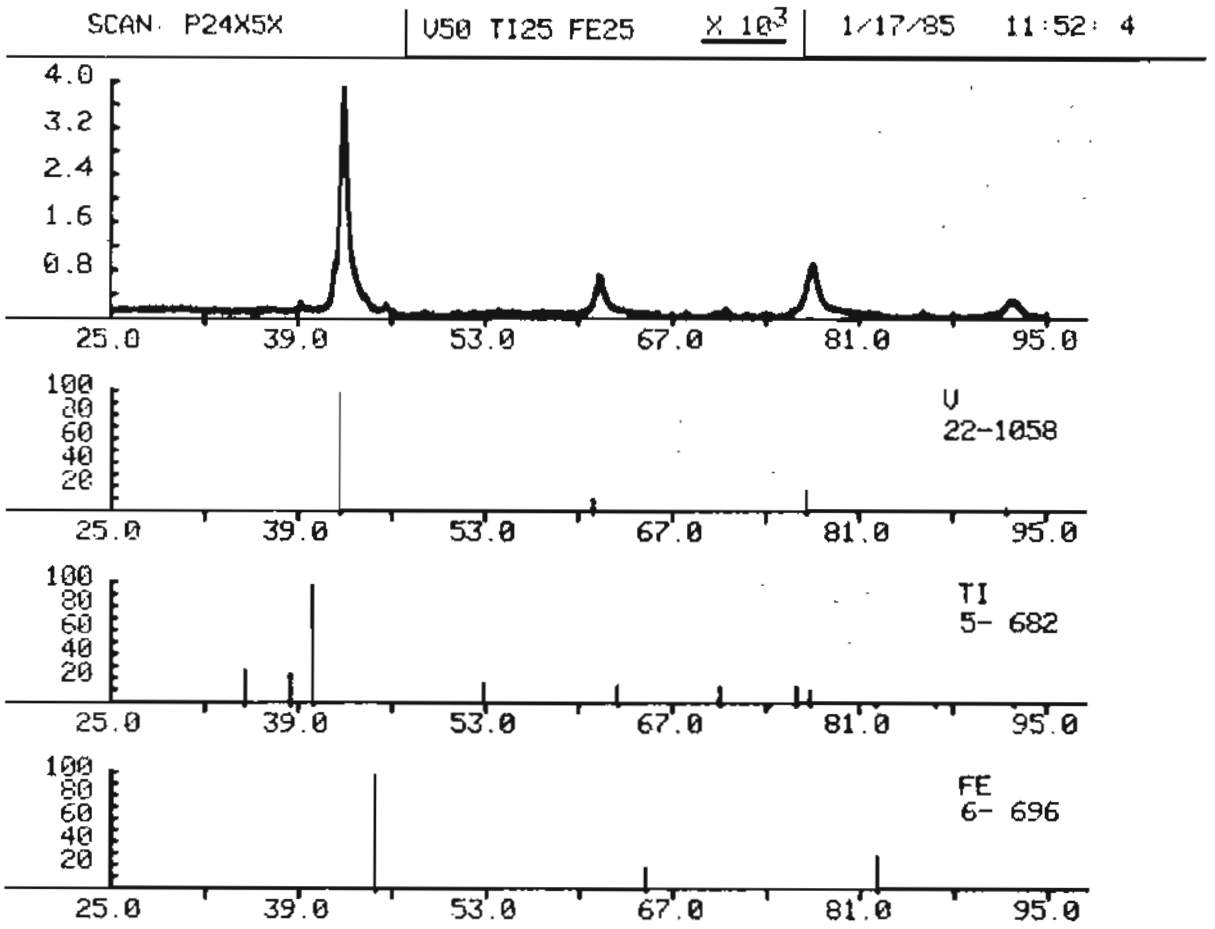

Figure D-29. X-RAY DIFFRACTOMETRY TRACE FOR SPECIMEN P-24 (49.5V-23.3Ti-27.2Fe).

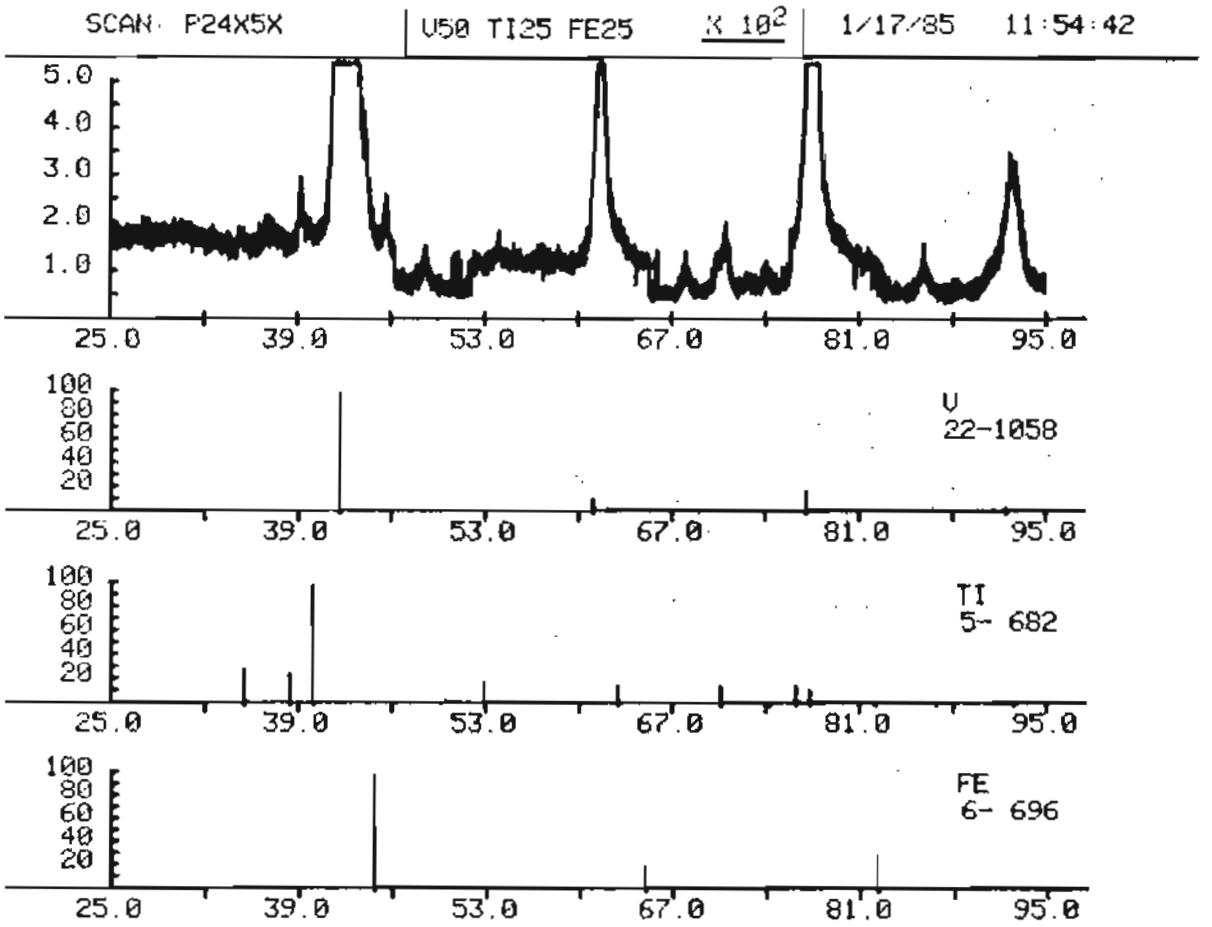

Figure D-30. X-RAY DIFFRACTOMETRY TRACE FOR SPECIMEN P-24 (49.5V-23.3Ti-27.2Fe).

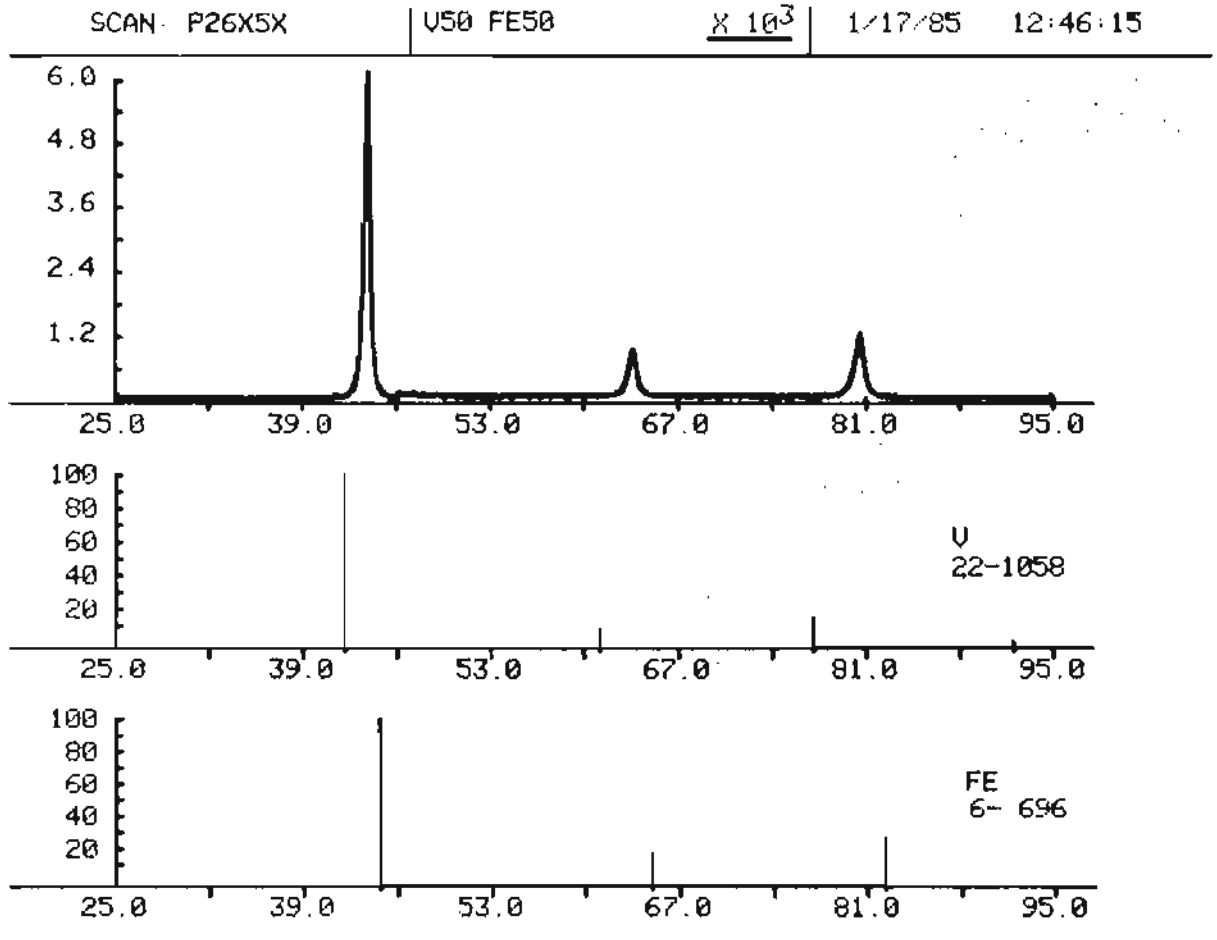

Figure D-31. X-RAY DIFFRACTOMETRY TRACE FOR SPECIMEN P-26 (47.7V-52.3Fe).

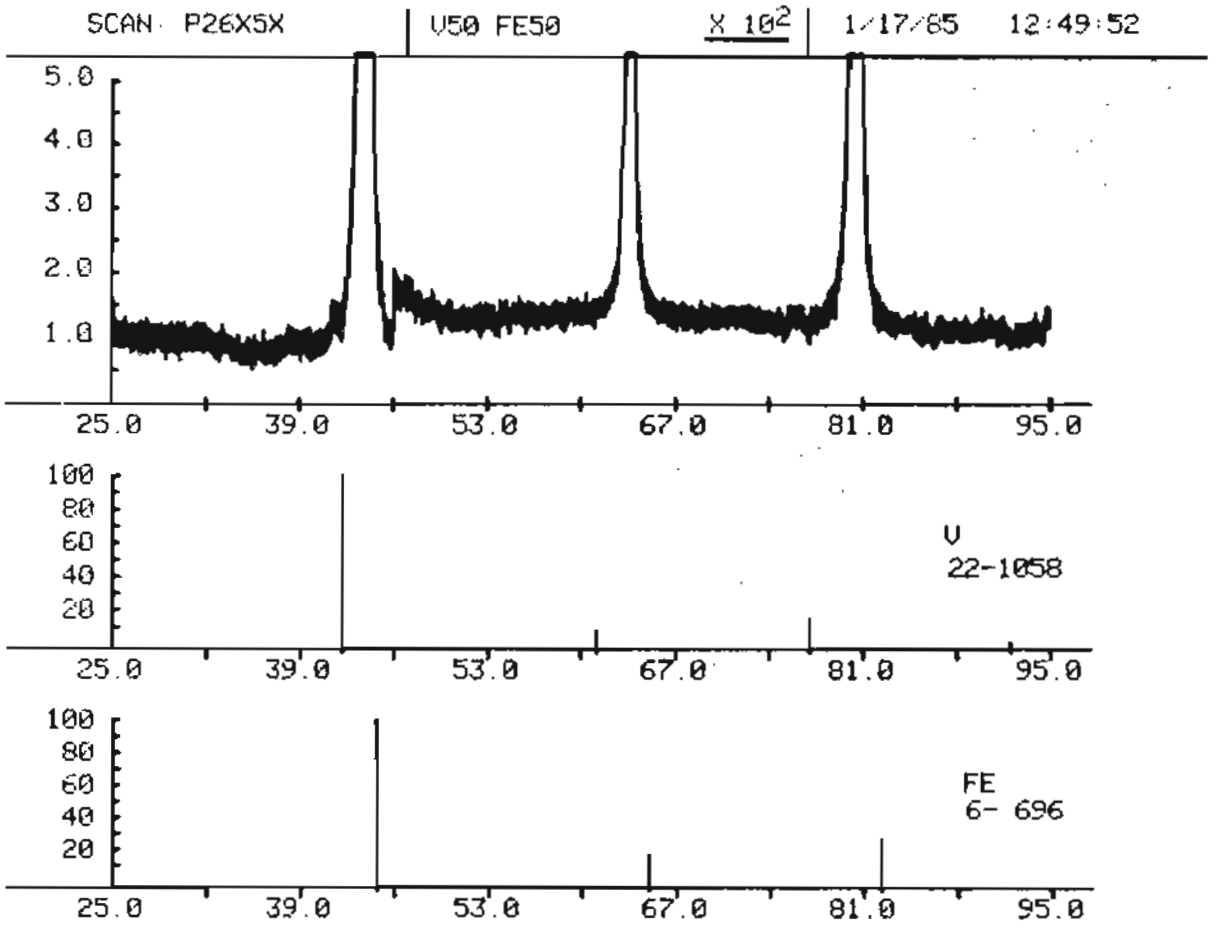

Figure D-32. X-RAY DIFFRACTOMETRY TRACE FOR SPECIMEN P-26 (47.7V-52.3Fe).

APPENDIX E

BEND TESTING LOAD-DISPLACEMENT CURVES

Table E-1.

VOLTAGE/LOAD CONVERSION VALUES FOR INSTRON DYNAMIC TEST SYSTEM

	Load (Lb) Load Range (%)			
Voltage(V)	10	20	50	100
10.0	2,495	5,000	12,502	
9.0	2,245	4,504	11,257	22,495
8.0	1,997	4,005	10,015	20,002
7.0	1,747	3,505	8,762	17,512
6.0	1,500	3,005	7,512	15,017
5.0	1,249	2,504	6,267	12,517
4.0	1,001	2,005	5,020	10,022
3.0	748	1,505	3,717	7,527
2.0	500	1,004	2,517	5,022
1.0	250	503	1,261	2,525
0.0	0	0	0	0

Table E-2.

VOLTAGE/DISPLACEMENT CONVERSION VALUES FOR INSTRON DYNAMIC TEST SYSTEM

	Displacement (In) Stroke Range (%)			
Voltage(V)	10	20	50	100
10.0	.2020	.403	1.002	1.997
9.0	.1820	.363	.903	1.794
8.0	.1615	.323	.803	1.597
7.0	.1415	.282	.704	1.407
6.0	.1215	.242	.604	1.201
5.0	.1010	.202	.504	1.001
4.0	.0810	.161	.403	.803
3.0	.0605	.121	.303	.602
2.0	.0405	.080	.202	.403
1.0	.0200	.040	.100	.200
0.0	.0000	.000	.000	.000

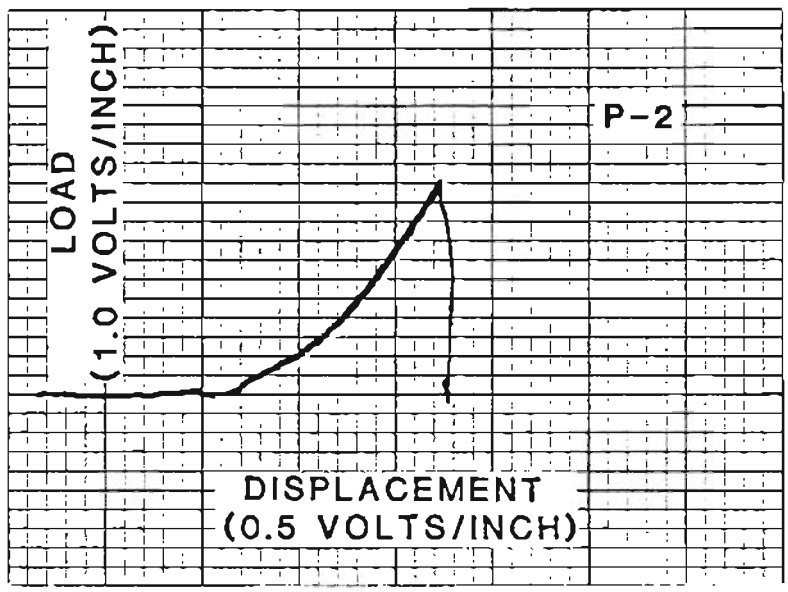

Figure E-1. BEND TESTING LOAD-DISPLACEMENT CURVE FOR SPECIMEN P-2 (90.5V-9.5Ti).

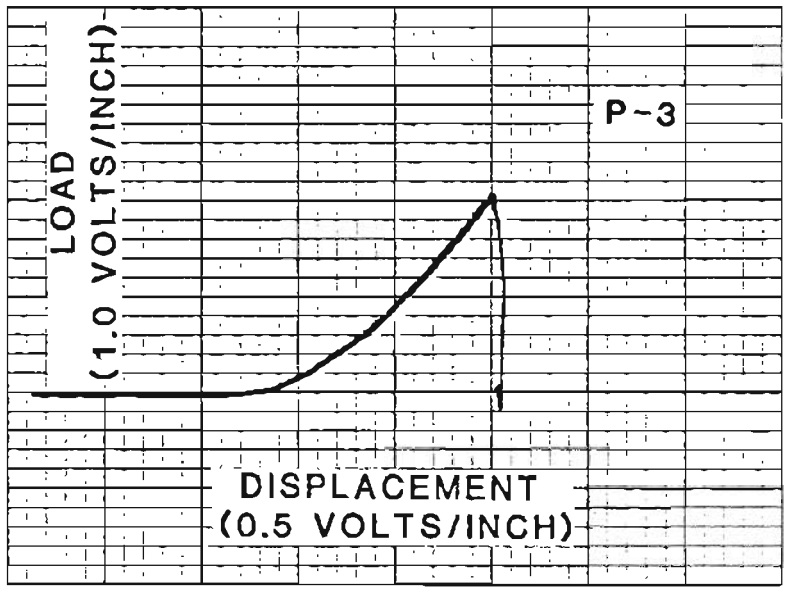

Figure E-2. BEND TESTING LOAD-DISPLACEMENT CURVE FOR SPECIMEN P-3 (90.2V-7.1Ti-2.7Fe).

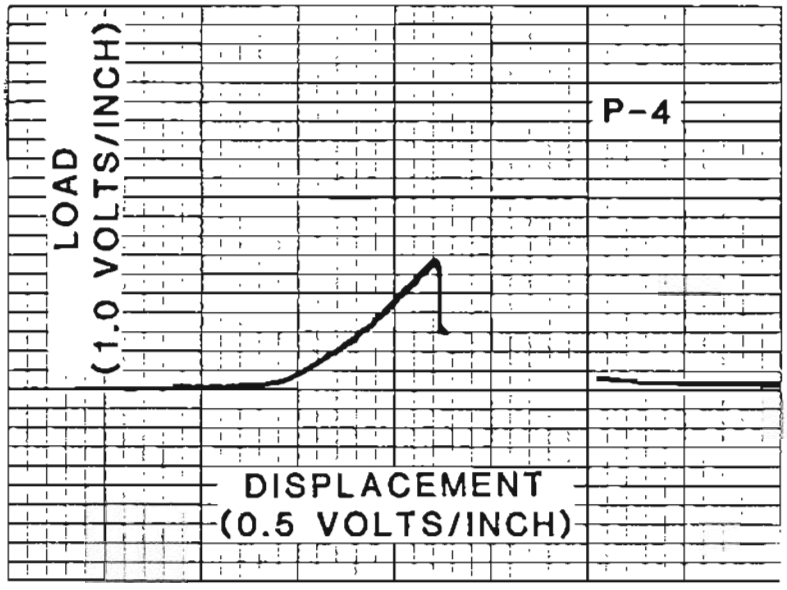

Figure E-3. BEND TESTING LOAD-DISPLACEMENT CURVE FOR SPECIMEN P-4 (89.8V-4.7Ti-5.5Fe).

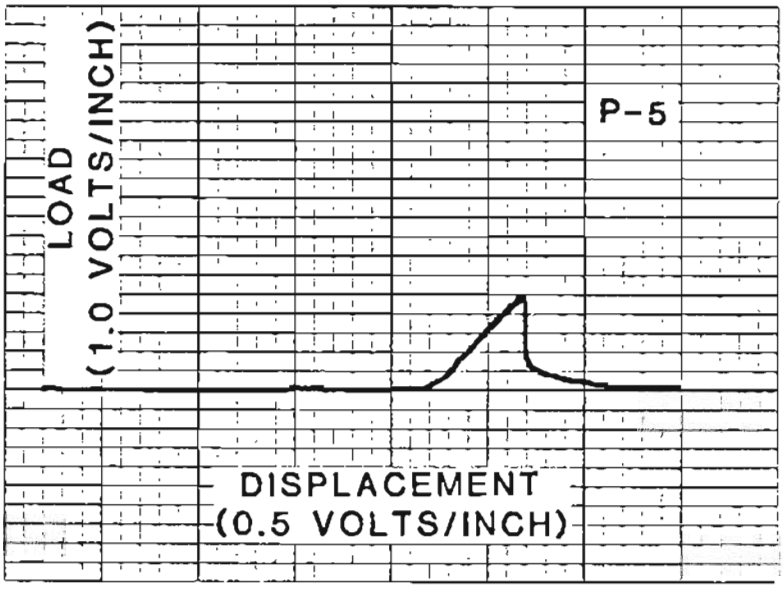

Figure E-4. BEND TESTING LOAD-DISPLACEMENT CURVE FOR SPECIMEN P-5 (89.5V-2.3Ti-8.2Fe).

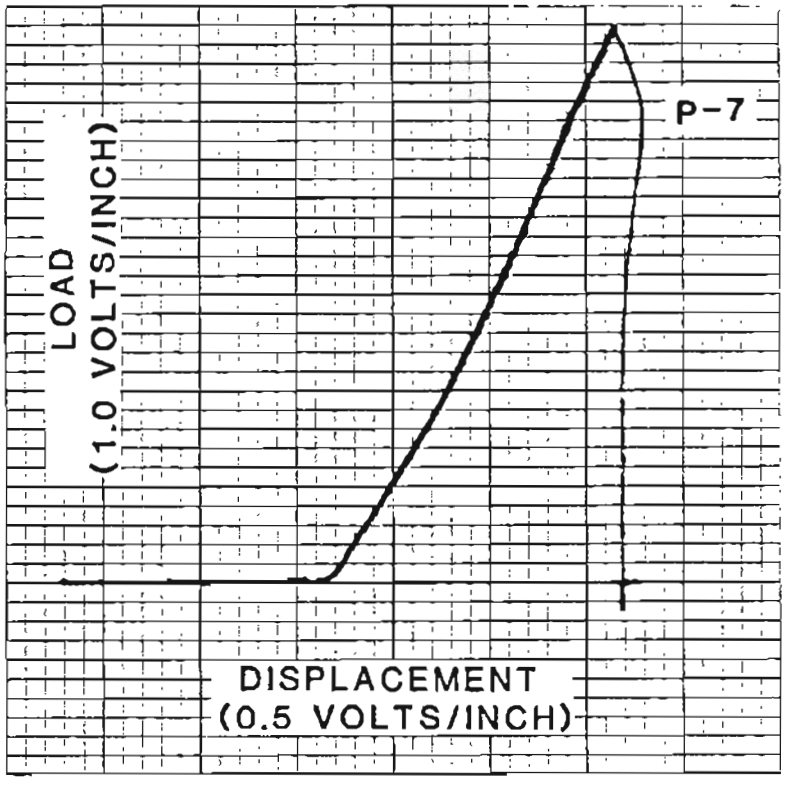

Figure E-5. BEND TESTING LOAD-DISPLACEMENT CURVE FOR SPECIMEN P-7 (81.0V-19.0Ti).

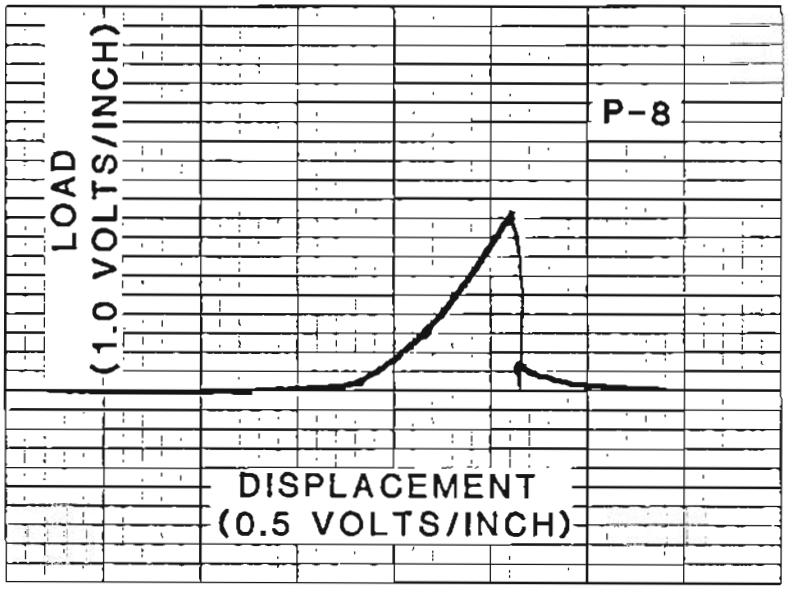

Figure E-6. BEND TESTING LOAD-DISPLACEMENT CURVE FOR SPECIMEN P-8 (80.3V-14.2Ti-5.5Fe).

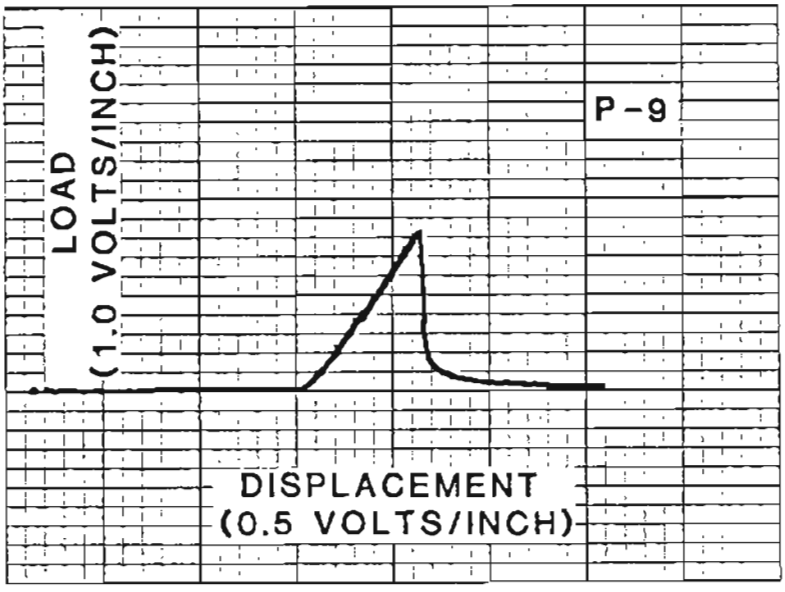

Figure E-7. BEND TESTING LOAD-DISPLACEMENT CURVE FOR SPECIMEN P-9 (79.7V-9.4Ti-10.9Fe).

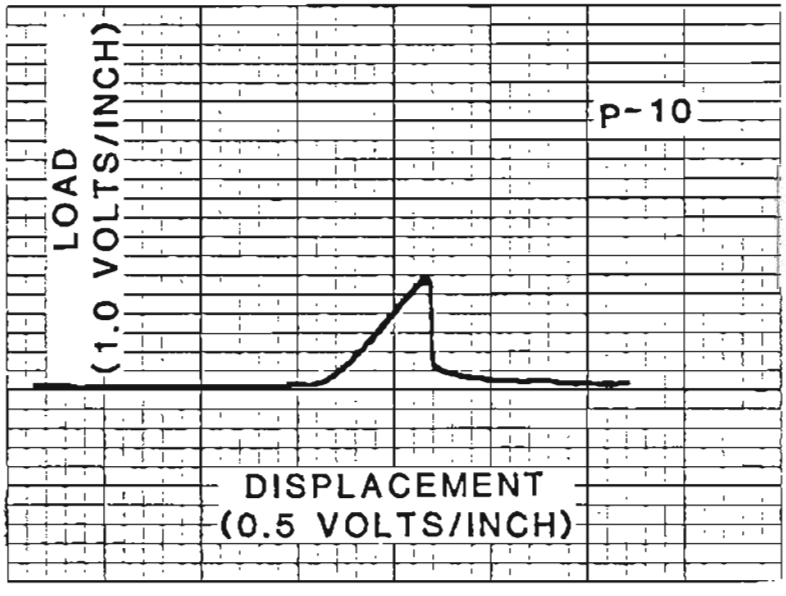

Figure E-8. BEND TESTING LOAD-DISPLACEMENT CURVE FOR SPECIMEN P-10 (79.1V-4.6Ti-16.3Fe).

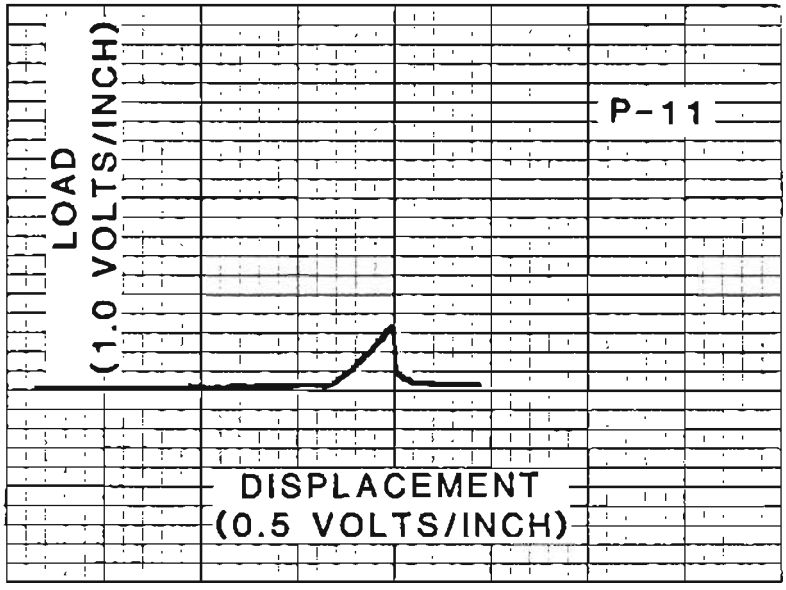

Figure E-9. BEND TESTING LOAD-DISPLACEMENT CURVE FOR SPECIMEN P-11 (78.5V-21.5Fe).

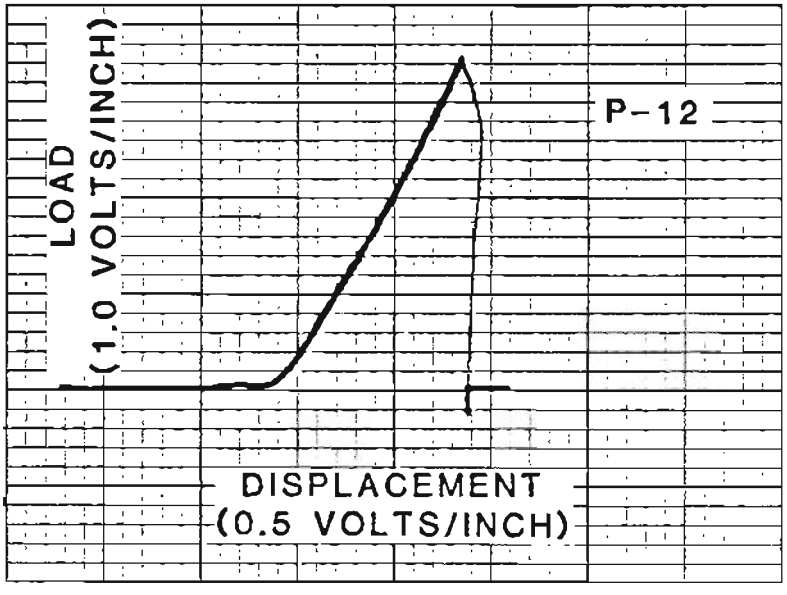

Figure E-10. BEND TESTING LOAD-DISPLACEMENT CURVE FOR SPECIMEN P-12 (71.3V-28.7Ti).

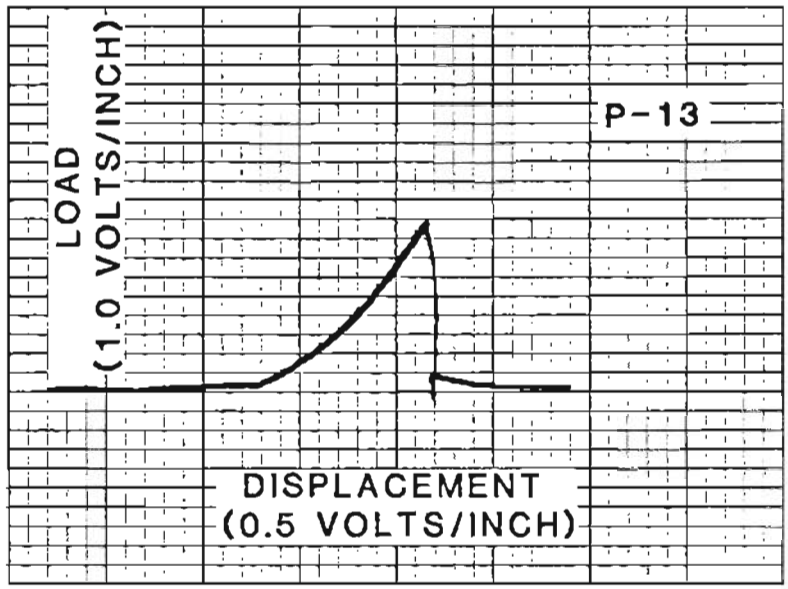

Figure E-11. BEND TESTING LOAD-DISPLACEMENT CURVE FOR SPECIMEN P-13 (70.4V-21.3Ti-8.3Fe).

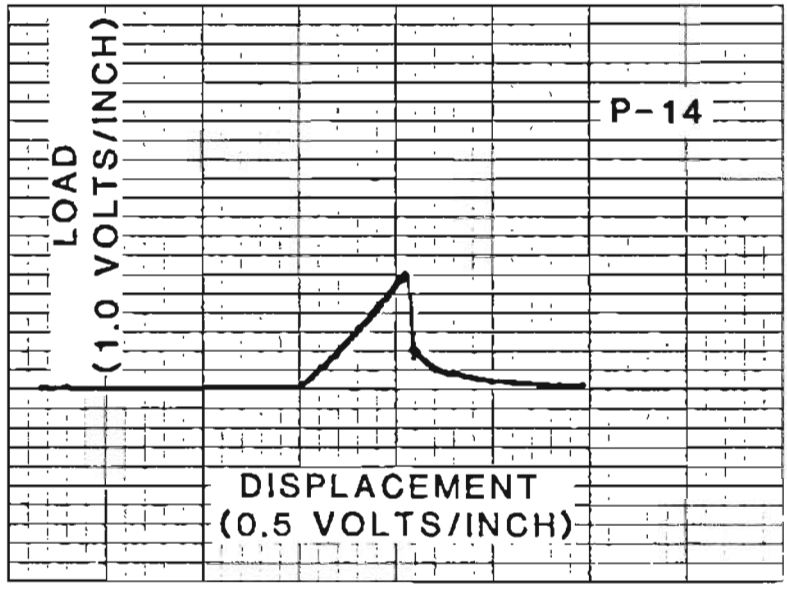

Figure E-12. BEND TESTING LOAD-DISPLACEMENT CURVE FOR SPECIMEN P-14 (69.6V-14.0Ti-16.4Fe).

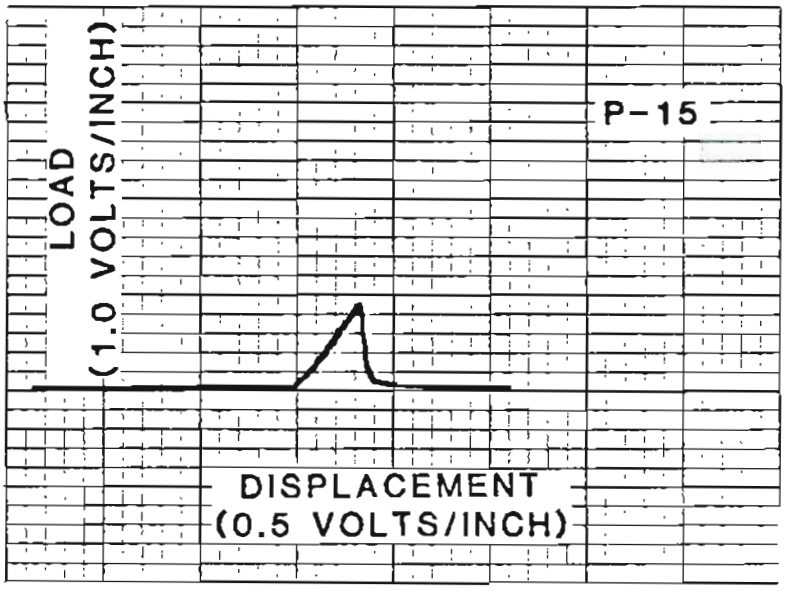

Figure E-13. BEND TESTING LOAD-DISPLACEMENT CURVE FOR SPECIMEN P-15 (68.8V-6.9Ti-24.3Fe).

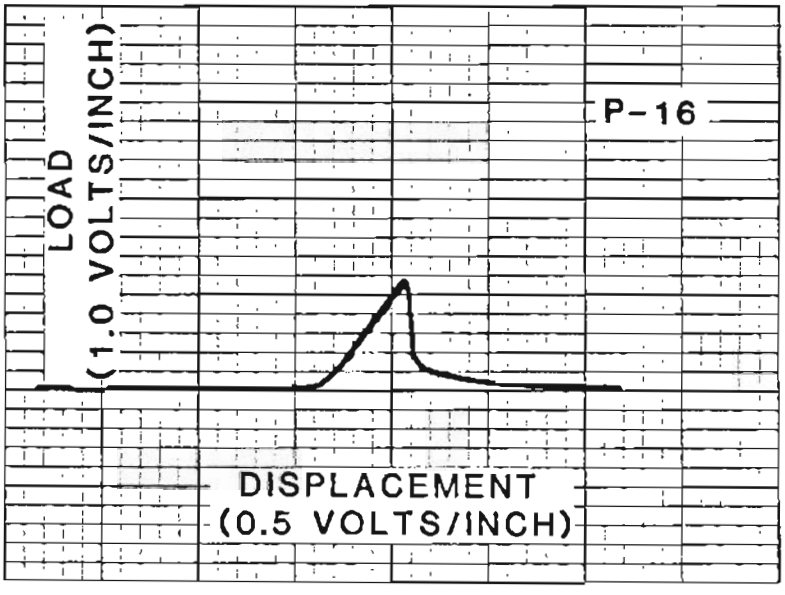

Figure E-14. BEND TESTING LOAD-DISPLACEMENT CURVE FOR SPECIMEN P-16 (68.0V-32.0Fe).

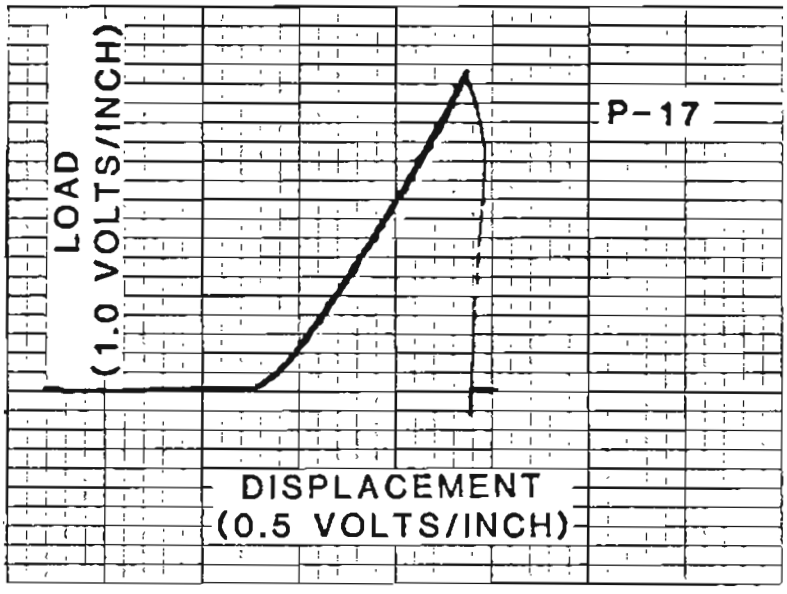

Figure E-15. BEND TESTING LOAD-DISPLACEMENT CURVE FOR SPECIMEN P-17 (61.5V-38.5Ti).

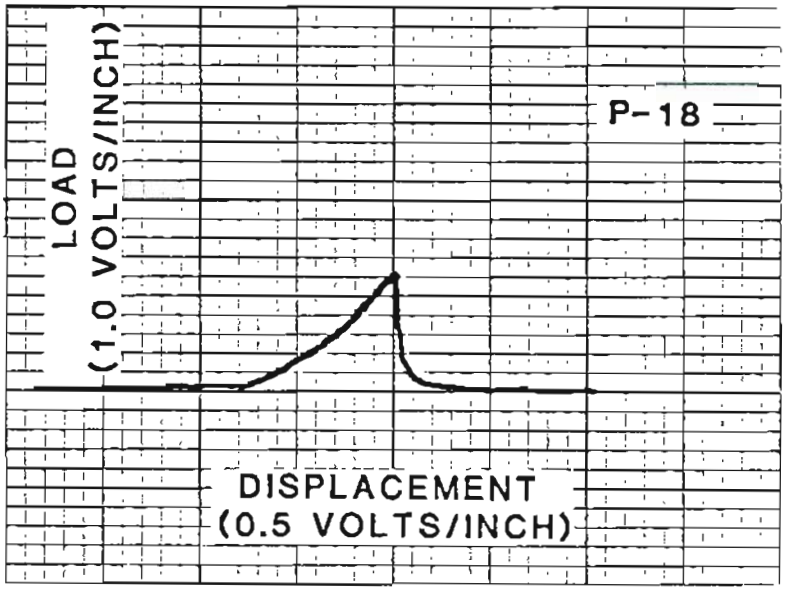

Figure E-16. BEND TESTING LOAD-DISPLACEMENT CURVE FOR SPECIMEN P-18 (60.5V-28.4Ti-11.1Fe).

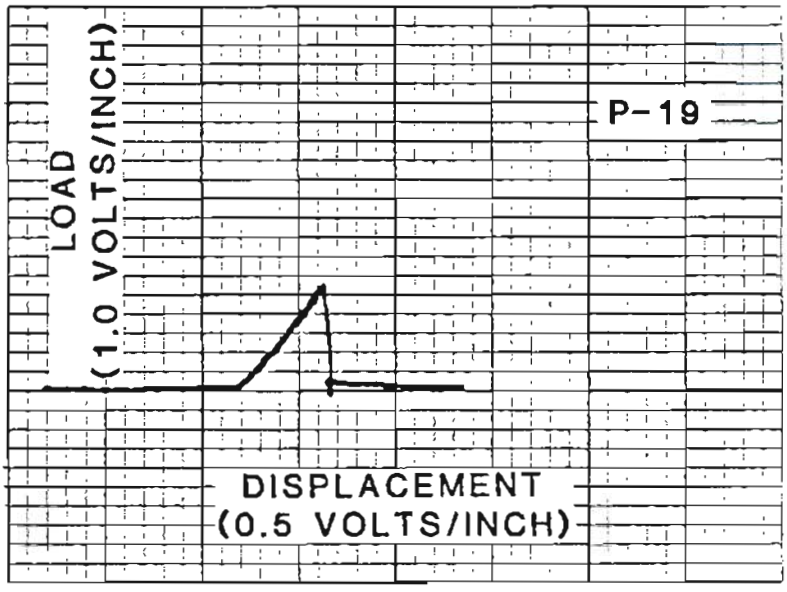

Figure E-17. BEND TESTING LOAD-DISPLACEMENT CURVE FOR SPECIMEN P-19 (59.5V-18.7Ti-21.8Fe).

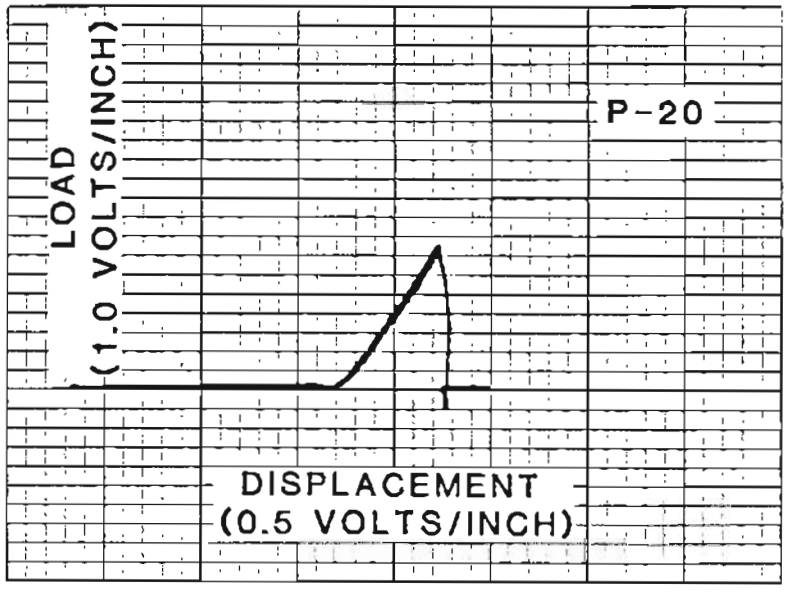

Figure E-18. BEND TESTING LOAD-DISPLACEMENT CURVE FOR SPECIMEN P-20 (58.6V-9.2Ti-32.2Fe).

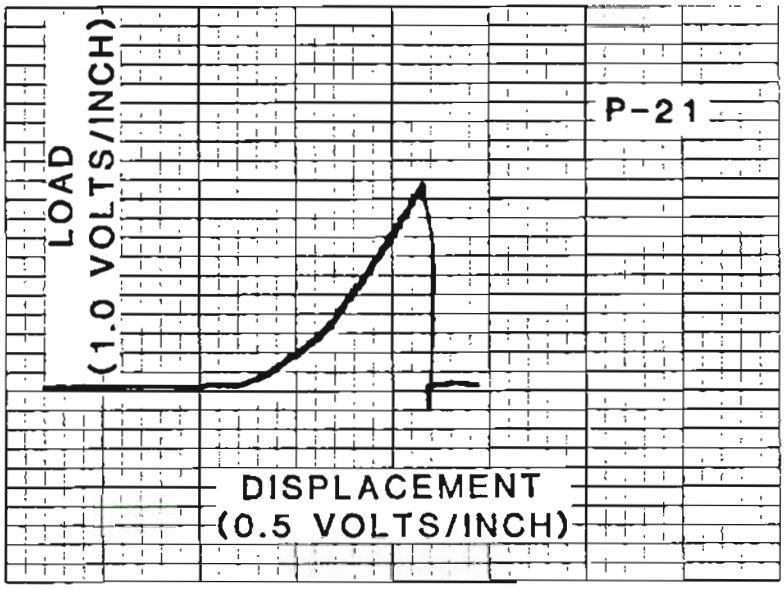

Figure E-19. BEND TESTING LOAD-DISPLACEMENT CURVE FOR SPECIMEN P-21 (57.8V-42.2Fe).

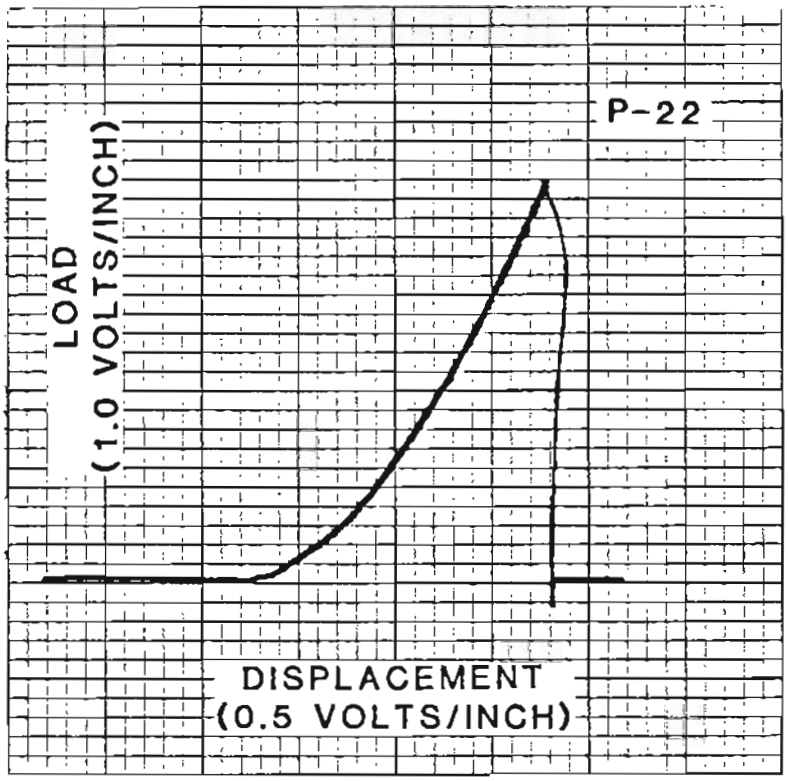

Figure E-20. BEND TESTING LOAD-DISPLACEMENT CURVE FOR SPECIMEN P-22 (51.5V-48.5Ti).

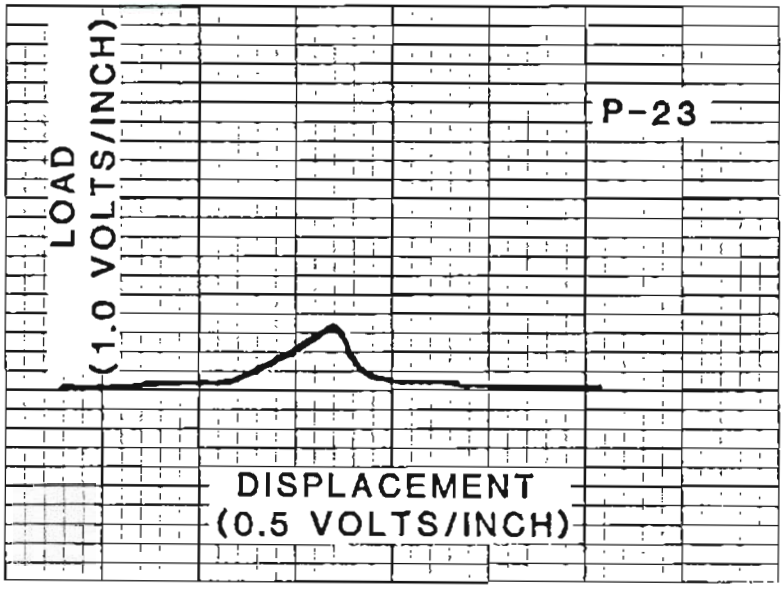

Figure E-21. BEND TESTING LOAD-DISPLACEMENT CURVE FOR SPECIMEN P-23 (50.5V-35.6Ti-13.9Fe).

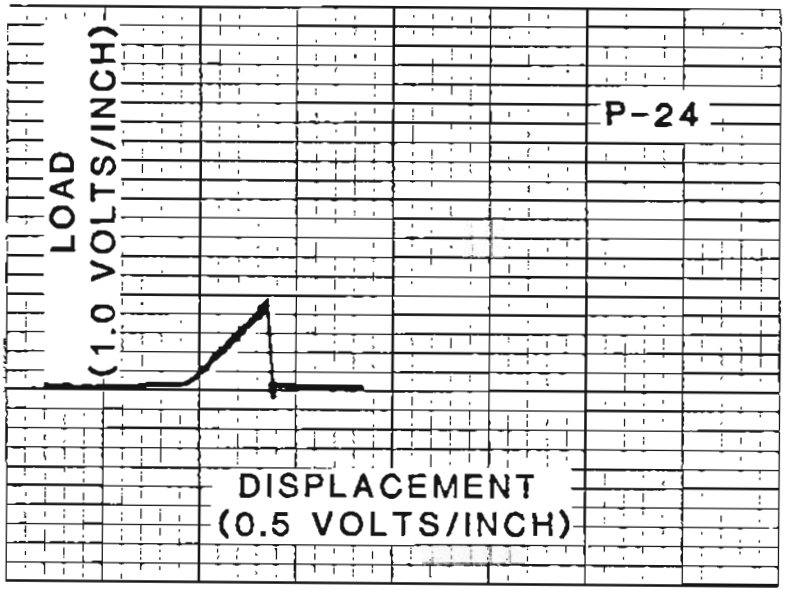

Figure E-22. BEND TESTING LOAD-DISPLACEMENT CURVE FOR SPECIMEN P-24 (49.5V-23.3Ti-27.2Fe).

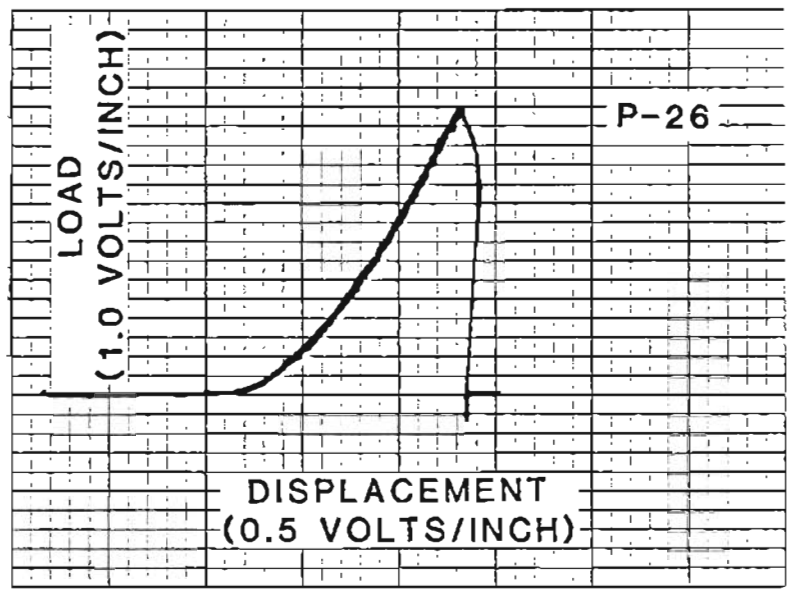

Figure E-23. BEND TESTING LOAD-DISPLACEMENT CURVE FOR SPECIMEN P-26 (47.7V-52.3Fe).

APPENDIX F

BEND TESTING FRACTURE SURFACE MICROGRAPHS

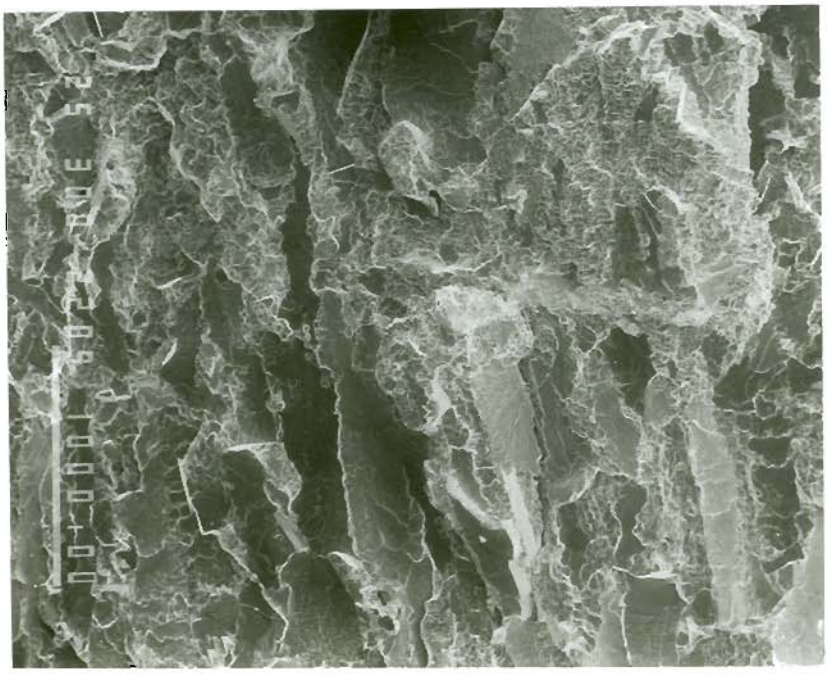

Figure F-1. SEM MICROGRAPH OF FRACTURE SURFACE OF BEND TESTING SPECIMEN P-2 (90.5V-9.5Ti), 30X.

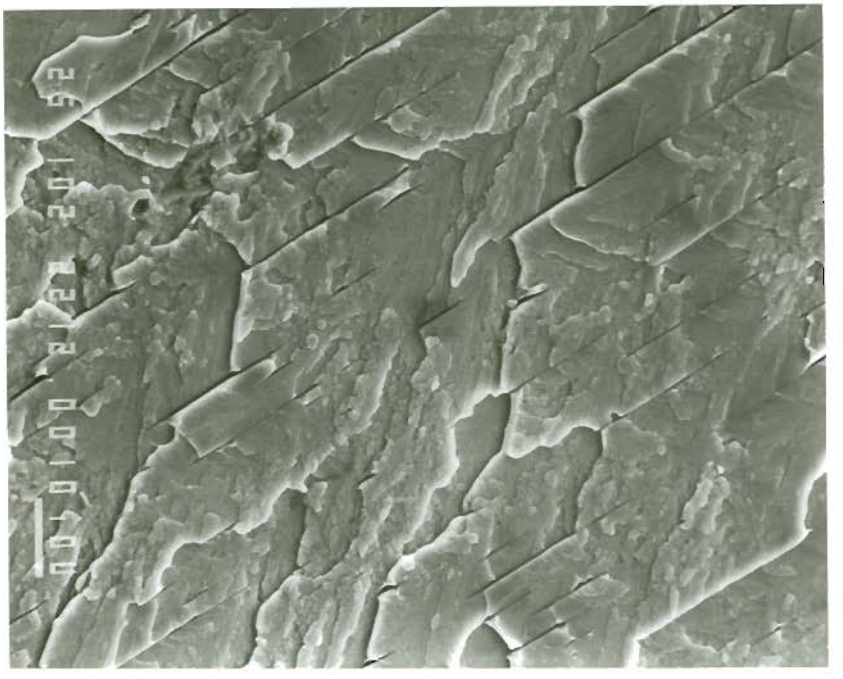

Figure F-2. SEM MICROGRAPH OF FRACTURE SURFACE OF BEND TESTING SPECIMEN P-2 (90.5V-9.5Ti), 1,000X.

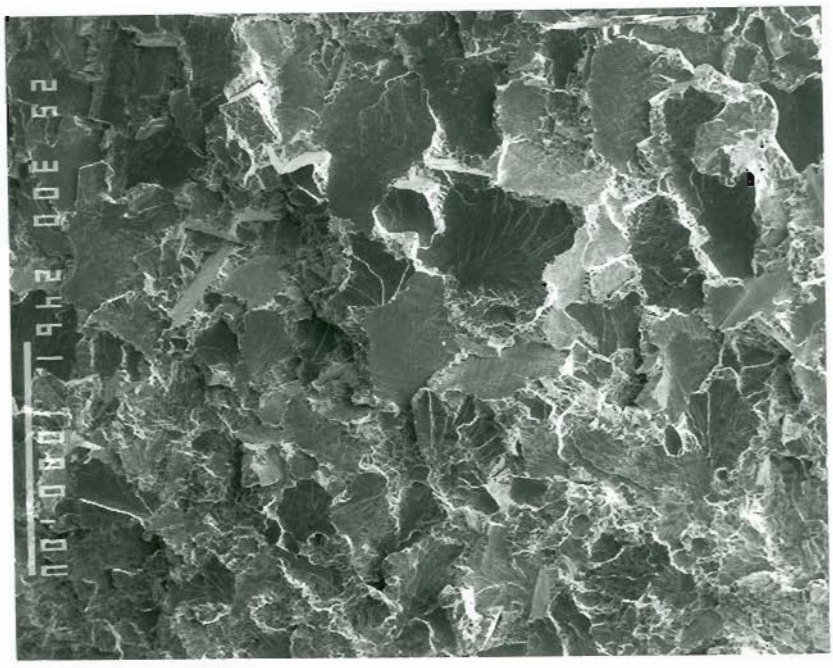

Figure F-3. SEM MICROGRAPH OF FRACTURE SURFACE OF BEND TESTING SPECIMEN P-3 (90.2V-7.1Ti-2.7Fe), 30X.

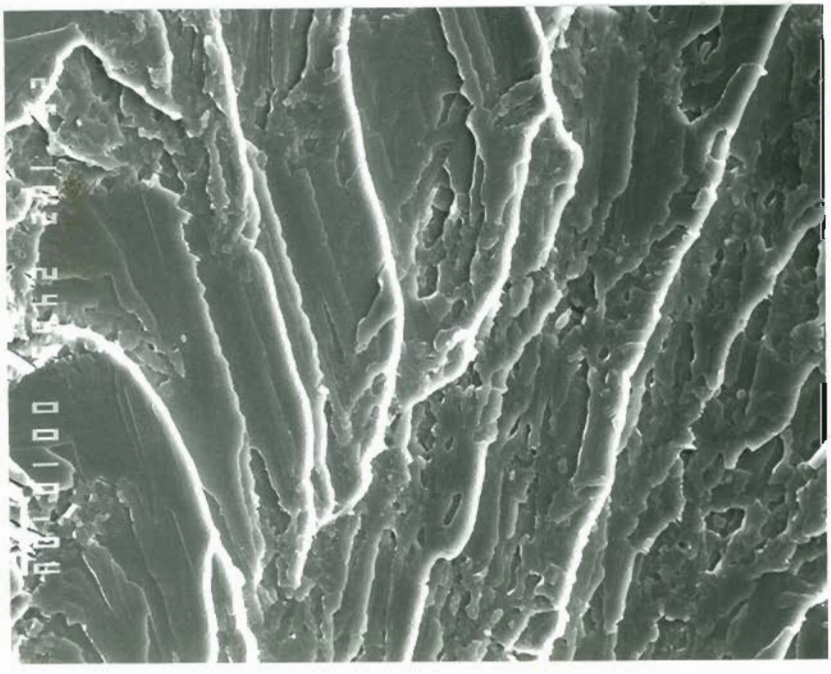

Figure F-4. SEM MICROGRAPH OF FRACTURE SURFACE OF BEND TESTING SPECIMEN P-3 (90.2V-7.1Ti-2.7Fe), 1,000X.

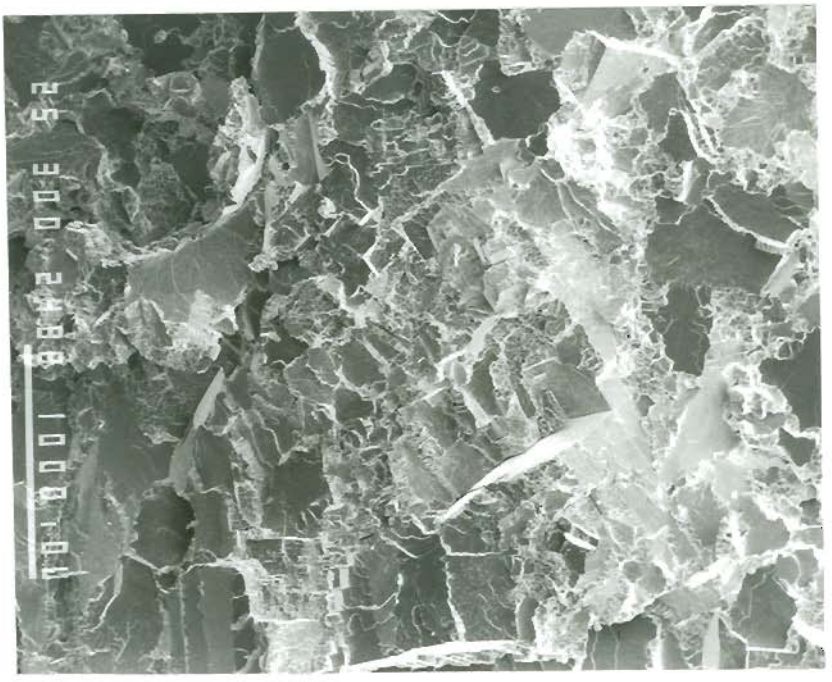

Figure F-5. SEM MICROGRAPH OF FRACTURE SURFACE OF BEND TESTING SPECIMEN P-4 (89.8V-4.7Ti-5.5Fe), 30X.

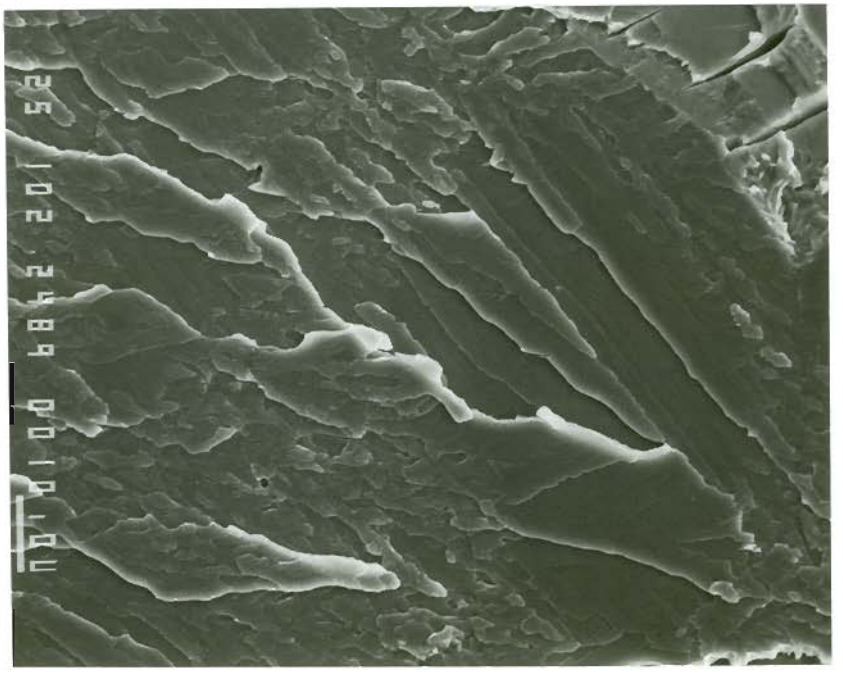

Figure F-6. SEM MICROGRAPH OF FRACTURE SURFACE OF BEND TESTING SPECIMEN P-4 (89.8V-4.7Ti-5.5Fe), 1,000X.

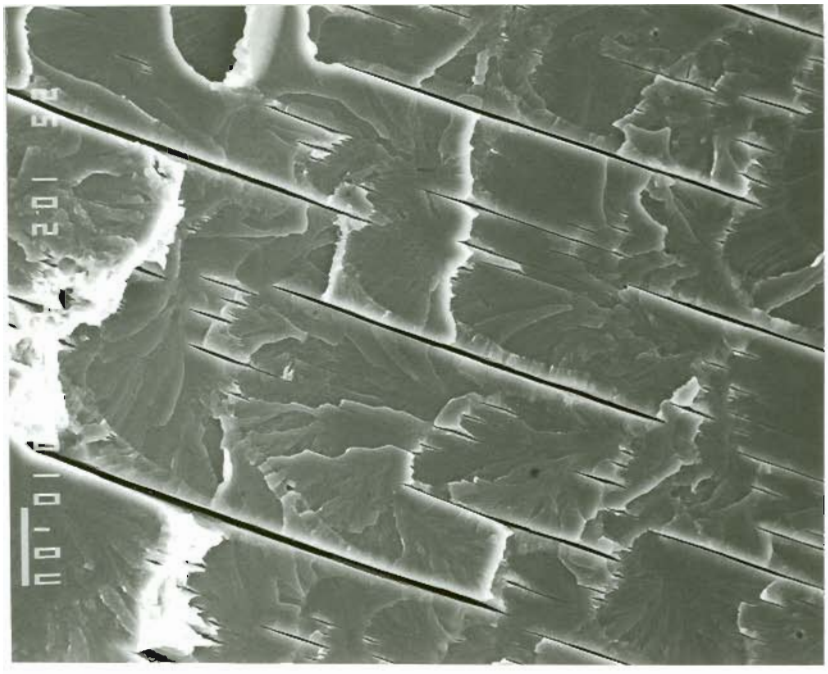

Figure F-7. SEM MICROGRAPH OF FRACTURE SURFACE OF BEND TESTING SPECIMEN P-4 (89.8V-4.7Ti-5.5Fe), 1,000X

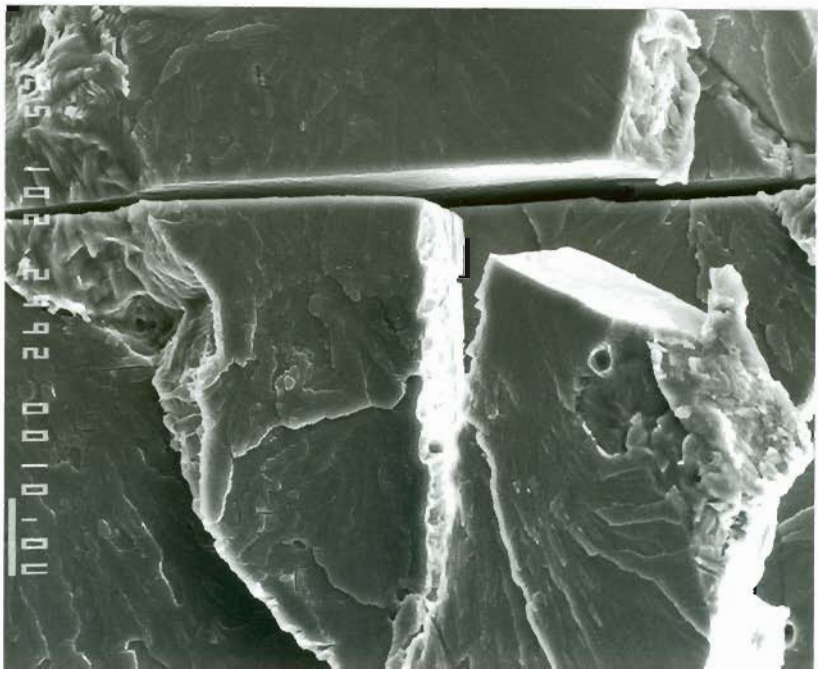

Figure F-8. SEM MICROGRAPH OF FRACTURE SURFACE OF BEND TESTING SPECIMEN P-4 (89.8V-4.7Ti-5.5Fe), 1,000X.

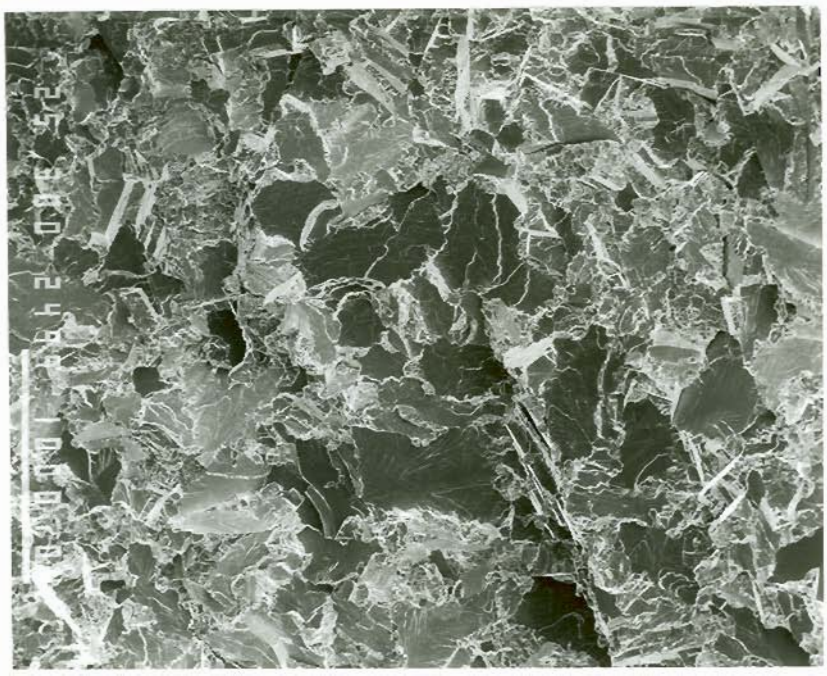

Figure F-9. SEM MICROGRAPH OF FRACTURE SURFACE OF BEND TESTING SPECIMEN P-5 (89.5V-2.3Ti-8.2Fe), 30X.

Figure F-10. SEM MICROGRAPH OF FRACTURE SURFACE OF BEND TESTING SPECIMEN P-5 (89.5V-2.3Ti-8.2Fe), 1,000X.

Figure F-11. SEM MICROGRAPH OF FRACTURE SURFACE OF BEND TESTING SPECIMEN P-7 (81.0V-19.0Ti), 30X.

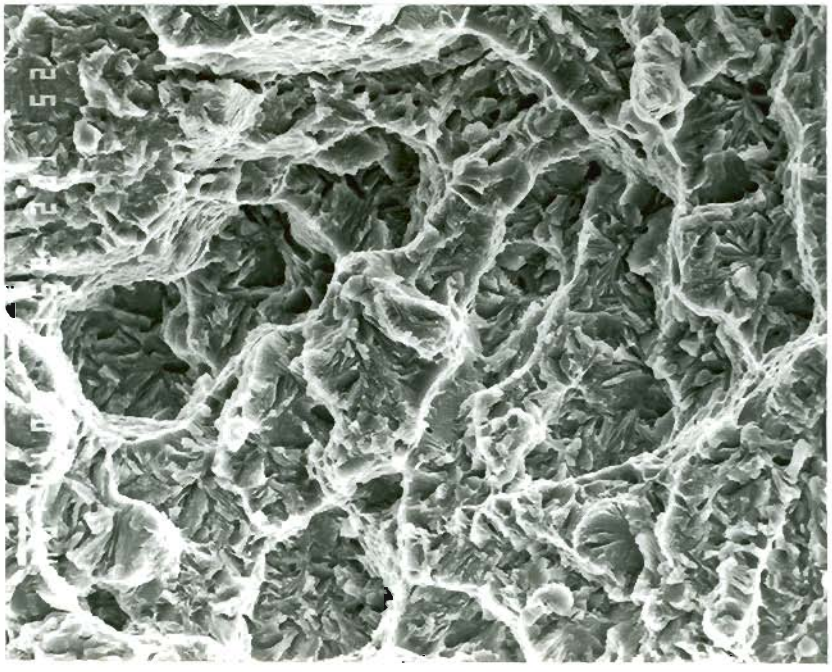

Figure F-12. SEM MICROGRAPH OF FRACTURE SURFACE OF BEND TESTING SPECIMEN P-7 (81.0V-19.0Ti), 1,000X.

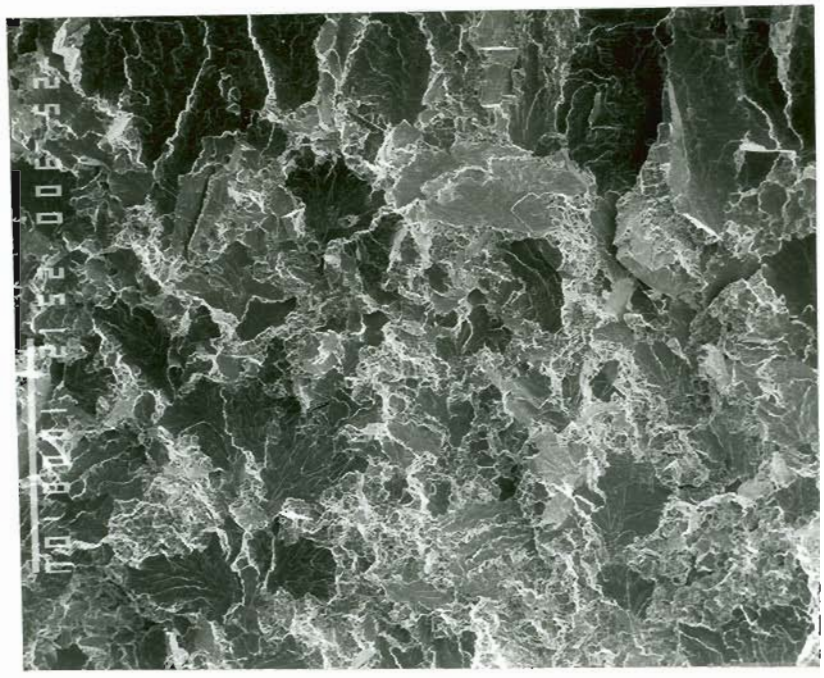

Figure F-13. SEM MICROGRAPH OF FRACTURE SURFACE OF BEND TESTING SPECIMEN P-8 (80.3V-14.2Ti-5.5Fe), 30X.

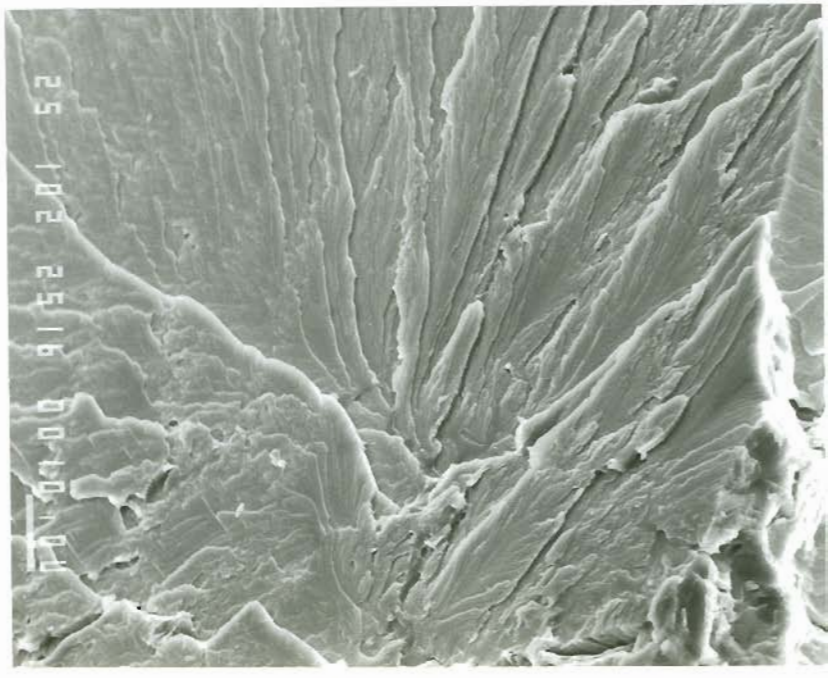

Figure F-14. SEM MICROGRAPH OF FRACTURE SURFACE OF BEND TESTING SPECIMEN P-8 (80.3V-14.2Ti-5.5Fe), 1,000X.

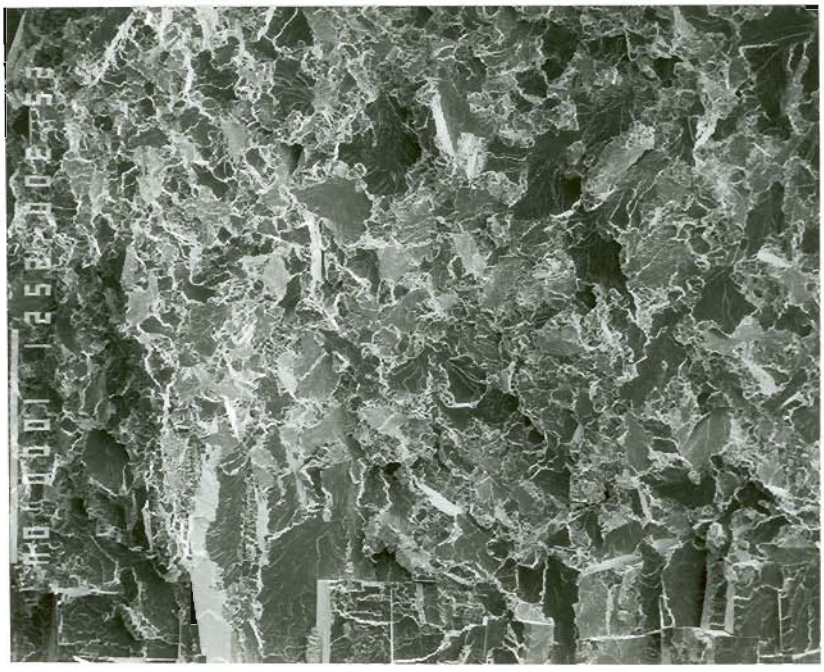

Figure F-15. SEM MICROGRAPH OF FRACTURE SURFACE OF BEND TESTING SPECIMEN P-9 (79.7V-9.4Ti-10.9Fe), 30X.

Figure F-16. SEM MICROGRAPH OF FRACTURE SURFACE OF BEND TESTING SPECIMEN P-9 (79.7V-9.4Ti-10.9Fe), 1,000X.

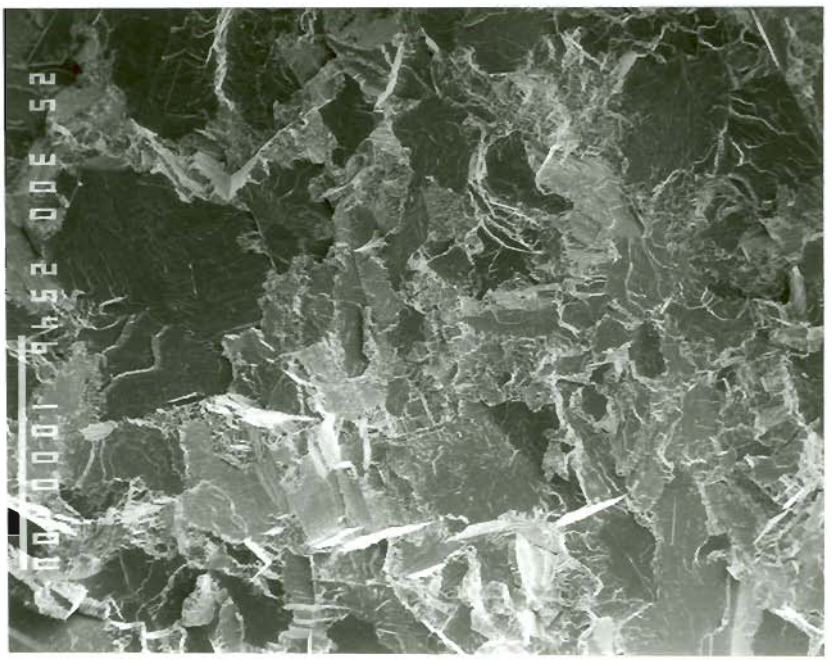

Figure F-17. SEM MICROGRAPH OF FRACTURE SURFACE OF BEND TESTING SPECIMEN P-10 (79.1V-4.6Ti-16.3Fe), 30X.

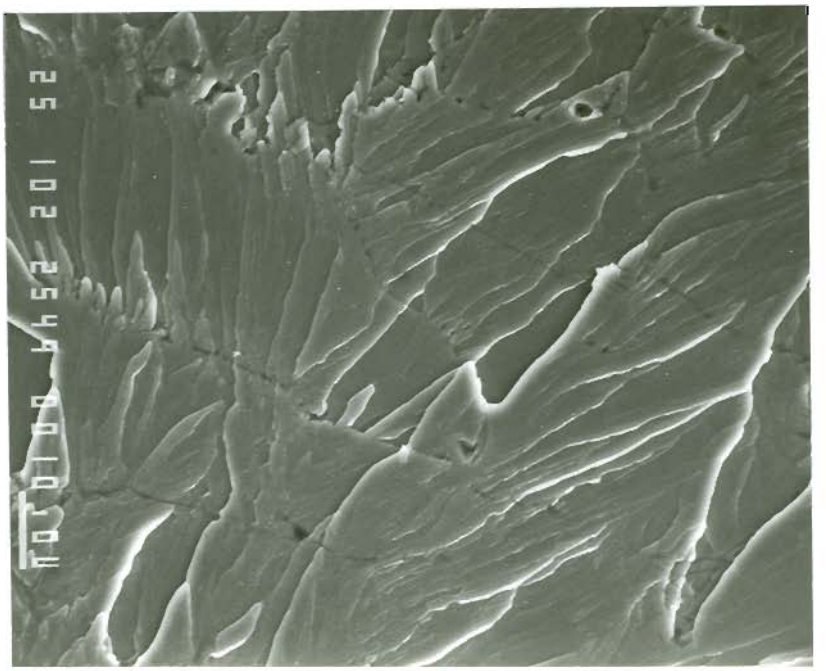

Figure F-18. SEM MICROGRAPH OF FRACTURE SURFACE OF BEND TESTING SPECIMEN P-10 (79.1V-4.6Ti-16.3Fe), 1,000X.

Figure F-19. SEM MICROGRAPH OF FRACTURE SURFACE OF BEND TESTING SPECIMEN P-11 (78.5V-21.5Fe), 30X.

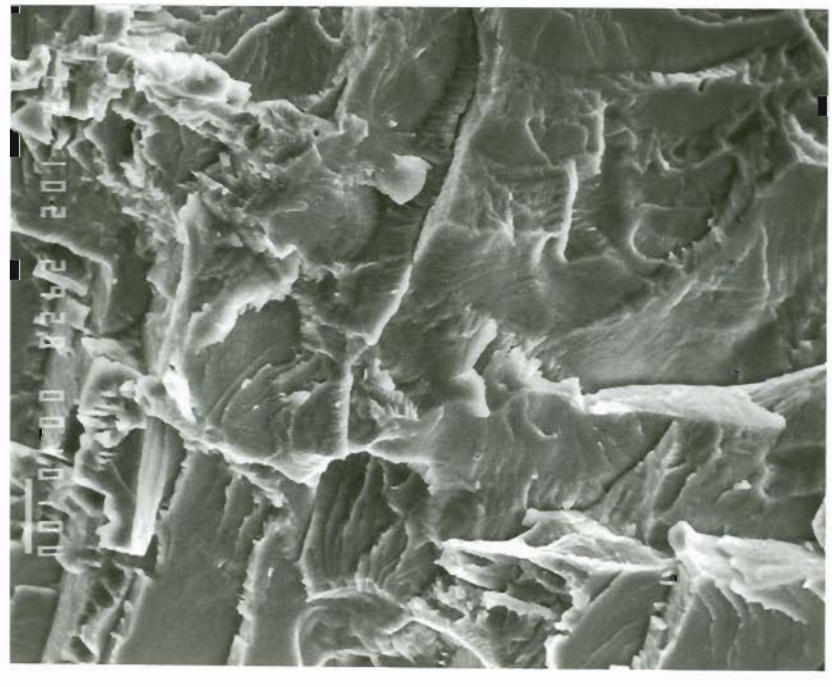

Figure F-20. SEM MICROGRAPH OF FRACTURE SURFACE OF BEND TESTING SPECIMEN P-11 (78.5V-21.5Fe), 1,000X.

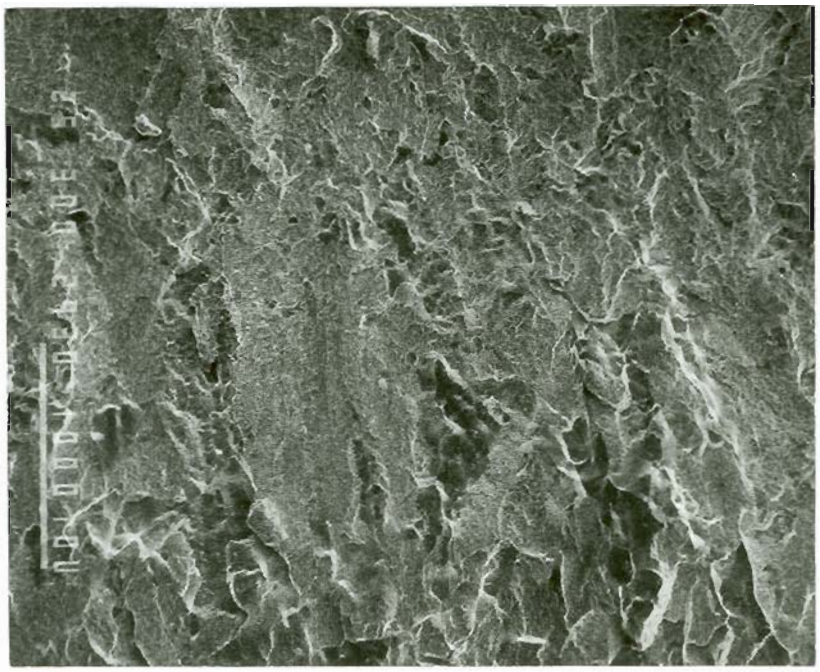

Figure F-21. SEM MICROGRAPH OF FRACTURE SURFACE OF BEND TESTING SPECIMEN P-12 (71.3V-28.7Ti), 30X.

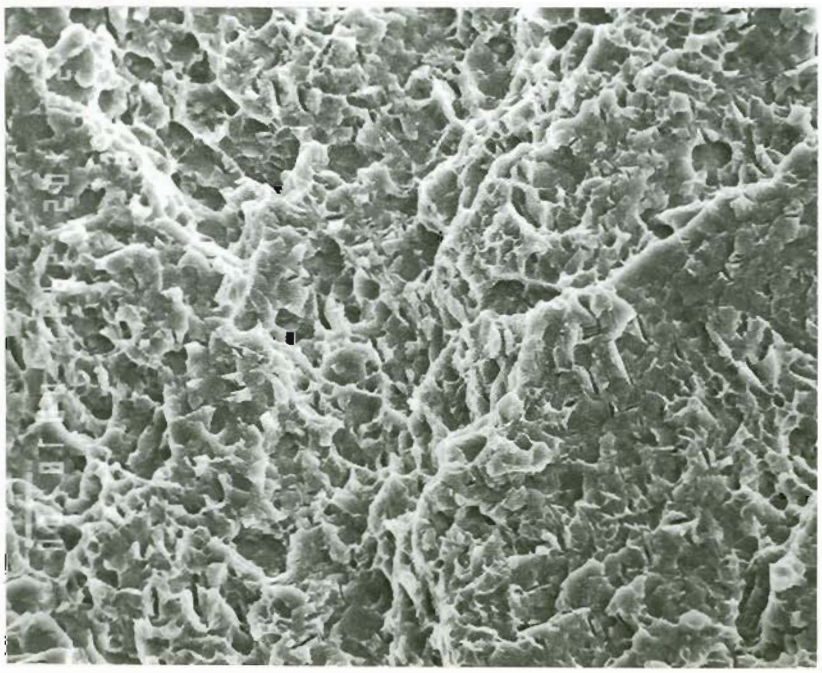

Figure F-22. SEM MICROGRAPH OF FRACTURE SURFACE OF BEND TESTING SPECIMEN P-12 (71.3V-28.7Ti), 1,000X.

Figure F-23. SEM MICROGRAPH OF FRACTURE SURFACE OF BEND TESTING SPECIMEN P-13 (70.4V-21.3Ti-8.3Fe), 30X.

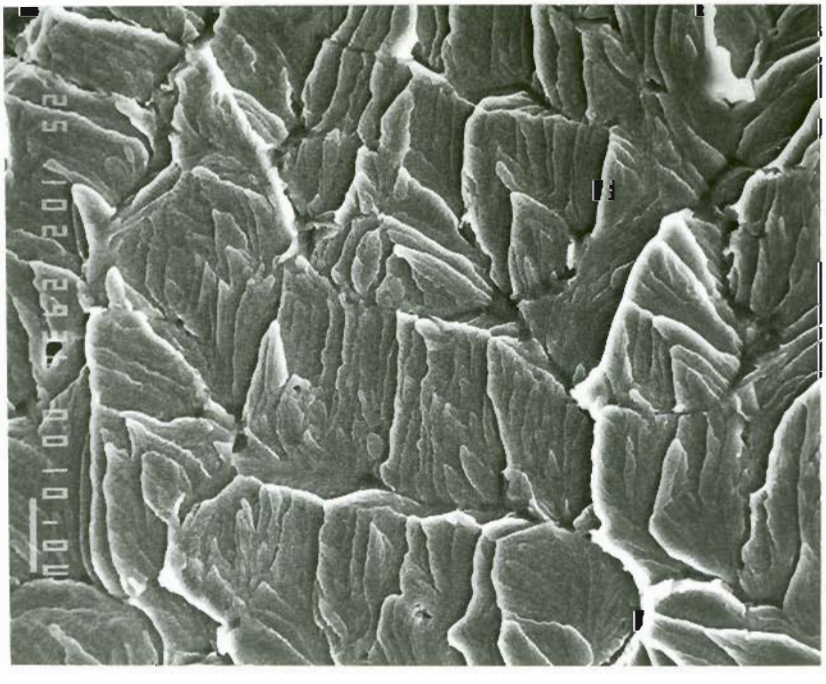

Figure F-24. SEM MICROGRAPH OF FRACTURE SURFACE OF BEND TESTING SPECIMEN P-13 (70.4V-21.3Ti-8.3Fe), 1,000X.

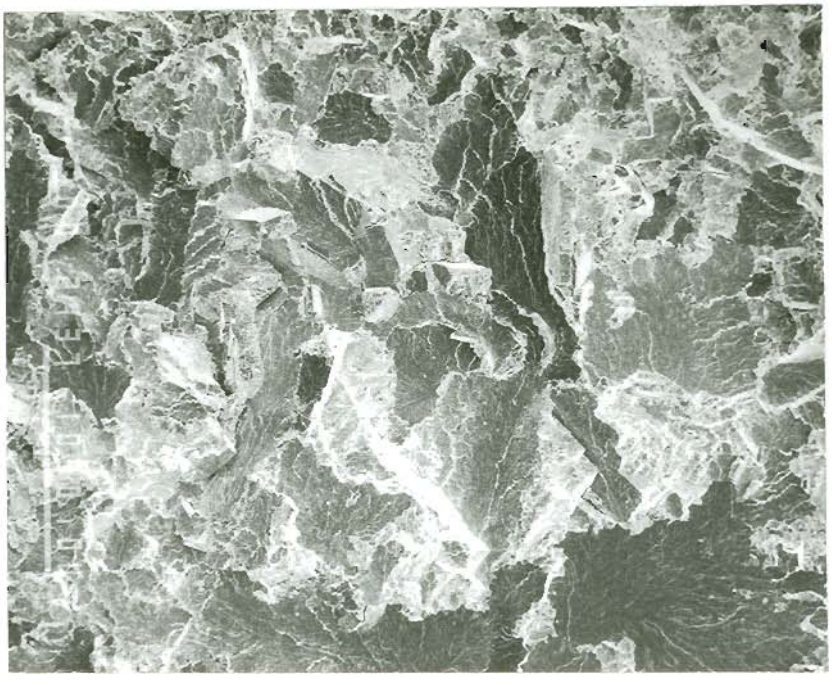

Figure F-25. SEM MICROGRAPH OF FRACTURE SURFACE OF BEND TESTING SPECIMEN P-14 (69.6V-14.0Ti-16.4Fe), 30X.

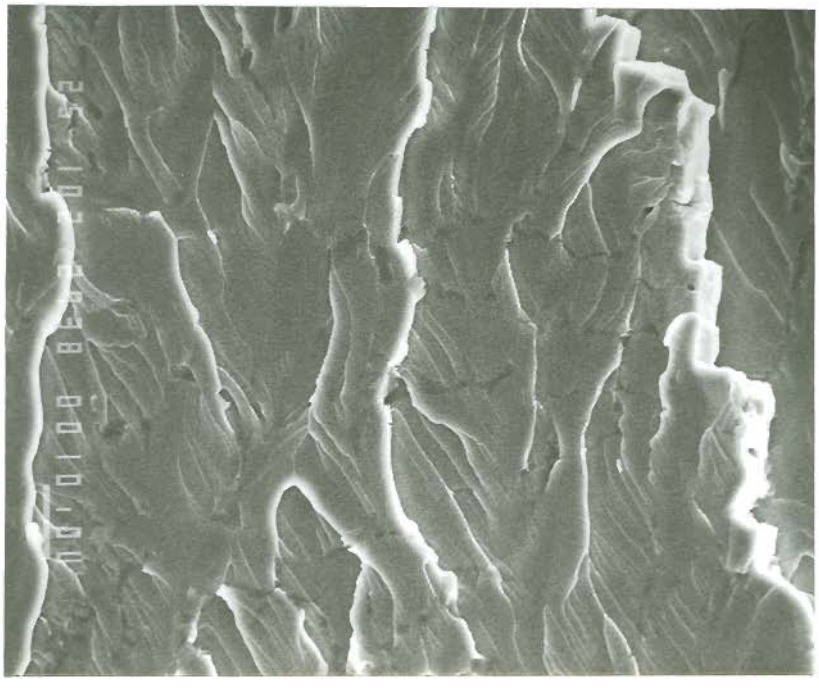

Figure F-26. SEM MICROGRAPH OF FRACTURE SURFACE OF BEND TESTING SPECIMEN P-14 (69.6V-14.0Ti-16.4Fe), 1,000X.

Figure F-27. SEM MICROGRAPH OF FRACTURE SURFACE OF BEND TESTING SPECIMEN P-15 (68.8V-6.9Ti-24.3Fe), 30X.

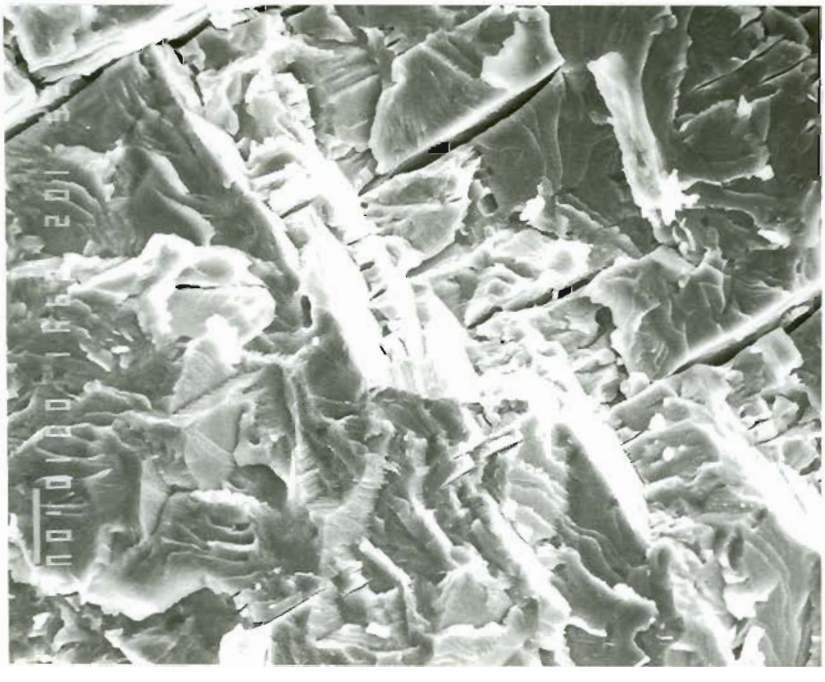

Figure F-28. SEM MICROGRAPH OF FRACTURE SURFACE OF BEND TESTING SPECIMEN P-15 (68.8V-6.9Ti-24.3Fe), 1,000X.

Figure F-29. SEM MICROGRAPH OF FRACTURE SURFACE OF BEND TESTING SPECIMEN P-16 (68.0V-32.0Fe), 30X.

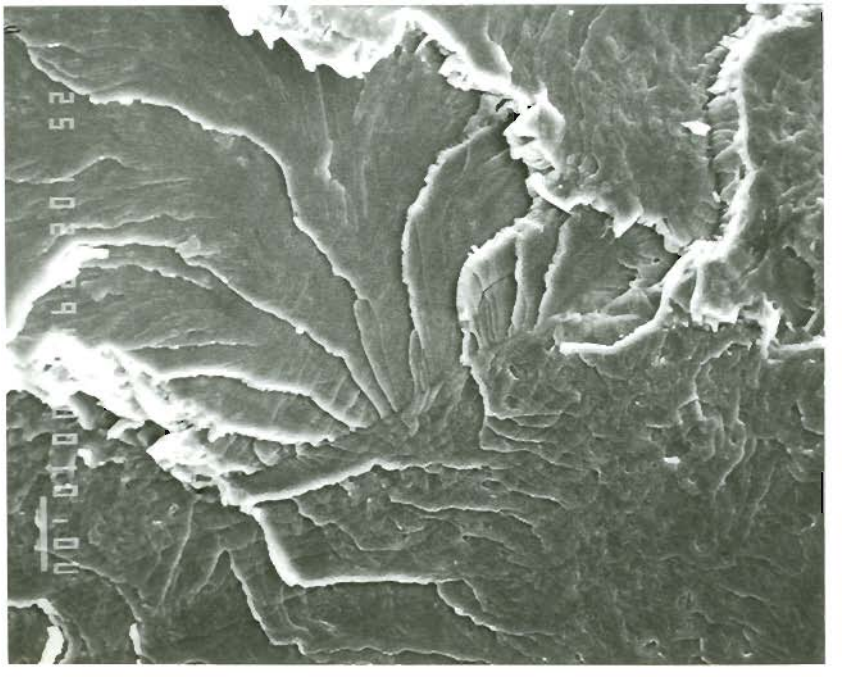

Figure F-30. SEM MICROGRAPH OF FRACTURE SURFACE OF BEND TESTING SPECIMEN P-16 (68.0V-32.0Fe), 1,000X.

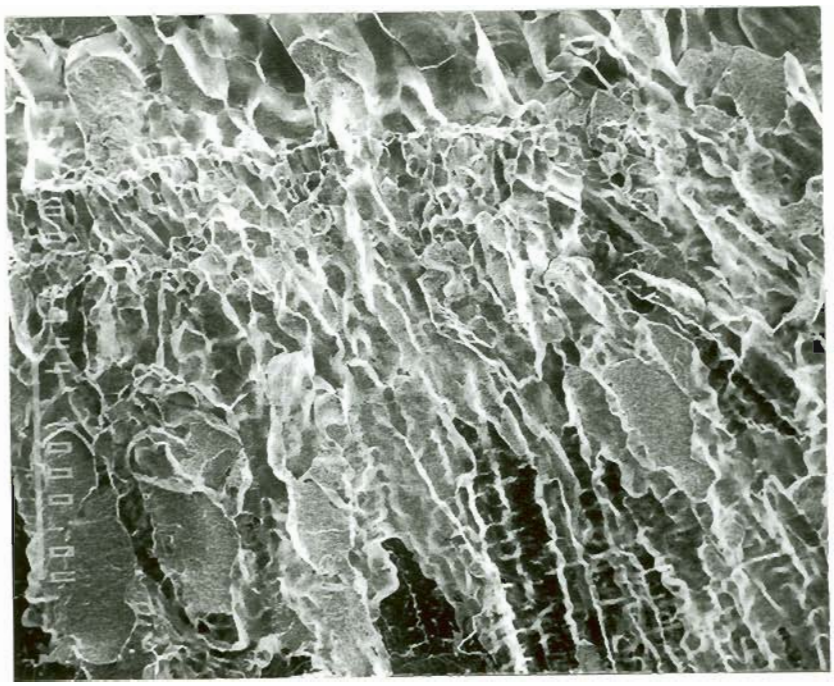

Figure F-31. SEM MICROGRAPH OF FRACTURE SURFACE OF BEND TESTING SPECIMEN P-17 (61.5V-38.5Ti), 30X.

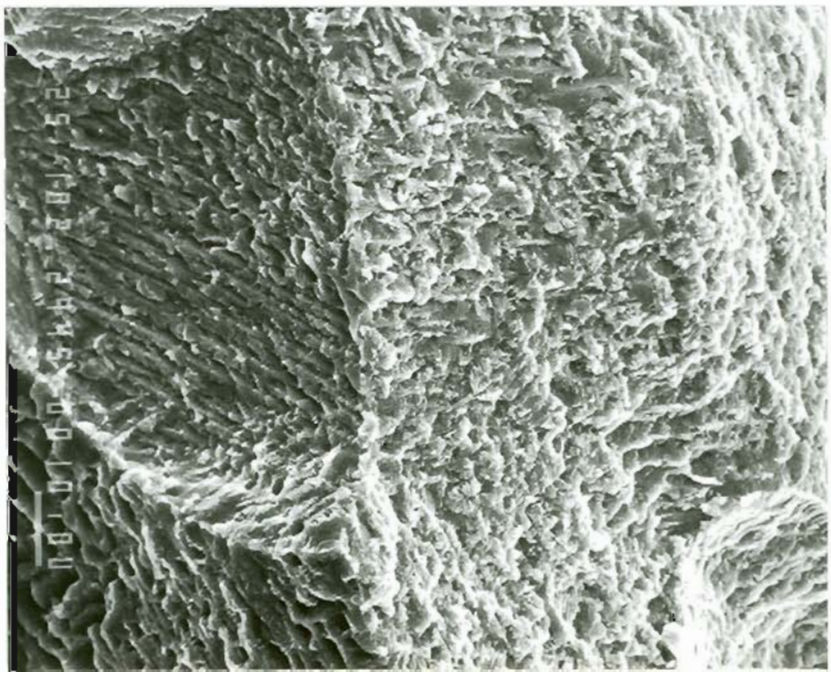

Figure F-32. SEM MICROGRAPH OF FRACTURE SURFACE OF BEND TESTING SPECIMEN P-17 (61.5V-38.5Ti), 1,000X.

Figure F-33. SEM MICROGRAPH OF FRACTURE SURFACE OF BEND TESTING SPECIMEN P-18 (60.5V-28.4Ti-11.1Fe), 30x.

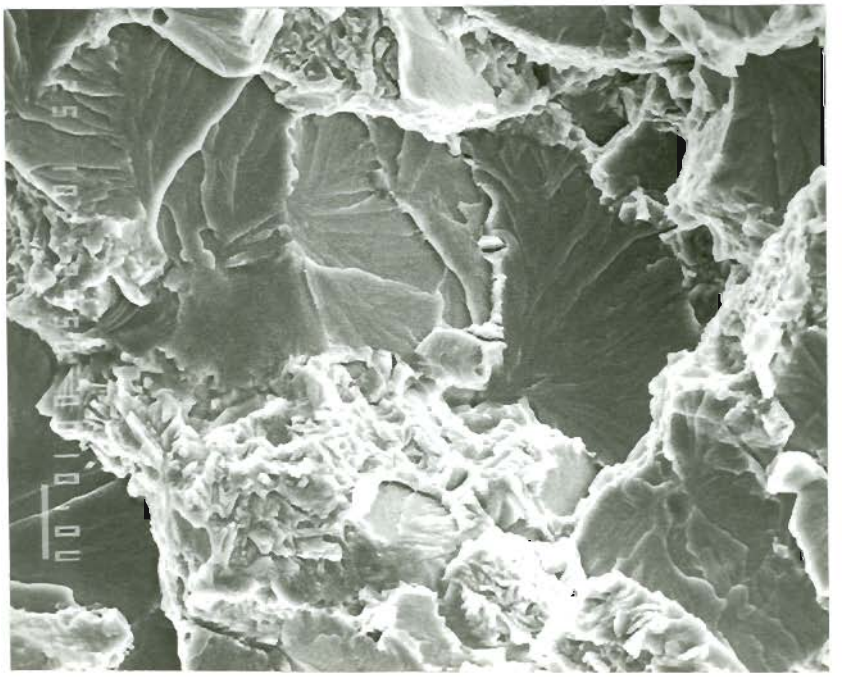

Figure F-34. SEM MICROGRAPH OF FRACTURE SURFACE OF BEND TESTING SPECIMEN P-18 (60.5V-28.4Ti-11.1Fe), 1,000X.

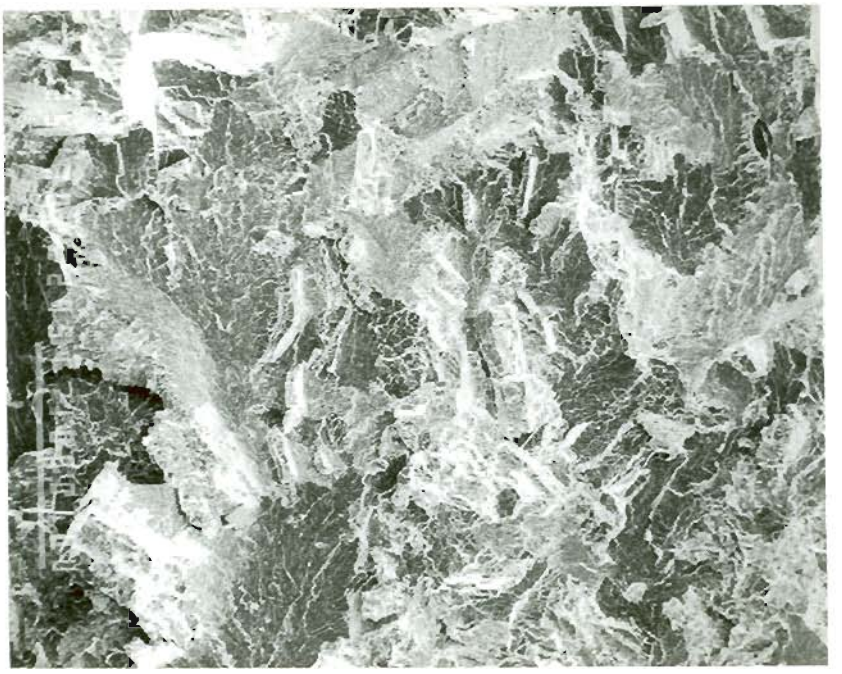

Figure F-35. SEM MICROGRAPH OF FRACTURE SURFACE OF BEND TESTING SPECIMEN P-19 (59.5V-18.7Ti-21.8Fe), 30X.

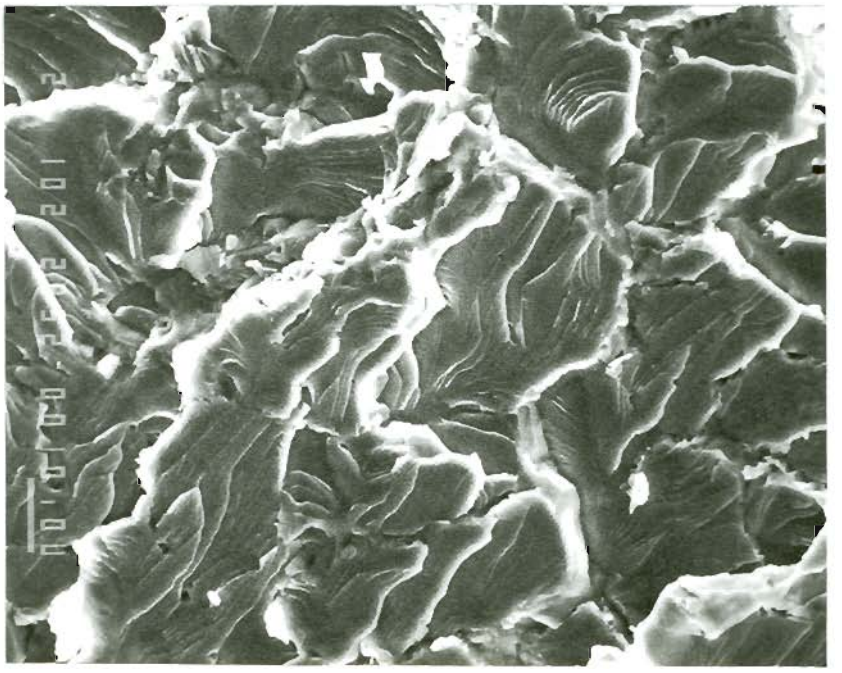

Figure F-36. SEM MICROGRAPH OF FRACTURE SURFACE OF BEND TESTING SPECIMEN P-19 (59.5V-18.7Ti-21.8Fe), 1,000X.

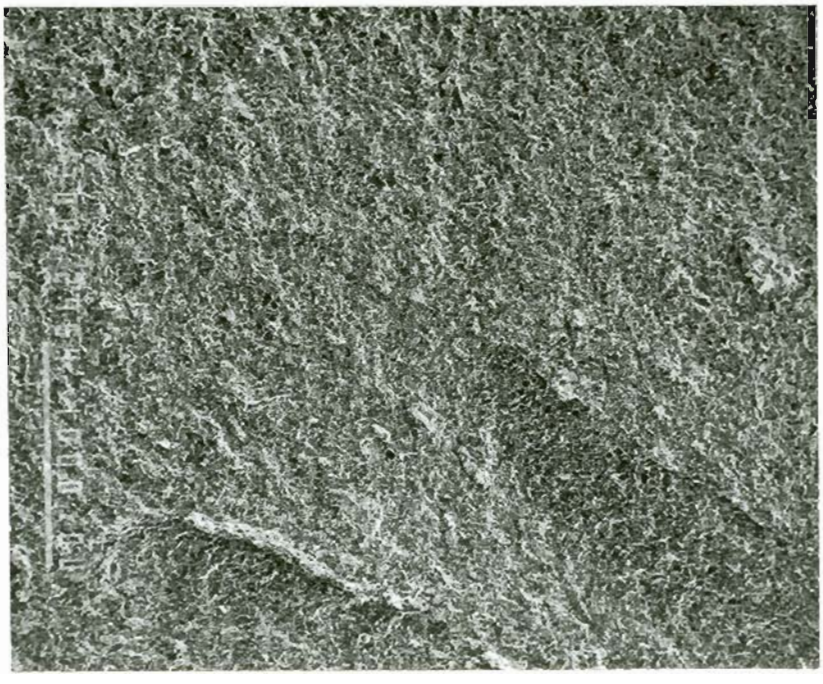

Figure F-37. SEM MICROGRAPH OF FRACTURE SURFACE OF BEND TESTING SPECIMEN P-20 (58.6V-9.2Ti-32.2Fe), 30X.

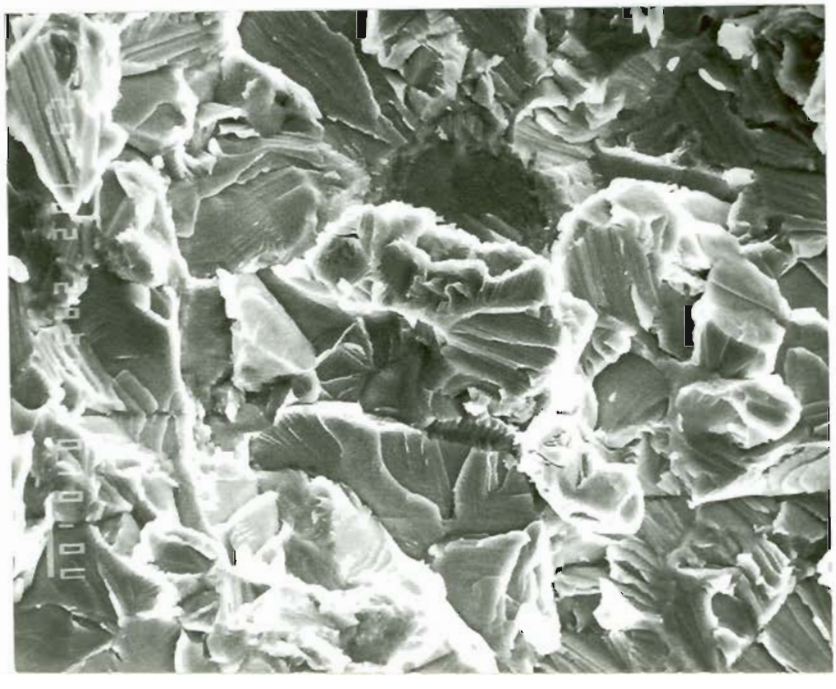

Figure F-38. SEM MICROGRAPH OF FRACTURE SURFACE OF BEND TESTING SPECIMEN P-20 (58.6V-9.2Ti-32.2Fe), 1,000X.

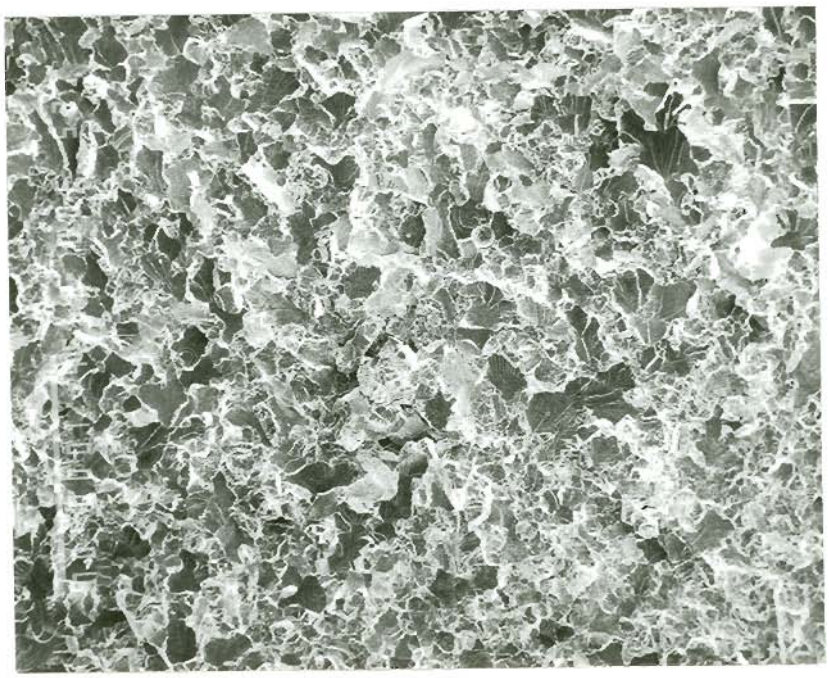

Figure F-39. SEM MICROGRAPH OF FRACTURE SURFACE OF BEND TESTING SPECIMEN P-21 (57.8V-42.2Fe), 30X.

Figure F-40. SEM MICROGRAPH OF FRACTURE SURFACE OF BEND TESTING SPECIMEN P-21 (57.8V-42.2Fe), 1,000X.

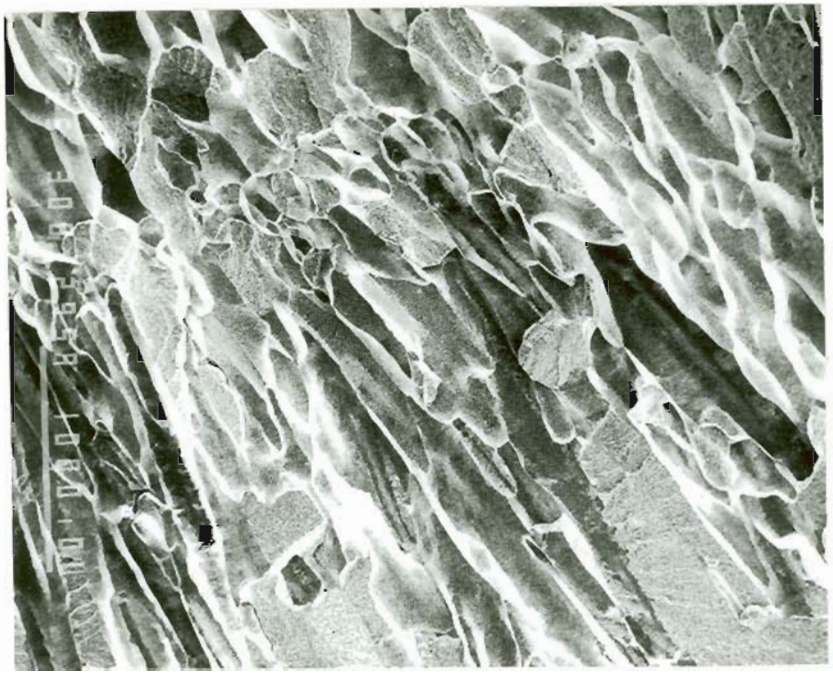

Figure F-41. SEM MICROGRAPH OF FRACTURE SURFACE OF BEND TESTING SPECIMEN P-22 (51.5V-48.5Ti), 30X.

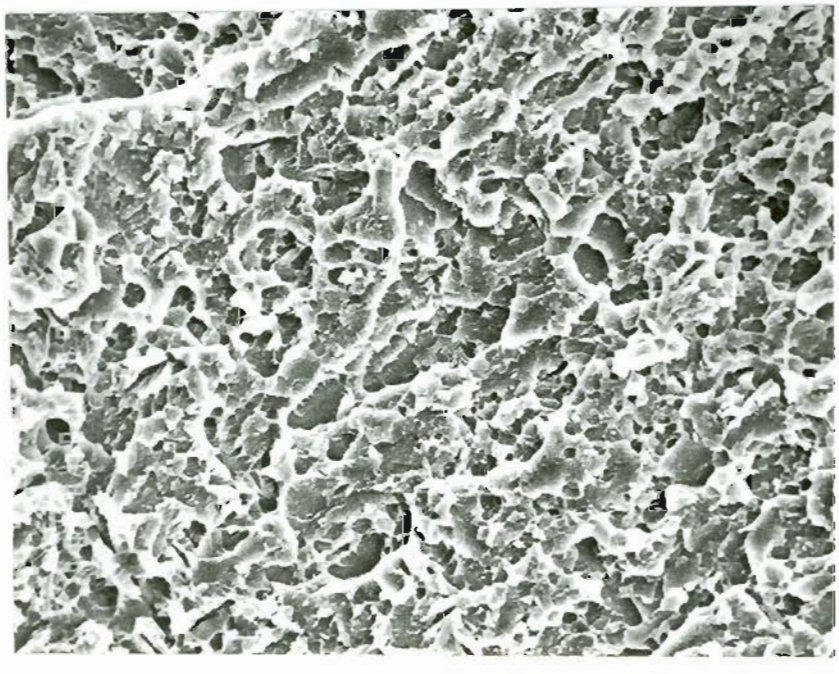

Figure F-42. SEM MICROGRAPH OF FRACTURE SURFACE OF BEND TESTING SPECIMEN P-22 (51.5V-48.5Ti), 1,000X.

Figure F-43. SEM MICROGRAPH OF FRACTURE SURFACE OF BEND TESTING SPECIMEN P-23 (50.5V-35.6Ti-13.9Fe), 30X.

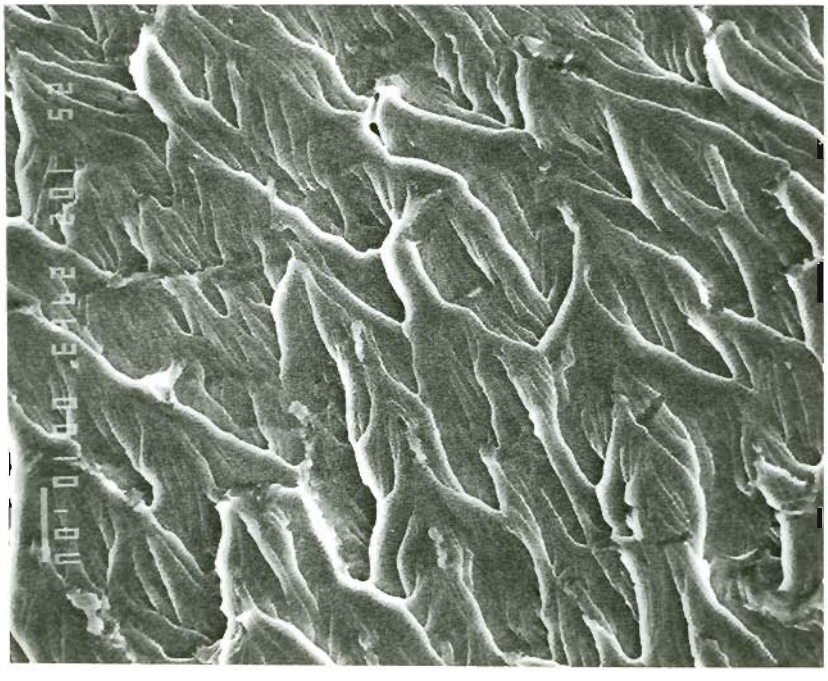

Figure F-44. SEM MICROGRAPH OF FRACTURE SURFACE OF BEND TESTING SPECIMEN P-23 (50.5V-35.6Ti-13.9Fe), 1,000X.

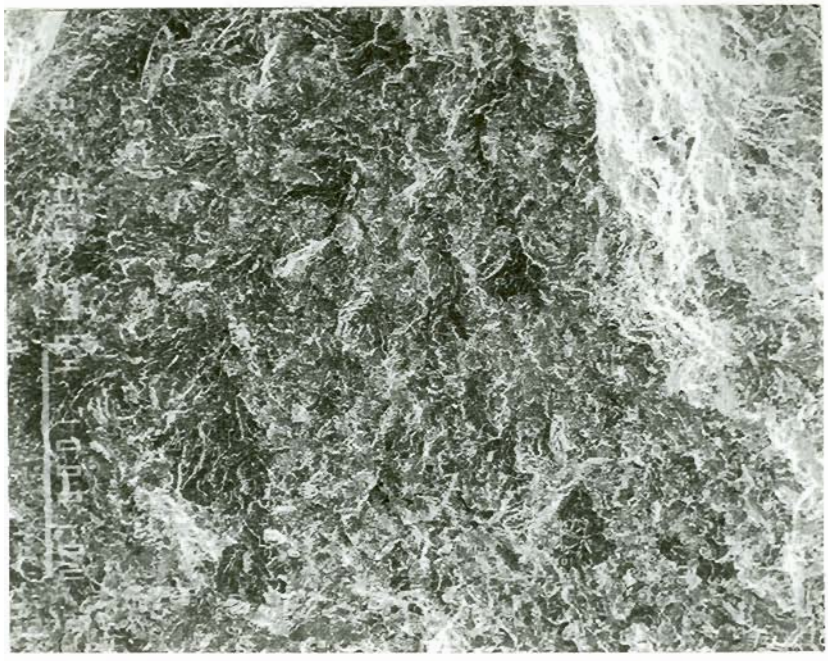

Figure F-45. SEM MICROGRAPH OF FRACTURE SURFACE OF BEND TESTING SPECIMEN P-24 (49.5V-23.3Ti-27.2Fe), 30X.

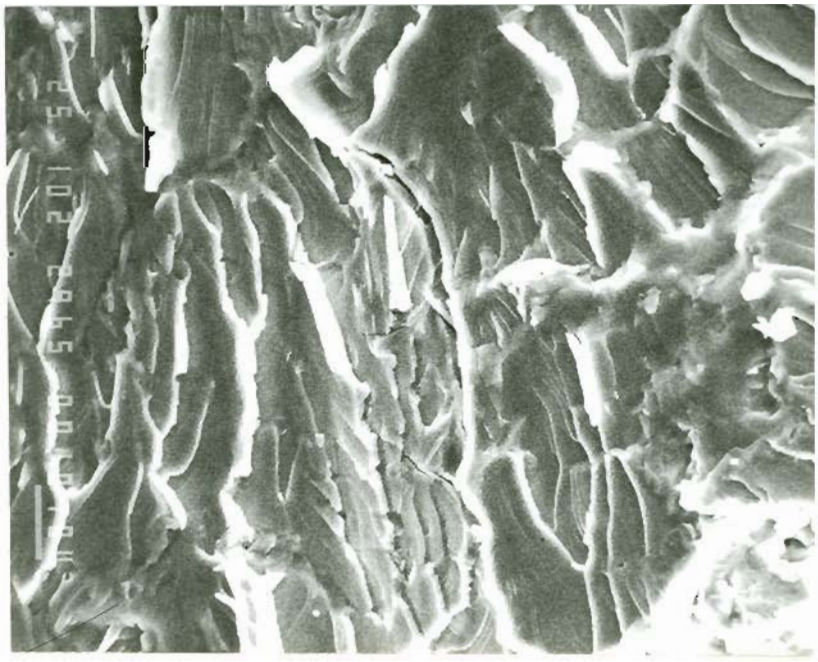

Figure F-46. SEM MICROGRAPH OF FRACTURE SURFACE OF BEND TESTING SPECIMEN P-24 (49.5V-23.3Ti-27.2Fe), 1,000X.

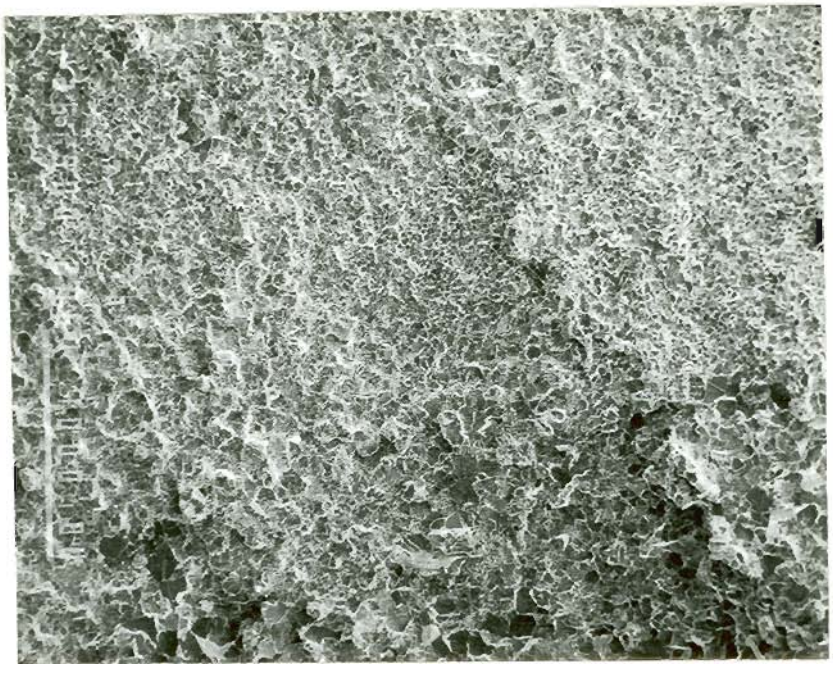

Figure F-47. SEM MICROGRAPH OF FRACTURE SURFACE OF BEND TESTING SPECIMEN P-26 (47.7V-52.3Fe), 30X.

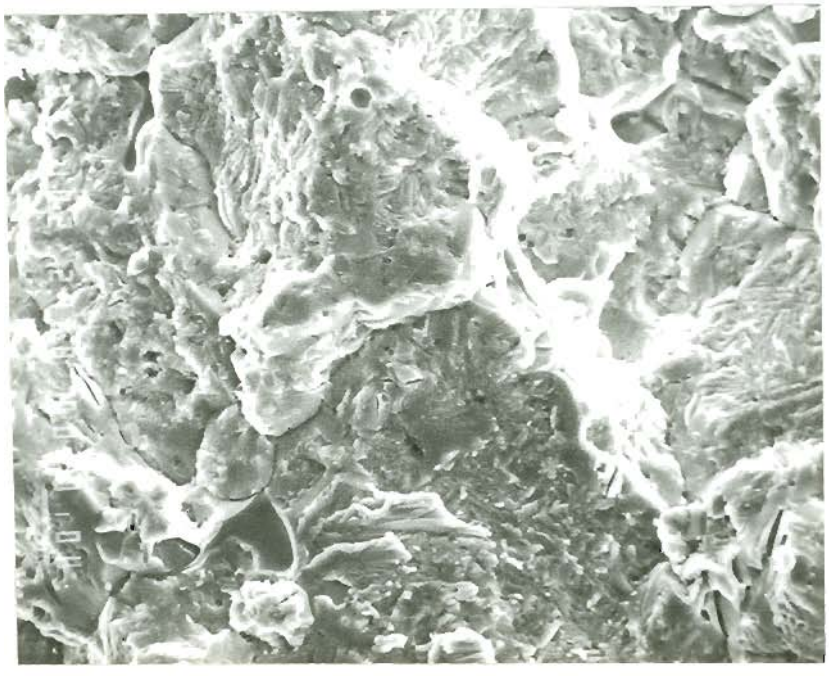

Figure F-48. SEM MICROGRAPH OF FRACTURE SURFACE OF BEND TESTING SPECIMEN P-26 (47.7V-52.3Fe), 1,000X.

BIOGRAPHICAL NOTE

John LeRoy Johnsen was born in Fresno, California, on 10 October 1933. He graduated from Roosevelt High School in 1951 and attended Fresno State College, prior to entering the U.S. Military Academy at West Point in 1952. He graduated from West Point and received a Bachelor of Science Degree in Engineering in 1956. Following his graduation from West Point, he entered the Armor branch of the Army, where he served for the next twenty years.

During this period, he commanded armored tactical units from platoon through battalion and served in staff positions at various levels, including the Office of the Chief of Research and Development and the Office of the Chief of Staff of the Army. In addition, he attended numerous military and civilian schools, including the U.S. Army Command and General Staff College in Leavenworth, Kansas, and Stevens Institute of Technology in Hoboken, New Jersey. He received the degree of Master of Engineering, Mechanical from Stevens Institute of Technology in 1971.

In 1977, a year following his retirement from the Army, he joined the Materials Science Department of the Oregon Graduate Center, where he worked initially as a laboratory technician and later as a senior research engineer. On 1 July 1981, he became a full-time graduate student research assistant, to pursue the degree of Doctor of Philosophy in Materials Science and Engineering.

He is married to Mary P. Johnsen, the former Mary Helene Pigott of Northford, Connecticut, who is now President of Racquet Sports Associates, Inc., an international racquet sports consulting firm located in Portland, Oregon. He has four sons: James, John (deceased), David, and Erik.

On 1 September 1985, he will depart the Oregon Graduate Center to assume a position as assistant professor of mechanical engineering at the University of Portland.